SANDIA REPORT
SAND2006–4914
Unlimited Release
Printed August 2006

Circulating Fluidized Bed Hydrodynamics Experiments for the Multiphase Fluid Dynamics Research Consortium (MFDRC)

Timothy J. O'Hern, Steven M. Trujillo, John R. Torczynski, Paul R. Tortora, John B. Oelfke, and Satish Bhusarapu

Prepared by
Sandia National Laboratories
Albuquerque, New Mexico 87185 and Livermore, California 94550

Sandia is a multiprogram laboratory operated by Sandia Corporation, a Lockheed Martin Company, for the United States Department of Energy's National Nuclear Security Administration under Contract DE-AC04-94AL85000.

Issued by Sandia National Laboratories, operated for the United States Department of Energy by Sandia Corporation.

Available to DOE and DOE contractors from
U.S. Department of Energy
Office of Scientific and Technical Information
P.O. Box 62
Oak Ridge, TN 37831

Telephone: (865)576-8401
Facsimile: (865)576-5728
E-Mail: reports@adonis.osti.gov
Online ordering: http://www.doe.gov/bridge

Available to the public from
U.S. Department of Commerce
National Technical Information Service
5285 Port Royal Rd
Springfield, VA 22161

Telephone: (800)553-6847
Facsimile: (703)605-6900
E-Mail: orders@ntis.fedworld.gov
Online ordering: http://www.ntis.gov/help/ordermethods.asp?loc=7-4-0#online

SAND2006-4914
Unlimited Release
Printed August 2006

Circulating Fluidized Bed Hydrodynamics Experiments for the Multiphase Fluid Dynamics Research Consortium (MFDRC)

Timothy J. O'Hern, Steven M. Trujillo, John R. Torczynski, Paul R. Tortora, John B. Oelfke
Engineering Sciences Center
Sandia National Laboratories
P.O. Box 5800
Albuquerque, NM 87185-0834

Satish Bhusarapu
Harper International Corporation
100 West Drullard Avenue
Lancaster, NY 14086

Abstract

An experimental program was conducted to study the multiphase gas-solid flow in a pilot-scale circulating fluidized bed (CFB). This report describes the CFB experimental facility assembled for this program, the diagnostics developed and/or applied to make measurements in the riser section of the CFB, and the data acquired for several different flow conditions. Primary data acquired included pressures around the flow loop and solids loadings at selected locations in the riser. Tomographic techniques using gamma radiation and electrical capacitance were used to determine radial profiles of solids volume fraction in the riser, and axial profiles of the integrated solids volume fraction were produced. Computer Aided Radioactive Particle Tracking was used to measure solids velocities, fluxes, and residence time distributions. In addition, a series of computational fluid dynamics simulations was performed using the commercial code *Arena-flow*™.

Acknowledgment

This has been a multiyear program with many laboratory, industrial, academic, and government partners too numerous to mention by name. However, several individuals are deserving of special recognition. The authors are especially grateful to Art Ratzel of Sandia National Laboratories for his efforts in initiating the Multiphase Fluid Dynamics Research Consortium (MFDRC) and managing the early years of this program. Mike Prairie of Sandia National Laboratories provided excellent technical management over the second half of the program. Tyler Thompson of the Dow Chemical Company is acknowledged as a strong leader from the initiation throughout the lifetime of the MFDRC. Ray Cocco and Bruce Hook of Dow Chemical Company provided a very knowledgeable industrial application link and were instrumental in the design of the Sandia Circulating Fluidized Bed (CFB). Rutton Patel of ExxonMobil Research also provided valuable insights in the experiment design and was always helpful throughout the program. Ted Knowlton and Reddy Karri of Particulate Solid Research Inc. (PSRI) helped us to recognize and resolve several operational limitations. Wen-Ching Yang and Dale Kearns of Westinghouse provided valuable hardware from an existing CFB along with a great deal of advice on how best to use it to assemble the Sandia CFB. Thanks also to Paul Merz of Chevron Oil Co. for the fluid catalytic cracking (FCC) catalyst particles.

Bucky Kashiwa and Brian VanderHeyden of Los Alamos National Laboratory were close collaborators in the MFDRC. Their early CFDLIB simulations were instrumental in designing portions of the Sandia CFB, and their insightful questions about the experimental work kept our group on track. Jim Fort and David Pfund of Pacific Northwest National Laboratory were important collaborators on diagnostic development and implementation. Tom O'Brien of the National Energy Technology Laboratory (NETL, Morgantown) was a continuing source of good ideas on what types of experiments were most needed, and Jerry Boyle (NETL, Morgantown) donated gamma detection equipment in the early stages of the project. Stuart Daw of Oak Ridge National Laboratory provided helpful discussions of the data acquisition and analysis procedures. Ken Williams and Dale Snider of Arena-flow, LLC, provided expert guidance in applying the gas-particle simulation code *Arena-flow*™ to the Sandia CFB.

Academic partners included Jennifer Sinclair Curtis of the University of Florida, Sankaran Sundaresan of Princeton University, Mike Dudukovic and Muthanna Al-Dahhan of Washington University in St. Louis (WUStL), and Dimitri Gidaspow of the Illinois Institute of Technology (IIT). Professor Steven Ceccio of the University of Michigan collaborated closely on the development and implementation of the electrical-impedance tomography system.

The authors especially want to acknowledge the excellent technical support at Sandia National Laboratories of Tom Grasser, Ray Cote, Lindsey Evans, Rocky Erven, and John O'Hare in the setup and operation of the CFB. Thanks also to Anthony Giunta, member of the DAKOTA development team at Sandia, for his tutoring in the use of DAKOTA. Dan Lucero of Sandia was extremely generous and gracious in loaning gamma detection electronics for use in this project. Susan Vosburg of Sandia's Radiation Protection group was very helpful in preparing for and undertaking CARPT and gamma densitometry tomography experiments.

Kim Shollenberger, now on the faculty of the California Polytechnic University, San Luis Obispo, was instrumental in the design and assembly of the CFB and the gamma densitometry tomography system.

Thanks also to the Sandia peer reviewers who provided valuable comments.

Sandia is a multiprogram laboratory operated by Sandia Corporation, a Lockheed Martin Company, for the United States Department of Energy's National Nuclear Security Administration under Contract DE-AC04-94AL85000. The authors gratefully acknowledge the financial support of the United States Department of Energy Office of Industrial Technologies, Brian Valentine, contract monitor.

Contents

Figures

Tables

Executive Summary

Gas-solid processes are widely used in the chemical industry, but are inefficient in terms of downtime, energy, and cost. In part, this is because, unlike single-phase flows, there are no validated computational tools for predicting gas-solid flow behavior. The chemical industry developed a vision, documented in the report *Technology Vision 2020: The Chemical Industry* (DOE/OIT, 1995), that included development of computational tools for accurate simulation of multiphase flows. For these reasons, the U. S. Department of Energy (DOE) Office of Industrial Technologies (OIT – now known as the Industrial Technologies Program, ITP) solicited proposals in this area. Two proposals were selected for funding under this solicitation, and their projects were combined into the Multiphase Fluid Dynamics Research Consortium (MFDRC). From 1998 to 2004, the DOE/OIT sponsored the MFDRC, a group of companies, universities, and national laboratories working to develop and validate multiphase computational fluid dynamics models. The role of Sandia National Laboratories (SNL) was to assemble and run experiments in a gas-solid circulating fluidized bed to provide validation-quality data for use by model developers. Primary data acquired included pressures around the flow loop and solids loadings at selected locations in the riser. Tomographic techniques were used to determine radial profiles of solids volume fraction in the riser, and axial profiles of the integrated solids volume fraction were produced. Computer Aided Radioactive Particle Tracking was used to measure solids velocities, fluxes, and residence time distributions. In addition, a series of computational fluid dynamics simulations was performed using the commercial code Arena-flow™.

1. Introduction

The Multiphase Fluid Dynamics Research Consortium (MFDRC) was assembled in 1998 when the proposal "A Research Consortium for Multiphase Fluid Dynamics: Simulating Industrial-Scale Turbulent Gas-Solid Flows" was selected for funding by the United States Department of Energy's Office of Industrial Technologies (DOE/OIT) in response to Solicitation No. DE-SC02-97CH10885. The MFDRC was a partnership of laboratories, industries, universities, and government agencies who collaborated to perform fundamental multiphase fluid dynamics research. Computational tools for understanding and predicting complex fluid dynamics were identified in *Technology Vision 2020: The Chemical Industry* as critical to developing advanced chemical reactors and separators. The MFDRC was assembled to address the need for experimentally validated computational tools.

Part of the motivation for this work is that despite their importance in the petrochemical, pharmaceutical, and power generation industries, many gas-solid units are troublesome and inefficient to operate, often having down-times of 40%, compared to less than 10% for other unit operations (Merrow, 1986). With domestic chemical products in particulate form valued at $61 billion per year and comprising more than half of the annual production of this country's two largest chemical companies, each percentage point improvement translates into a savings of $1 billion per year for the industry. The MFDRC was designed to seek a breakthrough in our ability to accurately model gas-solid flow in industrial applications as an aid to realizing these improvements.

The MFDRC was organized into two project teams investigating different aspects of gas-solid flows. These projects were referred to as "Group A" (Aeratable) and "Group C" (Cohesive) – engineering terms that denote the Geldart classification (size, weight, cohesiveness) of the primary particle types being examined (Geldart, 1973; see Section 2.1). Although each team had its own emphasis, statement of work, detailed goals, and budget, the two projects were coordinated as one program within the MFDRC. The participants, and their primary group affiliations, are given in Table 1.1.

Half of the products of two large MFDRC member companies, Dow Chemical and DuPont, are in the form of solid powders. Successful completion of this project could improve production efficiency for all of these products. Chevron and ExxonMobil, also consortium members, plan to use the newly developed and validated multiphase computational fluid dynamics (CFD) models to improve the efficiency of oil refining processes. Commercial CFD vendors and MFDRC partners AEA Technology and Fluent should benefit by having a proven, validated, multiphase flow tool incorporated into their products. According to the original Group A proposal, "The true measure of success for the project will be the number of government and industrial users who apply the resulting multiphase turbulence model for solution of their engineering problems."

The U.S. chemical industry has an annual energy consumption of approximately 6.3 quads per year (1 quad = 10^{15} BTU). This is almost 25% of all energy used in U. S. manufacturing. The models developed under this program could potentially increase efficiency in chemical industry multiphase processes by 5%. However, even a 1% improvement would save the equivalent of

Table 1.1. MFDRC Members: A = Group A, C = Group C

National Laboratories	Industry
Sandia National Laboratories (A)	AEA Technology (A)
Los Alamos National Laboratory (A)	Chevron (A)
Pacific Northwest National Laboratory (A)	Dow Chemical Company (A)
National Energy Technology Laboratory (C)	Dow Corning (C)
Oak Ridge National Laboratory (C)	DuPont (A)
Lawrence Berkeley National Laboratory (1997-1998) (C)	ExxonMobil (A)
University	Fluent (C)
Clarkson University (1997-1999) (C)	Millennium Inorganic Chemicals (A)
Illinois Institute of Technology (C)	Particulate Solids Research Inc. (joined 2001) (A)
Princeton University (A)	Siemens Westinghouse Power Corporation (A)
Purdue University (A)	
University of Colorado (joined 2000) (C)	
University of Michigan (joined 2000) (A)	
Washington University in St. Louis (A)	

100 million barrels of oil annually. The goal of this work was to provide a validated computational tool that could be used to improve industrial processes.

The consortium members were chosen based on their demonstrated experience in solving multiphase flows problems (laboratories, universities, and industry) and their application needs (industry). The DOE/OIT sponsored the National Laboratories. Industry shared the cost by donating equipment, instrumentation, and materials, in-kind labor, and funding of university partners. Industrial members committed funding, equipment, in-kind effort, and university faculty support totaling close to $1,000,000 for the first year and well in excess of $700,000 per year for subsequent years. This exceeded the 30% minimum cost share required in the original solicitation.

The ultimate goal of this research consortium was to develop and disseminate a general, experimentally validated model for turbulent multiphase fluid dynamics suitable for engineering design purposes in industrial-scale applications. The work focused on the particular case of a turbulent flow of a particle-laden gas at industrial conditions. One deliverable was a well-benchmarked model for this case that can be incorporated into commercially available software packages. The role of Sandia National Laboratories (SNL) in the MFDRC was to fabricate and operate a pilot-scale circulating fluidized bed (CFB) and to develop and apply diagnostics for acquisition of validation-quality data sets. This report documents SNL efforts in the MFDRC. Some of the design and early testing of the CFB were also included in an earlier SAND report (Trujillo, et al., 2001a).

General Approach. This consortium was designed to advance the state-of-the-art in simulating multiphase turbulent flows by developing advanced computational models for gas-solid flows that are experimentally validated over a wide range of industrially relevant conditions, with the goal of transferring the resulting validated model to interested U.S. commercial CFD software vendors. Since a lack of detailed data sets at industrially relevant conditions is the major roadblock to developing and validating multiphase turbulence models, a significant component

of the work involved flow measurements on a pilot-scale riser, incorporating hardware components contributed by Westinghouse and installed and operated at SNL. Desired measurements of flow quantities included data on solids volume fraction distributions at various locations in the riser. More complex data sets including velocity and velocity-fluctuation profiles for both gas and solid phases were desirable but required too much development to complete during this consortium. Even for solids volume fraction, it was recognized that additional techniques would have to be developed for these measurements beyond what was available at the initiation of this program. Experimental and diagnostic details will be provided in this report.

Work Plan for Group A: The overall topical area for this work was Multiphase Fluid Dynamics, and the work followed three essential lines of activity: (a) Numerical Methods, (b) Phenomenology/Constitutive Relations and Validation, and (c) Experimental Measurements. These activities embodied the three subtopics in the original OIT request for proposals. The interrelationships among activities required that all activity lines proceed simultaneously.

The specific work breakdown at the National Laboratories was that Los Alamos National Laboratory (LANL) worked primarily on Numerical Methods and Phenomenology/Constitutive Relations and Validation. They used the computational code CFDLIB as a testbed for developing, implementing, and validating new theoretical models (Kashiwa and VanderHeyden, 2000). SNL built and operated the experimental testbed; a pilot-scale, gas-solid, cold-flow (chemically non-reacting), CFB. Both SNL and Pacific Northwest National Laboratory (PNNL) developed diagnostics needed to acquire the necessary data for development and validation of the theoretical and computational models.

The requirements for validation-quality data are severe and are not normally met in data available in the literature or even in data acquired at the member companies and universities. The reason is that, in order for data to be considered validation-quality, the essential physical phenomena must be measured, the initial and boundary conditions must be well characterized, and the data must be of high quality, with well-established error bounds. Acquisition of validation-quality data sets involves more than just a carefully run experiment. It requires close collaboration between the experimental team setting up the experiment and acquiring the data, and the computational team that will use the data for validation. This close communication was a central element of the MFDRC consortium.

2. Background

2.1 Gas-solid flows

There are numerous surveys of gas-solid flows and their applications, including Kunii and Levenspiel (1991), Roco (1993), Grace et al. (1997), Rhodes (1998), Fan and Zhu (1998), and Jackson (2000), to name but a few. This short summary is intended to provide a brief overview of the field but is by no means exhaustive.

Many gas-solid applications involve fluidized beds (e.g., Lim et al., 1995; Yang, 2003). The behavior of the particles in fluidized beds depends not only on the flow parameters but strongly upon the particle characteristics as well. Figure 2.1 shows the general evolution of a fluidized bed as the gas flow rate is increased. When a bed of solid particles is subjected to an increasing gas flow from its base, the gas initially flows through the pores between the particles, and the pressure drop across the fixed bed increases with increasing gas flow rate as given by the Ergun equation (Fan and Zhu, 1998). In the fixed bed, the weight of the particles is supported by the particle-particle contact, and the stress is transmitted through the particles to the walls and floor of the vessel, as evidenced by the fact that pressure does not build up at the base of the fixed bed. As the gas flow rate is increased, the bed pressure rises until a transition eventually occurs and the pressure no longer rises but stabilizes at a fixed value. This transition occurs at the minimum fluidization velocity, u_{mf}, which is the minimum superficial gas velocity at incipient fluidization, or the point at which the drag force is sufficient to support the weight of the bed. Superficial gas velocity is defined as the velocity that the gas would have in an empty column, i.e., the total gas flow rate divided by the column cross-sectional area. In a two-phase flow the local velocity is generally higher than the superficial velocity because some of the flow area is taken up by the non-gas phase (liquid or solid). Beginning at u_{mf}, the gas-particle mixture takes on some of the characteristics of a fluid, including:

- The free surface of the fluidized gas-solid mixture will adjust to remain horizontal as the bed is tilted
- The mixture will change shape to conform to a vessel (as long as it remains fluidized)
- Objects with density lower than the fluidized mixture will rise to the top of the bed; more dense objects will sink
- The mixture will flow through openings in the vessel
- The levels between two connected beds will equalize
- The pressure at the bottom of the bed will be given by a hydrostatic relation ($\rho_{mix}gh$), where ρ_{mix} is the mixture density, g is gravitational acceleration, and h is the bed depth.

Incipient fluidization can generally be detected by examining pressure traces in the fluidized bed as the gas flow rate is increased. When operating in the fixed bed regime, the pressure drop

across the bed increases with increasing gas velocity, as per the Ergun equation. Minimum fluidization is indicated by the leveling off of the pressure with further increase in gas flow rate (Pell, 1990). Typical flow regimes are shown in Figure 2.1. After minimum fluidization is achieved, increasing the gas velocity further will cause different behaviors depending on the Geldart classification of the particles, but the pressure drop across the bed will remain essentially constant.

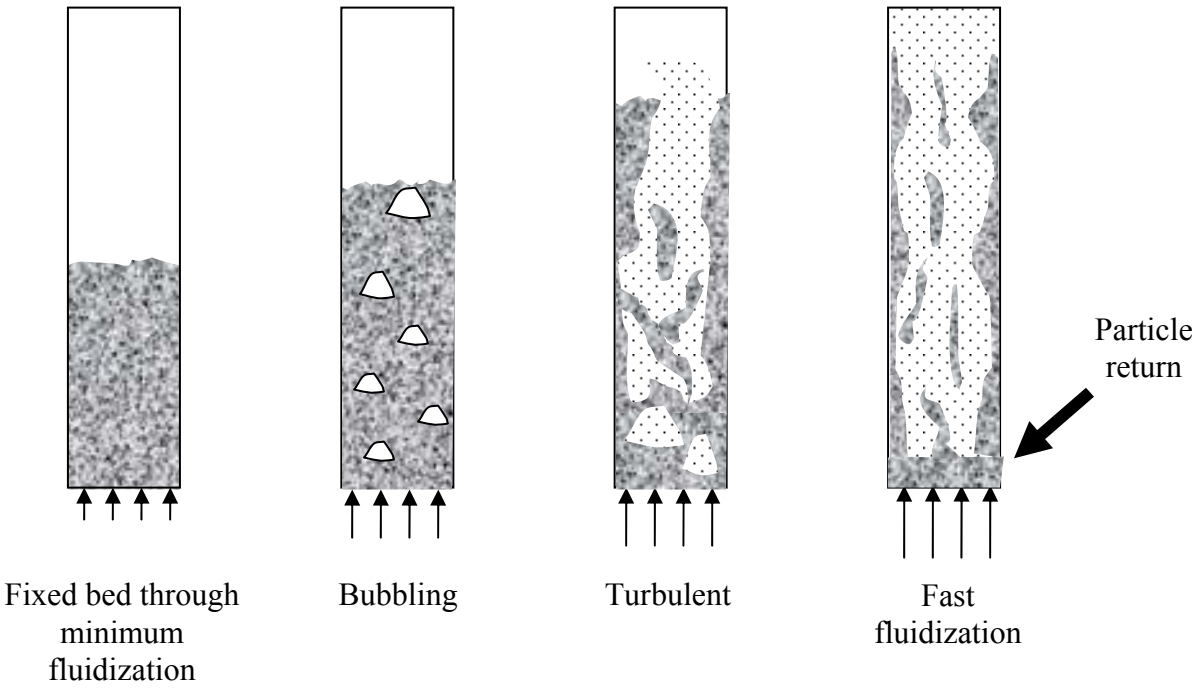

Figure 2.1. Flow regimes in risers with increasing gas flow rate.

Geldart (1973) proposed a scheme to classify particles according to their fluidization characteristics. Geldart classification is based on the particle diameter and density. A representative Geldart chart is shown in Figure 2.2, in which the lines indicating demarcations between groups are from correlations available in the literature. Specific characteristics of the Geldart classifications are:

- Group A ("aeratable") particles generally have low to moderate density and are in the 20 to 200 μm diameter range, depending on density. As gas flow rate is increased, a bed of Group A particles will expand before bubbling begins. For Group A particles there is therefore a bubble-free region between u_{mf} and the minimum bubbling velocity u_{mb}. Fluid catalytic cracking (FCC) catalyst particles usually belong in Group A.

- Group B ("bubbling") particles are generally larger and heavier than Group A particles. A bed of Group B particles will begin to bubble as soon as the gas velocity exceeds the minimum fluidization velocity u_{mf}. Many glass beads and other sand-like materials are Group B particles.

- Group C ("cohesive") particles are generally smaller and lighter, have strong interparticle forces, and often move as regions with gas channels flowing between them. These particles are difficult to fluidize. Fine powders like flour and talc are in Group C.

- Group D ("spouting") particles are larger and heavier than Group B particles, and often spout from the top of the bed. Roasting coffee beans are Group D, as are metal ores and other large and/or heavy particles.

Note that the ordinate value in Figure 2.2 is density difference between the particles and the fluidizing gas. Also shown in Figure 2.2 are the location in the Geldart classification scheme of the two particle types examined in this study, glass beads and fluid catalytic cracking (FCC) catalyst.

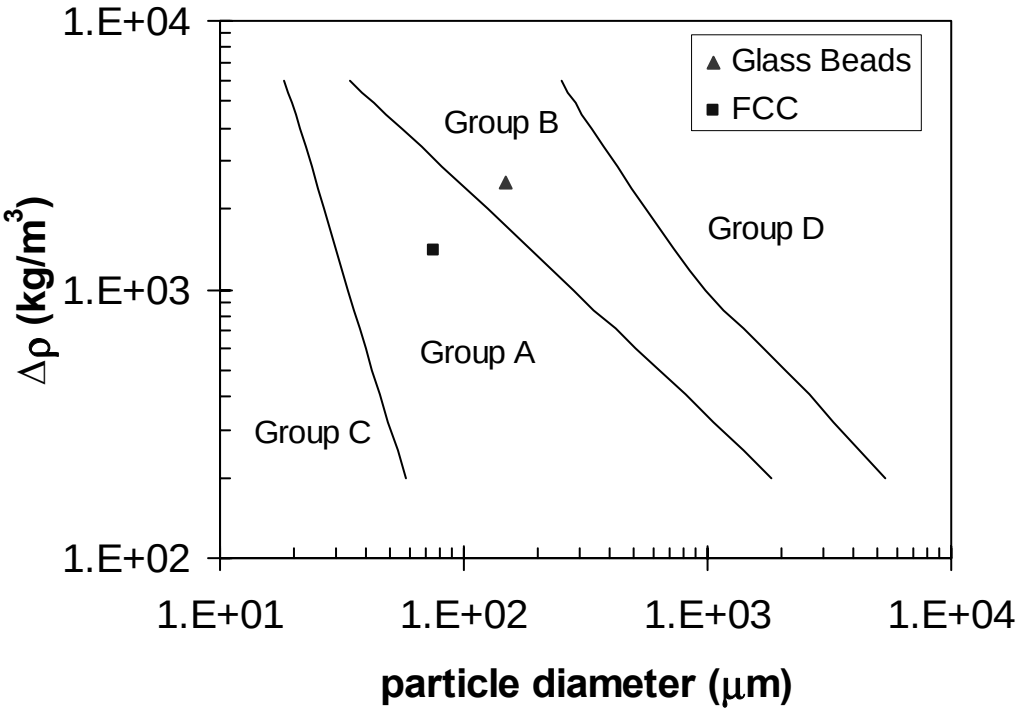

Figure 2.2. Geldart classifications. Classifications of the glass bead and FCC particle types examined in these studies are indicated.

For Groups B and D, where interparticle forces are less important, u_{mb} is equal to $u_{mf.}$ After the bubbling regime there can be a slugging regime (see Figure 2.1) in small diameter vessels or when large particles are used. When small particles and/or larger diameter vessels are used, a transition to a turbulent fluidization regime occurs (Bi et al., 2000) which is often characterized by a peak in the amplitude and/or standard deviation of pressure fluctuations. At still higher gas velocities, significant particle carryover from the top of the fluidized bed occurs. This begins at the onset of the fast fluidization regime. Particle capture and return to the base of the fluidization bed, as in a circulating fluidized bed, then becomes necessary for continued operation. Still higher gas velocities lead to dilute pneumatic transport (Lim et al., 1995).

The flow pattern in the riser section of a CFB operating under fast fluidization conditions is generally characterized as core-annular, with an upward-flowing central core with dilute solids loading and an annular, downward-flowing, wall region with higher solids loading. Particles in the annular region are subject to strong interparticle interactions leading to clustering (Figure 2.3). Circulating fluidized beds usually operate in the fast fluidization regime in which there is no distinct bed upper surface (Grace and Bi, 1997). Typical flow patterns in a riser are schematically represented in Figure 2.4. This shows that there is an indistinct transition from a denser flow at the base to a more dilute, core-annular flow higher in the riser. The area-averaged voidage typically transitions from low to high (dense to dilute solids loading), with a characteristic S-shaped axial distribution as shown schematically in Figure 2.5. Voidage is defined as the gas volume fraction, or percent gas in a given volume of the gas-solid flow, and is represented by the symbol ε. The solids volume fraction, ε_s, is therefore given by $\varepsilon_s = 1 - \varepsilon$.

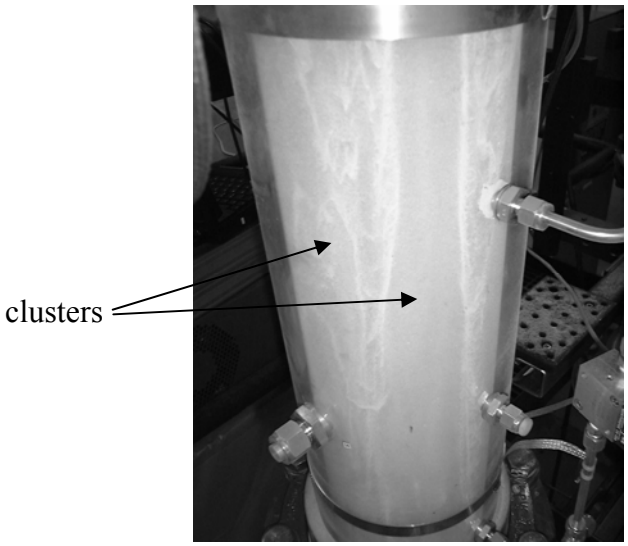

Figure 2.3. Clusters in riser section of Sandia CFB.

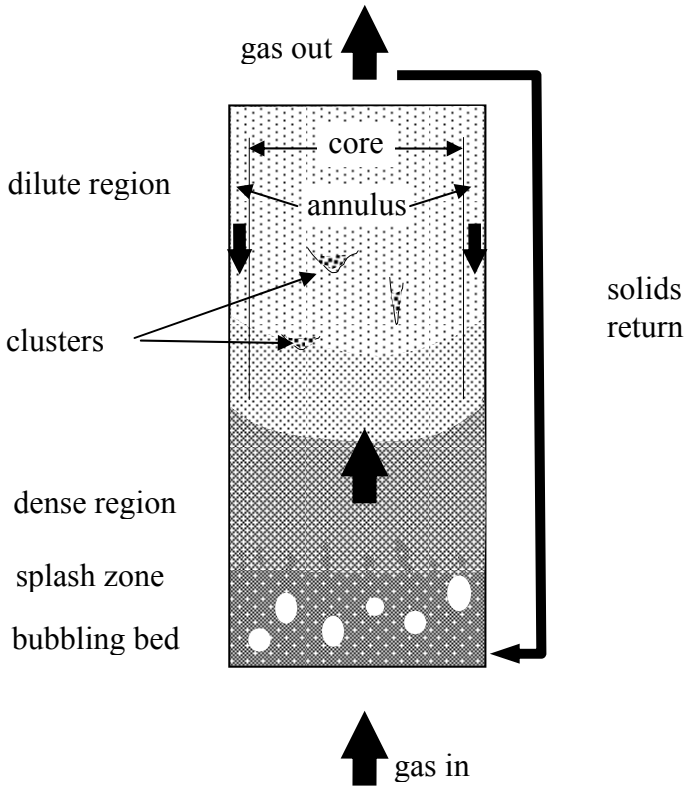

Figure 2.4. Flow structure in the riser section of a circulating fluidized bed operating in the fast fluidization regime (from Figure 2.3 of Horio, 1997).

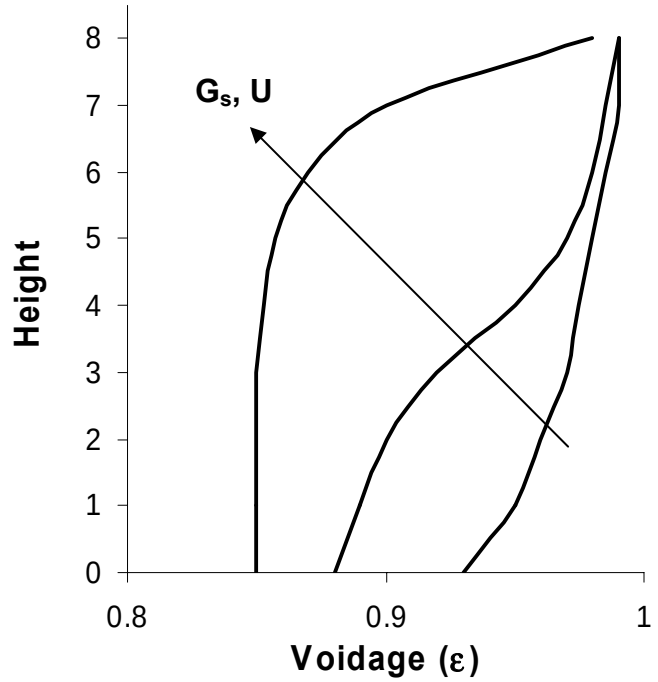

Figure 2.5. Schematic representations of S-shaped axial profiles of the area-averaged voidage in a riser for different combinations of solids flux and superficial gas velocity.

2.2 Gas-Solid Flow Industrial Applications

Gas-solid flows are used in a variety of chemical and petroleum industry applications because of the strong mixing that yields relatively uniform temperatures and concentrations, high heat and mass transfer rates, and relative ease of regenerating spent solid catalysts, among other reasons. Gas-solid reactions are often performed in a fluidized bed or a circulating fluidized bed (CFB). Widespread CFB applications include fluid catalytic cracking in the petroleum industry and pulverized coal combustion (Grace et al., 1997). Such reactors have found wide acceptance because of their reaction efficiency and high potential throughput (Fan and Zhu, 1998).

There are many examples of CFB processes accompanied by impressive usage statistics. FCC is a process by which heavy petroleum components are converted into lighter products in a CFB with solid catalyst particles. Avidan (1997) reports that FCC units process over 16 million barrels of oil per day, that the FCC process raises the value of a barrel of oil by as much as $US10, and that the production of FCC catalyst alone is a $US600 million per year business. Chen (2003) notes that about 45% of worldwide gasoline production involves FCC units. CFB boilers, used for energy production, have high efficiency and low emissions, and can burn a variety of fuels in contrast to other combustion processes. Lee (1997) reports that hundreds of CFB boilers are in operation with a total capacity over 9000 MW and that low combustion temperatures and the introduction of sorbents into the process lead to low emissions. Dry and Beeby (1997) discuss several other uses of CFBs including coal gasification and metal processing. These applications are not used as widely as FCC units or CFB boilers, but their variety is impressive and suggests great potential.

A variety of sources describe the economic importance of gas-solid processes. In addition to the sources above, Ennis et al. (1994) report that gas-solid processes are involved in the production of $US61 billion of chemical products in the United States. It is clear that this is a large industry and small improvements in efficiency will lead to large benefits, and there is indeed much room for improvement.

Gas-solid processes are widely used in the chemical industry but are inefficient in terms of downtime, energy, and cost. Part of this is due to the fact that, unlike single-phase flows, there are no validated computational tools for predicting gas-solid flow behavior. The chemical industry developed a vision, documented in the report *Technology Vision 2020: The Chemical Industry* (DOE/OIT, 1995) that included development of computational tools for accurate simulation of multiphase flows. Gas-solid and gas-solid-liquid flows are identified in *Technology Vision 2020: The Chemical Industry* as critical to the development of advanced chemical reactors. Significant progress is required before computational-simulation capabilities are advanced to the point of enabling industrial practitioners to rely on theoretical results for reactor design. A critical shortcoming in most simulations is the description of the interactions between phases, particularly when turbulent flow exists, as is typically the case for industrial conditions. Various multiphase turbulence models have been proposed to date. However, the software and hardware needed to perform these computationally intense simulations and the experimental data required to validate, compare, and refine multiphase-turbulence models, particularly at industrially relevant scales, are not generally available.

Optimal reactor performance is dependent on the designers' and operators' abilities to predict and control key parameters of the reactor's operation. These include such "static" variables as solid properties (e.g., density, size distribution) and "dynamic" variables (e.g., net solids throughput). A critical variable relating to the solids is the distribution of solids in the riser, since solids concentration and location have a profound effect on contacting and reaction efficiency.

2.3 Experimental Techniques in CFBs

Multiphase flow measurements are often more complicated than single-phase flow measurements since the two phases often have significantly different characteristics. Also, most gas-solid flows operating under industrially-relevant conditions are opaque, so laser-based techniques, highly useful in single-phase flow measurements, have very limited applicability. Louge (1997) provides an excellent review of experimental techniques for CFBs. Werther (1999) reviews instruments for fluidized bed measurements in general, with a particular focus on industrial applications. Several monographs covering measurements in multiphase flow are also available, including Soo (1999) and Chaouki et al. (1997).

Performing an assessment of a multiphase turbulence model at the requisite level of detail requires accurate, highly resolved data over a broad range of industrially-relevant conditions (e.g., gas flow rate, solids loading, riser diameter, particle diameter, etc.). The existing experimental data base is often lacking in both temporal and spatial resolution. The boundary and initial conditions are not well characterized, and the flow regimes are often not industrially relevant. Therefore, a major goal of this project was to acquire and present several new and more detailed sets of data for flow in vertical risers at scales, densities, and flow conditions of industrial importance. This required that the most appropriate instrumentation be employed. Much of the remainder of this report documents details of the techniques applied, tested, and/or developed during this program in order to acquire the required data.

2.4 Computational Modeling of Flow in CFBs

Computational modeling of CFBs is desirable so that, as in many single phase flow applications, CFD can be used as a design tool. Accurate CFD allows design decisions to be made without excessive hardware trial and error cycles, which can become very expensive, for example in a chemical industry scale-up study. However, multiphase CFD is not as well developed or validated as is single-phase CFD. Improved computational models have been developed and tested for years (see for example Crowe et al. (1996, 1997); Sundaresan (2000); Sinclair Curtis and van Wachem (2004)), and the overall goal of this project was the development, validation, and implementation of improved models. Some of the computational work performed in this program was reported in Kashiwa and VanderHeyden (2000), Zhang and VanderHeyden (2000, 2001a, b, 2002), Zhang et al. (1995), and Zhang et al. (1999). A review of CFB modeling is beyond the scope of this report, but the reader is directed to these references as a starting point for an introduction to this topic.

3. Experimental Facility

A brief summary of the CFB design approach is presented here, followed by detailed discussion of each riser component in subsequent sections. Instrumentation and measurement techniques are described in Chapter 4. Trujillo et al. (2001a) discuss the early design and development of the CFB in detail.

Because the focus of the present research is hydrodynamics and not chemical kinetics, the Sandia CFB was designed from the outset as a non-reacting ("cold-flow") unit. Design (see Figure 3.1) was primarily by Sandia with the assistance of MFDRC partners. The riser inner diameter of 14 cm (5.5 in.) was chosen to be as compact as possible while still meeting most industrial guidance recommending minimum test-unit sizing for acquisition of data that may be reliably applied to full-scale facilities. The downcomer inner diameter of 28 cm (11 in.) was chosen to create a solids reservoir that could accommodate a wide range of operating conditions.

A modular design approach was adopted, using identical 61- or 122-cm long (24- or 48-in.) sections to build the riser and downcomer. Each riser section was fitted with ports for installation or insertion of diagnostic probes. To reduce construction time and costs, off-the-shelf parts in standard sizes were used whenever possible. Two critical fabricated parts were the stainless steel engagement section at the base of the riser and the large (58-cm ID) disengagement chamber at the top of the riser. The riser also incorporated parts donated by Westinghouse Corporation as part of the MFDRC, notably the riser external support structure and working platforms, the cyclone separators, and the screw feeder and storage hoppers used in the original system configuration.

Particular efforts were made to preserve flow symmetry in the designs of the particle engagement and disengagement sections at the bottom and top of the riser, respectively. Annular designs were developed for each, and are discussed in more detail below.

Baseline diagnostics and controls incorporated into the initial riser design were pressure measurements around the flow loop, fluidization-air control and metering at several locations in the loop, and manual-valve control and orifice metering of the motive air supply. These diagnostics are discussed in Chapter 4 of this report.

The riser has been operated in three configurations through its lifetime. The first two of these are described by Trujillo et al. (2001a) and were "short" configurations ($L/D \approx 26$) with either batch or continuous solid-particle return. The third is a "tall" configuration ($L/D \approx 41$) with continuous solid-particle return and is the unit in which all data presented in this report were collected.

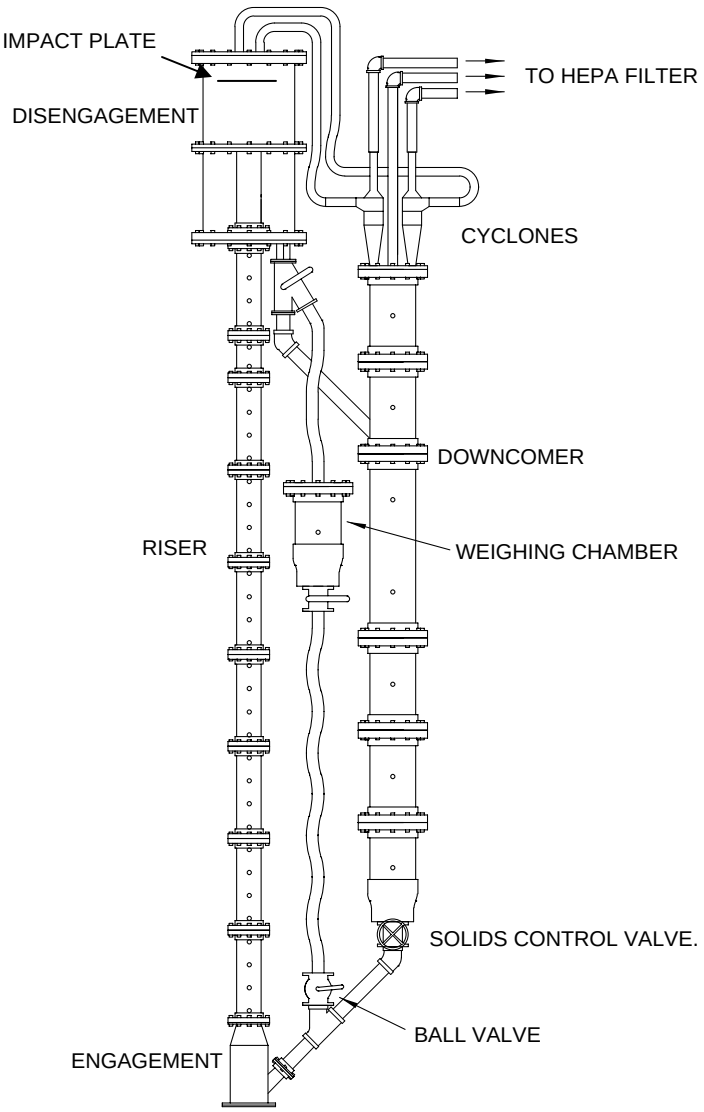

Figure 3.1. Overall layout of Sandia/MFDRC circulating fluidized bed (CFB).

The CFB was designed in English units (inches), reflecting the dominance of English-unit parts in the supply market. While dimensions presented in this chapter are in an "*xx* cm (*yy* in.)" format, round-off is inherent in the metric values; in general, the English-unit values are to be considered the nominal value from which metric values have been calculated. It should also be noted that when sizes are called out as "pipe" diameters, this refers to ASTM pipe sizing and thus may not reflect an actual measurement (e.g., the OD of ASTM 3-inch pipe is 3.5 inches, and its minimum allowable ID is 2.9 inches); "tube" diameters, on the other hand, are true values. In general, PVC parts used in construction of the riser facility are pipe-sized, and acrylic parts are tube-sized.

3.1 CFB Configuration

The CFB facility is shown in Figure 3.1. Particles are fed from the downcomer through a fluidized angled standpipe into a fluidized annular region in the engagement section. Motive air enters the engagement section through a central pipe. Particles are entrained by the motive air and are transported upward through the riser to an annular disengagement section. An aluminum impact plate at the top of the disengagement section inertially separates the gas-particle mixture. The separated particles settle into an annular fluidized bed, which empties into the downcomer via a fluidized angled standpipe. The air exits the disengagement section and passes through cyclone separators to remove particles that were not separated in the disengagement section. The motive air is then vented to atmosphere via a HEPA bag-filter exhaust unit.

A diverter-valve system for solids-flux measurement diverts the solids from their normal return path from the disengagement section to the downcomer, instead sending them to a separate weighing chamber. By measuring the mass of solids diverted in a given period of time, the solids flux in the riser may be estimated. After the measurement is completed, solids in the weighing chamber are returned to the main CFB loop via a standpipe that feeds into the downcomer-to-engagement standpipe.

3.1.1 Engagement Section

The engagement-section assembly is shown schematically in Figure 3.2. It is a two-piece assembly consisting of a lower, 9.5-mm (0.375-inch) thickness flange with a central motive air pipe and an upper housing incorporating the solid-particle feed and a contraction to match the inner diameter of the CFB. The resulting annular arrangement reflects an effort to achieve a gas-solid flow that was as symmetric as possible. The engagement section was fabricated using ANSI-standard stainless steel pipe sections by Sandia personnel.

Particles are fed into the engagement section from the downcomer via a standpipe. These particles form an annular fluidized bed around the central motive-air pipe. The bed is fluidized through the base at 8 locations through Swagelok™ P/N SS-400-1-4 fittings with sintered metal filters to prevent contamination by particles. In addition, a single fluidization fitting (a welded Swagelok™ SS-400-1-4 fitting) is located on the particle-feed standpipe.

The motive-air inlet pipe was originally constructed to a length of 38.4 cm (15.125 in.) (measured from the inside surface of the 9.5-mm (0.375-in.) base plate), as shown in Figure 3.2, but was later modified to allow the attachment of other lengths or configurations of air inlet. Data presented in this report were collected with the original motive-air-inlet-pipe length of 38.4 cm (15.125 in.).

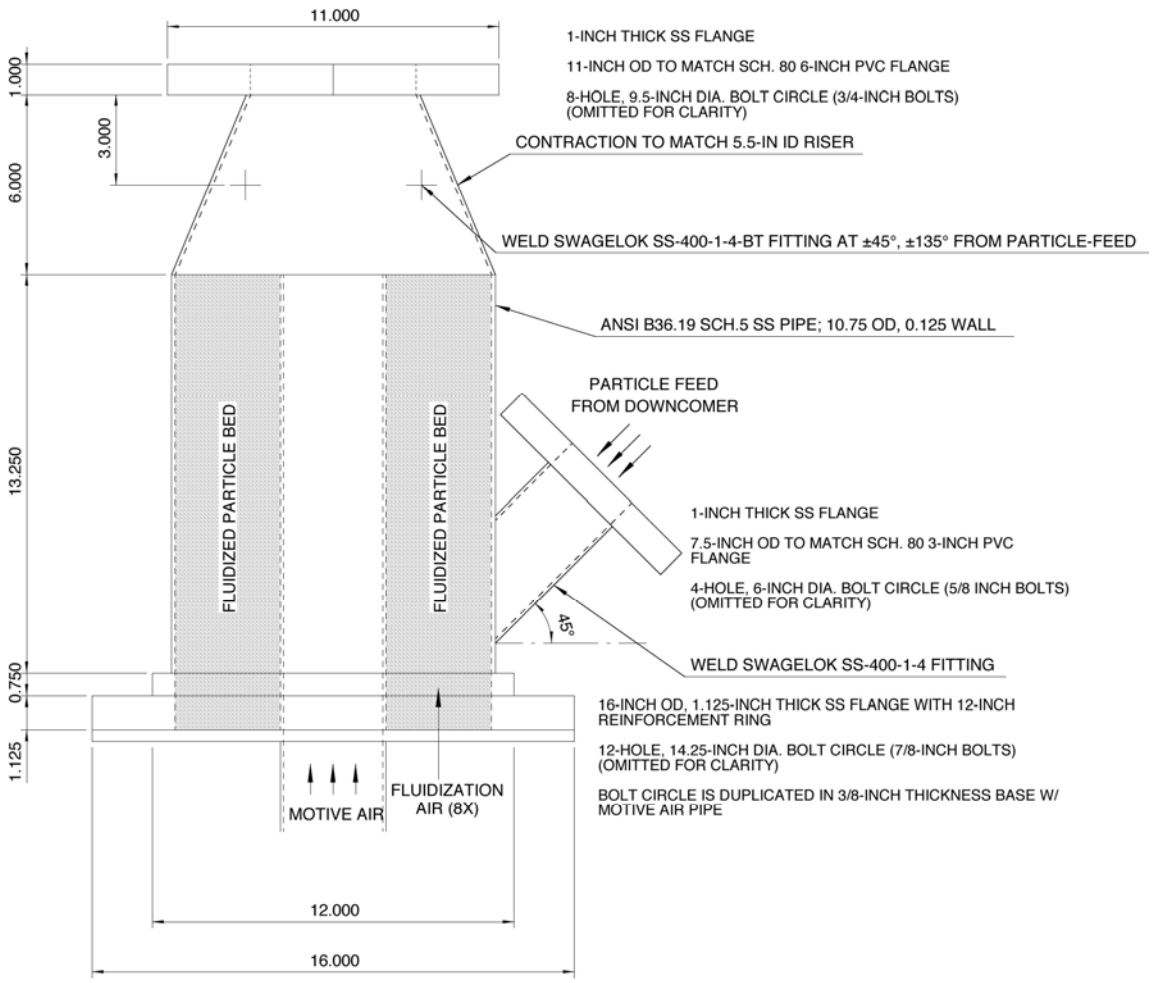

Figure 3.2. Sandia/MFDRC CFB engagement-section assembly.

3.1.2 CFB Riser Sections

The primary building block of the CFB riser is a 61 cm (24 in.) module, shown schematically in Figure 3.3. Each module comprises a 14-cm (5.5-in.) ID, 12.7-mm (0.5-in.) wall-thickness acrylic tube, Schedule-80 PVC mating flanges on each end (one fixed, one freely rotating), and a series of 6.35 mm (0.25 in.) and 12.7 mm (0.50 in.) instrumentation ports. In addition, one nominally half-height (27.94-cm (11-in.)) module was included in the riser assembly.

Standard Schedule-80 PVC flanges were used to mate the riser sections together. These were prepared by machining them to an overall height of about 5.7 cm (2.25 in.) to allow clearance for the installation of the instrumentation fittings closest to the flange. The pipe-seating shoulder on the ID of the flange was also removed to allow flush joints without internal gaps. Because of the discrepancy between tube and pipe ODs (the OD of a 6-inch PVC pipe is nominally 6.625 inches, vs. the riser acrylic-tube OD of 6.5 inches), two construction techniques were used. In the

initial fabrication of riser sections for the original, "short" riser configuration, the acrylic piece was centered in the prepared flange section and epoxied in place, with an excess of epoxy filling the gap between the acrylic and PVC flange pieces. In constructing later sections, a bushing was fabricated by machining the ID of a piece of Schedule-80 PVC pipe to match the OD of the acrylic. This bushing was solvent-welded to the flange, and, after curing, the flange/bushing assembly was solvent-welded to the acrylic tube. A detail of this assembly is shown in Figure 3.3.

The acrylic tube was prepared for assembly by fabricating mounting holes for the instrumentation ports. These operations consisted of drilling and tapping the mating holes and machining flat landings on which the fittings' O-ring seals would seat. Details of instrumentation-port locations are shown in Figure 3.4. Note that Figure 3.4 indicates that the tube stock was for the riser section was cut to a finished length of 60.6 cm (23.875 in.); the remaining 3-4 mm of each section was made up by a gasket inserted between sections. Acrylic tube stock used for riser construction was not ordered to any special dimensional tolerance. Typical out-of-roundness seen in riser sections was on the order of 1.3 mm (0.05 in.).

Instrumentation-insertion ports were Swagelok™ P/N SS-400-1-OR-BT (6.35 mm (0.25 in.) feed-through diameter) and SS-810-1-OR-BT (nominally 12.7 mm (0.5 in.) feed-through diameter). The "BT" part-number suffix indicates that the fitting has been bored through to allow the smooth insertion or extraction of a probe. Pressure-measurement ports were Swagelok™ P/N SS-100-1-OR (as 6.35 mm (0.25 in.) ports above, but not bored through). All ports were prepared for installation by machining the fitting's male thread depth to 12 mm (0.47 in.), so that it would not protrude into the riser's interior when properly seated. Pressure-measurement ports received the additional preparatory step of counterboring the end of the female thread to accept a sintered metal filter ("frit" or "snubber") to prevent contamination of pressure transducers with CFB particles.

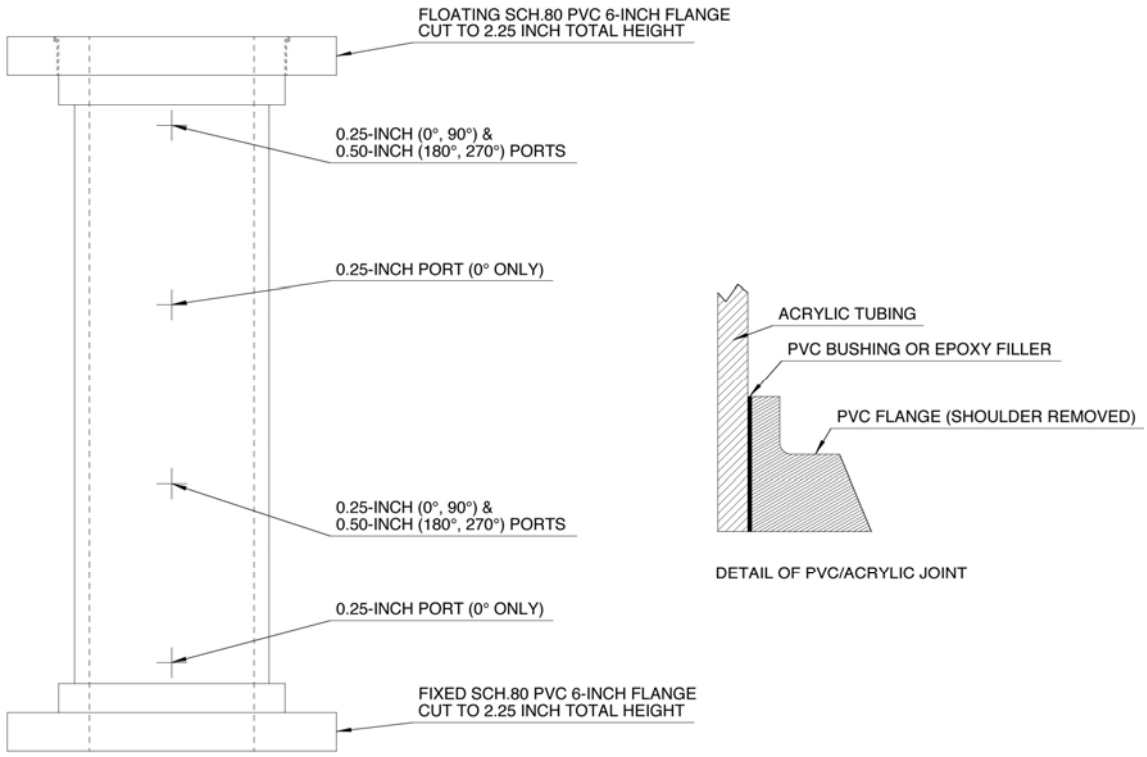

Figure 3.3. Sandia/MFDRC CFB riser section (left) and detail of PVC/acrylic joint (right).

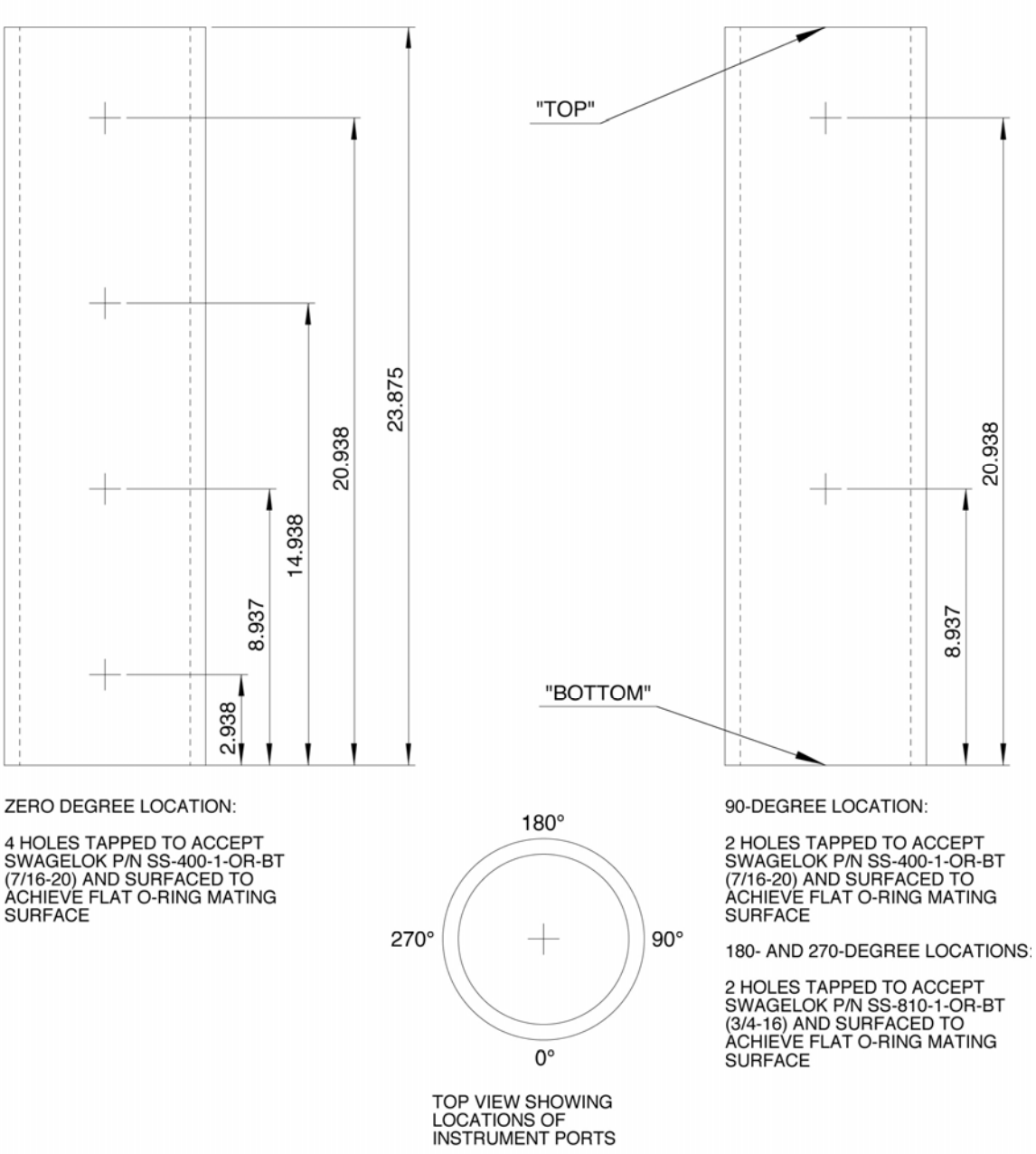

Figure 3.4. Detail of instrumentation port locations on Sandia/MFDRC CFB riser sections (dimensions in inches).

3.1.3 Disengagement Section

The disengagement section is shown schematically in Figure 3.5. It consists of two stacked 58.4-cm (23-in.) ID, 12.7-mm (0.5-in.) wall-thickness sections mated at a flange connection. The gas-solid flow in the riser enters the disengagement section coaxially via an acrylic tube that continues the ID of the riser to a penetration height of 61 cm (24 in.) inside the disengagement chamber. The air-particle mixture is turned by an aluminum plate, inertially separating the particles from the air. This behavior and separation efficiency was demonstrated by computational modeling using CFDLIB before the section was built (Kashiwa and VanderHeyden, 1998). The particles fall into an annular bed at the base of the chamber. The bed is fluidized by a sparger controlled by an Omega™ FMA-2417 controller. The bed flows back into the downcomer via a 6.35-cm (2.5-in.) ID underflow standpipe. The lean mixture of unseparated particles in air is exhausted through two 5.1-cm (2-in.) PVC pipes to the cyclones for further separation. As with the engagement section, the annular configuration of the disengagement section was driven by an effort to achieve as much symmetry as possible.

The aluminum plate in the disengagement section was originally bare, but a 3.2 mm (0.125 in.) nominal thickness rubber pad was later added to cushion the impact of the coated-scandium particle used for CARPT experiments.

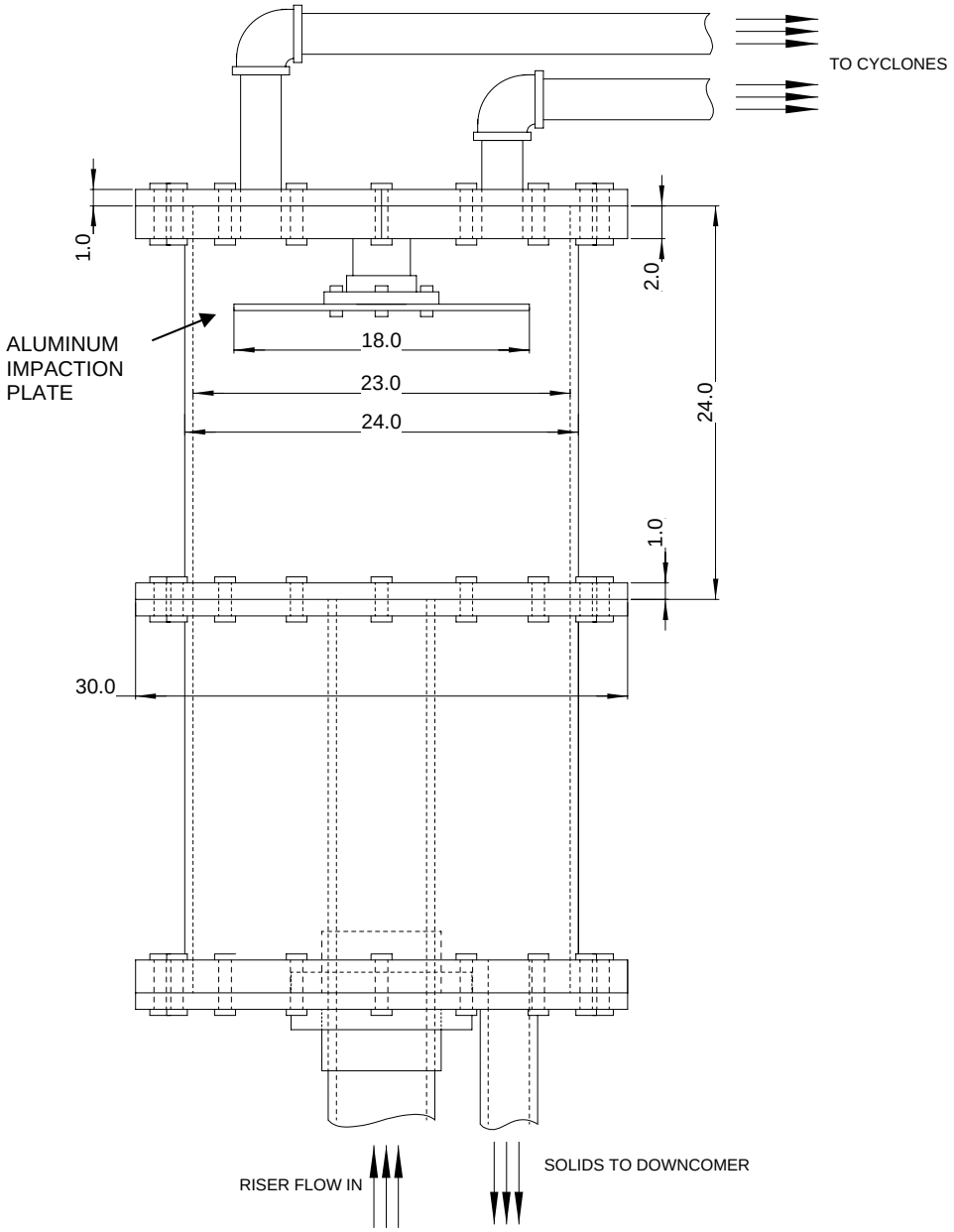

Figure 3.5. Sandia/MFDRC CFB disengagement section (dimensions in inches). Sparger is not shown.

3.1.4 Downcomer

The downcomer was constructed in modules similar to those used for the riser; the construction of individual modules was also similar to that used for the riser modules. The acrylic tubes used for the downcomer were 28 cm (11 in.) ID, with 12.7 mm (0.5 in.) wall thickness. Standard 12-inch Schedule-80 PVC flanges were used to mate sections together, with the tube/PVC OD discrepancy again made up using both methods described for the riser sections. All downcomer sections were 61 cm (24 in.) in length, except for one piece that was 122 cm (48 in.) long, and the downcomer base, the construction of which is described below. Instrumentation ports on the downcomer were also prepared as described for the riser, above, with the exception that the sintered metal filters installed in the downcomer's pressure-measurement ports were not pressed flush with the end of the female threads of the fitting, but instead rested on the inside shoulder of the fitting. A schematic of a 61-cm length downcomer section is shown in Figure 3.6. As in with the riser section in Figure 3.4, the downcomer-section height is slightly shorter than 61 cm (24 in.), providing allowance for insertion of a gasket between sections.

The downcomer base was constructed by adapting a piece of 28-cm (11-in.) ID, 12.7-mm (0.5-in.) wall thickness acrylic tubing to mate with a 30.5-cm (12-inch) to 25.4-cm (10-in.) bell reducer via a fabricated bushing as described in Section 3.1.2. The outlet of the bell reducer was stepped down to 7.62 cm (3 in.) via a pair of solvent-welded concentric PVC bushing reducers. A 7.62-cm (3-in.) PVC pipe stub was in turn solvent welded to the reducer, and a Schedule-80 PVC flange attached to the stub to mate to the solids-feed control valve. Eight tubular fluidization-air ports penetrate the base of the downcomer to an insertion depth of about 50 mm (2 in.), and turn upward to avoid the particle attrition that was observed to result from radial jet impingement in earlier implementations. These fluidization lines incorporate filters in fittings upstream of the tubular inserts.

The standpipe that returns solids from the disengagement to the downcomer penetrates the downcomer via a 6.35-cm (2.5-in.) ID, 12.7-mm (0.5-in.) wall-thickness mating stub which was solvent welded into place at a 45° penetration angle. The standpipe itself fed through this mating stub via a 5.84-cm (2.3-in.) ID, 2.54-mm (0.1-in.) wall-thickness adapter tube, which then expanded back out to a 6.35-cm (2.5-in.) PVC pipe. This pipe turned and ran coaxially down the downcomer, terminating at a location 61 cm (24 in.) above the bottom of the downcomer.

The top of the downcomer was closed off with a 2.54-cm (1-in.) thick acrylic plate, on which the disengagement-exhaust cyclones were mounted and through which the downcomer fluidization air exhausted. The cyclones returned solids to the downcomer via 38.1-mm (1.5-in.) Schedule-40 PVC pipe diplegs. As with the disengagement solids return standpipe, the cyclone diplegs penetrate the downcomer to a depth 61 cm (24 in.) above the bottom of the downcomer.

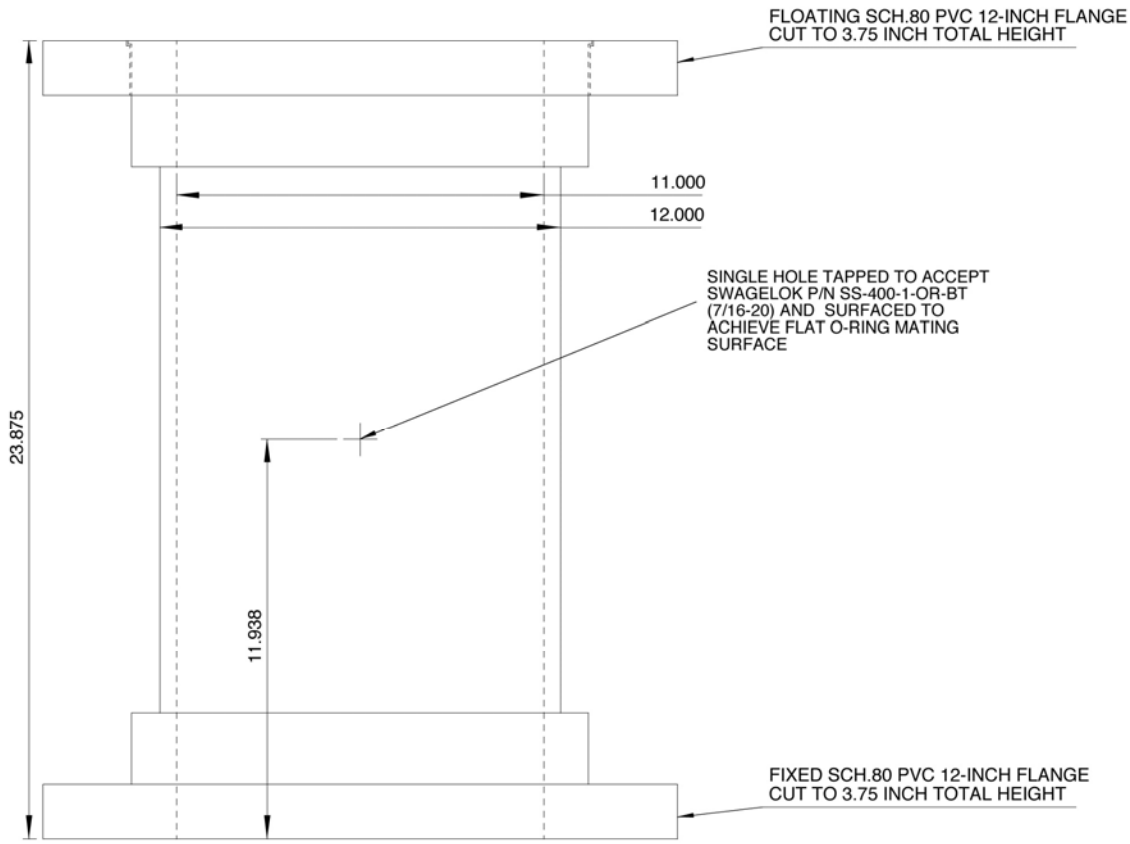

Figure 3.6. Sandia/MFDRC CFB downcomer section (dimensions in inches).

3.1.5 Standpipes

Standpipes used for solids transfer throughout the CFB loop were constructed of 63.5-mm (2.5-in.) ID, 12.7-mm (0.5-in.) wall-thickness acrylic tube and Schedule-80 PVC fittings (elbows, etc.). Because the true OD of 3-inch PVC pipe is 3.5 inches, 3-inch pipe fittings were able to be used without requiring adaptation. Fluidization air is fed into the standpipes via Swagelok™ P/N SS-400-1-OR fittings, with sintered metal filters installed inside the fitting against the internal shoulder.

The lower standpipe that transferred solids from the downcomer to the engagement section was fluidized from below at 10 equally-spaced locations (these do not include the fluidization port on the downcomer inlet shown in Figure 3.2). A vent line connected this angled standpipe to the relatively low-pressure region at the top of the downcomer, as suggested by the work of Karri et al. (1995). Use of the vent allowed gas to flow to the top of the downcomer, preventing choking in the angled standpipe and generally improving the solids flow behavior (see Trujillo et al., 2001a).

The upper standpipe that transferred solids from the disengagement section to the downcomer was fluidized in four equally-spaced locations along the angled portion of the standpipe (not including a fifth port on the downcomer-mating stub); fluidization air was not directly supplied to the vertical portion of this standpipe. Fluidization air for both the lower and upper standpipes was controlled and monitored by Omega™ FM2410 mass-flow controllers.

3.1.6 Diverter-Valve CFB Leg

The diverter-valve leg of the CFB loop diverts solids from the normal disengagement-to-downcomer return path into an isolated weighing chamber. Knowing the mass of solids diverted in a given amount of time, an estimate can be made of the solids flux in the CFB riser. The diverter leg used 76-mm (3-in.) ID wire-reinforced rubberized-fabric hose for solids transfer without additional fluidization. The design and construction of the solids-collection chamber mimicked the design of the downcomer base. However, the solids-collection chamber has a less sophisticated fluidization system than the downcomer base, using only four base-mounted Swagelok™ P/N SS-400-1-2 fittings with sintered metal filters.

Due to space considerations, the diverter-valve leg of the CFB system was removed during runs in which CARPT data were collected. Operation of the diverter-valve CFB leg for mass-flux measurements is described in Section 4.6.

3.1.7 Solids Control Valve

The solids-flow control valve at the base of the downcomer is a DeZurik model 933451 knife valve. This valve has a 76-mm (3-in.) bore with a knife closure actuated by a manually-operated screw mechanism. The screw mechanism requires about 21 turns to travel from fully closed to fully open. The knife mechanism linearly moves the knife across the valve bore; the fraction of the bore opened thus does not correspond linearly to the number of turns applied (see Figure 3.7).

The diverter valve used to route solids to the weighing chamber is a Buhler model MAYF80 flapper valve. This valve has an 80-mm (3.15-in.) bore and is designed to mate via a compression O-ring joint to 80-mm (3-in.) OD pipe. The installation of the valve in this application is such that the “straight-through” valve configuration corresponds to regular operating (solids returned to the downcomer), and the “diverted” valve configuration corresponds to solids-flux measurement conditions (solids routed to weighing chamber).

The solids-return valve at the base of the weighing chamber is a DeZurik knife valve similar to that at the base of the downcomer, but with a lever-actuated valve closure. This valve has a 76-mm (3-in.) bore. The geometry of the lever handle was modified from its stock configuration to accommodate tight installation space.

The diverter-valve leg is isolated from the rest of the CFB by a Sharpe 66-series 76-mm (3-in.) bore ball valve. Because the solids valves employed elsewhere in the loop do not reliably prevent the bleed of gas across the valves, this additional isolation element was required.

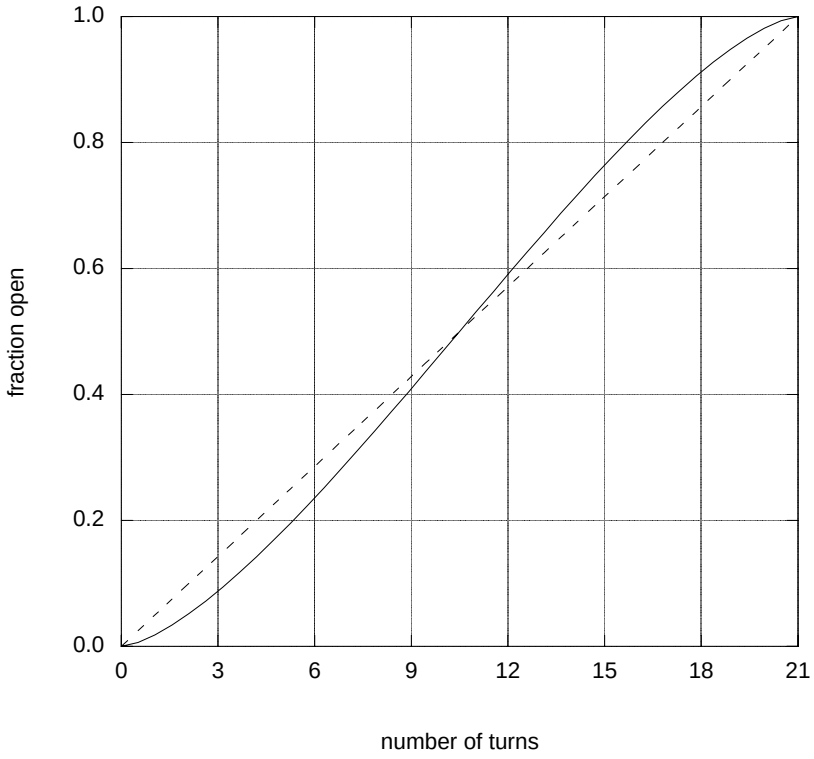

Figure 3.7. Dependence of fraction of bore area open on number of turns of screw handle for knife valve at base of downcomer (solids metering valve). Solid line: valve behavior; dashed line: linear behavior.

3.1.8 Air Supply

Motive air was supplied to the riser from the house air supply of 250 psig dry air. This was regulated down to nominally 70 psig supply via a two-stage arrangement of single-stage regulators. The two-stage arrangement helped to isolate the riser from fluctuations in supply pressure due to other experimental demands on the supply in the building. After regulation, supply to the riser was controlled by a ball valve. Supplied air was then humidified using deionized water supplied through a Bete™ fog nozzle. Nominal air-supply relative humidity during riser operations was about 15%. Motive-air flow rate was measured by an orifice gage, and motive-air temperature and relative humidity were measured by a Vaisala™ sensor package. These measurements were all made upstream of the riser engagement section.

Fluidization air was drawn from the same house air supply. It was regulated down to about 80 psi by a single-stage regulator, and supplied to the solids-transfer standpipes and solids disengagement section via flow controllers. Fluidization air was metered through separate manual valves and supplied to the downcomer and engagement sections, with flow-rate measurement conducted in separate off-line experiments. Fluidization air was not humidified.

3.2 Data Acquisition

CFB data were acquired with using National Instruments (NI) hardware and LabVIEW™ software. Data were collected via NI SCXI 1102C and 1121 modules mounted in a common SCXI 1001 chassis. SCXI 1303 terminal blocks were used in conjunction with the 1102C modules; an SCXI-1327 module was used to extend the input range of the 1121 module. This configuration allowed the collection of all ranges of data output from the various transducers and meters in the riser system with minimal hardware overhead.

Data were acquired on a Windows™ PC-based system via an NI PCI-6034E data-acquisition card. Data were acquired at a 1 kHz "background" rate and reported and stored at a user-selected rate. Typical reporting rates were 2 Hz, though for some applications, results were reported as frequently as 250 Hz. Real-time output included user-selectable strip-chart traces of any desired channels, along with quantitative values and alarm warnings at user-set conditions (e.g., high pressure drop across the baghouse filter, indicating filter clogging). Data were logged directly to text files for post-processing and analysis.

3.3 Solid-Particle Properties

The riser was operated with two different particle loads: fluid catalytic cracking (FCC) catalyst particles and solid glass beads. FCC was used extensively as it represents the most typical application of CFB risers. Glass beads were used to match the density of the coated scandium particle used in CARPT experiments. Property-measurement techniques and measured properties of these particles are discussed below.

3.3.1 Fluidized Catalytic Cracking (FCC) Catalyst Particles

The fluidized catalytic cracking (FCC) catalyst particles used in the riser experiments were equilibrium FCC supplied by Chevron Chemical Company as part of the MFDRC. The specific chemical formulation of this catalyst was proprietary, but it was described as a typical zeolite base particle carrying nickel, cobalt and other catalyzing metals specific to the FCC process. A photograph of the FCC particles used in the experiment is shown in Figure 3.8. In handling the FCC particles for determination of properties, it was assumed that the polydispersity of the particles had the potential to skew results. As such, particles were sampled in accordance with Knowlton (2000). In general, particles for property measurements were sampled with a "J"-shaped tube from several locations (depths and radii) in a 55-gallon container. The resulting sample pile was then repeatedly halved until a sufficiently small sample was available for the sizing or other measurement operation being performed.

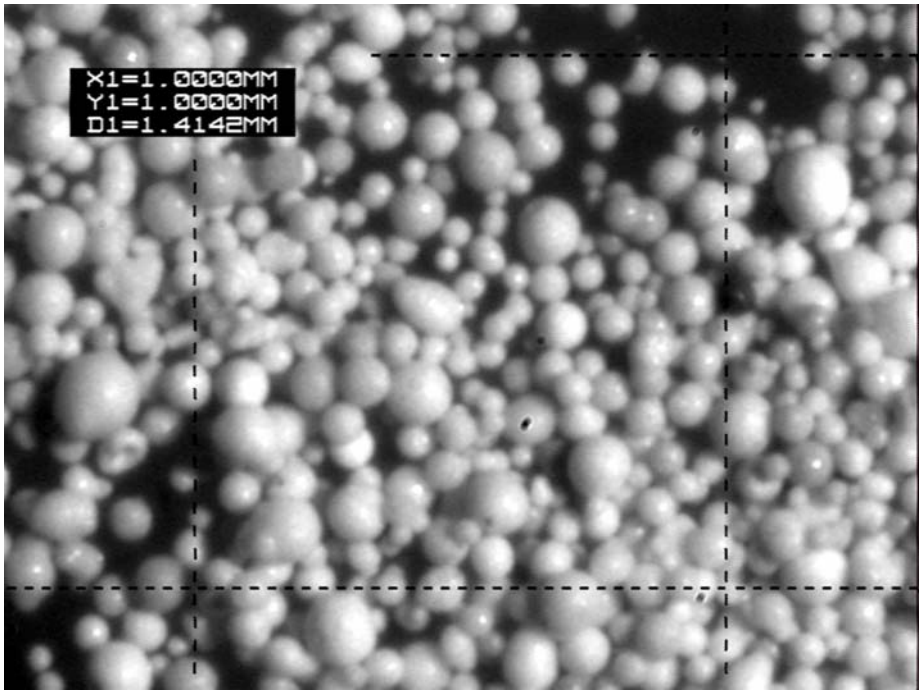

Figure 3.8. Photograph of FCC particles used in MFDRC riser experiments. The centered area defined by dashed lines represents a 1 x 1 mm square.

Zeolite FCC particles are porous, and as such, have three distinct densities. The first, bulk density, is the dry mass of a large collection of particles per unit volume; this density is easily determined by weighing a known volume of particles in, say, a graduated cylinder. The second, particle density, is the density of the particle material within the particle's spherical volume; it is the density of the particle material as it is distributed within the volume of the porous particle itself. The third is the material density, representing the ratio of the mass of material in the particle to only the volume the material itself occupies. This relationship is illustrated in Figure 3.9. As such,

$$\rho_{material} > \rho_{particle} > \rho_{bulk}, \tag{3.2.1}$$

$$\rho_{particle} = \frac{\rho_{bulk}}{(1-\alpha_{bulk})}, \tag{3.2.2a}$$

$$\rho_{material} = \frac{\rho_{particle}}{(1-\alpha_{particle})}, \tag{3.2.2b}$$

where, in each case, α represents the appropriately defined void fraction.

For the FCC particles used in this experiment, bulk density was determined by repeated weighings to be $\rho_{bulk} = 856 \pm 50$ kg/m^3.

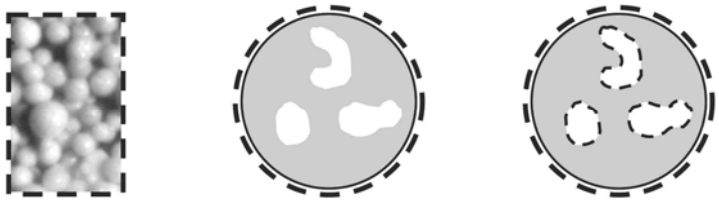

Figure 3.9. Concepts of masses and volumes required to compute densities. Left: bulk density is bed mass per containing volume. Center: particle density is particle mass per containing volume. Right: material density is material mass per material volume.

To determine bulk void fractions and thus particle densities, beds of FCC particles were immersed in water for 24-48 hours to allow the particles to fully saturate. Small samples (grams) of saturated particles were then run through a thermogravimetric analyzer (TGA). These samples were transferred to the TGA pan on a small spatula, and were placed in the sample pan in a thin layer to minimize the presence of liquid external to the particles. The TGA heats the pan in a prescribed temperature history while the mass of the sample pan is monitored and recorded. The lost mass represents the water originally contained in the sample particles' porosity:

$$M_{lost} = \rho_{water} V_{particles} \alpha_{particle} \ , \tag{3.2.3}$$

and the final mass represents the dry particle mass:

$$M_{final} = \rho_{particle} V_{particles} \ , \tag{3.2.4}$$

Rearranging,

$$\frac{M_{lost}}{M_{final}} = \frac{\rho_{water} \alpha_{particle}}{\rho_{particle}} \ . \tag{3.2.5}$$

This allows the application of the TGA results for a relatively small-number sample of particles to the entire saturated bed. Returning to consideration of the saturated bed, the mass of the entire saturated bed is given by:

$$M_{wet\ bed} = M_{particles} + M_{water\ in\ particles} + M_{water\ between\ particles} \ , \tag{3.2.6}$$

or, expanding, and noting that the mass of the particles in the dry bed is simply the mass of the dry bed itself,

$$M_{wet\ bed} = M_{dry\ bed} + \rho_{water} \alpha_{particle} V_{bed} (1 - \alpha_{bed}) + \rho_{water} V_{bed} \alpha_{bed} \ , \tag{3.2.7}$$

Using (3.2.5) to replace the $\rho_{water}\alpha_{particle}$ product in the 2nd term on the right-hand side,

$$M_{wet\ bed} = M_{dry\ bed} + V_{bed}(1-\alpha_{bed})\frac{M_{lost}\rho_{particle}}{M_{final}} + \rho_{water}V_{bed}\alpha_{bed} \quad . \tag{3.2.8}$$

Using (3.2.2a) to replace $\rho_{particle}$ with $\rho_{bed} / (1 - \alpha_{bed})$ gives:

$$M_{wet\ bed} = M_{dry\ bed} + V_{bed}\frac{M_{lost}\rho_{bed}}{M_{final}} + \rho_{water}V_{bed}\alpha_{bed} \, . \tag{3.2.9}$$

Or, noting that $M_{dry\ bed} = \rho_{bed}V_{bed}$,

$$M_{wet\ bed} = M_{dry\ bed} + M_{dry\ bed}\frac{M_{lost}}{M_{final}} + \rho_{water}V_{bed}\alpha_{bed} \tag{3.2.10}$$

The void fraction of the bed α_{bed} (which is identically equal to α_{bulk} as in Equation (3.2.2a)) can now be estimated from a series of lab measurements: masses of dry and wet beds, the (bulk) volume of the wet bed, and the TGA data:

$$\alpha_{bed} = \alpha_{bulk} = \frac{1}{\rho_{water}V_{bed}}\left(M_{wet\ bed} - M_{dry\ bed} - M_{dry\ bed}\frac{M_{lost}}{M_{final}}\right) \tag{3.2.11}$$

With α_{bulk} thus determined, Equation (3.2.2a) can be used to determine the particle density $\rho_{particle}$. If desired, the TGA data can then be used with Equation (3.2.5) to determine the particle porosity represented by $\alpha_{particle}$, followed by the determination of the material density $\rho_{material}$ from Equation (3.2.2b).

Repeated estimates of bulk voidage α_{bulk} were made using the method described above and Equation (3.2.11). The resulting estimate of α_{bulk} applied throughout the MFDRC riser experiments is $\alpha_{bulk} = 0.34 \pm 0.03$. The significant contributor to uncertainty in this calculation was scatter in the TGA measurement results corresponding to estimation of water absorption by particles. Using this mean, the resulting particle-density estimate applied across MFDRC riser experiments with FCC was $\rho_{particle} = 1275 \pm 95$ kg/m^3; contributions to the uncertainty in this value from bulk-density and bulk-voidage estimates are of the same order of magnitude.

FCC particle size distributions were measured using a Malvern model 2600 particle sizing system. The basis of the measurement is a factory-calibrated analysis of the diffraction of a laser beam passed through a suspension of particles. Reliable operation of the Malvern system was verified by comparison to results of microscopy-based sizing measurements (i.e., individual particle counting) for both unsieved particle samples and for sieved samples in which a narrowed range of particle sizes was selected for analysis. Typical Malvern size-distribution measurement results are shown in Figure 3.10. The measured size distribution is approximately log-normal. The measured Sauter mean particle diameter for the FCC catalyst used in the riser is 65 μm.

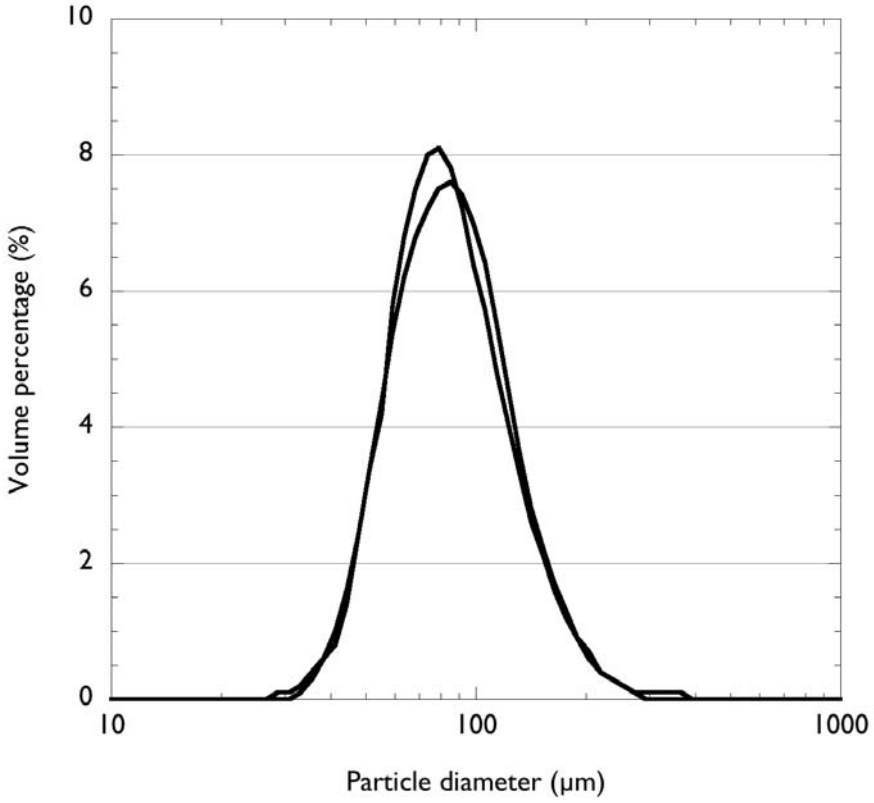

Figure 3.10. Volumetric size distributions of FCC particles used in Sandia/MFDRC riser, from Malvern 2600 measurements. Multiple lines indicate repeat runs. No fit was applied to the raw Malvern data.

3.3.2 Glass Beads

The glass particles used in the riser were Potters Industries A-Series glass beads. These beads are delivered sieved in an 80-120 sieve range, or a diameter range of 120-180 μm. Because they are solid beads, bulk void fraction, bulk density, and particle density can be measured by simple fluid displacement measurements. The resulting values are a particle density $\rho_{particle}$ = 2.5 g/cm^3 and a bulk solids fraction of α_{bulk} = 0.57. Glass-bead particle sizing was performed using a Beckman-Coulter laser-diffraction analyzer. Sauter mean particle size was found to be 154 μm, with an approximately normal distribution about the expected range.

4. Diagnostics

Many different diagnostic techniques were examined and implemented in this project. While some worked very well and provided useful and important data (differential pressure, gamma-densitometry tomography, electrical-impedance tomography, solids flux, and computer-aided radioactive particle tracking), others were found to produce inaccurate or ambiguous results or were limited to very dilute flow conditions (suction probe, fiber-optic voidage probe, and optical techniques) and were therefore not normally applied during CFB operations. This section provides descriptions of each and comments on their performance for the flows of interest.

4.1 Differential Pressure

Pressures in the riser were measured using Validyne DP15 series variable reluctance pressure transducers. In general, these were configured as differential transducers measuring pressure differences across sections of the riser or downcomer. In some cases, the transducers were configured as gage transducers by leaving the low-pressure side of the transducer open to atmosphere. These transducers can be reconfigured to allow different measurement ranges by swapping the transducer's internal diaphragm.

The transducers are excited by a set of Validyne CD18 carrier demodulator mounted in Validyne MC1-10 module cases. The MC1-10 cases are essentially multi-slot module cases that provide uniform, regulated carrier and power supplies to each CD18 module. The CD18 units supply a 3-kHz bridge excitation to the DP15 transducers, with simple capabilities for return-signal conditioning (250 Hz filtering, with zero and span trimming). Output from the CD18 unit is a ±10 VDC signal corresponding to the full range of the installed transducer.

As discussed in Section 3.1, the pressure transducers were installed with in-line sintered metal filter discs ("frits" or "snubbers") to prevent the contamination of the transducers by the solid material in the riser. Details of the filter installation varied with location in the CFB loop, and are discussed in the appropriate sections within Section 3.1. The filters were effective in protecting the transducers but had a significant effect on transducer frequency response.

To investigate the effect of the filters on transducer frequency response, the response of the unfiltered system was first estimated by applying techniques provided by Validyne. Sensor, plumbing, and electronics responses were considered, to provide a lower-bound estimate of the unfiltered system's natural frequency. The natural frequency of the transducer alone is expected to increase as transducer range increases (this is a result of the transducer diaphragm's thickness increasing with range, with mechanical stiffness of the diaphragm increasing correspondingly). However, for the lowest differential range available – which was lower than any transducer used in the riser – the natural frequency of the transducer itself is expected to be around 2 kHz. This relatively high natural frequency is a result of the very small physical displacements (around 50 μm) required for variable-reluctance transducers.

Validyne suggests the following relationship for estimation of plumbing natural frequency ω_n:

$$\omega_n = \frac{c}{L \cdot \sqrt{\frac{1}{2} + \frac{Q}{aL}}} \tag{4.1.1}$$

where c is the local speed of sound, L is the length of tubing, Q is the transducer cavity volume, and a is the cross-sectional area of the tubing. Ignoring elbows and shorter runs of tubing and using a 30-cm length typical of straight tubing runs for transducers installed on the riser itself, the resulting estimate is

$$\omega_n = \frac{334 \text{ m/s}}{0.3 \text{ m} \cdot \sqrt{\frac{1}{2} + \frac{6.55 \times 10^{-8}}{1.78 \times 10^{-5} \text{ m}^2 \cdot 0.3 \text{ m}}}} = 1555 \text{ rad/s} \rightarrow 248 \text{ Hz} \tag{4.1.2}$$

This estimate obviates the 2 kHz of the transducer itself and roughly matches the 250 Hz cutoff frequency of the CD18 carrier demodulator units. The best expected frequency response for the unfiltered system is thus about 250 Hz.

The effect of the sintered filter on frequency response was examined experimentally by driving filtered and unfiltered transducers with a sinusoidally excited speaker. The speaker was mounted against a flat plate, creating a driven cavity. The unfiltered transducer was in turn mounted as flush as possible to this cavity to minimize the L term in Equation (4.1.1), and, similarly, the largest-diameter mounting bore possible was used to maximize the a term in (4.1.1). The mounting port for the filtered transducer mimicked the ports on the riser. A variety of filtered configurations were tested, including a flush configuration in which the transducer was mounted with a filter in place and minimal other plumbing, and an as-installed condition, using a run of plumbing and fittings identical to those used in riser installation. The low-pressure side of each transducer was left open to atmosphere. The experimental setup is shown schematically in Figure 4.1 and in a photograph (of an as-installed test configuration) in Figure 4.2.

In each case, the response of the filtered transducer was characterized by comparing to the unfiltered transducer as a reference. Two sets of results are presented in Figures 4.3 and 4.4. Note that in each case, the amplitude ratio has been converted to a sound pressure ratio in units of dB. Figure 4.3 presents frequency-response results for a mounting configuration with as-installed plumbing but without the sintered metal filter. There is distinct amplitude peak in the region of 250 Hz driving frequency, followed by a small roll-off in amplitude but a large increase in phase delay. Agreement with the 248 Hz natural frequency predicted by Equation (4.1.1) is thus good.

Figure 4.4 presents frequency-response results for the same configuration (plumbed as installed on the riser), but including the sintered metal filter. Two sets of data are shown; these sets were collected with identical plumbing but with different filters to test variation of filters within the lot used on the riser. Amplitude-ratio roll-off and phase lag are immediate, and are significant for frequencies over about 5 Hz (the 3 dB crossing for each data set is somewhere between 5 and 8 Hz driving frequency).

In light of the above analysis, the pressure transducers installed on the riser are considered suitable for time-averaged measurements only. With this in mind, pressure data were typically sampled at 2 to 3 Hz and statistics generated from those data were limited to temporal means.

Pressure-transducer locations and ranges are presented in Table 4.1. Locations are measured relative to the bottom of the CFB engagement section. Pressure transducer ranges were chosen as compromises between values expected during CFB operation and overpressures expected to occur due to such off-normal conditions as choking or slugging flow. Details of reported transducer location include:

- Locations of differential pressure transducers on the riser and downcomer correspond to the center of the difference range they span. For instance, the transducer on the riser at a height of 0.84 m measures the pressure difference between taps at 0.69 and 0.99 m.

- Locations of the gage-pressure transducers on the riser and downcomer correspond to the actual location of the tap to which they are connected.

- The gage-pressure transducer at the top of the disengagement section taps directly into the top cover of that section.

- Riser motive-air inlet pressure is measured upstream of the engagement section.

- The two orifice pressure transducers (pressure drop across the orifice and gage pressure upstream of the orifice) are tapped in accordance with standard orifice flow-metering practices.

- The HEPA filter differential transducer measures the pressure drop across the filter in the exhaust baghouse, and serves as a monitor on the health of the filtration system.

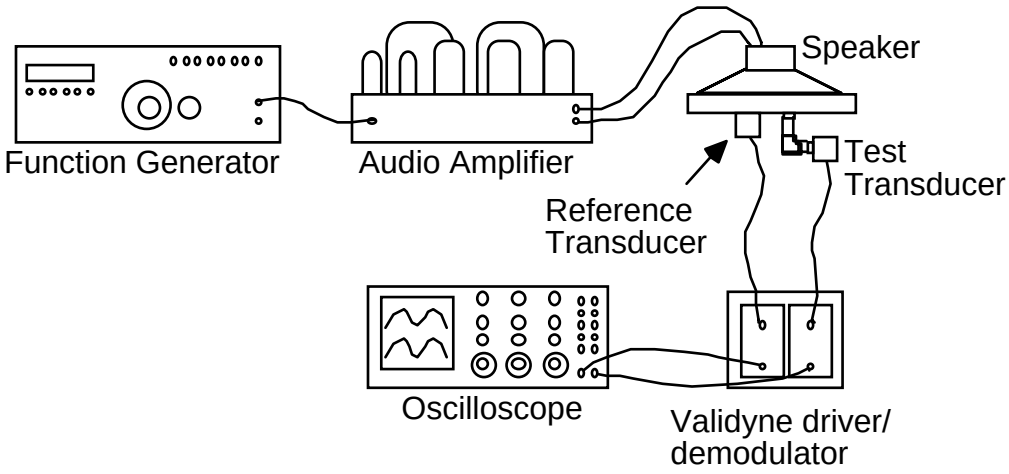

Figure 4.1. Schematic of pressure transducer frequency response measurement experiment.

Figure 4.2. Pressure transducer frequency response experiment driven cavity (speaker and plate) assembly with reference transducer and as-installed-on-riser transducer with plumbing.

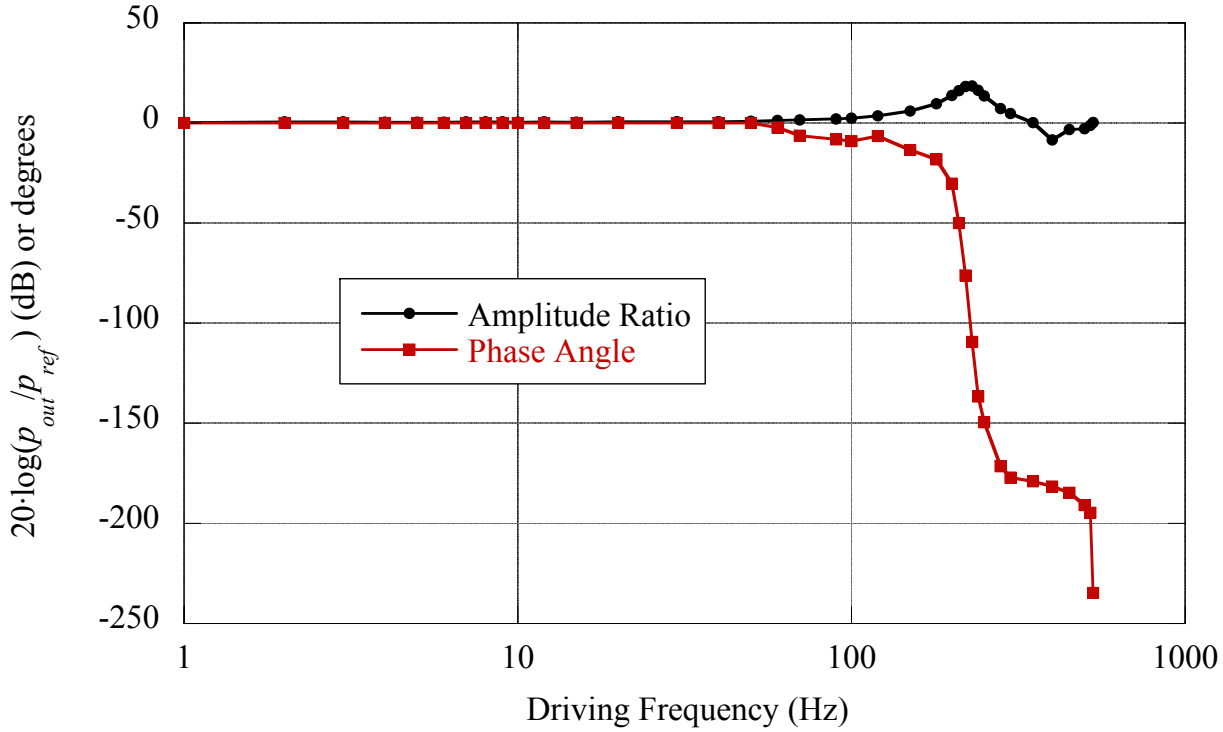

Figure 4.3. Frequency response plot (amplitude ratio and phase angle) for Validyne DP15 pressure transducer mounted with all plumbing associated with riser installation but without sintered metal filter.

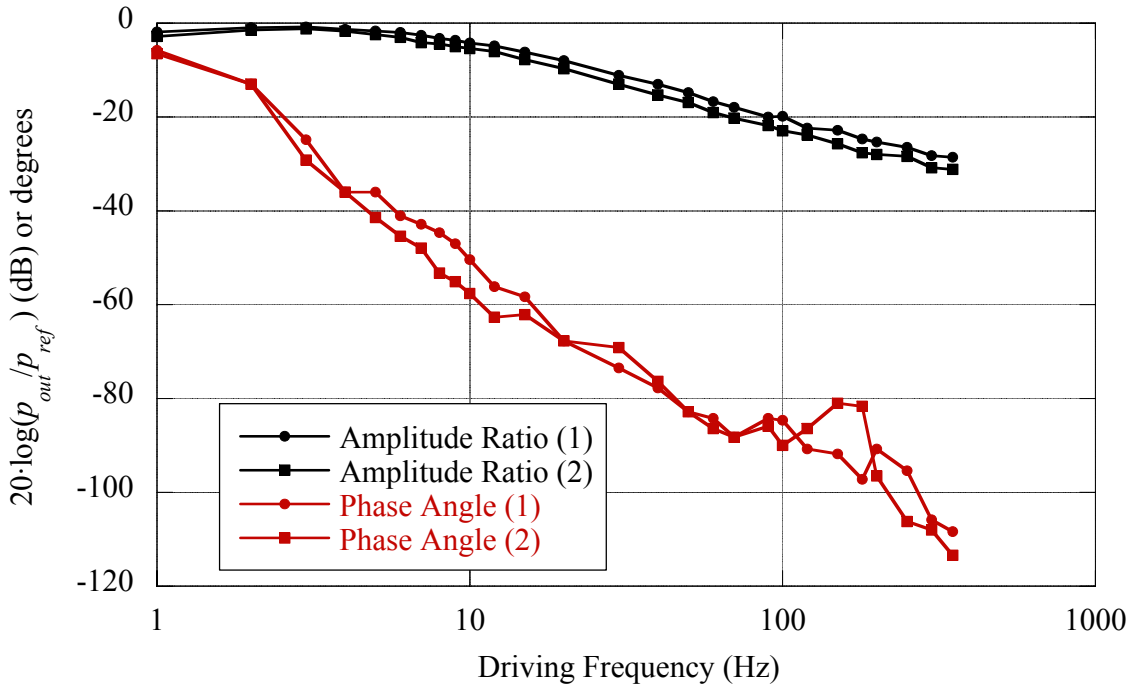

Figure 4.4. Frequency response plot (amplitude ratio and phase angle) for Validyne DP15 pressure transducer mounted with all plumbing associated with riser installation, including sintered metal filter. Data are presented for experiments with two filters.

Table 4.1. Pressure-transducer installation locations on CFB and measurement ranges. Locations are measured from the base of the engagement section. Locations in meters, ranges in psi (kPa). See text for explanation of locations.

Location (m)	Range (PSI, (kPa))	Comments
Differential-pressure transducers on CFB riser & disengagement		
0.56	2 (14)	
0.84	2 (14)	
1.14	2 (14)	
1.45	2 (14)	
1.75	1.25 (8.6)	
2.06	1.25 (8.6)	
2.36	0.8 (5.5)	
2.68	0.8 (5.5)	
2.97	0.8 (5.5)	
3.28	0.5 (3.5)	
3.58	0.5 (3.5)	
3.88	0.5 (3.5)	
4.19	0.5 (3.5)	
4.49	0.32 (2.2)	
4.80	0.32 (2.2)	
5.10	0.2 (1.4)	
5.41	0.2 (1.4)	
5.56	12.5 (86)	Gage pressure transducer at top of riser
TDE	5 (35)	Gage pressure on top of disengagement
Whole DE	0.8 (5.5)	
Differential-pressure transducers on CFB riser & disengagement		
Whole DC	12.5 (86)	
1.88	2 (14)	
2.48	2 (14)	
3.10	2 (14)	
3.71	2 (14)	
4.32	2 (14)	
4.93	2 (14)	
5.24	12.5 (86)	Gage pressure in downcomer freeboard
Lower standpipe connecting downcomer to riser		
Top of standpipe	12.5 (86)	Gage pressure
Bottom of standpipe	12.5 (86)	Gage pressure
Auxiliaries		
Riser air inlet	20 (140)	Gage pressure
Orifice differential	5 (35)	
Orifice gage	20 (140)	Gage pressure
HEPA filter DP	2 (14)	
Exhaust line	1.25 (8.6)	Gage pressure

4.2 Gamma-Densitometry Tomography

Gamma-densitometry tomography (GDT) uses measurements of gamma ray attenuation along multiple paths through a vessel to determine the radial profile of its phases (e.g., Werther, 1999). It is a noninvasive technique, which makes it attractive for multiphase flow measurement, and the gamma attenuation physics are well-understood. For these reasons, a number of gamma-densitometry tomography systems have been assembled and applied for multiphase flow measurement worldwide (e.g., Petrick and Swanson, 1958; van Santen et al., 1997; Mudde et al., 1999). Sandia National Laboratories has experience with multiphase GDT in two- and three-phase flows in bubble columns (Shollenberger et al., 1997; Torczynski et al., 1997; George et al., 2000ab, 2001). The GDT system designed and assembled for this project was based on this experience.

4.2.1 GDT System

The GDT system (Figure 4.5) consists of a 100-mCi ^{137}Cs (cesium 137) source and an array of NaI(Tl) (thallium activated sodium iodide) scintillation detectors. ^{137}Cs has a half-life of approximately 30 years and produces a fairly monoenergetic spectrum of gamma photons centered on 661.6 keV. The source is housed in a tungsten vault, which shields personnel from exposure when the source is not in use. The source is exposed by supplying compressed air to a piston that raises the source to align it with a fan-shaped collimator (Figure 4.6). The source opening collimator produces a fan-shaped gamma beam that passes through the riser to the detector array, where the gamma intensity along each distinct ray is measured. The detector array contains 13 detectors, as shown in Figures 4.7 and 4.8, but only 8 at a time are used, as indicated in Figure 4.8, since the detection electronics are currently limited to eight channels. Dead time occurs when the detector and/or electronics are unable to process a new count because they are still tied up processing the previous count. The sum of "live" time, where data are acquired, and "dead" time give the total elapsed measurement time. The source is attenuated to keep the system dead time below 40% of the total measurement time (Knoll, 2000) by the placement of lead sheets in front of the source (typically 1.9 cm of lead total) and by a collimator in front of the detectors, consisting of a 5.1 cm (2 in.) thick steel plate with 1.3 cm (0.5 in.) wide, 5.1 cm (2 in.) long slots in front of each detector (Figure 4.7). In addition to reducing dead time, the collimator slots improve the spatial resolution of the system. The collimator slots approximately determine the spatial extent of the measurement. Each collimator functions by reducing the magnitude of the radiation that reaches the face of the detector outside of the collimator slot. The magnitude of this reduction can be quantified by calculating the ratio of the radiation flux through the steel surrounding the slot to the radiation flux through the slot as follows:

$$\text{ratio} = \frac{I_0\, e^{-\mu x}(A_d - A_s)}{I_0\, A_s}, \tag{4.2.1}$$

where I_0 is the initial radiation intensity, μ is the attenuation coefficient (0.58/cm for steel at 661.6 keV), x is the thickness of the collimator plate (5.1 cm), A_d is the area of the detector face (20.2 in^2), and A_s is the area of the slot (6.4 cm^2). The ratio for these conditions is 0.11, thus indicating suitable collimation. Figure 4.8 shows which eight detectors were used for data

acquisition. The fan-shaped beam of radiation is approximately 5 cm high where it intersects the riser. This results in a measurement volume of approximately 7.7×10^{-4} m^3. Figure 4.9 is a photograph showing the GDT system installed on the riser.

Each scintillation detector (Bicron Model 2M2/2, run at 900 V DC) is connected to an Ortec® ACE Mate™ 925-SCINT amplifier and bias supply, which amplifies and shapes the detector pulses, then to an Ortec® 916A multichannel analyzer (MCA) in a personal computer. Ortec® Maestro software is used to collect data from the eight detectors. The complete energy spectrum is measured by the MCA, and the counts around the 661.6-keV ^{137}Cs peak are used in the analysis presented below.

Two traverses were added to the riser setup to accommodate GDT. First, an axial traverse was mounted to the riser superstructure, allowing vertical movement of the source and detector array assembly. The computer-controlled traverse with two feet of vertical travel is incorporated into the extended vertical traverse via a stepping scheme. Second, a lateral traverse was added to move the detector array laterally at a fixed axial location, without moving the source. Use of this traverse gave improved spatial resolution for near-wall measurements. Since the detectors themselves are quite large (2 in. diameter), it is not possible to pack enough detectors in to improve the spatial resolution. Instead, the lateral traverse is used to make small lateral movements of the detector array. In this implementation, the detectors were moved to seven different lateral positions (centered, ±0.75 in., ±1.00 in., ±1.25 in.). Thus, the eight-detector array was used to make 56 attenuation measurements. This is important for resolving radial solids-loading gradients in this core-annular flow where such gradients are expected to be strong. Figure 4.10 shows the radial locations of the 56 measured attenuation rays, along with a curve fit to the data and radial reconstruction described below. The typical acquisition time for riser data was 30 seconds at each traverse position. The software control began acquisition on each detector sequentially, which took on the order of one second per detector. Therefore, each eight-detector data set was acquired essentially simultaneously. The detector array was then translated horizontally and the next data set acquired. Full acquisition across each horizontal section therefore took approximately five minutes.

Attenuation of monoenergetic gamma photons is given by $I = I_o e^{-\mu L}$, where I_0 is the initial, unattenuated intensity, μ is the linear attenuation coefficient of the attenuating material, and L is the thickness of attenuating material. If more than one attenuating material is present, the separate effects can be included by summation of the attenuation of each material. GDT requires that the two phases in a two-phase flow have significantly different attenuation coefficients for good image resolution and useful quantitative results. For gas-solid mixtures, the gamma attenuation of the gas is generally negligible. Note that the linear attenuation coefficient is equal to the mass attenuation coefficient multiplied by the material density. For measurement of multiphase mixtures for which the attenuation coefficient μ is not known and may vary from batch to batch, the amount of attenuating material in the beam path can be determined by using a ratio between empty and full measurements. “Empty” data are taken with the riser empty of particles but full of air and “full” data are acquired with the riser containing a packed bed of solid particles (FCC or glass beads) in air with a volume fraction of 0.66. The data can be processed as:

$$\ln(I/I_{empty}) = -\mu L \tag{4.2.2}$$

and the full and empty data can be arranged to yield:

$$\ln\left(I_{full}/I_{empty}\right) = -\mu L_{full}\,. \tag{4.2.3}$$

Taking the ratio, the percent full (solids fraction) is then given by

$$\frac{L}{L_{full}} = (1-\varepsilon) = \frac{\ln(I/I_{empty})}{\ln(I_{full}/I_{empty})}\,. \tag{4.2.4}$$

For these experiments, the values of I, I_{full}, and I_{empty} were taken from the peak intensity region as measured using the MCA. At least 10^4 counts were recorded around the 661.6-keV peak in order to achieve 1% or better uncertainty due to inherent Poisson statistics of the gamma source (uncertainty = $N^{-1/2}$). The gamma data are thus inherently time-averaged. Typical acquisition time for riser data presented below is 30 s at each position. Figure 4.11 shows the measured energy spectrum for gamma measurements of steel plates.

Operation of the GDT system and analyses were validated by verifying the thickness of steel plates and of containers of water for which the linear attenuation coefficients for gamma radiation at 661.6 keV were known. The linear attenuation coefficient for water is μ_{water} = 0.086/cm and for steel is μ_{steel} = 0.576/cm. These results, shown in Figures 4.12 and 4.13, indicate that the average error in measured thickness was 2%, with maximum error of 5%. The range of attenuations covered in these static tests was much broader than expected in the gas-solid riser flow. Repeated static packed bed tests have shown variability less than 3%.

GDT data with the column empty and full of solids are used to calculate the path length along each trajectory through the column and are shown in Figure 4.14 along with the predicted path length. Agreement is within 1%. Figure 4.15 shows the repeatability of the measurement and flow; path-averaged solids volume fraction plotted as a function of detector location for nine repeated runs of the same nominal flow condition.

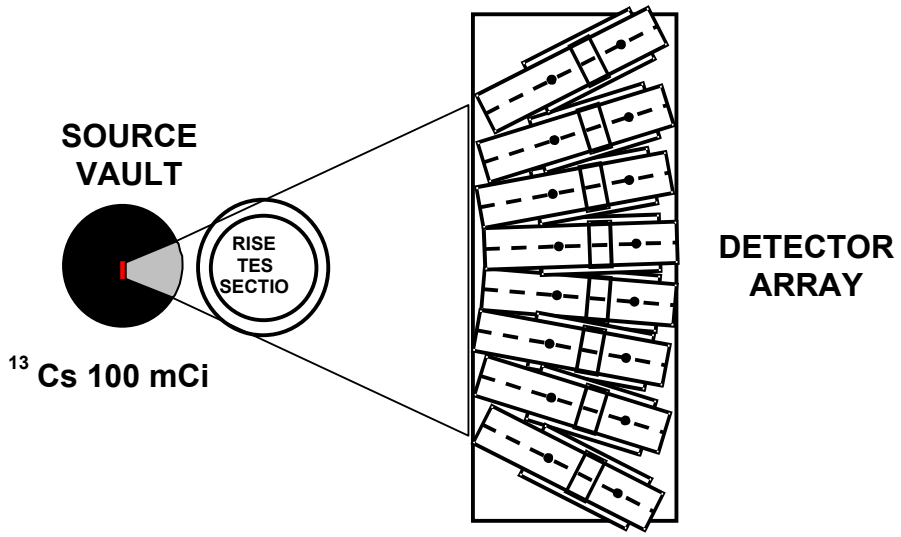

Figure 4.5. Gamma-densitometry tomography system layout. Source is 100 mCi ^{137}Cs.

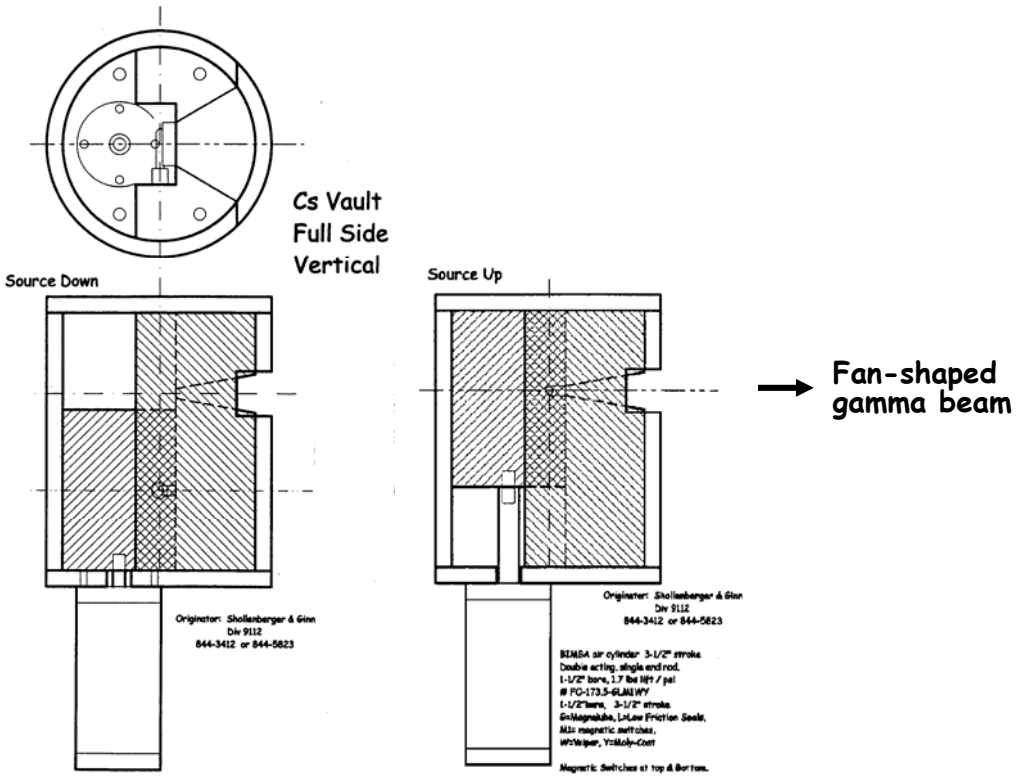

Figure 4.6. Schematic of source vault for gamma-densitometry tomography system. Above, top view. Lower left, side view with source down or not exposed. Lower right, side view with source up or exposed.

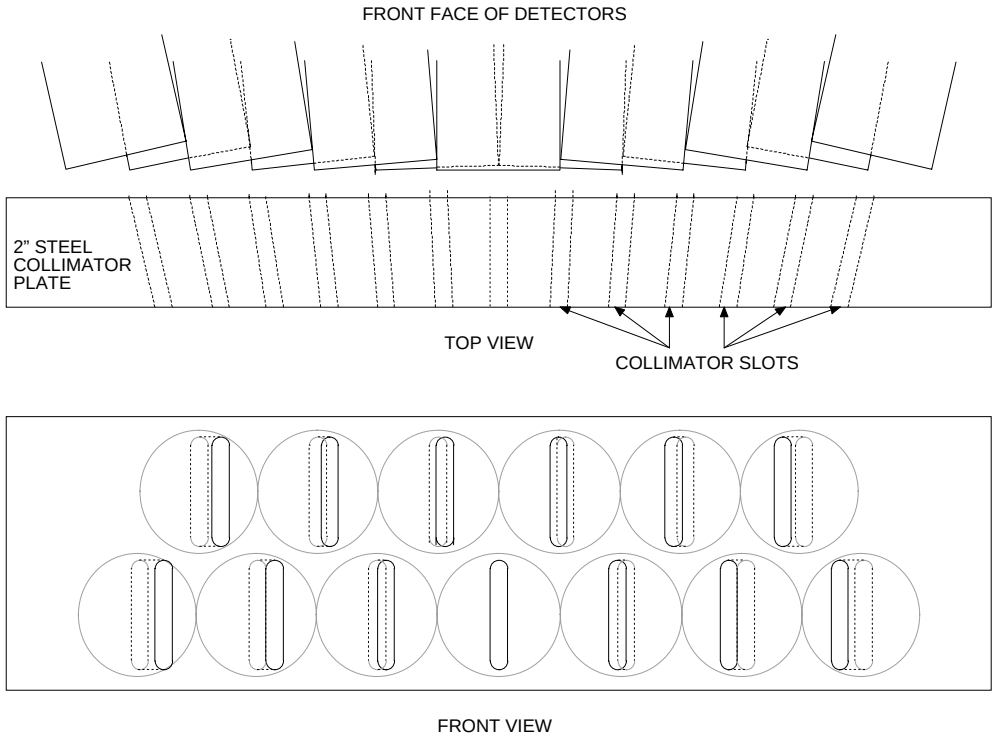

Figure 4.7. Schematic diagram of steel collimator plate and detector array.

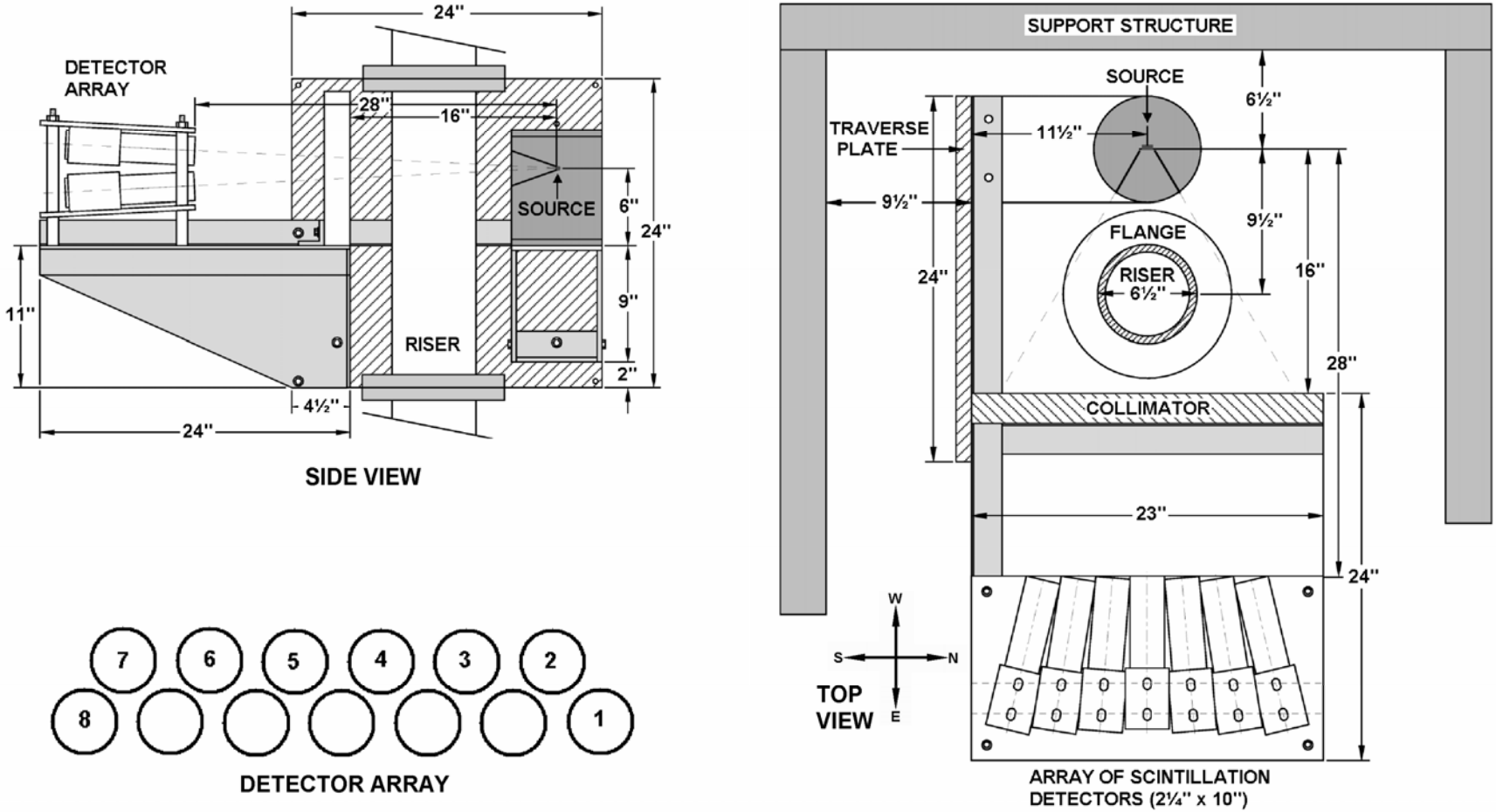

Figure 4.8. Schematics of GDT system (from Trujillo et al., 2001a). The data processing electronics limited acquisition to eight channels, so the eight detectors indicated in the lower left figure were chosen.

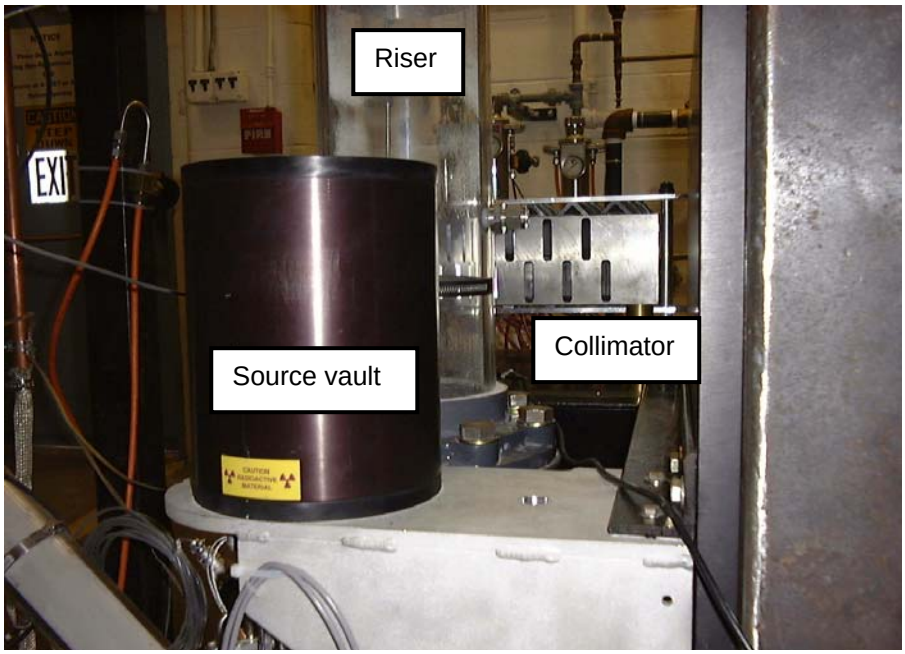

Figure 4.9. Photograph of GDT system showing source vault (black canister), riser, and steel collimator plate. Detectors are located behind the collimator.

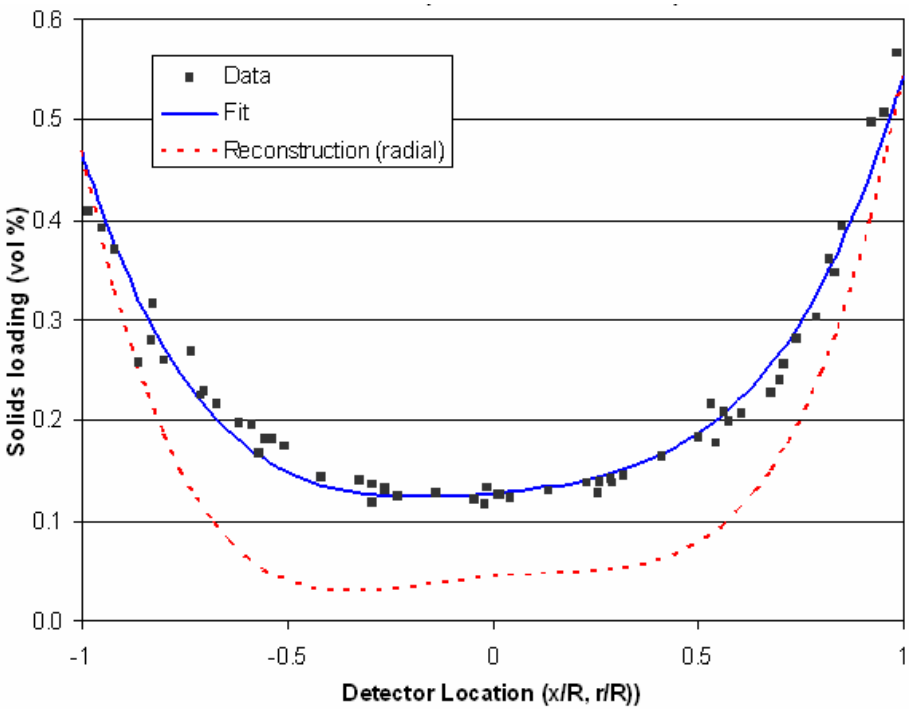

Figure 4.10. Time averaged bulk solids volume fraction measured with GDT. Symbols and solid curve are path averaged values and dashed curve is non-axisymmetric reconstruction of the radial variation. *z/D* = 3.27. Low solids flux, low superficial gas velocity (Case 1). Area-averaged solids volume fraction is 0.18.

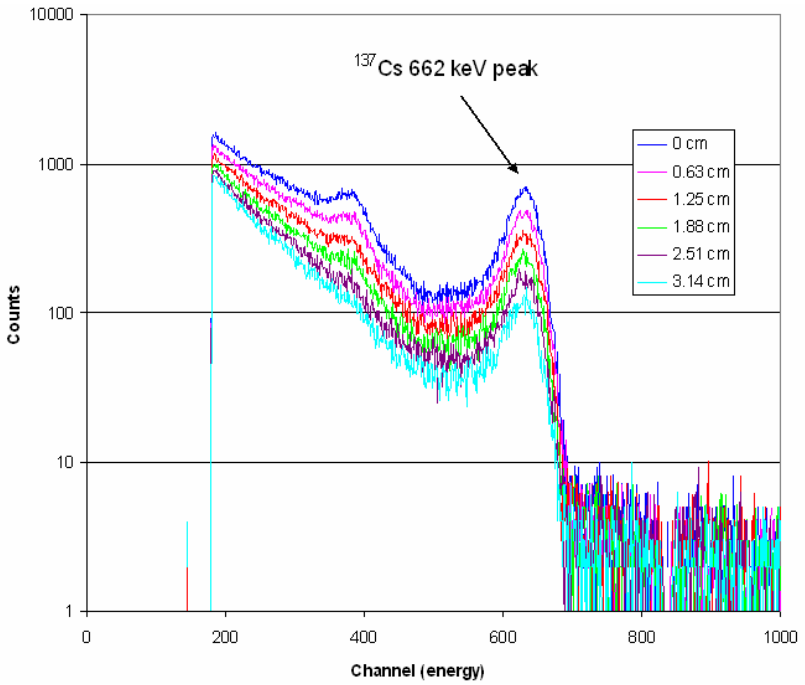

Figure 4.11. Energy spectra measured by a single detector as steel plates were placed in the beam path between the source and detector. Data acquisition "live" time was 240 seconds in each case. The sum of the 20 peak channels was used as the measure of intensity.

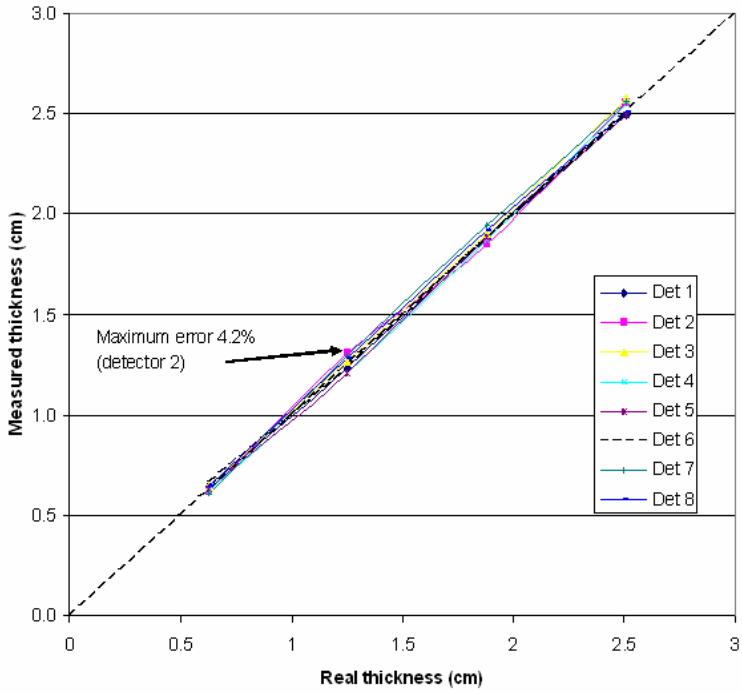

Figure 4.12. Thickness of steel plates calculated using Equation (4.2.4) and the known linear attenuation coefficient of steel (0.576/cm).

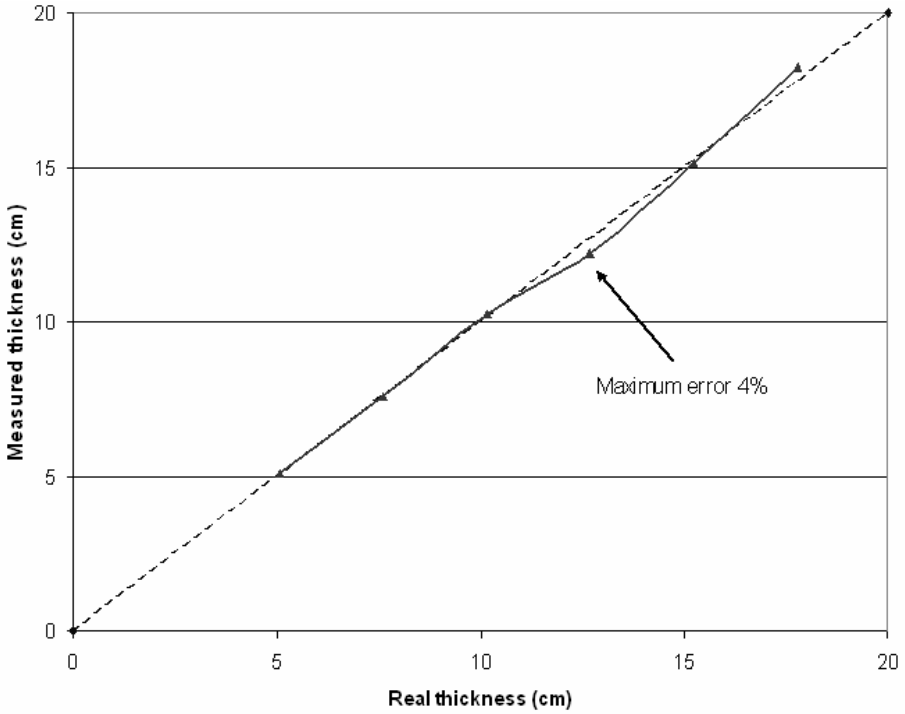

Figure 4.13. Thickness of water boxes calculated using Equation (4.2.4) and the known linear attenuation coefficient of water (0.086/cm).

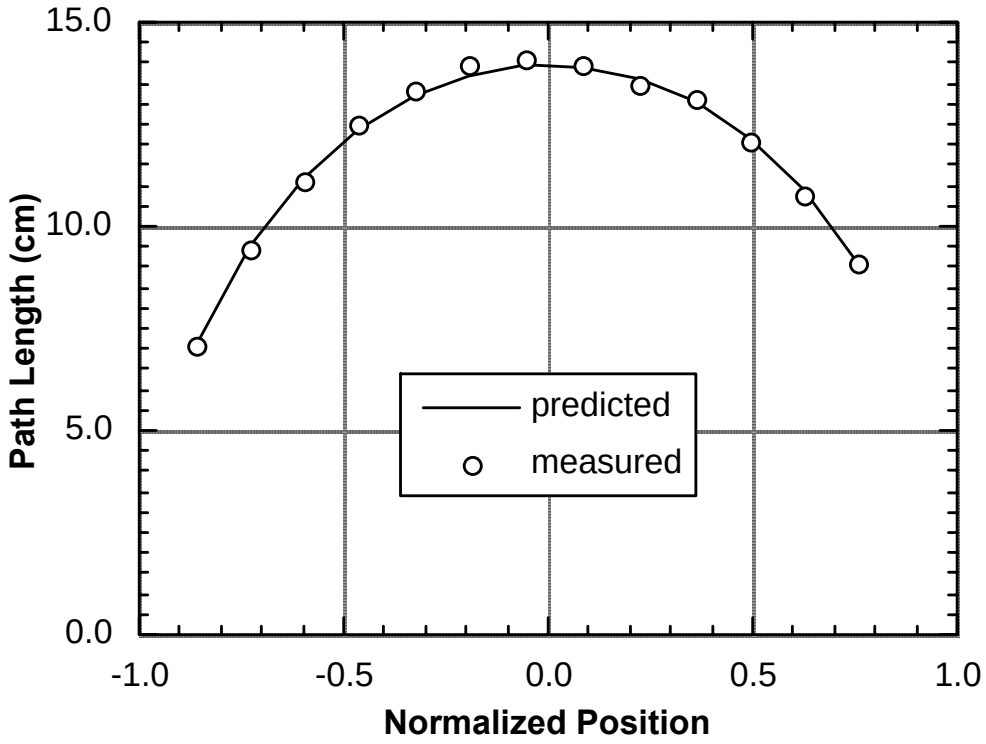

Figure 4.14. Path length through column calculated using GDT measurements with the column empty and full of solids compared to predicted values.

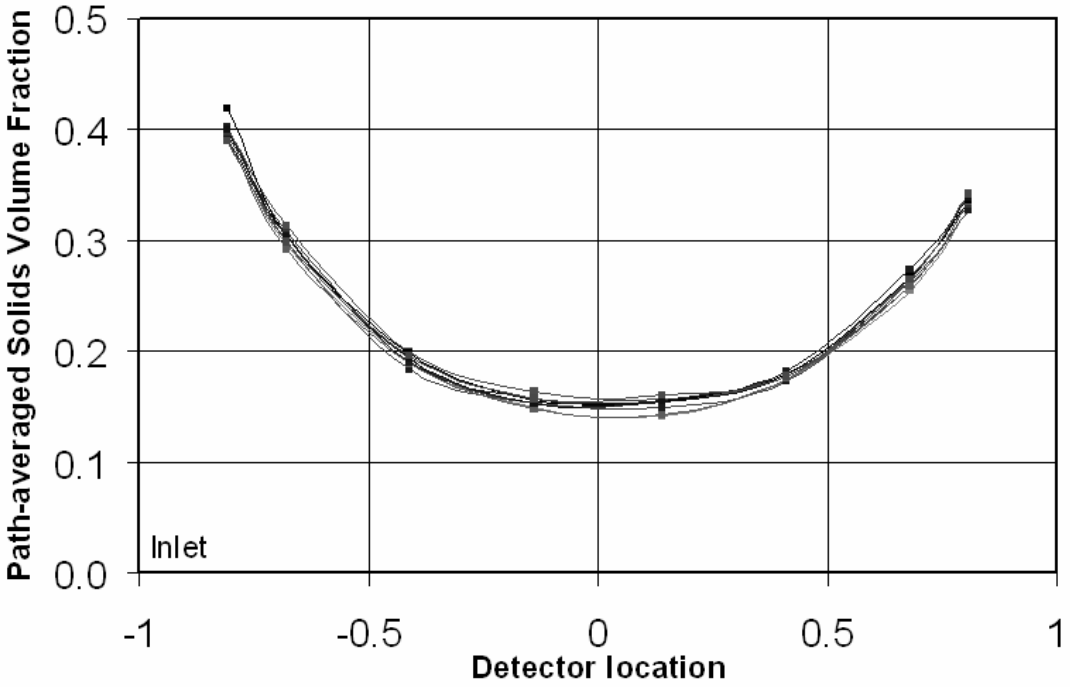

Figure 4.15. Path-averaged solids volume fraction plotted against horizontal detector position for repeated runs at the same position (*z/D* = 3.4) and same nominal run conditions (superficial gas velocity U_g = 5.2 m/s, solids flux G_s = 90 kg/m^2·s), showing repeatability of measurement and flow. The "Inlet" at the left side indicates the side of the riser where particles are returned from the downcomer.

4.2.2 GDT Reconstruction

The measured gamma ray attenuation along each ray is converted to solids volume fraction by comparing baseline measurements of the column empty and full of FCC catalyst (with measured close packing of 0.67). To do this, the path-averaged intensity for each of the 56 detector positions while flowing, I, are normalized with the empty and full attenuation data

$$1-\varepsilon = \frac{\ln(I / I_{empty})}{\ln(I_{full} / I_{empty})} \times 0.67 . \tag{4.5}$$

Note that the factor of 0.67 scales the results to a packed bed of solids. These values are then fit with a fourth-order polynomial expression including even powers of r (r^2 and r^4) and, in some cases, allowing a tilt along the radius (r dependence).

For reconstruction in which a tilt is allowed, a generalized Abel transform (Vest, 1985; Shollenberger et al., 1997) that allows for asymmetric phase distributions is used to convert the

path-averaged solids volume fraction into a radial solids volume fraction profile in the circular domain.

The fit assumes that the solids distribution was axially symmetric except for a possible linear variation (tilt) along the diameter in the direction in the solids are reintroduced at the base of the riser:

$$f(r,x) = a_0 + a_1(x/R) + a_2(r/R)^2 + a_4(r/R)^4, \tag{4.2.6}$$

which gives the solids volume fraction f at a radial position r and horizontal position x as a function of normalized position in the riser and a set of coefficients a_i. The Abel transform is used to convert the data curve fit $f(r,x)$ to a radial profile of solids loading, as depicted in Figure 4.16 (Torczynski et al., 1997). The Abel transform of $f(r,x)$ is:

$$g(x) = b_0 + b_1(x/R) + b_2(r/R)^2 + b_4(r/R)^4 \tag{4.2.7}$$

The second term in Equations (4.2.6) and (4.2.7) (x/R term) represents the linear variation in solids distribution in the direction solids enter the riser base (north-south), and is unaffected by the transform, since it is a function of x in both forms. The generalized equations for relating the coefficients of an even polynomial function and its Abel transform are given by Torczynski et al. (1997), and here they are related by:

$$a_0 = b_0 - \frac{1}{2}b_2 - \frac{1}{8}b_4 \tag{4.2.8}$$

$$a_2 = \frac{3}{2}b_2 - \frac{3}{4}b_4 \tag{4.2.9}$$

$$a_4 = \frac{15}{8}b_4 . \tag{4.2.10}$$

Figure 4.10 includes a representative radial profile of solids fraction measured using GDT when an asymmetric fit was used.

An inherent assumption in the reconstruction is that the rays from source to detector passing through the riser correspond to parallel rays of the same length to match the geometry of the Abel transform, as illustrated in Figure 4.18. This was considered a reasonable approximation because of the small angles subtended by the rays (14º) and the difficulty involved in using the Abel transform in multiple rotated coordinate systems or some other method. The curve fit, transform, and conversion of coefficients embodied in Equations (4.2.6) – (4.2.10) were all done automatically using Excel™ functions. In practice, the reconstruction is performed using an Excel™ spreadsheet with functions used to derive the radial profiles from the normalized data (Equation (4.2.6)). The 56 experimental values of normalized position $\tilde{x} = x/R$ and normalized attenuation (Equation (4.2.5)) are entered into the correct spreadsheet columns and the corresponding $\tilde{x}^2$ and $\tilde{x}^4$ values are calculated in adjacent columns. The Excel™ function

LINEST is used to fit a linear combination of the functions $\{1, \tilde{x}, \tilde{x}^2, \tilde{x}^4\}$ to the data $\overline{f}_{\text{expt}}$. The resulting coefficients $\{b_0, b_1, b_2, b_4\}$ are extracted from this fit using the Excel™ function INDEX, and the coefficients $\{a_0, a_1, a_2, a_4\}$ for the function f are calculated. A flag is incorporated to enable selection of the quartic polynomial or the quadratic polynomial for the reconstruction: a value of 0 selects the quartic polynomial, whereas any other value selects the quadratic polynomial. The experimental data $\{(\tilde{x}, \overline{f}_{\text{expt}})\}$, the fit $\overline{f}$, and the reconstruction f are displayed graphically for comparison purposes. Figure 4.17 show representative profile of solids fraction measured using GDT and the corresponding radial reconstructions.

The "hump" in the middle of the reconstructed curve (see Figure 4.10) is sometimes present because the coefficients in Equation (4.2.6) were not constrained to positive values. This was done because negative coefficients allowed a more accurate reconstruction of the solids distribution near the sides of the riser where the values are higher, and the error caused by the hump was assumed to be small. The hump appears in many, but not all, cases.

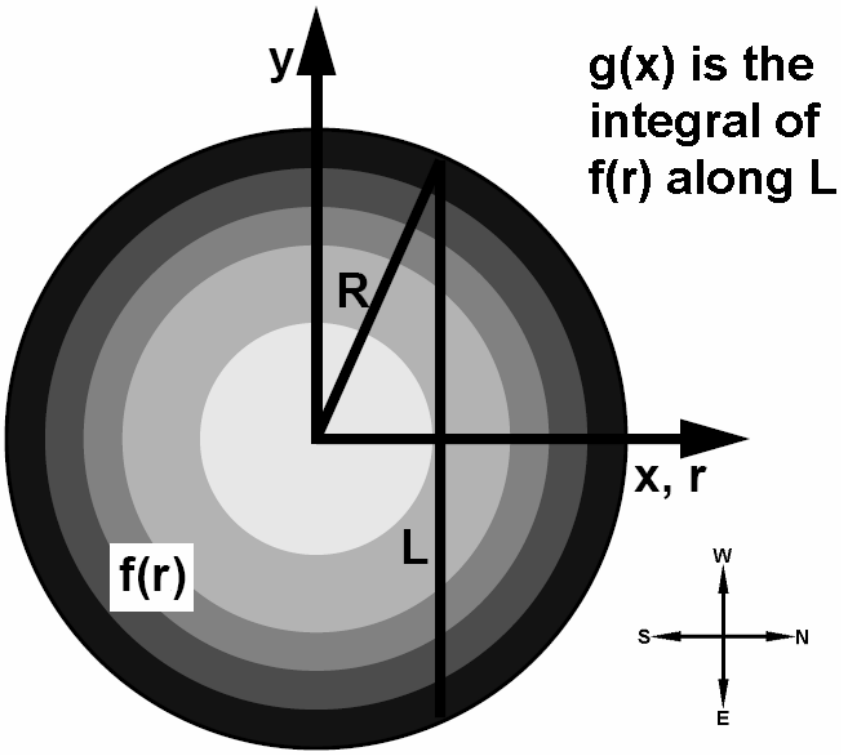

Figure 4.16. Schematic of Abel transform geometry (Torczynski et al., 1997).

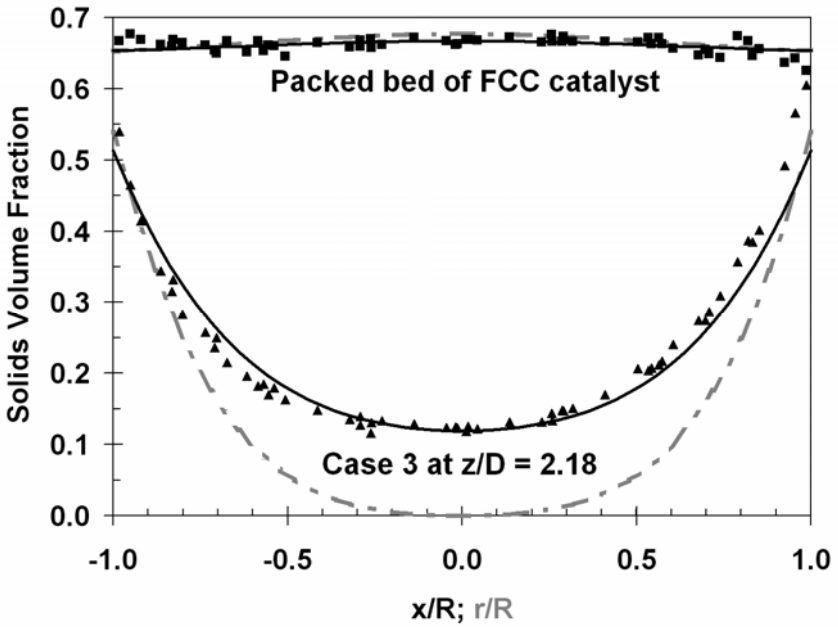

Figure 4.17. GDT reconstructions of two riser solids distributions; points are measured path-averaged solids volume fractions (function of *x*/*R*), solid lines are polynomial fits to measured values (Eq. (4.2.6), function of *x*/*R*), and dashed lines are reconstructed solids volume fraction profiles (Eq. (4.2.7), function of *r*/*R*). Case 3 refers to the run conditions shown in Table 5.1.

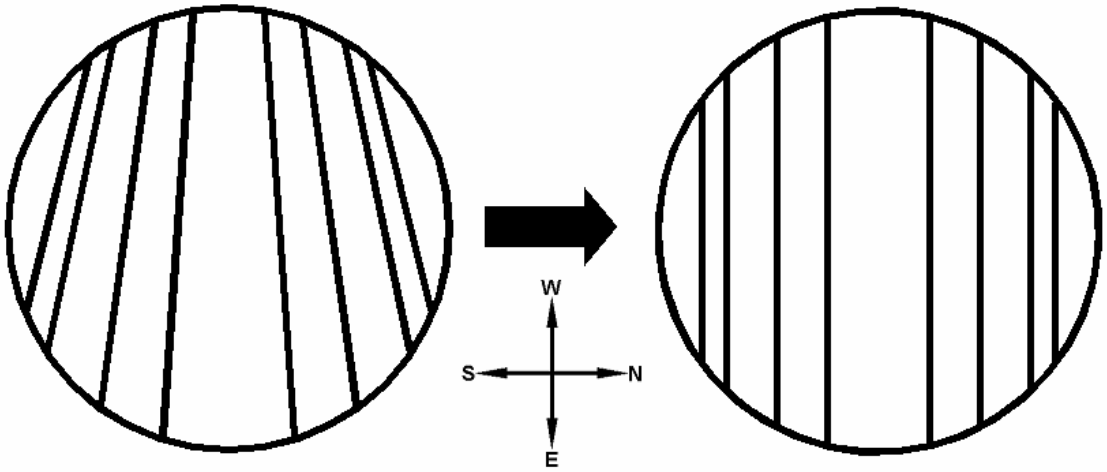

Figure 4.18. Approximation of paths used for Abel transform (eight of 56 shown).

More commonly, including all remaining reconstructions in this report, the tilt term in Eq. (4.2.6) was not included, in which case the time-averaged distribution was assumed to be axially symmetric and represented by the polynomial

$$f(r) = a_0 + a_2(r/R)^2 + a_4(r/R)^4 \qquad (4.2.11)$$

which relates the solids volume fraction f at a radial position r to the inner radius of the riser R and coefficients a_i. This functional form was used for three reasons. First, this form is physically realistic for riser flows in that it can represent conditions ranging from uniform to core-annular distributions. Second, this axisymmetric polynomial form is both efficient and mathematically convenient. Third, the same form was used for both GDT and EIT, so the results from both methods can be compared straightforwardly. Although Xu et al. (2004) and others describe the solids distribution as a function of its cross-sectional average or, alternatively, of its values at the center and wall, their approach cannot be used here because these quantities were not known *a priori*.

The GDT system measures the average solids volume fraction along multiple paths that intersect the flow region as described above. Again referring to Figure 4.16, if a particular path has length L and is located at lateral position x, the solids volume fraction $g(x)$ averaged along this path is related to $f(r)$ as follows:

$$g(x) = \frac{1}{L}\int f\left(\sqrt{x^2 + y^2}\right) dy \tag{4.2.12}$$

The Abel transform is used to relate $g(x)$ to $f(r)$. When applied to the previously specified polynomial in r for $f(r)$, the Abel transform yields a polynomial of the same degree in x for $g(x)$ (Torczynski et al., 1997):

$$g(x) = b_0 + b_2(x/R)^2 + b_4(x/R)^4 \tag{4.2.13}$$

and the a coefficients in Eq. (4.2.11) are exactly as given in Eqs. (4.2.8) through (4.2.10). Additionally, the coefficients were constrained to be positive. Since this constraint is not possible in the reconstruction in Excel, the reconstruction was performed using the design optimization software DAKOTA (Eldred et al., 2002ab, 2003). DAKOTA is designed to work with any simulation code for design optimization (among other functions) by iteratively adjusting the inputs to the simulation to achieve the optimal output. DAKOTA was used for GDT reconstruction in the following manner. First, starting values were selected for the a coefficients in Eq. (4.2.11). These values were input to a FORTRAN program that calculates the b coefficients using Eqs. (4.2.8) through (4.2.10) and calculates 56 predicted path-averaged solids volume fractions for the 56 detection paths using Eq. (4.2.13). The predicted values are subtracted from the measured values, the differences are squared, and the squares are summed. The FORTRAN program outputs this sum, which is passed back to DAKOTA. DAKOTA then determines new values for the a coefficients using the Fletcher-Reeves conjugate gradient algorithm (Eldred et al., 2003) and repeats the process until convergence. The convergence tolerance, a parameter in DAKOTA (related to gradients, not absolute error, as described by Eldred et al., 2003) was set to 0.001.

The quality of a GDT reconstruction is described by its correlation (R^2) value. The correlation value is a measure of the goodness-of-fit between the predicted and measured values. A value of 1 indicates a perfect match, and a value of 0 indicates that the fit and the average measured value represent the measured values equally well (or poorly). The correlation for the path-averaged solids volume fraction g is calculated from the measured values g_M, the predicted values g_C, and

the average of all measured values $\bar{g}_M$ as below, where $j = 56$ is the number of g values used in the reconstruction:

$$R^2 = 1 - \frac{\sum_{i=1}^{j} \left(g_{M,i} - g_{C,i} \right)^2}{\sum_{i=1}^{j} \left(g_{M,i} - \bar{g}_M \right)^2} \tag{4.2.14}$$

Figure 4.17 shows the measured path-averaged solids volume fractions and a reconstructed solids volume fraction distribution for one of the riser flow conditions. The R^2 value of this fit was 0.949.

GDT results are presented in Section 5.

4.2.3 Industrial Gamma-Densitometry Tomography

Application of tomographic techniques in general, and GDT in particular, to industrial process tomography typically has different requirements and goals than for many research systems. This technique has been known and applied for many years. For example, Bartholomew and Casagrande (1957) applied GDT in fluidized vessels with diameters ranging from 6 inches (0.15 m) to 40 ft (12 m). As radiation detection equipment and computers (for tomographic reconstruction) improve these techniques become more accessible to researchers, but widespread application in industry has not yet occurred. Industrial process tomography has become an area of interest over the past decade as tomography systems have become available, affordable, and accurate. There have been books (Scott and Williams, 1995) and conferences (e.g., World Congress on Industrial Process Tomography series) specifically related to this topic.

Specific differences between industrial and laboratory GDT include:

1. Most industrial vessels have metal walls, often thick steel for pressure reasons. These are often much more attenuating than research systems which are generally smaller, have thinner walls, and often have plastic walls or windows
2. Most industrial vessels are operated at elevated pressures and temperatures
3. Flow conditions, e.g., solids flux, often exceed those achievable in lab systems
4. Internals such as heat exchanger tubes are often present inside industrial vessels
5. Access to industrial vessels is often limited
6. Radiation safety can be more of a concern in a plant environment where not everyone in the area is aware of the diagnostic test
7. The desired outcome is not always data sets with the best possible temporal and spatial resolution but sometimes an indicator of problems or a trouble-shooting tool

With these differences in mind, this section describes some of the design considerations for an industrial GDT system.

Design, analysis, and some testing of industrial gamma tomography systems have been performed by Darwood et al. (2003) and Stitt and James (2003). They performed simulations, phantom tests, and field implementations on FCC risers and packed distillation and absorption columns (6.2 m diameter). They determined that accurate reconstruction requires viewing from a number of directions, so use of a fan beam is preferable to extensive scans on a regular rectangular grid.

The radiation source for industrial measurements must produce radiation of sufficient energy to penetrate walls of the flow vessel and provide sufficient contrast to distinguish between the phases. The attenuation coefficient of any material is strongly related to its density; denser materials attenuate more gamma photons. In a metal vessel, often with thick walls for pressure containment, the attenuation by the walls can dominate the attenuation by the multiphase mixture inside the vessel. Shollenberger et al. (1997) discuss one application in such a system and demonstrate application in a large lab-scale bubble column with ½-inch thick stainless steel walls.

Another radiation phenomenon that must be considered is beam hardening, which is important for beams such as x-rays that are not single energy. Beam hardening is the effect that the multiple energy beam becomes "harder," i.e., higher energy and therefore more penetrating, the further it passes through the wall material. For example, medical x-rays often have a fairly broad energy spectrum. As they pass through matter, the "softer" lower-energy end of the spectrum, having higher attenuation coefficients, is preferentially attenuated, leaving the remaining beam of higher energy. Beam hardening therefore causes the effective attenuation coefficient of a material to be dependent on the thickness of material through which the beam passes. This can lead to undesirable artifacts such as cupping in computed tomography images. Beam hardening is not an issue for monochromatic gamma beams.

There are companies that are available to perform industrial tomography (e.g., Quest TruTec, LP, see Mixon and Xu, 2005; Xu and Pless, 2005).

4.3 Suction Probe

The use of suction probes for measurement of local solids flux in gas-solid risers was introduced by van Breugel *et al.* (1970). In this technique, a sampling tube is inserted parallel to the riser mean flow, and a sample of gas and solids is withdrawn from the column. The gross mass flux normal to the probe's sampling surface can then be determined from the resulting sample mass, sample time, and the sampling area presented normal to the flow. The net mass flux in any particular direction can be determined from the difference in the opposing fluxes measured along that direction.

An important consideration in this technique is whether the sampling is performed isokinetically, *i.e.*, the gas velocity of the sampling suction is matched to the local riser gas velocity in that direction. For gas velocities and particle sizes and loadings typical of riser flows, a low suction velocity results in an underestimation of the directional mass flux, while a high suction-velocity similarly results in an overestimation of the directional mass flux. Miller and Gidaspow (1992) present results demonstrating this phenomenon in a riser flow of FCC catalyst Additionally, failure to achieve isokinetic conditions can result in a particle-size distribution within the sample that is not reflective of conditions at the sampling location. Isokinetic sampling results have been reported by several experimental groups, including van Breugel *et al.* (1970), Nguyen *et al.* (1989), Harris and Davidson (1992), Coronella and Deng (1998), and Reinhardt *et al*. (1999, in cyclone flows).

Limitations of isokinetic sampling include the inability to match the suction to the riser gas velocity beyond a time-mean sense, and the practical requirement that some suction must always be applied to prevent probe plugging, even in cases where this is physically unrealistic. Several groups of workers (e.g., Miller and Gidaspow, 1992; Rhodes and Laussmann, 1992; Zhang et al., 1995; Malcus et al., 2002) have overcome this using non-isokinetic sampling, at suction rates far in excess of the local gas speed. While increased sampling-suction velocities correspondingly increased measured values of directional mass fluxes, they found that the net flux represented by the difference in directional fluxes remained relatively invariant. Furthermore, where available, independent measures of mass flux were demonstrated to agree well with integrated probe-based flux measurements. Issangya et al. (1988) used a nearly-isokinetic sampling, applying a suction velocity equal to the system's superficial gas velocity, for upward-flowing mass flux sampling; and a gravity-driven sample-collection technique which required no suction for downward-flowing mass flux measurements. Qi and Farag (1993) used a similar, gravity-driven sample-collection scheme to estimate lateral fluxes in a riser.

Early experiments with non-isokinetic sampling at Sandia are described by Trujillo et al. (2001ab) and are summarized here. The Sandia flux-probe system originally consisted of a 9.5 mm (0.375 in.) OD, 7.4 mm (0.29 in.) ID tube, a sample collector, a rotameter for suction air flow measurement, and a vacuum pump as a suction source. Results presented by Trujillo et al. (2001ab) indicated that, while qualitatively informative, the measurements were quantitatively inconsistent. Three significant observations emerged.

First, introduction of the probe into the riser introduced asymmetries to the flux-profile measurements which were apparently unrealistic – the asymmetries reversed when the flux-probe insertion location was shifted by 180° to the other side of the riser. The 9.5 mm OD sampling tube was clearly a significant intrusion on the flow.

Second, efforts to extract quantitative estimates of mass flux in the riser from the measured up- and downward particle-transit profiles were subject to significant variations in run-to-run results. Because the net flux estimate depends on the differences in two numbers, often of similar magnitudes, the uncertainty in the result often is on the order of the result itself. This problem is most pronounced near the wall, where the magnitudes of up- and downward fluxes are most similar. In this region, the difference representing the point net flux is relatively small, and is subject to the largest area weighting ($2\pi r \cdot dr$) in the net-flux estimate. Additionally, the upward, downward and net fluxes are changing rapidly with respect to radial position in this region, and small variations in probe positioning result in significant changes to the measurements. In cases examined by Trujillo *et al.* (2001), repeated measurements resulted in net mass-flux estimates that ranged over an order of magnitude.

Third, the flux probe was subject to choking in high-particle-loading situations. It is difficult to estimate the effect of this behavior on the measurement. During high-flux periods, when the probe chokes, the particle flow is likely to be undersampled. However, once choked, the probe may oversample, as it traps but does not sweep incoming particles into the sample collector.

On the basis of these observations, the sampling system was redesigned. To improve the suction applied to the probe in an effort to relieve the choking that was observed in high-concentration locations, the restrictive rotameter was removed and was replaced with a low-restriction, vortex-shedding flowmeter. The output voltage from this meter was sampled and recorded with a high-speed digital oscilloscope. Also, to reduce the probe's collection of particles and possible initiation of choking during periods in which the probe was not actively sampling (i.e., periods during which the probe was being positioned in the riser, etc.), a purge line was added to the system. A standard two-port valve which controlled sampling in the early configuration was replaced with a three-way valve that selected either purge air (no sampling) or sampling. The resulting configuration is shown schematically in Figure 4.19. It is similar to configurations used by Miller and Gidaspow (1992), Wei et al. (1997), and Issangya et al. (1998); and similar in principle to that used by Wang et al. (1995), whose sampling system was modified for use in a high-temperature system.

These modifications resulted in improved repeatability of measurements, as samples were collected more uniformly with less choking of the sampling probe. Results of sample measurements and net flux profiles are presented in Figure 4.20 for three different heights in the riser. The riser operating condition is a superficial gas velocity U_g = 5.2 m/s, and an average mass flux of 84 kg/m^2·s; the suction gas speed is $3.4 \cdot U_g$. As a demonstration of repeatability, each plot presents two sets of upward, downward and computed net flux data. In these plots, the sign of the presented flux value indicates upward (positive) or downward (negative) particle movement. Results of integration of the net mass flux across the riser cross section are fairly consistent at each location, but vary considerably from location to location. At the lowest point in the riser, z = 0.90 m, integrated net fluxes are the highest, at 189 and 191 kg/m^2·s for the two

sets of measurements presented. The integrated net flux values decrease with increasing measurement height: 138 and 160 kg/m^2·s at z = 2.73 m, and 32 and 53 kg/m^2·s at z = 4.42 m. All of these were sampled at a time-averaged suction gas velocity of 3.4·U_g.

Unlike the results of other workers, described above, it was also noticed here that the net mass-flux estimate was dependent on suction velocity. Figure 4.21 compares two sets of sample profiles with net mass-flux estimates for time-averaged suction velocities of 3.4 and 2.5 times the superficial gas velocity U_g at the measurement location z = 4.42 m. As in Figure 4.20, the sign of the presented flux value indicates upward (positive) or downward (negative) particle movement. Agreement is reasonably good for repeated suction velocities, but disagreement between suction-velocity cases is significant. The 3.4·U_g case repeats the results presented in Figure 4.20, with cross-sectionally integrated net mass fluxes of 32 and 53 kg/m^2·s; while 2.5· U_g case yields integrated net mass-flux estimates of 86 and 89 kg/m^2·s.

The intrusiveness of the sampling probe was also studied by inserting a 12.7 mm (0.5 in.) OD dummy probe into the riser across its entire diameter. For this complete insertion, the dummy probe blocks about 11% of the riser's cross-sectional area; for the flux probe at full insertion, the blockage is about 8%. The resulting differential profiles in the riser are shown in Figure 4.22. It is clear that the insertion of the probe has a significant effect on the flow both up- and downstream of the probe insertion. Effects are seen in a region about 10 riser diameters – not probe diameters – in length, both upstream and downstream of the probe-insertion location. For the lower probe insertion, the effect is dominant downstream of (above) the probe, while the situation is opposite for the higher probe insertion. Unfortunately, the design of the Sandia sampling probe, as well as most other sample probes in the literature, requires full insertion of the probe into the riser to obtain critical near-wall measurements; this produces the worst case of intrusiveness.

Because of the inconsistency of results with measurement location, the inconsistency of results with suction velocity, and the intrusiveness of the technique, it was concluded that sampling probes were not an effective measurement technique in the Sandia/MFDRC riser.

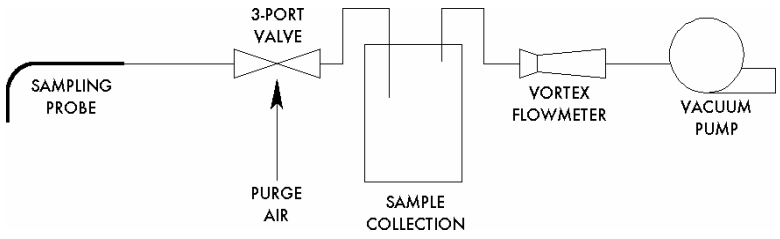

Figure 4.19. Schematic of final configuration of Sandia sampling-probe system.

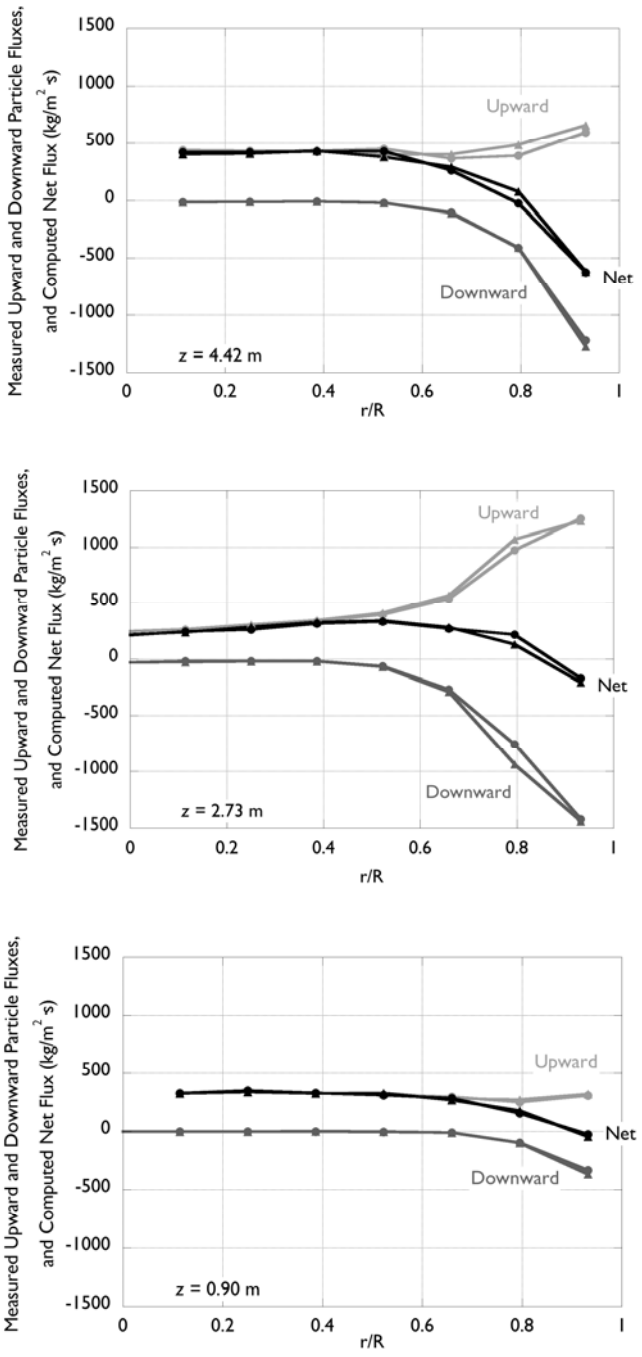

Figure 4.20. Sampled upward and downward particle-flux profiles, and net flux profiles estimated by differencing. Riser superficial gas velocity U_g = 5.2 m/s and mass flux G_s = 84 kg/m^2·s. Measurement locations are z = 4.42 m (top), 2.73 m (middle) and 0.90m (bottom). Mean suction gas velocity is 3.4·U_g.

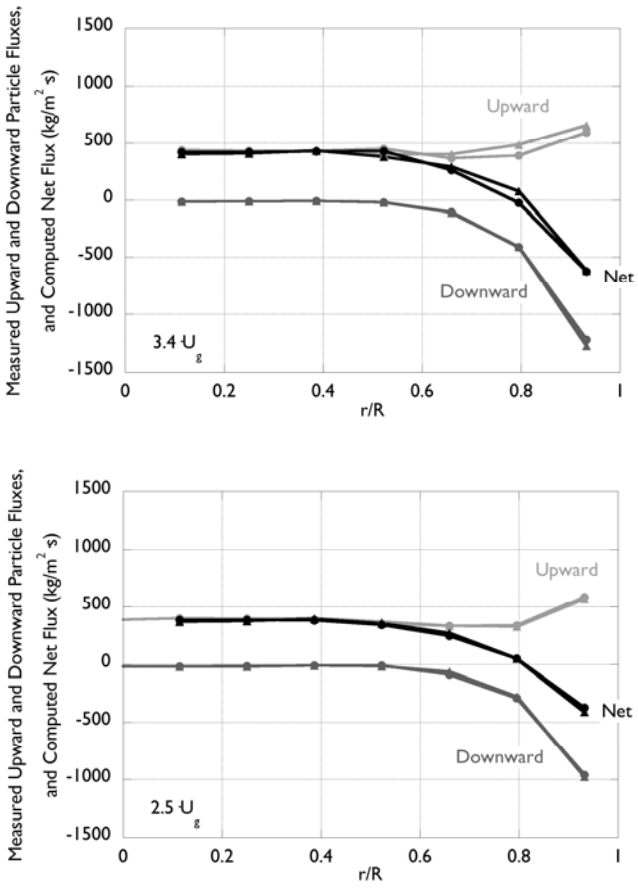

Figure 4.21. Sampled upward and downward particle-flux profiles and net flux profiles estimated by differencing measured for a single operating condition at one location on the riser for sample suction velocities of 3.4·U_g (top) and 2.5·U_g (bottom).

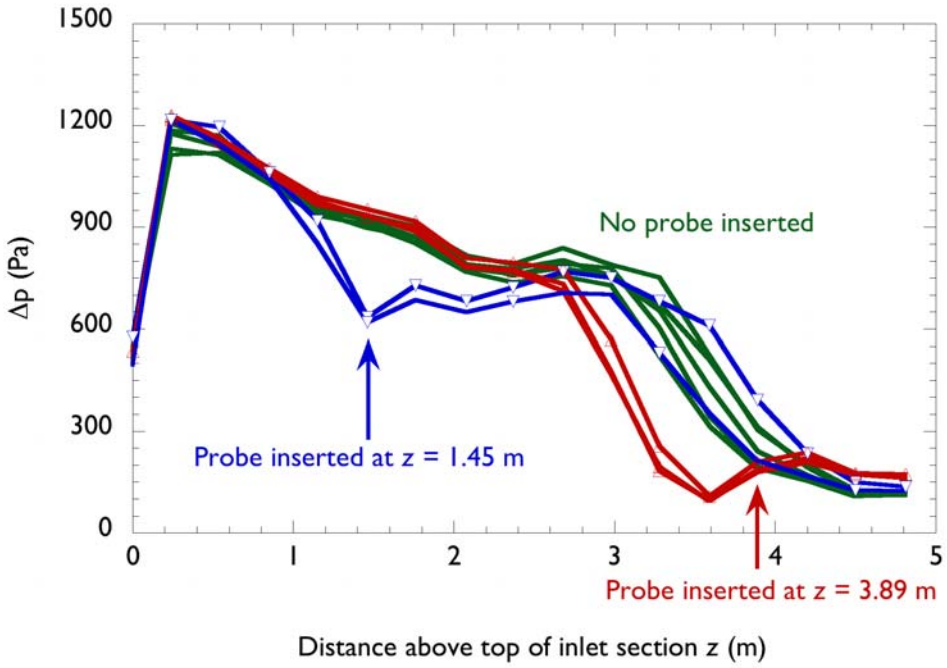

Figure 4.22. Effect of probe insertion on time-averaged $\Delta p(z)$ profile in riser for probes inserted at z = 1.45 m (blue) and z = 3.89 m (red).

4.4 Fiber-Optic Voidage Probe

Fiber-optic probes have been used in gas-solid flows for measurement of particle concentration and, in some cases, particle velocity. The basis of the measurement is the introduction of a light source inside the flow, and the correlation of a received signal to the measured quantity. Voidage measurements have been based on transmission through the flow field, requiring essentially two probe heads, one for transmission and one for reception; and on reflectance from the flow field, requiring a probe head incorporating both the transmit and receive fibers. Velocity measurements have been based on return-signal rise rate (by, e.g., Cocco et al., 1995) and on time-of-flight principles using multiple signal returns (see, e.g., Zhang and Zhu, 2000). This section focuses on reflectance-type probes because the probes used in the present experiment were of that type.

Fiber-optic probes require calibration prior to use. Zhou et al. (1994) calibrated their probe by inserting it into liquid-solid systems of known particle concentrations. For void fractions below 0.8, the probe was inserted in liquid-solid fluidized bed; above void fractions of 0.8, a stirred beaker of known bulk particle concentration was used, with the assumption that particles were evenly distributed throughout the beaker. Using this technique, Zhou et al.(1994) found that the calibration was nearly linear over the range of interest.

Other workers (e.g., Zhang et al., 1998) have pointed out that differences in index of refraction call into question the applicability of such calibrations in gas-solid flows. Our own calibration

experiments with suspensions of FCC particles in water suggest, in addition, that the reflectivity of wet particles may differ from that of dry powder, introducing further complications to liquid-bed calibrations. Matsuno et al. (1983) calibrated their fiber probe in air by dropping particles from a vibrating-sieve apparatus past a probe positioned far enough below the particles' release point that the particles would be at a terminal velocity. Knowing the mass of particles dropped in a given time and the particle density, the time-mean concentration of particles passing the probe could be estimated, and a calibration curve constructed. This technique was limited to low concentrations, and measurements were made only in the freeboard region of a fluidized bed. Zhang et al. (1998) improved on this calibration method by improving the apparatus to force greater particle concentrations by including a contraction in their calibration downer column and by applying a backpressure at the base of the column to increase holdup. Concentrations were compared to direct measurements of column holdup performed using quick-closing valves to isolate the particles in the calibration location. Calibrations in their experiments were distinctly non-linear.

Besides calibration of probes for output signal strength as a function of voidage, the measurement volume of the probe must be characterized. Parallel-fiber probes suffer from an ambiguous definition of probe volume, as the intersection of the cones of transmitted and reflected light extend infinitely out from the probe tip. This is illustrated in Figure 4.23 for a two-fiber example for simplicity, but the extension to multi-fiber probes is apparent. Thus, particles far from the probe tip may continue to have some effect on probe signal, depending on the concentrations of particles between the probe tip and those particles. It is also apparent that the measurement volume for this type of probe varies with particle concentration: a higher concentration near the tip will limit the contributions of particles further from the tip, resulting in a smaller measurement volume. For lighter particle loadings, the converse is true. The practical extent of the measurement volume can be estimated by measuring the separation distance at which the presence of a highly reflective surface normal to the probe introduces additional reflected signal strength to the measurement. Several workers (e.g., Reh and Li, 1990; Cocco et al., 1995) have designed probes to provide a defined measurement volume by angling the transmission and reflection fibers. This approach is shown in Figure 4.24.

Figure 4.23 also identifies the "dead space" that exists between the probe tip and the measurement volume, regardless of straight or angled fiber arrangement. The ambiguity in measurement volume and measurement location that is introduced by this gap has typically been avoided by the inclusion of a window at the probe tip that is as thick or thicker than the dead-space distance (e.g., Reh and Li, 1990; Cocco et al., 1995). Alternatively, Cui et al. (2003) note that dead-zone effects can be minimized by constructing the probe as a randomly arranged bundle of small fibers.

Two types of reflectance-based probes were used in the Sandia/MFDRC riser. The first is a two-fiber probe of the type used by Cocco et al. (1995). In this probe, single fibers are each used for light transmission and collection, and the fibers are angled to limit the measurement volume as described above. In addition, the probe incorporates a flat window to eliminate the dead space between the fiber ends and the measurement volume. In their work, Cocco et al. (1995) demonstrated use of this probe to measure particle concentration based on the intensity of signal return, and particle velocity based on the rise rate of the returned signal. The second probe type

used in the present work is a multiple-fiber configuration supplied by Professor J. Grace's research group at the University of British Columbia. Similar probes, and their application in gas-solid riser flows are described by Zhou et al. (1994).

Sandia's experiments with both types of probes did not yield useful quantitative data. Both types of probes quickly fouled with particles in the riser, returning either a constant reflectance signal if the entire probe face was fouled, or a fluctuating signal if a portion of the probe face had collected particles. In the latter case, this had the result of mimicking a valid signal but at an erroneously low signal level. In addition, efforts to calibrate the probes were unsuccessful. As mentioned above, it was found that calibration results differed in liquid and gas suspensions, indicating a change in reflectivity of FCC particles in wet and dry conditions. It was also found that settled-bed calibration conditions, intended to provide an upper bound to calibration curves, were unacceptably scattered and often duplicated calibration points at lower concentration values. It is believed that this was due largely to a coupling between the non-monotonic collection efficiency of reflectance probes with increasing distance from reflective targets (Krohn, 1986) and the scales of random arrangements of particles in the bed relative to the scales of probe measurement volumes.

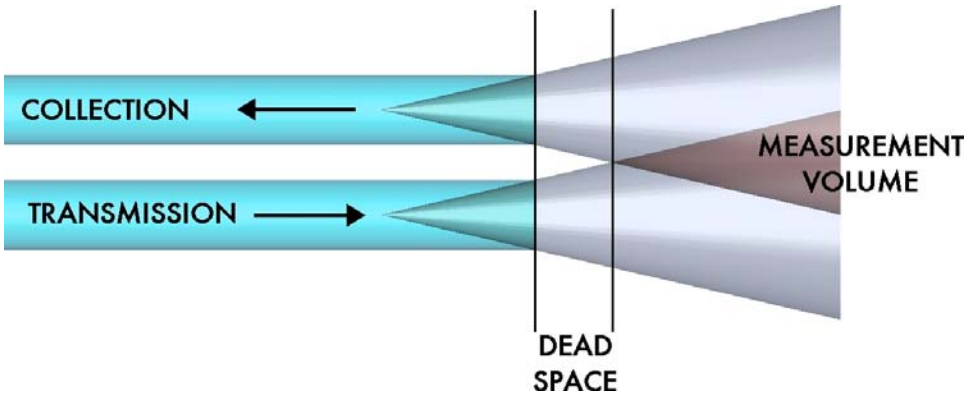

Figure 4.23. Two-fiber probe arrangement, showing definition of measurement volume by intersection of transmission and collection cones, and dead space between fiber tips and measurement volume.

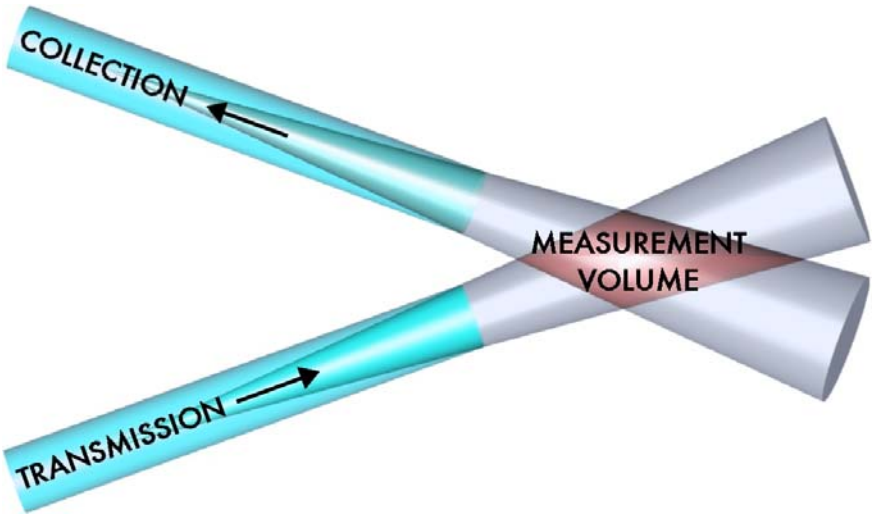

Figure 4.24. Two-fiber probe arrangement, showing unambiguous definition of measurement volume resulting from relative angling of transmission and collection fibers.

4.5 Electrical-Impedance Tomography

EIT, like GDT discussed earlier, is another method capable of non-invasively measuring spatial distributions of materials in multiphase flows. Ceccio and George (1996) provide a review of EIT techniques and applications in multiphase flows. EIT uses measurements of electrical currents at the boundary of a domain to infer the impedance distribution within the domain. Since the electrodes usually do not protrude into the domain, EIT can be completely non-invasive. For multiphase flows, the local material distribution can be determined from the local impedance using a mixture model if there is sufficient contrast between the electrical impedances of the materials. Several researchers have applied EIT systems to the study of gas-solid flows, including Halow et al. (1993), Dyakowski et al. (2000), Rao et al. (2001), Warsito and Fan (2003), Makkawi and Wright (2003), and Pugsley et al. (2003). These researchers have used a variety of data gathering and reconstruction methods to determine time-averaged and time-varying solids distributions. However, it is difficult to assess the overall accuracy in many reported measurements since independent determinations of the solids distributions are often lacking. One notable exception is the work of Pugsley et al. (2003) in which EIT measurements were validated with a fiber optic probe.

A 16-electrode electrical-impedance tomography (EIT) system was created under the auspices of this program and is described in detail by Tortora (2004). EIT measures radial solids volume fraction profiles, just as GDT does, but is of great interest as an alternative to GDT because it is much faster, safer, and less expensive to implement. However, the reliability of EIT is not yet well-established for measurements of solids volume fractions in gas-solid flows, so part of this work was to acquire data sets with both EIT and GDT so that the GDT data could be used to validate the EIT technique. The main elements of the EIT system are the impedance

measurement hardware, the reconstruction method, and the impedance mixture model. Each is described below.

4.5.1 Impedance Measurement System

The EIT electrode ring is shown in Figure 4.25. The 16 electrodes are slightly curved brass rectangles 114-mm high × 12.7 mm wide × 4.76 mm thick. Two 16.5-cm ID, 22.5-cm OD, 2.50-cm high acrylic rings hold the 16 electrodes flush against the outer (curved) surface of the riser. The entire assembly is 11.4 cm high, leaving 6.35 cm of air-filled space between the upper and lower rings. Stainless steel shielding is fastened around the outside of the rings and is penetrated by 16 feedthroughs, each of which is connected by a coaxial cable to the corresponding electrode. An exact measurement volume cannot be defined for EIT as with GDT, because the electric field is unconfined and weakens with distance from the electrodes. A reasonable estimate is that the significant portion of the electric field exists directly between the electrodes, resulting in a measurement volume of $1.7 \times 10\text{-}3$ m^3 (approximately twice that of GDT).

Impedance measurements are taken between all 120 distinct electrode pairs using the bridge circuit shown in Figure 4.26. In each measurement pair, the first electrode, referred to as the power electrode, is driven by a 5-V, 100-kHz AC voltage V_E supplied by a Hewlett-Packard 8904A multifunction synthesizer. The second electrode, referred to as the sensing electrode, is held at virtual ground by an operational amplifier (Analog Devices OP42), which supplies the necessary current to keep its inputs at the same potential (zero in this case). Prior to experiments, when the measurement domain is filled with air, the amplitude and phase of the null voltage V_N is adjusted to bring the magnitude of the output voltage V_{OUT} to zero. The null voltage is provided by the same synthesizer as the 5-V source voltage, and the relative phase and amplitude of the two signals are precisely controlled. The phase of the null voltage is usually very close to that of the source voltage for dielectric domains. When the capacitance of the measurement domain C_D changes (i.e., when particles are introduced), current flows from the output of the op-amp to keep the sensing electrode at zero potential. The output voltage indicates the current flow in proportion to the feedback resistance R_F by Ohm's law. Similar measurement schemes are reported by Huang et al. (1992), Williams and York (1999), and Georgakopoulos et al. (2001).

Under ideal circumstances, the output voltage would be related to the domain capacitance C_D, the angular frequency ω, and other system parameters by

$$V_E\omega(C_D+C_E) = V_N\omega C_N + V_{OUT}/R_F \tag{4.5.1}$$

The stray capacitance C_E accounts for constant parasitic currents (such as the parasitic capacitance shown in Figure 4.26). However, whereas the circuit behaves linearly, experiments have shown that the behavior does not follow Eq. (4.5.1), with differences likely due to higher-order parasitic currents and/or cable inductance. Since the circuit responds linearly to impedance changes in the domain, it was calibrated using dielectric oils with known permittivity values. The FCC particle bed was also determined to have a permittivity of $\varepsilon = 2.5$ by comparing it to two dielectric oils.

The output voltage of the circuit is measured by an analog-to-digital (A/D) converter on a data acquisition board (Measurement Computing™ PCI-DAS4020/12) and recorded on a personal computer with Labview™ software. The signal is sampled at 1 MHz, which is ten times the 100-kHz carrier frequency. The signal is demodulated using a fast Fourier transform. A sample time of 1.28 ms (128 100-kHz cycles) was selected to obtain a maximum variation of approximately 1 mV in measuring a constant 1-V signal.

Multiple measurement circuits were constructed on printed circuit boards to enable rapid reconfiguration of each electrode as passive (*i.e.*, high input impedance), power, or sensing. The circuitry is controlled by Labview™ data acquisition software on a personal computer. A complete set of current measurements is acquired in the following manner. First, the bridges are balanced for each of the 120 electrode pairs while the measurement domain is full of air. Then, with particles flowing through the measurement domain, the circuitry is switched through all 120 electrode pairs, applying the different null voltages acquired during calibration at each step and recording circuits' output voltages. One set of measurements takes approximately one second to acquire, and 600 sets (approximately 10 minutes of sampling time) are acquired while the CFB is operating. This allows for temporal averaging of flow fluctuations.

4.5.2 Impedance Reconstruction

There are many techniques of EIT reconstruction (Dyakowski et al. 2000, Huang et al., 2001). In the present work, EIT reconstruction was similar to the GDT reconstruction. The design optimization software DAKOTA (Eldred et al., 2003) was again used, and the CFD program FIDAP (Fluent, Inc., 1998) was used to predict the currents flowing through electrodes for comparison with the currents corresponding to the measured voltages (see Appendix A for details). The simulations were performed as heat-conduction problems because the equations governing electrostatics are of the same form mathematically as those governing steady heat conduction. Two-dimensional FIDAP simulations were performed to reduce the computational cost and were found to have less than 3% error compared to three-dimensional simulations.

FIDAP was set up to simulate the configuration inside the grounded shielding of the electrode rings (shield, air space, electrodes, acrylic rings, riser walls, and flow domain). The assumed solids distribution within the riser had the same form as that used for the GDT reconstruction, given by Eq. (4.2.11). Note that this makes the reconstruction highly over-constrained. The a coefficients of Eq. (4.2.11) were passed directly to FIDAP, which used the Rayleigh mixture model (in a user subroutine) to convert the solids distribution into a permittivity field within the flow domain.

Mesh refinement studies found that, with successive grid refinements, all of the predicted electrode currents increased by the nearly same factor: the ratio between nominally identical currents on the coarsest and finest meshes varied by less than 0.2%. In other words, the currents at essentially infinite refinement could be determined to within 0.2% by multiplying the corresponding currents from the coarsest mesh by a (near-unity) constant factor. Therefore, a relatively coarse mesh was used, which reduced the computational cost.

The FIDAP results for the riser EIT system have the following feature. When the permittivity in the flow region is increased while holding the injection-electrode voltage fixed, the currents exiting the adjacent electrodes are decreased (although the currents to all other electrodes are increased). Thus, since the complex impedance is inversely proportional to the permittivity, decreasing the impedance in one region of the domain is observed to decrease the current somewhere else. At first glance, this phenomenon appears to contradict Ohm's law, which indicates that decreasing impedances should increase currents. Figure 4.27 shows very simple circuits for which a current I_2 decreases rather than increases as an impedance R_3 (equivalent to $1/j\omega C_3$) also decreases (the limiting cases of zero or infinity are easy to see).

Thus, decreasing the impedance somewhere in a domain and having the current somewhere else also decrease (rather than increase) is physically allowable. While the circuits in Figure 4.27 are not direct models of the riser EIT system, certain similarities are apparent, with the "1" quantities corresponding to the injection electrode, the "2" quantities corresponding to the adjacent electrodes, and the "3" quantities corresponding to the flow region and the other electrodes. The fact that the current decrease predicted by FIDAP is 4% for a mesh-refinement uncertainty of 0.2% is further evidence that the FIDAP results are correct for the physics modeled (purely capacitive behavior). Because of this behavior, currents between adjacent-electrode pairs were eliminated from the comparison of predicted and measured currents, reducing the number of measurements from 120 to 104.

EIT reconstruction was performed as follows. Recall that each measured voltage is proportional to the current that flows between the corresponding electrode pair. Thus, to compare measured and predicted currents, the measured voltages were normalized using the empty and full voltages, and the predicted currents were normalized using the empty and full currents. For a given power electrode p and ground electrode g, the voltages measured for empty, full, and flowing conditions are denoted by $V_{e(p,g)}$, $V_{f(p,g)}$, and $V_{m(p,g)}$, respectively, and the currents predicted for empty, full, and flowing conditions are denoted by $J_{e(p,g)}$, $J_{f(p,g)}$, and $J_{m(p,g)}$, respectively. The normalized measured currents $K_{M(p,g)}$ and the normalized predicted currents $K_{C(p,g)}$ have the following forms:

$$K_{M(p,g)} = \frac{\left(V_{m(p,g)} - V_{e(p,g)}\right)}{\left(V_{f(p,g)} - V_{e(p,g)}\right)}, \tag{4.5.2}$$

$$K_{C(p,g)} = \frac{\left(J_{m(p,g)} - J_{e(p,g)}\right)}{\left(J_{f(p,g)} - J_{e(p,g)}\right)}. \tag{4.5.3}$$

This normalization was performed because the currents spanned approximately 1 order of magnitude (adjacent electrode currents were approximately an order of magnitude greater than cross-electrode currents). With this normalization, the measurements were all treated with equal weight in the reconstruction. Simulations were performed for an empty domain (a uniform

permittivity of 1, corresponding to air) and for a full domain (a uniform permittivity of 2.5, corresponding to a bed of FCC particles).

DAKOTA was then executed to minimize the difference between the normalized predicted and measured currents. A simulation with initial values for the *a* coefficients was first performed by FIDAP, and the currents predicted by FIDAP – normalized using Eq. (4.5.3) – were extracted and recorded in a file. The predicted currents were then subtracted from the measured currents, and the differences were squared and summed as with GDT. This sum was passed back to DAKOTA, which minimized this value by adjusting the *a* coefficients and repeating the process until convergence. The method used to calculate correlation values for GDT – Eq. (4.2.14) – was also used for EIT with the normalized measured and predicted currents (j = 104 electrode pairs):

$$R^2 = 1 - \frac{\sum_{i=1}^{j} \left(K_{M,i} - K_{C,i} \right)^2}{\sum_{i=1}^{j} \left(K_{M,i} - \bar{K}_M \right)^2} \tag{4.5.4}$$

4.5.3 Impedance Mixture Model

It was found early in the design of the EIT system that the mixture model used to convert electrical impedances to solids volume fraction significantly affects the results of the measurement. Therefore, several simulations of regular arrays of cubes and spheres were performed and compared to commonly used mixture models, expanding on other mixture model studies such as the one by Louge and Opie (1990). These results are presented in Tortora et al. (2005).

The models commonly used to determine the solids volume fraction from the mixture impedance include series and parallel impedance models, the Maxwell mixture model (Scaife, 1989), the Böttcher model (van Beek, 1967), and the Rayleigh model (Meredith and Tobias, 1960). Bares (1988) found that the surface conductivity of glass spheres is negligible at frequencies greater than 1 kHz. Because the EIT system operated at 100 kHz, interparticle contact does not play a role here, so it is reasonable to use a single continuous function over the range of possible distributions. The Rayleigh model has the best agreement with experiments and computational simulations over the widest range of solids volume fractions: from dilute conditions up to the packing limit of 0.66. The simulations and models all agree at low solids volume fractions (<0.4), but there are some differences in the intermediate range (0.4-0.6). The Rayleigh model was selected for EIT data reduction because it agreed best with the simulations in the intermediate range and agreed with the experimental value for a packed bed (Tortora et al., 2005).

In the Rayleigh model, the permittivity of the gas-solid mixture ε_m is related to the gas permittivity ε_g, the solid permittivity ε_s, and the gas volume fraction ϕ by:

$$\varepsilon_m = \frac{\varepsilon_g \left(\frac{2\varepsilon_g + \varepsilon_s}{\varepsilon_g - \varepsilon_s} - 2\phi + 0.409 \frac{6\varepsilon_g + 3\varepsilon_s}{4\varepsilon_g + 3\varepsilon_s} \phi^{7/3} - 2.133 \frac{3\varepsilon_g - 3\varepsilon_s}{4\varepsilon_g + 3\varepsilon_s} \phi^{10/3} \right)}{\left(\frac{2\varepsilon_g + \varepsilon_s}{\varepsilon_g - \varepsilon_s} + \phi + 0.409 \frac{6\varepsilon_g + 3\varepsilon_s}{4\varepsilon_g + 3\varepsilon_s} \phi^{7/3} - 0.906 \frac{3\varepsilon_g - 3\varepsilon_s}{4\varepsilon_g + 3\varepsilon_s} \phi^{10/3} \right)} \quad (4.5.5)$$

4.5.4 EIT System Evaluation

The EIT system was used to measure the solids volume fraction profile of a homogeneous material distribution, in a procedure similar to that done with the GDT system (Figure 4.17). In this case, an empty riser section and one filled with dielectric oil were used for the empty and full conditions, respectively, and the reconstructed permittivity profile of a bed of FCC catalyst was determined. To simplify this test, the conversion to solids volume fraction was not performed; otherwise, the reconstruction is the same as described above. The permittivity profile is shown in Figure 4.28, along with a predetermined uniform reconstruction (performed by allowing DAKOTA to adjust only the constant of the polynomial and setting the other coefficients equal to zero). The "flat" reconstruction closely predicts the permittivity of a bed of FCC catalyst (within 1%), but the polynomial reconstruction shows a negative bias of 4% near the riser center and a positive bias of 6% near the walls. This bias is discussed in the following section on the validation of EIT against GDT.

Asymmetries are more difficult to detect in the raw EIT data than in the raw GDT data because the EIT data are related to the material distribution in a more complicated fashion. Some measured voltages (say, at the electrodes adjacent to the power electrode) do show variations around the electrode ring on the order of several percent. These variations could be due to asymmetry, but they could also be due to noise since they appear uncorrelated between cases and are relatively small. Therefore, an axisymmetric EIT reconstruction was judged to be sufficiently accurate. As indicated earlier, axisymmetric EIT reconstructions can thus be directly compared to axisymmetric GDT reconstructions.

The resolutions of the EIT and GDT systems are difficult to determine because their sensitivities vary differently with position in the riser. Pugsley et al. (2003) divide the riser cross section into uniformly-sized pixels and have a radial resolution of 16 pixels (16 pieces of information across the riser radius). They do note different levels of sensitivity depending on radial position, and their reconstruction is under-constrained. The polynomial representation of solids volume fraction used here does not lend itself well to a definition of resolution based on pixels. In the case of GDT, 28 rays (albeit unevenly spaced) are arranged along the riser radius, so the GDT system has a resolution approximately equivalent to 28 pixels across the riser radius. In the case of EIT, there are 7 angular separations from the power electrode to the sensing electrodes (excluding the adjacent electrodes) around one half of the electrode ring, so the EIT system has a resolution approximately equivalent to 7 pixels across the riser radius. With only 3 parameters, the quartic profile used here is over-constrained in both cases.

4.5.5 EIT Results and Discussion

Comparison of EIT and GDT material distributions

EIT and GDT were applied at the riser conditions shown in Table 5.1. Examples of solids volume fraction profiles obtained from GDT and EIT are shown in Figure 4.29, and the complete set of results is given in Section 5. The high R^2 values show excellent fits to the data, indicating that higher-order terms in the polynomial representation of solids volume fraction are not necessary. The uncertainty analysis leading to the error bars in these plots is discussed below. The EIT and GDT profiles are seen to agree closely for all flow conditions examined. More particularly, the wall and center values and the widths of the core and wall regions are determined with good accuracy, even when close-packing (solids volume fraction around 0.66) is observed near the walls and extremely dilute flow (solids volume fraction near zero) is observed in the core region.

Although agreement is quite good, some minor systematic differences are seen. For run conditions with relatively low overall solids loadings (Cases 1 and 2), EIT slightly overestimates solids volume fraction in comparison to GDT near the riser walls at low riser heights (z/D = 2.18, 3.27), as shown in Figure 4.29a. For the same cases, the error bars for EIT and GDT completely overlap at the middle riser heights (z/D = 5.45, 6.55), as shown in Figure 4.29b. Finally, for the same cases and at the largest riser heights (z/D = 9.82, 12), EIT underestimates solids volume fraction in comparison to GDT near the riser walls, as shown in Figure 4.29c. For run conditions with relatively high solids loadings (Cases 3 and 4), EIT either underestimates solids volume fraction in comparison to GDT near the riser center (as in Figures 4.29d and 4.29e) or overestimates it (as in Figure 4.29f). At the riser wall, EIT overestimates solids volume fraction by no more than 0.07 in most cases (in a single case the overestimate was 0.12) and underestimates it by no more than 0.05 (in a single case the underestimate was 0.08) relative to GDT. In most cases both EIT and GDT predict nearly zero solids loading near the riser center. The bias error in the EIT system (Figure 4.28) is a contributor to the overestimate at the walls.

In the case of random error, the numbers of EIT and GDT measurements performed (1 or 2 for many cases) were too small to calculate meaningful uncertainties from statistical methods. Collecting a number of samples large enough to do so would be preferred (as this would account for most measurement uncertainty and repeatability uncertainty) but was not possible in this study. The measurement uncertainties (e.g., uncertainties in the A/D cards and op-amps) are known, but the reconstruction method is too complicated to propagate them through. The method of perturbation could be used (i.e., randomly perturbing the values of the measured voltages, according to measurement uncertainties, and performing reconstructions), but this would have required an excessive number of reconstructions. Finally, reconstruction could be performed on individual time-resolved measurements sets (recall that the data used for reconstruction are averages of 600 measurement sets), but, in addition to requiring an excessive number of reconstructions, this would account only for "moment-to-moment" variations in experimental conditions, rather than run-to-run variations in CFB operating conditions. In any case, the run-to-run variations were assumed to be the most significant contributor to uncertainty (see Figure 4.30). Therefore, as is described below, differential pressure (DP) data were used to estimate the repeatability uncertainty since a large number of DP measurements was available.

Differential pressure (DP) data can be used to estimate volume-averaged solids volume fractions based on the vertical pressure gradient $\partial p/\partial z$, the particle density ρ_s, the gravitational acceleration g, the solids volume fraction $(1 - \phi)$, and the solids flux G_s (Louge and Chang, 1990; Louge, 1997):

$$\frac{\partial p}{\partial z} = -\rho_s g\left(1-\phi\right) - \frac{G_s^2}{\rho_s}\frac{\mathrm{d}}{\mathrm{dz}}\left(\frac{1}{1-\phi}\right) \tag{4.5.6}$$

The latter term accounts for regions with steep vertical gradients in solids loading. A first-order approximation was used to estimate this term, and it was found that the correction to solids volume fraction – always negative – did not exceed 0.01 in any case. This is negligible in most cases but may be significant near the top of the riser where solids volume fractions are on the order of 0.05. Eliminating the latter term and integrating Eq. (4.5.6) over a section of the riser of height Δz gives the hydrostatic relation:

$$\frac{\Delta p}{\Delta z} = -\rho_s g\left(1-\phi\right) \tag{4.5.7}$$

This relation gives a good estimate of average solids volume fraction but is inaccurate compared to EIT and GDT, as discussed in the following section. The DP measurements were used with this relation to estimate the uncertainty due to the run-to-run variation in CFB flow conditions. The contribution of friction to the pressure gradient would only be significant at velocities far exceeding those encountered in risers (Louge, 1997).

For each flow condition and riser height, a set of DP values was measured (as in Figure 4.30) and converted to a set of average solids volume fraction values using Eq. (4.5.7). Uncertainties were then calculated using the method described by Figliola and Beasley (2000); the uncertainty u of the mean $\overline{x}$ is given by

$$u = \pm t_{v,p}\,\frac{S_x}{N^{1/2}}$$

$$S_x^2 = \frac{1}{N-1}\sum_{i=1}^{N}(x_i - \overline{x})^2 \tag{4.5.8}$$

where the values $t_{v,p}$ are obtained from the Student-t distribution for a 95% confidence interval. In cases where the location (height) of a GDT or EIT measurement did not match that of the DP measurement, the uncertainties were interpolated.

Multiple EIT and GDT profiles acquired at the same conditions and height were averaged. Individual profiles are shown in Figure 4.31 for comparison. Beginning with each averaged profile (or single profile where only one was acquired), a set of possible curves in the range of solids volume fraction corresponding to the uncertainty can be produced. Using methods described by Tortora (2004), the upper and lower bounds of this set of curves are determined, producing the uncertainty bars shown in Figure 4.29.

The curves shown in Figure 4.31 can be used to make a qualitative judgment regarding the soundness of using DP data to estimate solids volume fraction uncertainty for GDT and EIT. In many cases, the uncertainty should be less than the maximum variation between samples but of the same order of magnitude. Even though there are a small number of individual EIT and GDT curves in Figure 4.31, this indeed appears to be the case. The method of perturbation (using measurement uncertainties) described above was not attempted here but is reasonable given current computational speeds and should be a topic of future research.

In summary, most of the solids volume fraction profiles obtained from EIT and GDT agree closely, with EIT having a small positive bias at the walls (generally no more than 0.07). Considering that the EIT and GDT methods were developed relatively independently from one another to determine solids volume fraction profiles through the measurement of different material properties (electrical permittivity and radiation attenuation), the agreement between the curves is impressive. This level of agreement suggests that, where feasible (i.e., with dielectric walls and materials possessing different electrical properties), EIT can be used instead of GDT, which is more expensive and can have radiation safety and permitting issues. Although in this study long time averages were used, EIT is generally much faster than GDT. The sensitivity of reconstructed solids volume fraction profiles to the number of sample sets taken by the EIT system should be a topic of future study.

Comparison with previously published results

Solids volume fraction profiles have been reported by several other researchers, and it is instructive to compare the present data with these published results. Zhang et al. (1991) obtained profiles with a traversed optical fiber probe and report the following correlation relating solids volume fraction $(1-\phi)$ to radius r and average solids volume fraction $(1-\phi)_A$:

$$(1-\phi) = (1-\phi)_A^{\left(0.191+(r/R)^{2.5}+3(r/R)^{11}\right)} \tag{4.5.9}$$

Xu et al. (2004) report on these and other recent measurements using inserted probes (along with one data set obtained with an x-ray camera) and present correlations for the solids volume fraction profile. They present the following correlation for dense flow, for which $(1-\phi) > 0.25$:

$$(1-\phi) = (1-\phi)_{r=R}\left(\frac{(1-\phi)_{r=0}}{(1-\phi)_{r=r}}\right)^{F(r/R)},$$

$$F(r/R) = 1.0 - 0.06\left(\frac{r}{R}\right) - 1.34\left(\frac{r}{R}\right)^2 + 2.65\left(\frac{r}{R}\right)^3 - 2.25\left(\frac{r}{R}\right)^4, \tag{4.5.10}$$

and for dilute flow, for which $(1-\phi) < 0.25$:

$$(1-\phi) = (1-\phi)_A^{\left(a(r/R)^{11}+(r/R)^{2.5}+b\right)}, \qquad a = \frac{\ln(1-\phi)_{r=R}}{\ln(1-\phi)_A} - 1 - b \quad , \quad b = \frac{\ln(1-\phi)_{r=0}}{\ln(1-\phi)_A}, \tag{4.5.11}$$

where the average solids volume fraction and solids volume fractions at the wall and at the centerline must be known in order to predict the profile.

These correlations are compared to the EIT and GDT data, for all four cases at a height of 6.55 diameters, in Figure 4.32. The correlation of Zhang et al. (1991), Eq. (4.5.9), is based solely on the average solids volume fraction, and the values used were determined from EIT: 0.079 for Case 1, 0.040 for Case 2, 0.203 for Case 3, and 0.252 for Case 4. The correlation of Xu et al. (2004) for dilute flows, Eq. (4.5.11), is based on average and wall solids volume fractions, which were also determined from EIT, and on the centerline solids volume fraction, which was set to 0.01 or to the value measured by EIT, whichever was higher (the correlation does not work for a centerline solids volume fraction of zero because the logarithm is undefined).

The correlation of Zhang et al. (1991) predicts relatively high solids volume fractions near the walls compared to the correlation of Xu et al. (2004) and the GDT and EIT reconstructions. Indeed, for Case 4 the correlation of Zhang et al. (1991) predicts an unphysical solids volume fraction (0.7) at the walls, and Xu et al. (2004) notes that the correlation produces unphysical values for average solids volume fractions greater than 0.18. The correlation of Zhang et al. (1991) also predicts relatively high centerline solids volume fractions for Cases 3 and 4 compared to the EIT and GDT reconstructions and the correlation of Xu et al. (2004). Still, the correlation of Zhang et al. (1991) agrees well with the other results for low average solids volume fraction (Cases 1 and 2, falling within 0.03 of the other profiles) and would be useful in situations involving lows solids volume fractions where only the average solids volume fraction is known. The profiles of Xu et al. (2004) fall within 0.05 of the EIT and GDT profiles. Note that there may be considerable uncertainty associated with the correlations, as the variability in the underlying data and confidence intervals are not reported.

The determination of solids volume fraction at the riser center calls for further exploration. Recall that the EIT and GDT reconstructions indicate a center solids volume fraction of zero or nearly zero in most cases. This may be due to the form used for reconstruction. The reconstruction algorithm attempts to accurately predict the apparently steep axial gradient in solids volume fraction near the riser walls, which drives the predicted solids volume fraction near the center to zero, where the low values of solids volume fraction contribute much less to the difference between measured and predicted quantities (attenuation for GDT, and current for EIT) than the high values near the walls. Also, EIT is influenced by negative bias at the centerline.

Indeed, it seems unlikely that the solids volume fraction at the centerline is exactly zero since a finite overall solids flux is observed and the majority of the upward solids flux occurs in the core of the flow, as discussed by Rhodes et al. (1992). They report solids fluxes at the centerline (measured using flux probes) that are two to three times the cross-sectionally averaged flux for flows similar to the ones examined here.

The centerline gas velocity is reported by Moran and Glicksman (2003) to be 1.5-2 times the average superficial gas velocity. Assuming homogenous flow at the centerline (i.e., no slip between the particles and the gas), the model of Rhodes et al. (1992) may be used to

approximately relate the solids volume fraction to the solids flux at the center $G_{r=0}$, the gas velocity at the center $U_{r=0}$, the overall solids circulation rate G_s, and the superficial gas velocity U by

$$(1-\phi)_{r=0} \approx \frac{G_{r=0}}{\rho_s U_{r=0}} \approx 1.5\frac{G_s}{\rho_s U} \tag{4.5.12}$$

This relation yields centerline solids volume fractions of 0.01 to 0.02 for the cases examined here. Thus, the correlation of Zhang et al. (1991) appears to overestimate the centerline values for Cases 3 and 4, as was also concluded by Xu et al. (2004). Since these values (0.01-0.02) are similar to the uncertainty bounds of EIT and GDT, a measurement of zero by EIT or GDT is not in disharmony with the above relation.

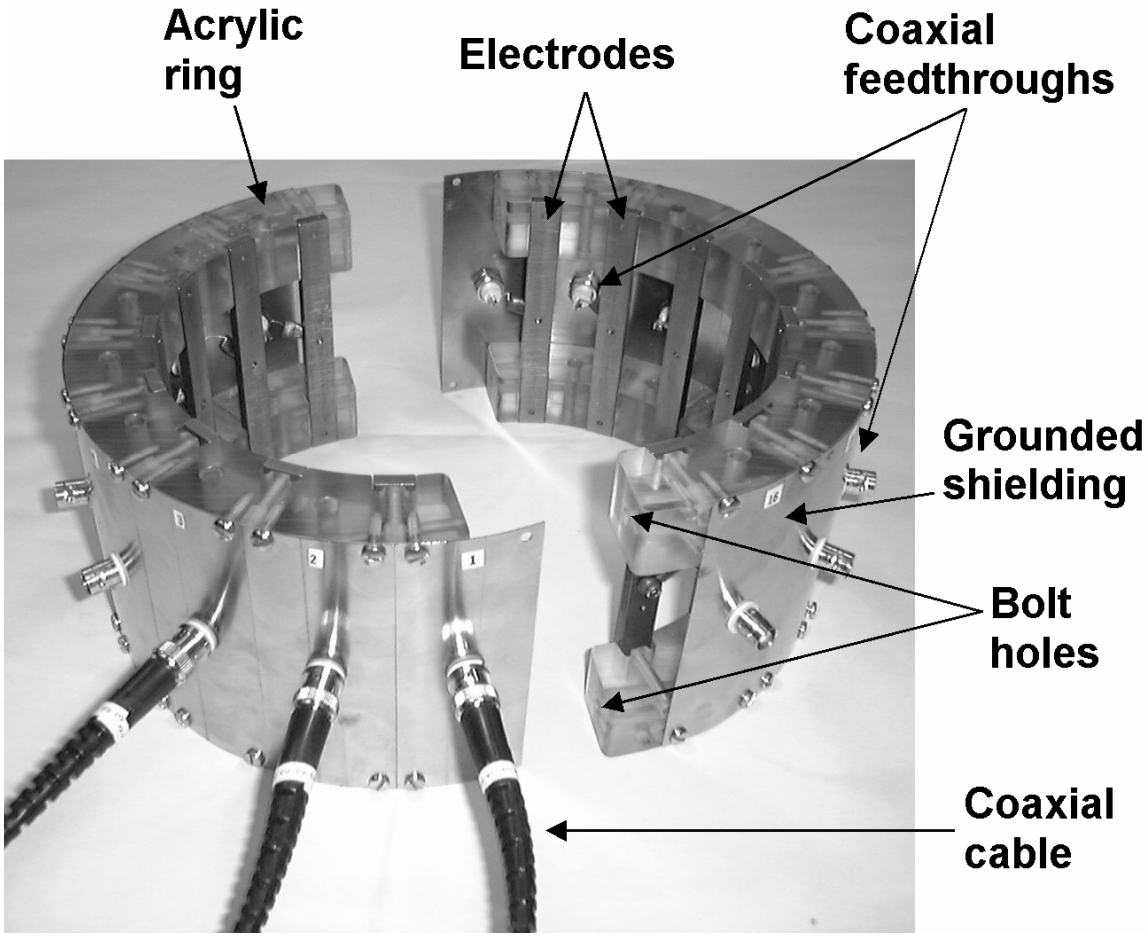

Figure 4.25. The EIT electrode ring that is clamped onto the riser column. The electrode assembly is shielded with a ground plane.

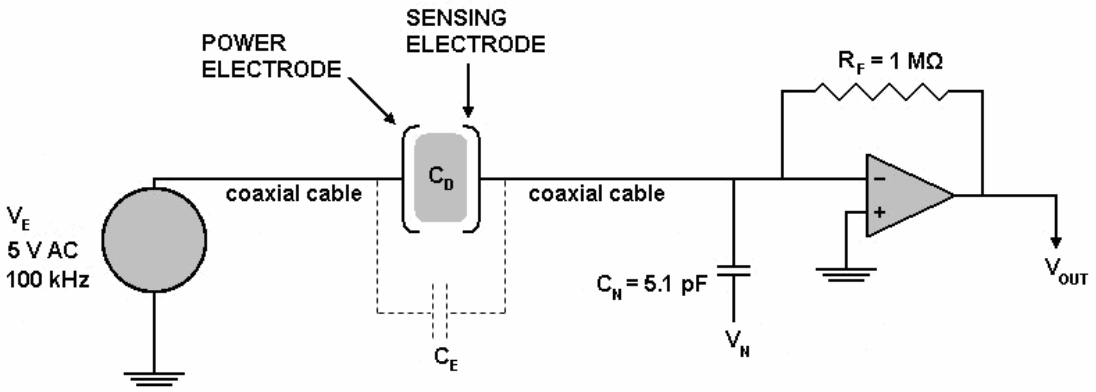

Figure 4.26. Impedance measurement circuit.

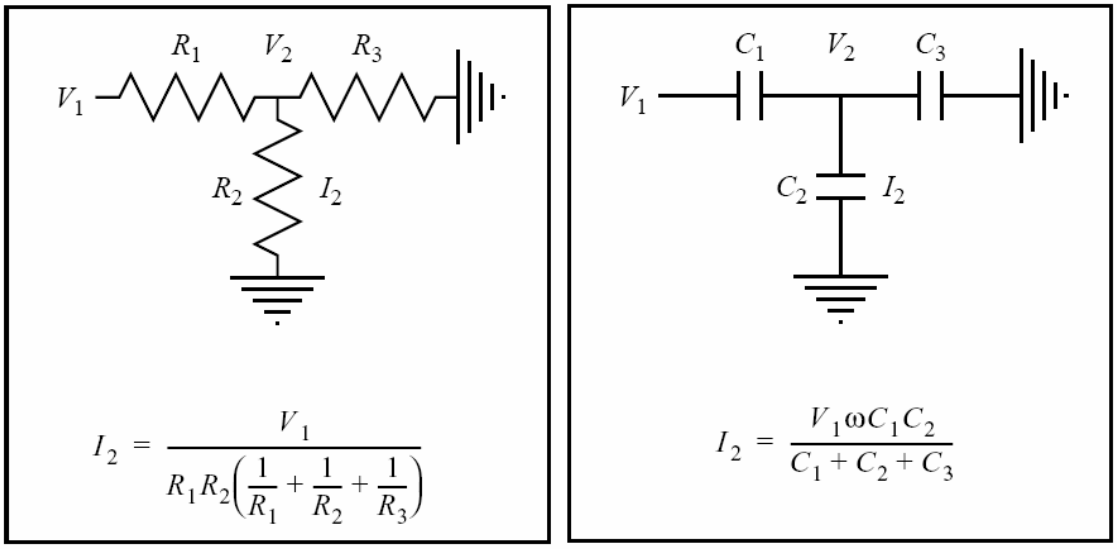

Figure 4.27. Simple circuits analogous to EIT circuit adjacent electrode configuration.

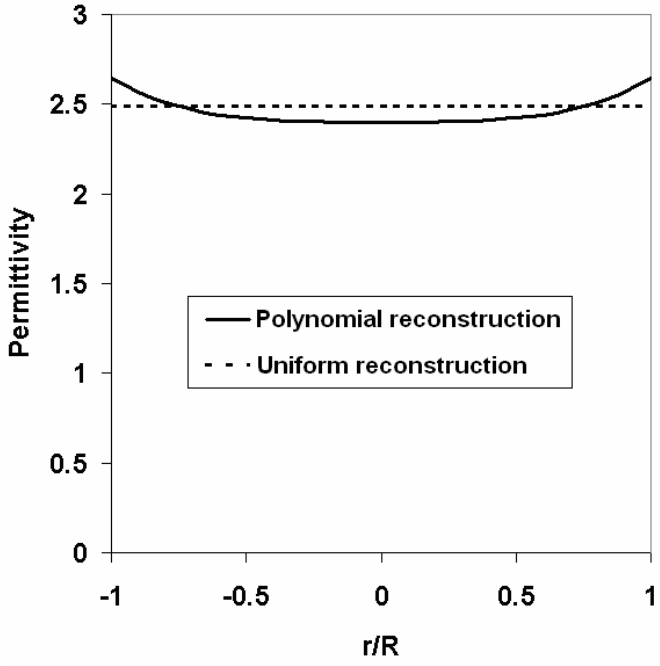

Figure 4.28. Reconstructions of homogeneous permittivity distribution; polynomial reconstruction is biased +6% at walls and -4% at center compared to flat reconstruction.

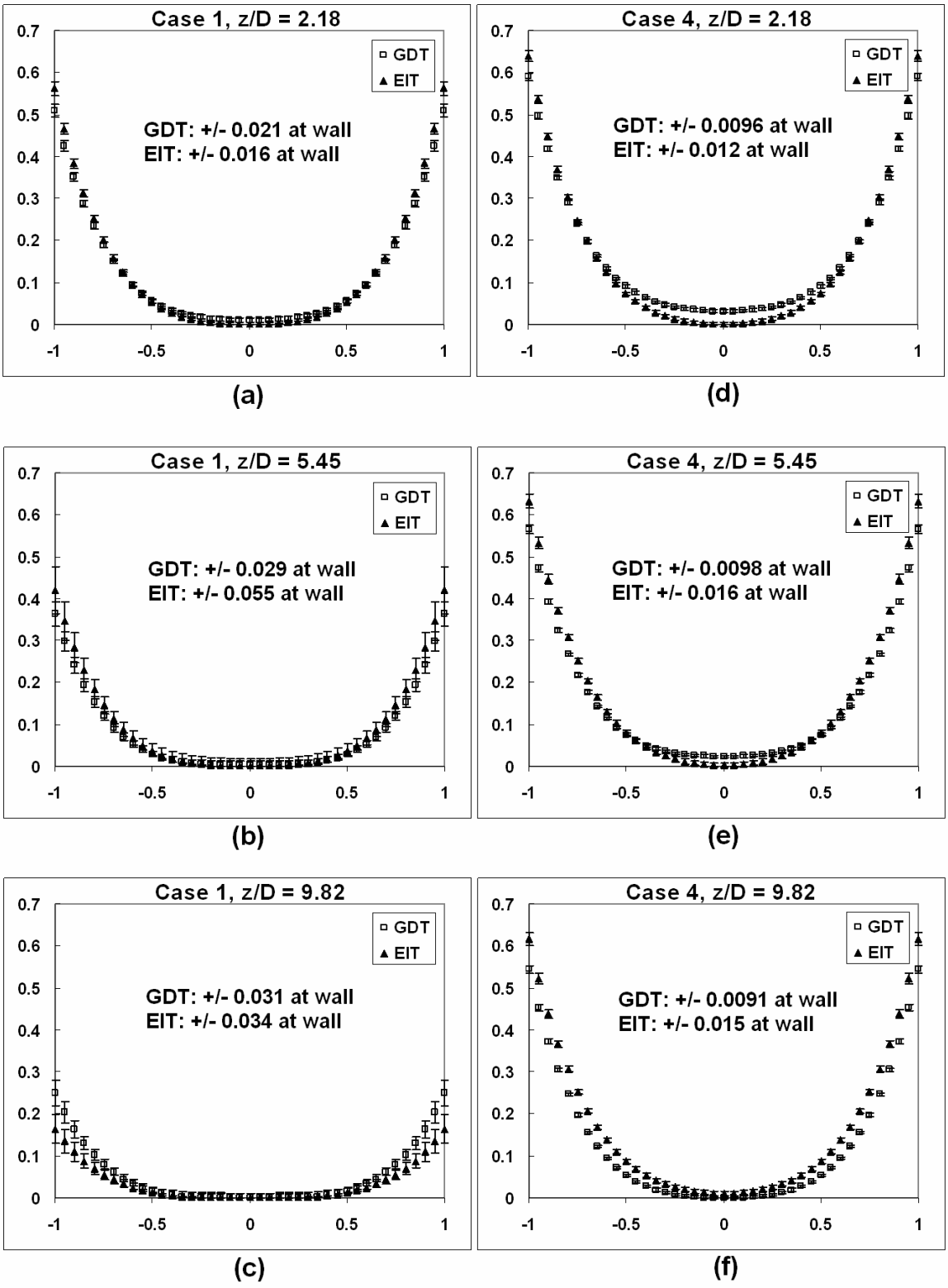

Figure 4.29. EIT and GDT solids volume fraction vs. dimensionless radial position; maximum uncertainties for each case are given on the plots.

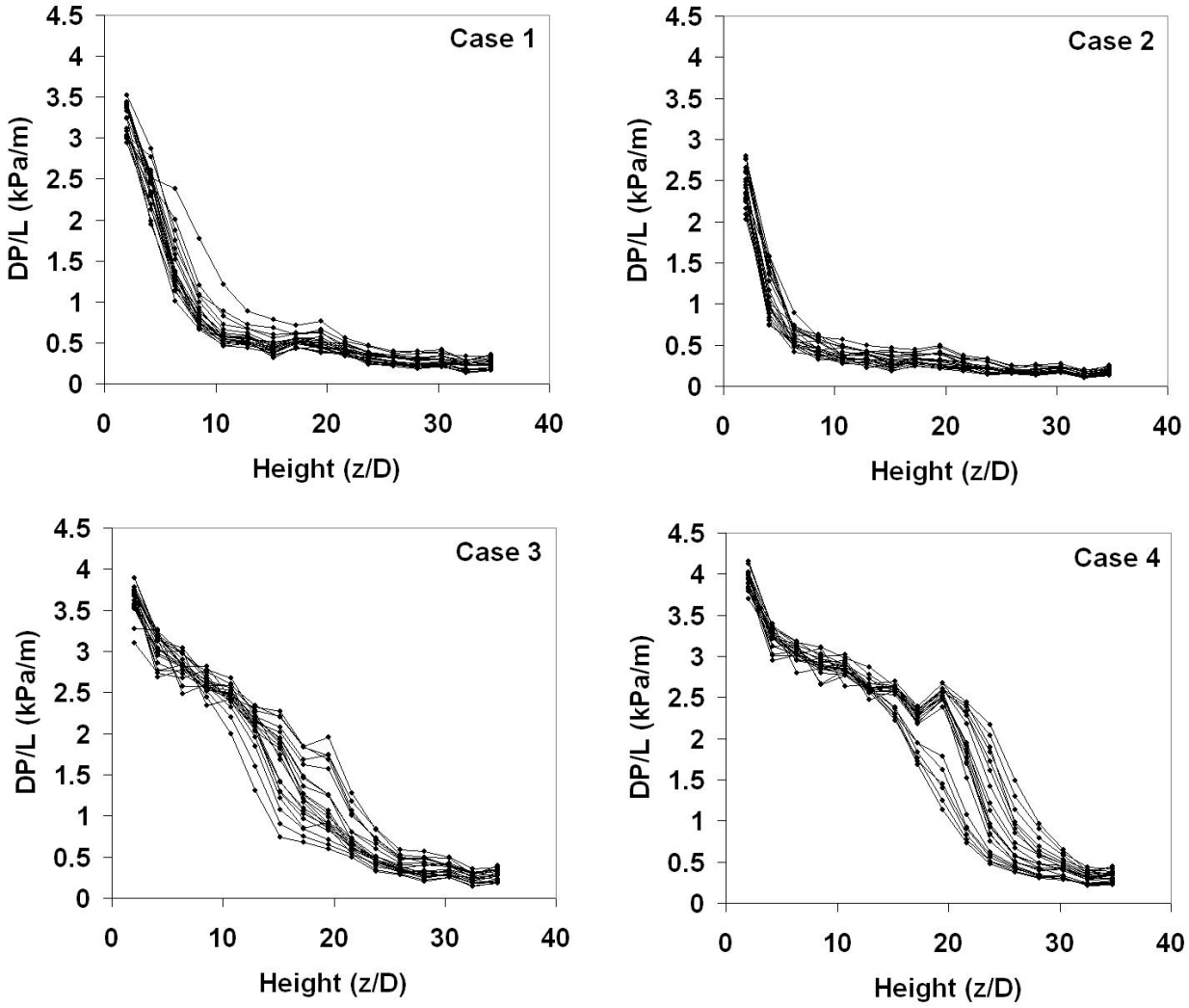

Figure 4.30: Pressure gradient vs. height for cases in Table 5.1; multiple traces show repeat runs at nominally identical conditions.

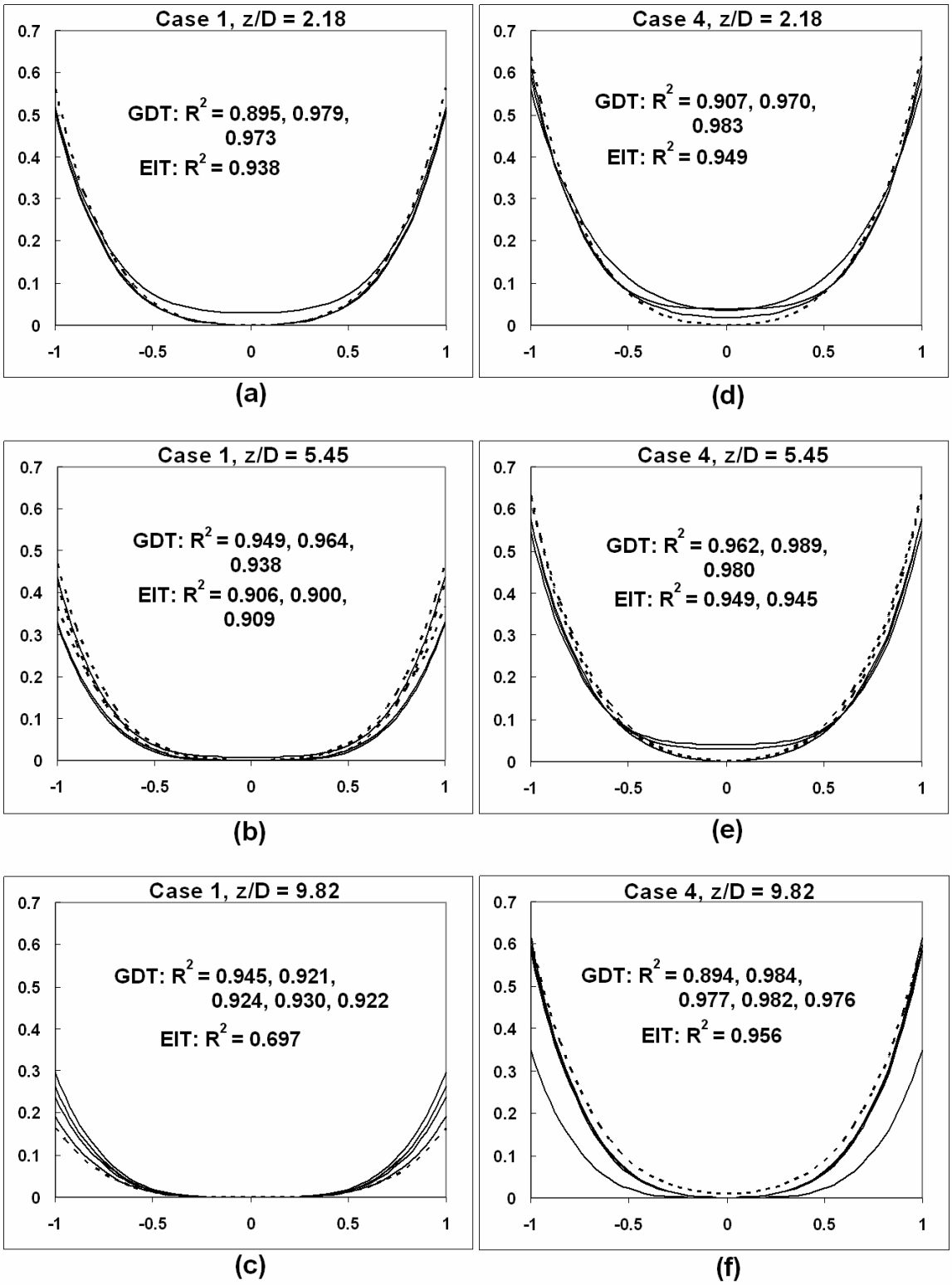

Figure 4.31. Individual reconstructed EIT (dashed) and GDT (solid) profiles and corresponding R^2 values; averaged to obtain profiles shown in Figure 4.29.

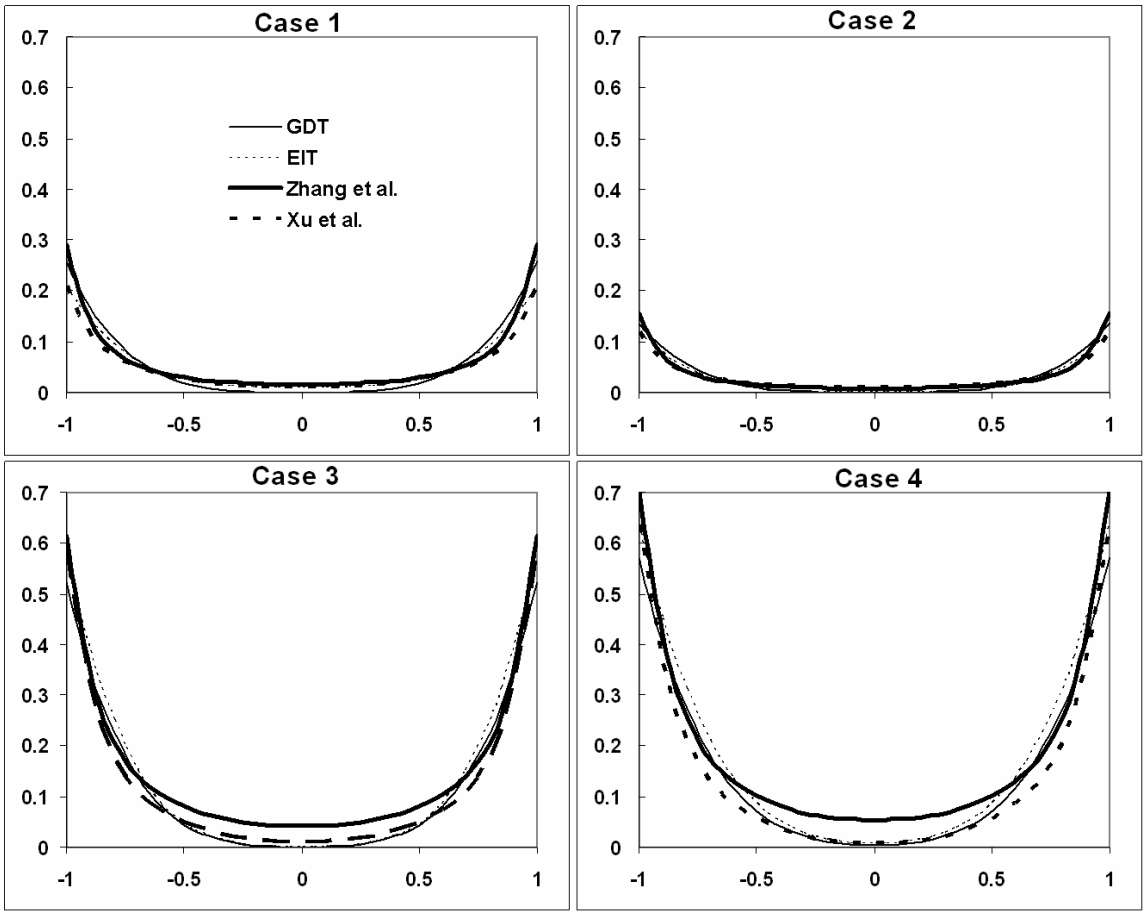

Figure 4.32. Solids volume fraction vs. dimensionless riser radius for EIT, GDT, and correlations for all cases at a height of 6.55 diameters. The conditions for the cases are defined in Table 5.1.

4.6 Solids Flux

A diverter-valve setup was used to measure solids mass flux in the riser. Diverter-valve installation and installation of its associated hardware are described in Sections 3.1.6 and 3.1.7. In the diverter-valve flux measurement, the normal solids return path from the disengagement to the downcomer is altered to route particles to an isolated weighing chamber. This diversion is maintained for a short, known amount of time. Knowing the mass of solids diverted in that time, an estimate can be made of the solids flux in the CFB riser. Diverter-valve flux measurements are common in CFB literature (e.g., Arena et al., 1985; Hartge et al., 1985; Srivastava et al., 1998; Zhang and Zhu, 2000).

As described in Chapter 3, the key components of the diverter-valve CFB leg were the diverter valve itself (Buhler model MAYF80 flapper valve), the solids collection chamber, a knife valve at the chamber base (DeZurik model 933451 with lever actuation), a ball valve isolating the leg from the rest of the CFB loop, and associated plumbing and fittings. The collection chamber itself is suspended by an Omega model LCCA-200 (200 lb. (91 kg) rated capacity) "S" beam load cell. A relatively high load-cell capacity was required to support the empty weight of the collection chamber and knife valve. The load cell is excited by a DC source and returns a DC signal proportional to the applied load. The load cell's electrical output could be tied to the riser data acquisition system and be collected and stored for later examination.

In operation, the mass-flux measurement was conducted as follows. A set of known loads were applied to the load cell at the beginning of the CFB run to check load-cell function and to establish scaling factors (i.e., voltage output per pound load input) for the load cell. Working with a scale factor determined *in situ* removes effects of power-supply drift, etc. from the measurement. The CFB was started up and operated normally. When it was determined that a steady condition had been reached, the diverter valve was manually actuated to its "diverting" position (i.e., solids directed to collection chamber), held for a pre-selected amount of time, and returned to the "normal" position (i.e., solids returning to downcomer). During this operation, the riser operator monitored the data-acquisition display to track elapsed time, to note where in the data record the diversion took place, and to observe any unexpected behavior in the load cell output. Collected solids were retained in the chamber for a short period (20-30 s) to obtain an unambiguous plateau for this condition in the data record. The slide valve at the base of the collection chamber and the ball valve isolating the diverter leg from the downcomer-to-engagement standpipe were then opened, the collection chamber was fluidized, and collected particles were "drained" back into the main CFB loop. When this was completed, fluidization of the collection chamber was stopped, the slide and ball valves were closed, and the CFB loop was thus returned to its original condition. At the end of the riser run, the procedure of applying known loads to the load cell from the beginning of the run was repeated, to attach a second set of known-load data to the data record in the event one was required to resolve ambiguities, etc.

Figure 4.33 presents diverter-valve results as sample mass collected as a function of sample duration for a series of measurements (multiple runs) conducted over several days. Measurements are for FCC powder with a superficial gas velocity U_g = 7.0 m/s. The data are fit

well by a zero-intercept straight line over the range of durations considered. Each sample mass can be converted to a riser mass flux G_s as

$$G_s = \frac{m_{sample}}{A_{riser} \cdot t_{sample}}, \tag{4.6.1}$$

where m_{sample} is the sample mass, A_{riser} is the cross-sectional area of the riser, and t_{sample} is the sample duration. The resulting distribution of estimated solids fluxes from Figure 4.33 is presented in Figure 4.34. Note that tightly-grouped samples (e.g., 2-s sample duration) are scattered by the small sample-time divisor in Eq. (4.6.1).

The mean mass flux can then be estimated from the ensemble of calculated mass fluxes, as in Figure 4.34, where the estimated mean mass flux is 82.3 kg/m^2·s. A statistical uncertainty u of the mean mass-flux value can be estimated from an ensemble of N samples as

$$u = t \frac{S_{Gs}}{N^{1/2}}, \tag{4.6.2}$$

where t is the value of the Student-t distribution for the desired confidence interval and based on $N - 1$ degrees of freedom, and S_{Gs} is the sample standard deviation of the ensemble of calculated mass flux values. This methodology was applied to determine the riser mass fluxes and uncertainties reported throughout this report. It is noted that the uncertainty approach presumes that the mass flux is invariant from run to run (and within runs as well) and that the scatter in the data represents solely precision uncertainty. The approach applied here effectively considers the CFB itself to be part of the measurement apparatus and the dominant contributor to precision uncertainty in the mass-flux measurement. This repeatability uncertainty is the dominant contributor to the overall uncertainty in the measurement; that is, it is significantly larger than any other observed uncertainties in the measurement (load cell specifications, hysteresis, etc.).

The effect of the diverter-valve measurement can be examined by considering the behavior of the riser during the valve closure. This is shown in Figure 4.35 for one of the 5-s closure cases presented in Figures 4.33 and 4.34. The mean differential-pressure profile is shown as a solid black trace; this profile was generated from a 140-s span of data preceding the valve closure. Traces at one-second intervals subsequent to valve closure are overlaid. No clear trend is apparent, indicating that riser behavior is unaffected by diverter-valve closure.

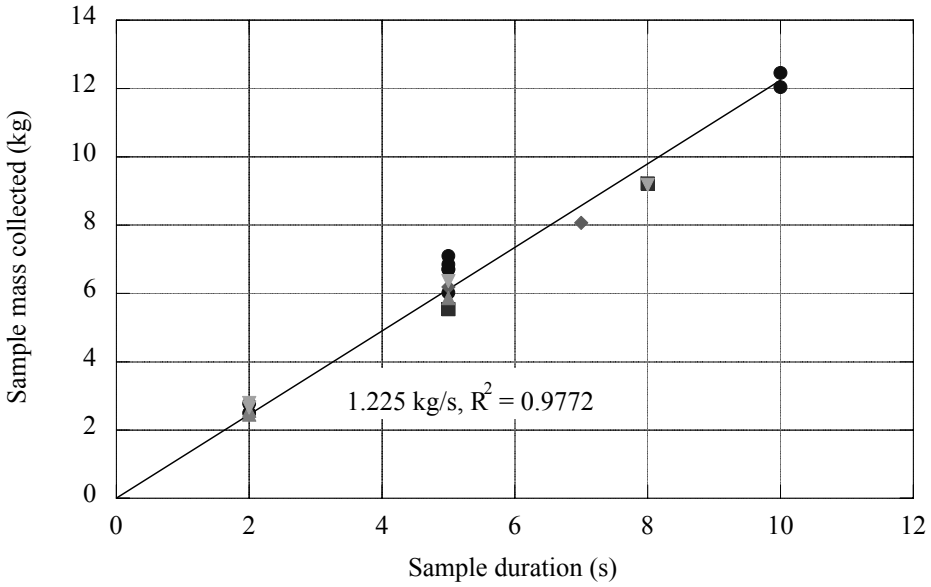

Figure 4.33. Mass of samples collected for diverter-valve measurements. Repeated runs (symbols) over several days. FCC particles, superficial gas velocity U_g = 7.0 m/s.

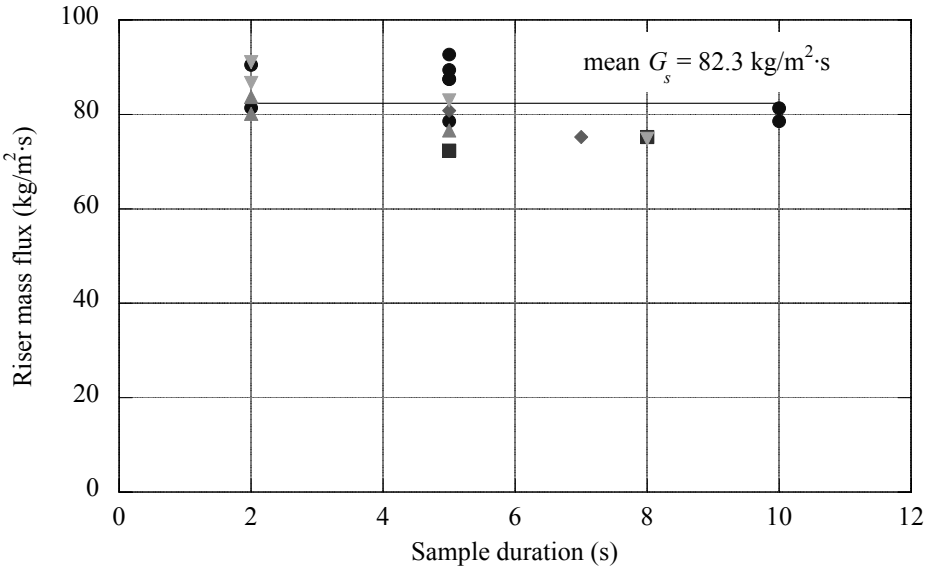

Figure 4.34. Samples from Figure 4.33 converted to riser mass flux by Equation (4.6.1). Estimated mean mass flux is 82.3 kg/m^2·s

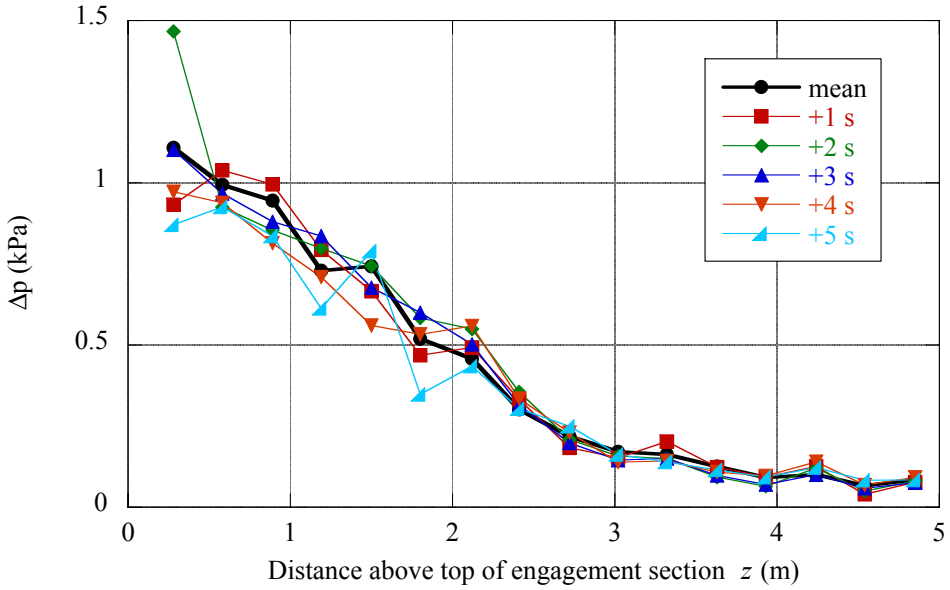

Figure 4.35. Behavior of riser differential pressure profile during 5-s diverter-valve closure, compared to mean profile (black).

4.7 Computer Aided Radioactive Particle Tracking (CARPT)

Measurement of solids velocity is difficult in gas-solid flows except under very light loading conditions (see Section 4.8). One technique that holds promise for measurement of particle velocity and residence time under densely loaded conditions is Computer Aided Radioactive Particle Tracking (CARPT). In a CARPT experiment, a single radioactive tracer particle with properties matching the phase of interest (solid, in this case) is introduced into the flow and its motion during flow is captured by an array of detectors. By tracking the particle over a large number of passages, statistics on the particle velocity field can be derived. For a CFB application the particle should have physical characteristics (size, density) similar to those of the other particles in the CFB.

CARPT was performed on the Sandia CFB by personnel from Washington University in St. Louis (WUStL). WUStL personnel have experience with CARPT in bubble columns (Degaleesan et al., 1996), digesters (Karim et al., 2004), stirred tanks (Rammohan et al., 2000; Khopkar et al., 2005), and CFBs (Bhusarapu et al., 2004ab, 2005, 2006; Bhusarapu, 2005). Larachi et al. (1994) and Cassanello et al. (1999) discuss application of CARPT to a spouted bed. Roy et al. (2002) discuss optimization of CARPT performance for CFB applications. One of the authors (SB), at the time a Ph.D. student in Chemical Engineering at WUStL under the

guidance of Professors Al-Dahhan and Dudukovic, ran the CARPT experiments at Sandia with Sandia staff and technologist support.

4.7.1 CARPT Experimental Setup and Procedure

For implementation at Sandia, the radioactive particle was ^{46}Sc (scandium-46) pellet encapsulated in a protective coating of Parylene-N polymer, as shown in Figure 4.36. This single tracer particle matched the size and density of the glass beads run in the CFB during these tests. While the size and density of the tracer particle matched perfectly the size and density of the particles run in the riser, the restitution coefficient was not measured and was assumed comparable. ^{46}Sc has an 83 day half-life. Special procedures were developed to allow safe handling and tracking of the particle in the CFB, including positioning numerous handheld radiation detectors around the CFB flow loop. The radioactive particle was locked in a shielded housing when not in use.

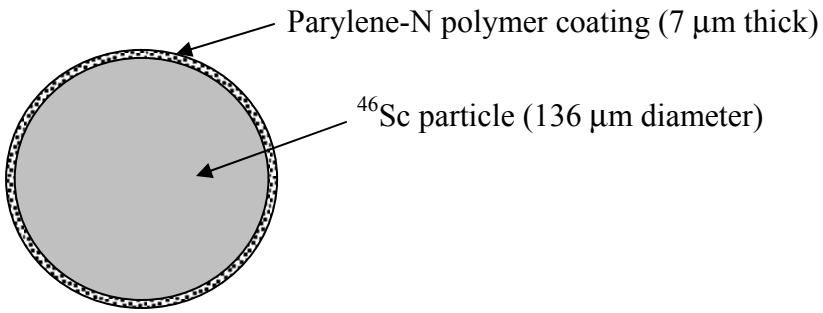

Figure 4.36. Composite radioactive tracer particle used for CARPT.

CARPT measurements were performed in a special riser segment instrumented with a framework to accurately hold detectors at fixed locations and with access ports for insertion of a calibration probe. The CARPT section was 4 feet long, and replaced the 4th and 5th 2-foot sections of the riser. The zone of investigation for the CARPT experiments was therefore at an axial height ranging from 2.08-2.79 m with a dimensionless height (z/D) range from 14.9 to 20. The middle (4th) set of calibration ports in the set of 7 rings of ports was thus 8 feet above the top of the engagement section, or at z/D = 17.45; three rings of ports were below this height, and three were above, at 4.72-inch intervals ($\Delta z/D \approx 0.86$). Figures 4.37 and 4.38 are photographs of the CARPT section installed in the CFB. The section included a framework that held 18 NaI(Tl) scintillation detectors at fixed locations to record the gamma photons at every 'instant' emitted by the radioactive particle as it moved past them.

Prior to each CARPT run, the detectors were calibrated by placing a radioactive source at a series of known locations in the CARPT section using an intrusive rod, running the flow at the test conditions of interest, and recording the count rates (gamma photons) on each of the scintillation detectors. The source used in these calibrations was the same radioactive particle shown in Figure 4.36 and used in the flowing experiments, but it was sealed in a small capsule

and held rigidly at the tip of the calibration rod. The calibration data were used to determine detector response and to convert the measured detector signals during CARPT to instantaneous particle locations and trajectories, as explained in Bhusarapu (2005). Data were collected at a sampling rate of 5 ms (i.e., frequency of 200 Hz).

Figure 4.37. CARPT operating under Flow Condition 1. Only 8 of the 18 scintillation detectors are visible in this view. Particles are glass beads.

After calibration, the radioactive tracer particle was introduced into the Sandia CFB, using handheld radiation detectors to track its entry into the CFB loop. The flow was then run and data were acquired. In order to achieve sufficient particle passages to assure good turbulence statistics, the flow had to be run for approximately 50 hours. Finally, the particle was removed when the run was completed, its activity checked to assure that attrition had not occurred, and the particle was placed into safe storage.

Radioactive particle tracking was used both for CARPT velocity measurements and to measure the residence time distributions (RTD) in the riser and overall CFB loop. Representative data from Bhusarapu (2005) are included in this chapter to show that the technique was successfully implemented; for full experimental description, data processing steps, and full results see that dissertation and papers extracted from it (Bhusarapu et al. 2004ab, 2005, 2006). In addition, CARPT experiments in the CFB at WUStL are not covered in this report but are discussed in these references.

Figure 4.38. CARPT section installed on riser.

Three flow conditions were used for solids RTD and CARPT measurements by varying superficial gas velocities (U_g^{riser}) and different solids inventory. Overall solids mass flux (G_s) and the flow regime at these operating conditions are given in Table 4.2. The overall solids mass flux was determined using the time of flight method described in Bhusarapu et al. (2004 ab). Operating flow regimes were identified from the idealized flow regime map of Bi and Grace (1995).

Table 4.2. Operating conditions and flow regimes for solids RTD measurements and CARPT.

U_g^{riser} (m/s)	5.49	5.56	7.71
G_s (kg/m^2·s)	102	119	145
Regime	FF/Trans	FF	DPT

FF - Fast Fluidization, DPT - Dilute Phase Transport, Trans - Transition.

4.7.2 Solids Residence Time Distribution (RTD)

One of the key factors in designing and operating CFB reactors is knowledge of the residence time distribution (RTD) of solids in various segments of the CFB loop. Many techniques have been applied to determine solids RTD in risers (Berruti et al., 1995). During CARPT runs, detectors at the base and top of the riser were used to detect each passage of the single radioactive tracer particle to measure RTD. This technique has the advantage that the particle can be tracked each time it passes a point in the flow, so there is no confusion over whether the particle left through the inlet and then reentered the measurement region.

For these solids RTD measurements, three shielded detectors were used to track the particle as it circulated in the CFB. These detectors were placed at the following locations:

i) at the base of the riser, at 3.5 inches above the engagement section,
ii) at the riser exit, 10.5 inches below the disengagement section,
iii) at the start of the downcomer, 2 inches below the top of the downcomer.

Figure 4.39a shows typical detector locations. From the detector responses, the time spent by the tracer between the cross-sectional planes of the detectors can be found and used to determine the residence times in the riser.

Figure 4.39a shows a representative trajectory of the tracer particle in the riser. Every passage of the tracer particle near a detector will give a spike in count rate. Therefore, many peaks occur in the detector time trace as the tracer particle repeatedly passes each detector plane. Such behavior is shown in Figure 4.39b, which displays a part of the raw data from the detectors located at the riser inlet, exit and top (entry) of the downcomer (from the WUStL riser). The time elapsed between spikes recorded at different detectors is used to determine whether the tracer passed the inlet detector several times entering and exiting the system at the inlet, or whether it passed the detector at the riser exit straight after passing by the inlet detector. The different magnitudes of the spikes detected (see Figure 4.39b) indicate that the tracer crossed the detector plane at different distances from the detector face. In order to ensure that the detectors view only the cross-sectional plane of interest, they were heavily shielded by wrapping the column above and below the cross-section with lead sheet. Therefore, by counting in pairs, the entry and exit of the tracer into the system (region of the riser between the cross-sectional planes viewed by the detectors), the time that the tracer particle spent inside the system and outside the system can be precisely calculated.

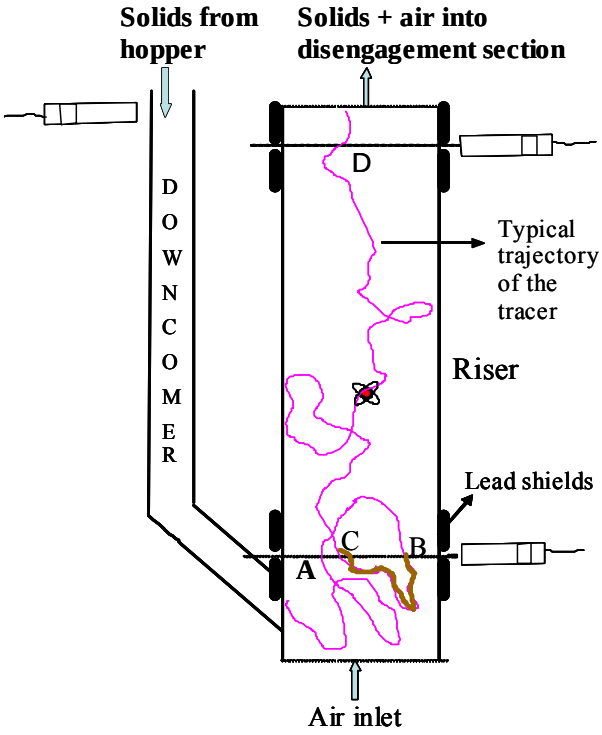

(a)

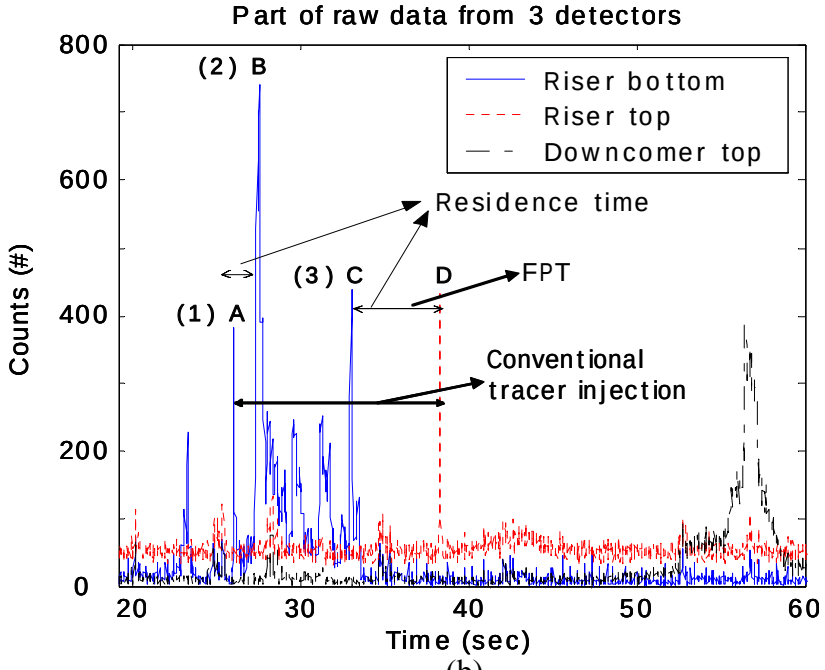

(b)

Figure 4.39. a) Schematic of the three detectors along the CFB loop with a typical trajectory. b) Part of the raw data obtained from the three detectors showing residence time, first passage time, and conventional tracer response (reprinted from Bhusarapu (2005) with permission of the author).

In the trajectory shown in Figure 4.39a, the tracer enters the system at point A, corresponding to spike 1 in Figure 4.39b, then exits at point B at the same plane, corresponding to spike 2, and finally re-enters the system again at point C, corresponding to spike 3. The time spent by the tracer between positions B and C should not be counted as residence time in the riser, and only the time spent between positions A and B and between positions C and D is taken as the residence time. The same approach is applied near the exit of the riser at the cross-sectional plane D. In this way, accurate estimates of the solids RTD in the riser were made. Details of the differences in the RTD, first passage time distribution (FPTD), and discussion of conventional tracer studies (injection-detection methods) are given in Bhusarapu (2005).

Data for solids probability density functions (PDFs) of RTDs exhibit a single peak occurring before their mean residence times in the dilute phase transport (DPT) regime and multiple peaks in the fast fluidization (FF) regime as shown in Figure 4.40. These results are in agreement with additional low solids flux cases (from the WUStL riser) presented in Bhusarapu (2005). Examining the solids RTD (F-curves in Figure 4.40), smaller slopes are observed on the dimensionless time scale when an indication of a multiple peaks are seen in the PDF curve. Absence of the multiple peaks and rapid rise of the RTD (high slope) seem to be indicative of DPT. In contrast, solids flow pattern in Figures 4.40ab are in the FF regime. Thus, the shape of the RTD seems to be indicative of the flow regime.

Figure 4.40 shows that, for all flow conditions, the PDFs of the RTD curves are wide and have long tails. This indicates a considerable degree of solids mixing, probably due to solids circulation in the riser and exchange of solids between the dilute core and the dense annular region. The large standard deviation of the RTD can be explained by examination of the raw data of the three detectors used for obtaining the RTD curve, which show both cases in which the particle moves rapidly from bottom to top of the riser and cases in which the tracer particle recirculates in the dense bed at the riser bottom before moving slowly through the riser, often showing up at the base again before finally exiting the top of the riser. The residence times for these extreme cases can vary by two orders of magnitude, explaining the long tail in the RTD curve and the large dispersion coefficient (Bhusarapu, 2005).

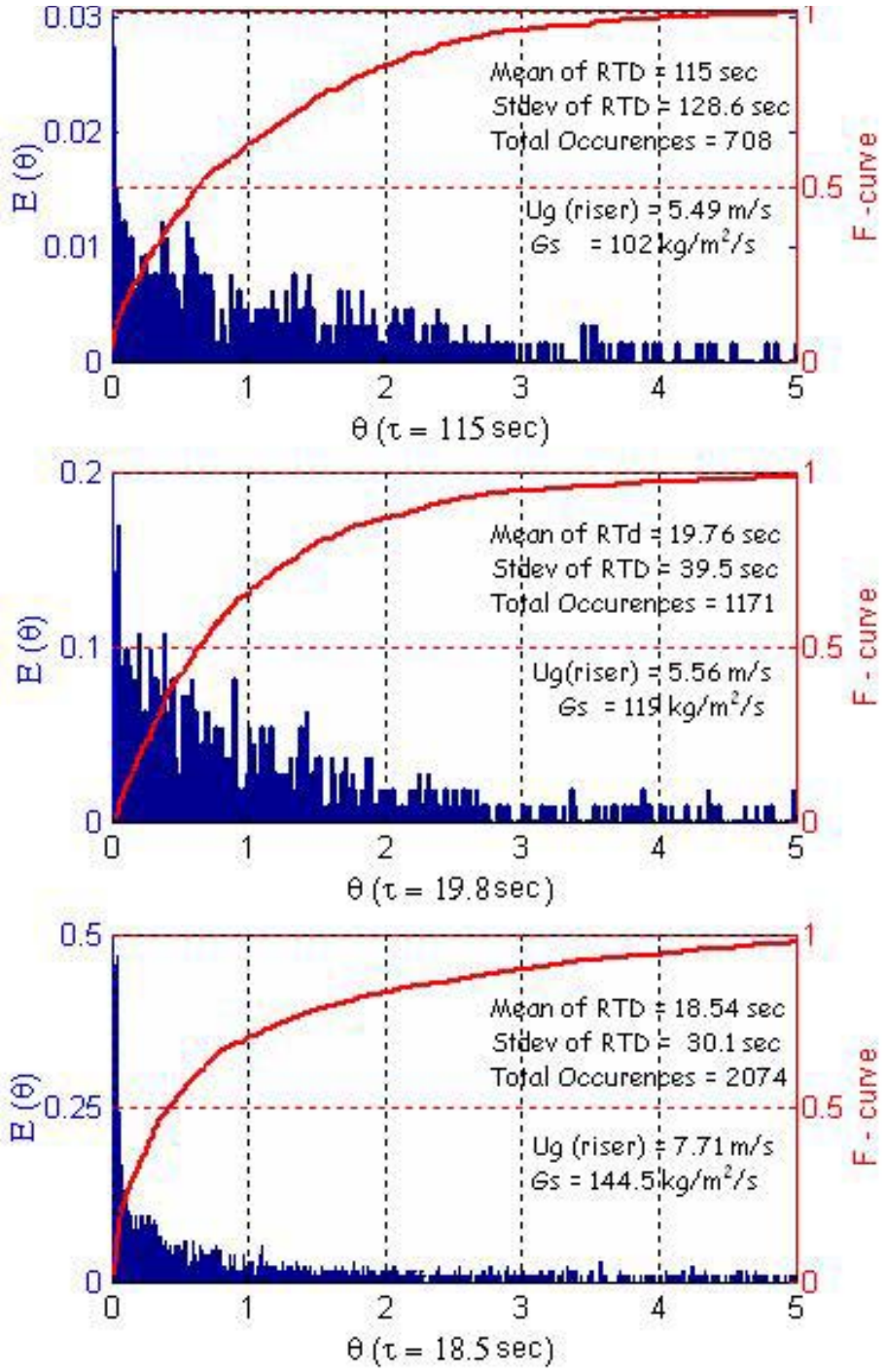

Figure 4.40. Solids RTD and its cumulative distributions at U_g^{riser} and G_s of: a) 5.49 m/s, 102 kg/m^2·s; b) 5.56 m/s, 104 kg/m^2·s; c) 7.71 m/s, 144.5 kg/m^2·s (reprinted from Bhusarapu (2005) with permission of the author).

Mixing parameters, such as moments of the RTD and the dispersion coefficient for all the flow conditions, are evaluated and discussed in Bhusarapu (2005) and are presented in Table 4.3. As expected, mean residence time decreases with increasing solids mass flux at constant gas superficial velocity. The means of FPTDs are less than those of RTDs, while those of the conventional injection-detection method (T_{Conv}) are even higher. The dimensionless variances from a conventional injection-detection method are smaller since the mixing occurring near the boundaries (injection and detection) is not accounted. The error listed in Table 4.3 is the percent difference between the values obtained from the residence time distribution curves and those obtained from conventional impulse injection-response method. It can be seen that the error in the means is around 40%, while the error in dimensionless variance ranges from 2.5 to 14%.

Table 4.3. Mixing parameters for the entire riser for high-flux flow conditions in FF and DPT regimes (reprinted from Bhusarapu (2005) with permission of the author).

U_g^{riser}	5.49 m/s				5.56 m/s				7.71 m/s			
G_s	102 kg/m^2·s				119 kg/m^2·s				144.5 kg/m^2·s			
Regime	FF/Trans				FF				DPT			
	FPTD	RTD	T_{Conv}	Error %	FPTD	RTD	T_{Conv}	Error %	FPTD	RTD	T_{Conv}	Error %
τ,.s	45.55	115	159.61	39	6.86	19.76	28.53	44	8.95	18.54	25.11	35
σ^2, -	1.8	1.3	1.4	5	1.2	4	3.9	-2.5	3.9	2.8	3.2	14
$D_{z,ax}$ (m^2/s)	0.2	0.08	0.06	-33	2.6	0.73	0.54	-26	3.2	0.7	0.5	-29

Further analysis of RTD results, including estimates of axial dispersion coefficients and axial Peclet numbers, are given in Bhusarapu (2005).

4.7.3 CARPT Velocity and Velocity Statistics

Each passage of the radioactive particle through the CARPT section was measured by the scintillation detectors. Application of the calibration to the measured data then gave a particle trajectory and velocity traces for each passage. Summing the data for each flow condition (using the ergodic hypothesis that the collected particle passages are representative of the particle flow field) allowed velocity statistics to be calculated, indicating the flow patterns and therefore the mixing of solids in the riser. Representative data samples are shown in Figures 4.41 through 4.44.

Figure 4.41 shows PDFs of the solids axial velocity. The axial velocity PDFs for both regimes (fast fluidization and dilute phase transport) display significant negative velocities near the wall, transitioning to only positive velocities at the center. This is interpreted to indicate that the flow in these high solids flux conditions (G_s > 100 kg/m^2·s) has a central core that always flows upwards. In the DPT regime (Figure 4.41b), the ensemble-averaged solids axial velocities near the wall are negative, which was not the case at the low solids flux conditions in the DPT regime. This is probably due to the increase in the solids concentration at high solids flux,

resulting in increased tendency for clustering near the wall which in turn increases the solids down-flow. Also, the negative velocities at low-flux conditions were interpreted to be occurring due to the clustering phenomenon (Bhusarapu, 2005). Thus, the velocity PDFs from FF and DPT regimes suggest that the clustering phenomenon is localized near the walls at high solids fluxes, whereas it is common throughout the riser cross section (FF regime) at low solids fluxes. Each of the axial velocity PDFs shown in Figure 4.41 was obtained based on the statistics from a single compartment at a particular angular position. Similar data exist for every angular compartment at each radial location. Hence, this indicates a nearly axisymmetric solids flow.

Figure 4.42 shows that the ensemble-averaged radial and azimuthal velocity components are small compared to their axial values. The radial profile of the velocity vectors in Figure 4.42 shows solids flowing upward in the central core and downward in an outer annulus. This indicates the upward core flow and downward annular flow often mentioned in the literature. These strong radial gradients are also evident in the differences between the solids axial velocity PDFs shown in Figure 4.41.

Figure 4.43 shows tracer particle occurrence profiles visualized in different *r-z* planes. Radial segregation is very strong in both FF and DPT regimes at high solids fluxes (in agreement with GDT data, see Section 5). The thickness of the annulus indicated by the contours in Figure 4.43 was found to be higher in the FF regime as compared to that in the DPT regime. The annulus thickness was seen to increase with increasing solids flux at constant gas superficial velocity (U_g^{riser} = 5.5 m/s; G_s = 102 and 144.5 kg/m^2·s, not shown). The DPT regime at high solids flux conditions exhibits a dense film of solids moving downwards (Figure 4.43b), in contrast with the low solids flux cases (Bhusarapu, 2005). Although the total number of particle occurrences was different in each of the flow conditions in Figures 4.43a and 4.43b, the relative magnitude of the contour values suggests that the annulus is denser and thinner in the DPT regime, while it is less concentrated and thicker in the FF regime. This result indicates that radial segregation is more severe in the DPT regime at high solids fluxes (beyond a certain solids volume fraction limit). Absence of any contour lines in the central core region, for both the FF and DPT regimes, indicates very small and relatively uniform solids concentration in the core region. Thus, the solids aggregation tendency or cluster formation is negligible in the core region at high solids fluxes, supporting the conclusion from the velocity PDFs shown in Figure 4.41.

Figure 4.44 shows the radial profiles of the ensemble-averaged and spatially averaged solids axial velocity for all the operating conditions investigated. These data from Bhusarapu (2005) include both the high-solids-flux Sandia CFB and the low-solids-flux WUStL CFB. All of the profiles were azimuthally and axially averaged to investigate the effect of operating conditions on the one-dimensional riser flow structure. To assess the similarity of the mean axial velocity profiles, velocities shown in Figure 4.44a were normalized with the corresponding cross-sectional averaged values given in the legend. Figure 4.44a suggests that the shapes of the mean solids axial velocity profiles are similar in both risers and at low and high solids fluxes. This is discussed in further detail in Bhusarapu (2005). The flow condition at U_g^{riser} = 5.5 m/s and G_s = 102 kg/m^2·s, exhibits a slightly different functional form near the center of the column (Figure 4.44a). This deviation is probably due to the flow being close to the regime transition (based on the flow regime map of Bi and Grace, 1995), resulting in the oscillating flow of the suspension, moving in slugs. The mean axial velocity, as seen in Figure 4.44b, increases with the

increase in solids mass flux at constant gas velocity, which agrees with most of the reported studies (e.g., Berruti et al., 1995). A substantial increase in the mean solids axial velocity is observed in the center of the column when superficial gas velocity and solids mass flux are increased from the FF to the DPT regime (Figure 4.44b). Within the spatial resolution of the velocity reconstruction, the inversion point of the axial solids velocity profile (corresponding to annulus thickness) was found to be located in the same compartment (with r/R = 0.81). Hence, the downflow of solids at the wall is expected to cause considerable backmixing in the solids phase. It can also be observed from Figure 4.44b that the error bars indicated on the velocities are relatively small (within 15%), supporting the conclusion of the solids flow being close to fully-developed. In the profiles shown in Figure 4.44b, the error bars represent the range of the values encountered while circumferentially and axially averaging the data.

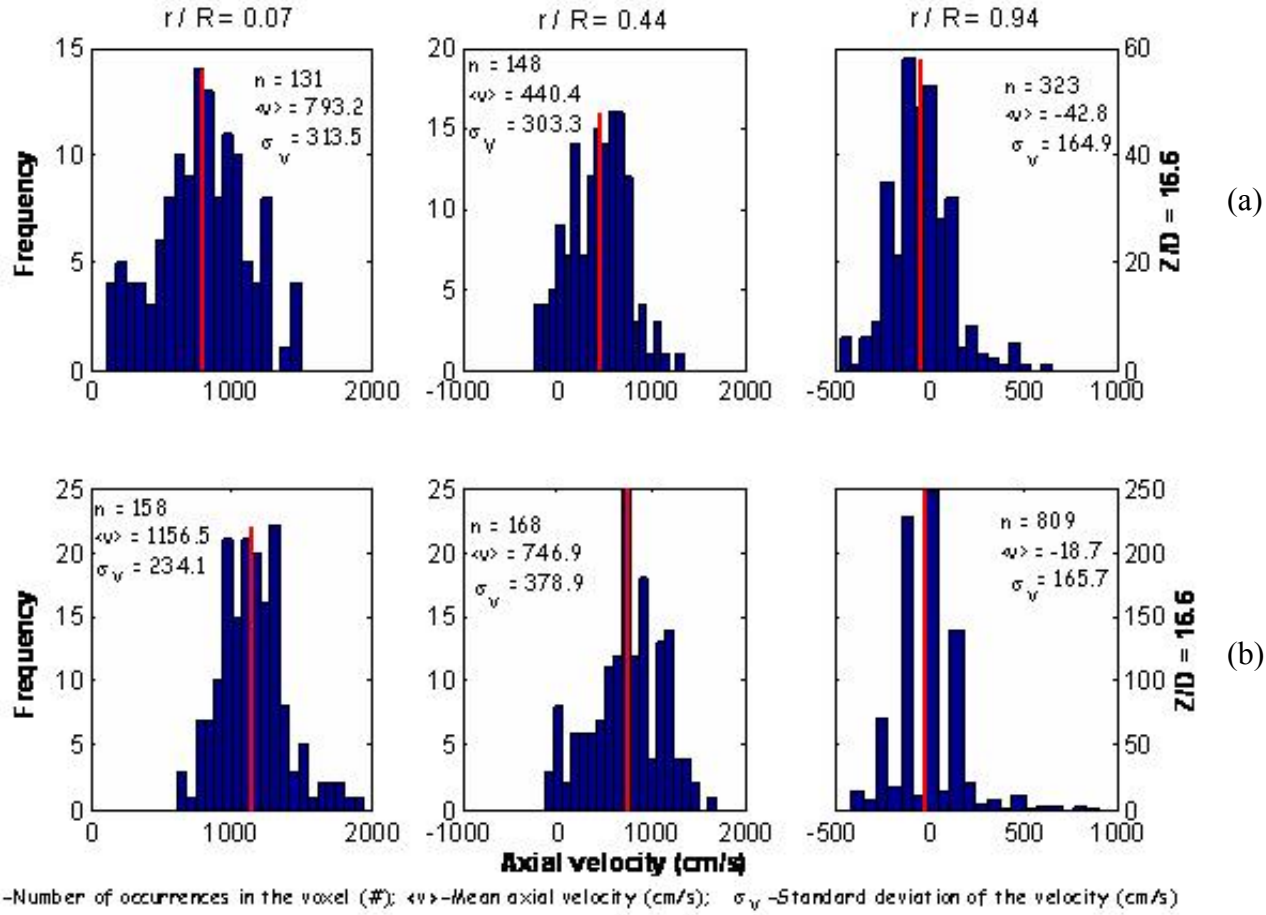

Figure 4.41. Probability density functions of the axial velocity at three radial locations: a) FF (U_g = 5.5 m/s; G_s = 144 kg/m^2·s); b) DPT (U_g = 7.7 m/s; G_s = 119 kg/m^2·s) (reprinted from Bhusarapu (2005) with permission of the author).

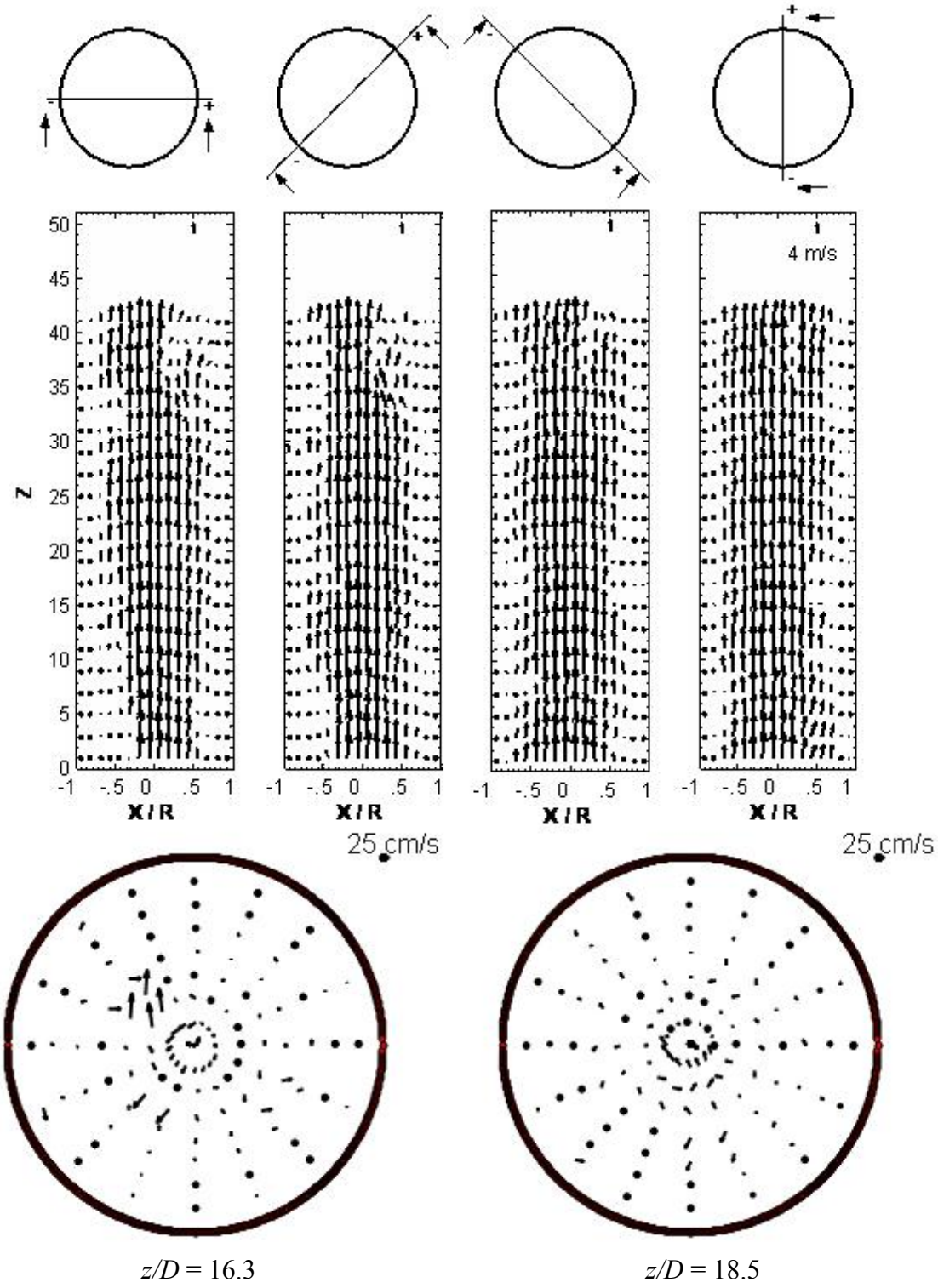

Figure 4.42. Visualization of the velocity vectors in the zone of interrogation in a) *r-z* plane at different angles; b) *r-θ* plane at different axial heights (*z/D* = 16.3, 18.5). The operating conditions are in FF regime at U_g = 5.56 m/s; G_s = 144.5 kg/m^2·s (reprinted from Bhusarapu (2005) with permission of the author).

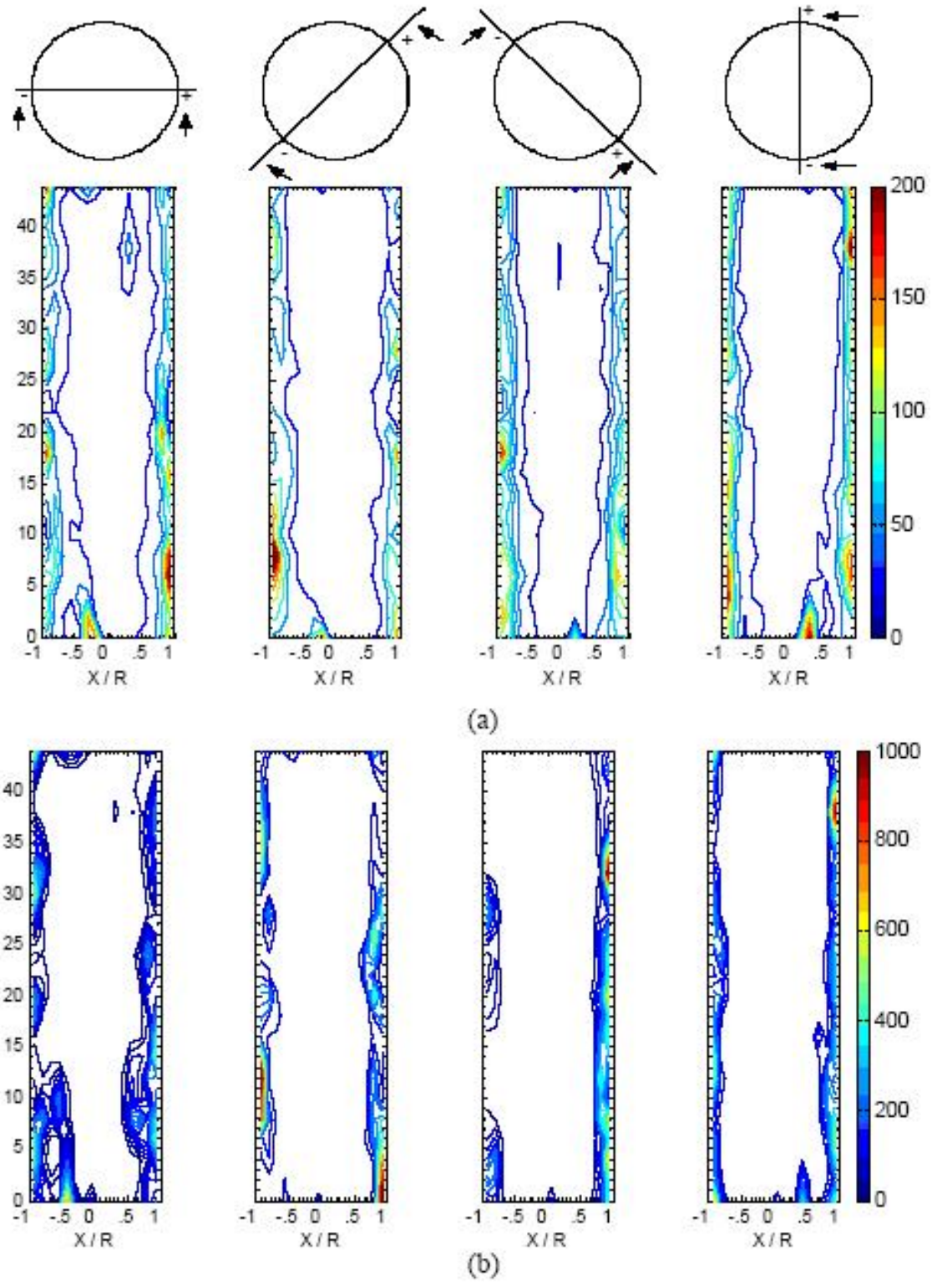

Figure 4.43. Contour plots visualized at different longitudinal views of the particle occurrences per unit volume (#/cm^3): a) FF regime (U_g^{riser} = 5.56 m/s; G_s = 144.5 kg/m^2·s); b) DPT (U_g^{riser} = 7.71 m/s; G_s = 119 kg/m^2·s) (reprinted from Bhusarapu (2005) with permission of the author).

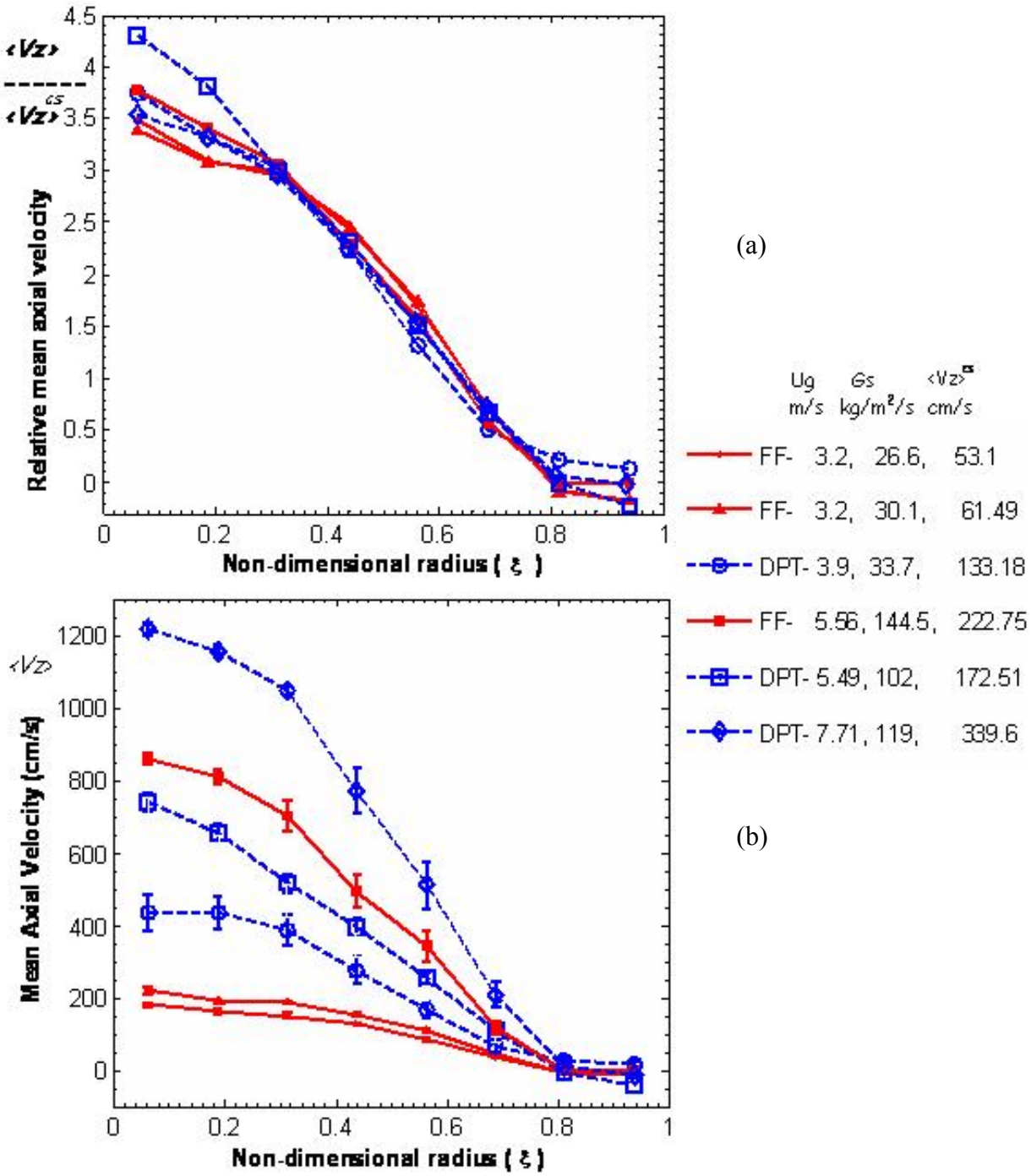

Figure 4.44. Circumferentially and axially averaged time-averaged radial profiles: a) relative axial velocity; b) axial velocity for all the flow conditions investigated. Note that the data were obtained from two different risers, at low solids fluxes in the CREL riser and at high solids fluxes in the SNL's riser (reprinted from Bhusarapu (2005) with permission of the author).

Further velocity statistics derived from CARPT data are included in Bhusarapu (2005) including axial and radial Reynolds stresses, turbulent kinetic energy, and granular temperature. In addition, Lagrangian information was obtained, which complements by providing solids local backmixing parameters. These include circulation time distribution, macromixing index, sectional RTDs, which help in understanding the internal re-circulation patterns. Solids eddy diffusivities and integral time scales, which can help in modeling the turbulent transport terms in a Euler-Euler type of CFD model were also obtained. Further details can be obtained from Bhusarapu (2005).

The CARPT technique was successful in acquiring solids RTD and velocity information that would be extremely difficult, if not impossible, to obtain in any other way.

4.8 Optical Techniques

In general, flows in CFBs under industrially relevant conditions are nearly opaque due to the high solids loading, even when the flow system has transparent walls or windows. Viewing the flow at the wall may provide some insights into cluster formation, size, and persistence but generally does not provide much quantitative data.

There have been exceptions in which optical techniques have been successfully applied and these are mentioned below. However, they were all conducted under conditions of very low solids loadings. These include videos, laser-light-sheet visualization, laser Doppler anemometry, and PDPA.

Under most flow conditions of interest, the gas-solid mixture in the riser is optically opaque and thus not amenable to optical diagnostics.

4.8.1 Video

The riser walls are transparent acrylic, so the particle motion at the walls can be seen. Videos were routinely taken of the flow in the riser at different elevations for each of the four standard flow conditions run with FCC catalyst. Figures 4.45 and 4.46 show selected frames extracted from such videos under heavy and light solids loading, respectively. Such videos were found to provide good qualitative visualization under the lighter loading conditions and/or higher in the riser. Under the heavy loading conditions shown in Figure 4.45, the turbulent, unsteady character of the flow at the riser wall is evident, but it is difficult to extract further information.

4.8.2 Laser Light-Sheet Illumination and Particle Image Velocimetry (PIV)

Using laser illumination in the riser requires that a light sheet penetrate into the riser. This becomes difficult as solids flux is increased because the particles are not distributed uniformly but are more concentrated near the walls, thus blocking a laser light sheet if generated external to

the riser. The three-dimensional visualization done by Horio and Kuroki (1994) used a laser light sheet but was limited to solids volume fractions less than 0.1% and solids fluxes less than 1 $kg/m^2 \cdot s$.

PIV was performed high in the Sandia riser under very dilute flow conditions. This was really just a feasibility assessment and demonstrated that PIV could be used under the lightest loading conditions, essentially just using a few particles to act as seed particles for PIV in an otherwise single-phase flow in the riser. Figure 4.47 shows example images acquired during PIV with a pulsed Nd:YAG laser.

4.8.3 Laser Doppler Velocimetry (LDV) and Phase Doppler Particle Analyzer (PDPA)

Laser Doppler Velocimetry (LDV) is a laser-based technique for measuring the velocity of particles passing through a measurement volume defined by the crossing of two laser beams. Light scattered by the moving particles is Doppler shifted so accurate measurements of the scattered light frequency can be used to resolve the instantaneous particle velocity (Goldstein, 1996). LDV has been applied for fluctuating velocity measurements in CFBs by Van engelandt et al., 2004. The Phase Doppler Particle Analyzer (PDPA) is an extension of LDV to measure particle size as well as velocity. This is done by using multiple photodetectors to measure spatial variations in the Doppler signal caused by the scattering properties of the individual particles (Bachalo, 1994). The PDPA technique is optimized for measurements of spherical spray droplets. Nonsphericity and surface imperfections (scratches, etc.) can cause the technique to fail. Despite this limitation, several groups have used PDPA to measure particle size, velocity, and some characteristics such as cluster voidage in very dilute flows in fluidized beds and CFBs. For example, Liu et al. (2005) applied PDPA to measure cluster characteristics in a riser circulating glass beads at solids fluxes of 1 $kg/m^2 \cdot s$ and below. Du et al. (2005) applied PDPA to study particle separation in unique separation devices at solids fluxes below 5 $kg/m^2 \cdot s$. Mathiesen et al. (2000) studied particle size segregation in the radial and axial directions in a laboratory-scale CFB. Neither LDV nor PDPA were applied in the present study. Attempts to use a PDPA for particle sizing of glass beads in studies outside the CFB gave spurious results, seemingly due to surface imperfections on the beads.

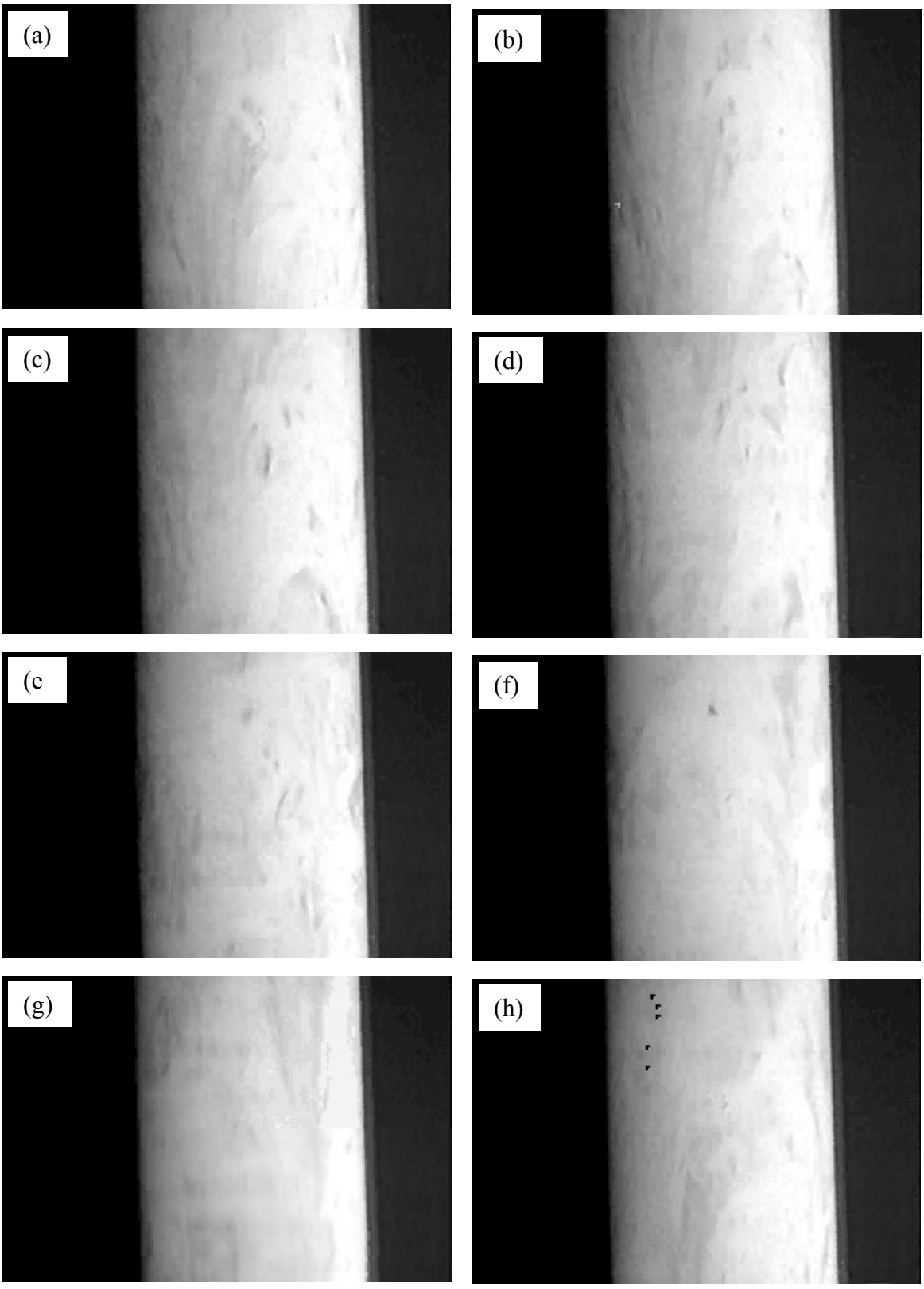

Figure 4.45. Selected frames from video of flow in riser under "heavy" solids loading conditions. Particles are FCC catalyst.

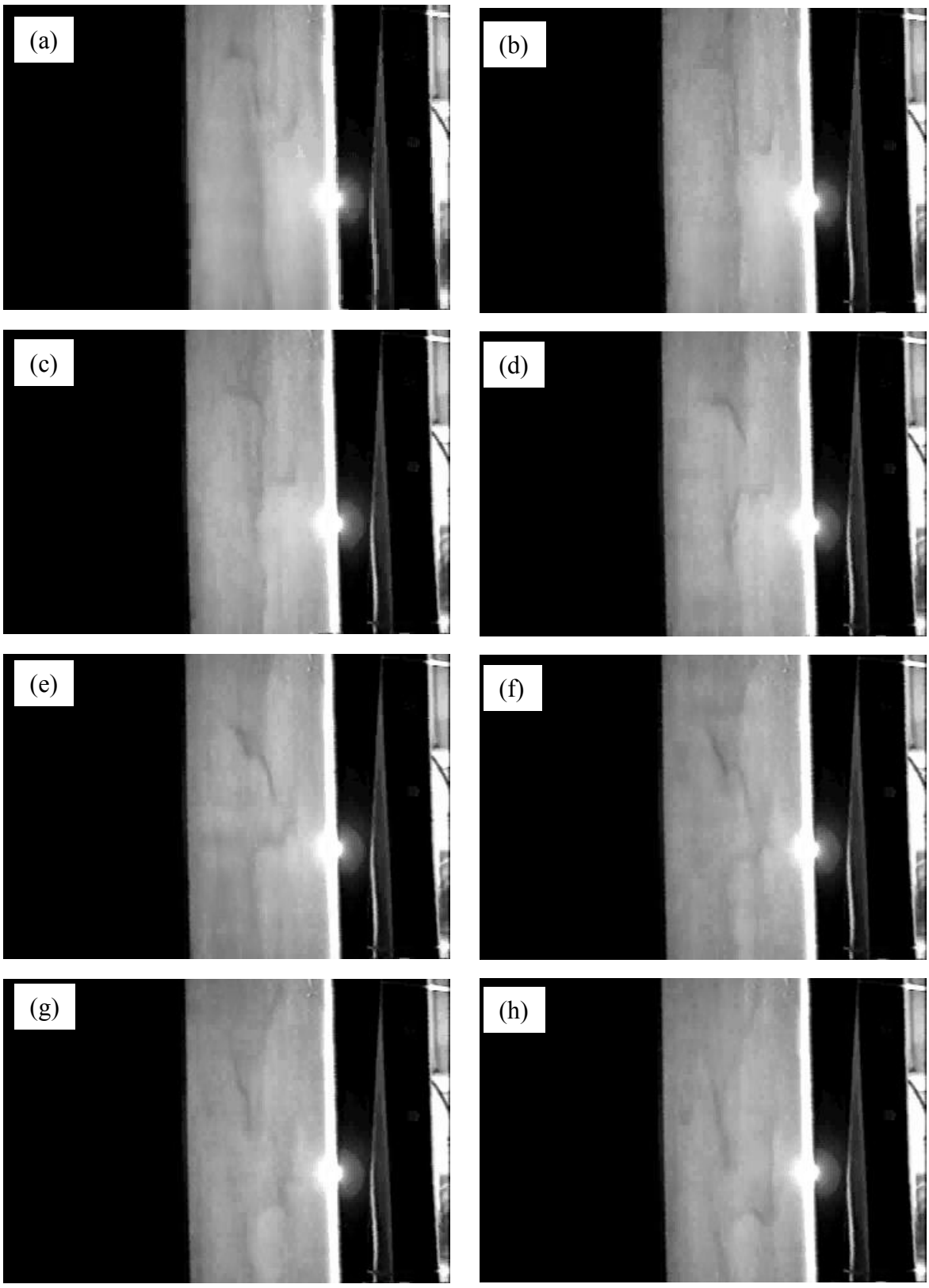

Figure 4.46. Selected frames from video of flow in riser under "light" solids loading conditions. Particles are FCC catalyst.

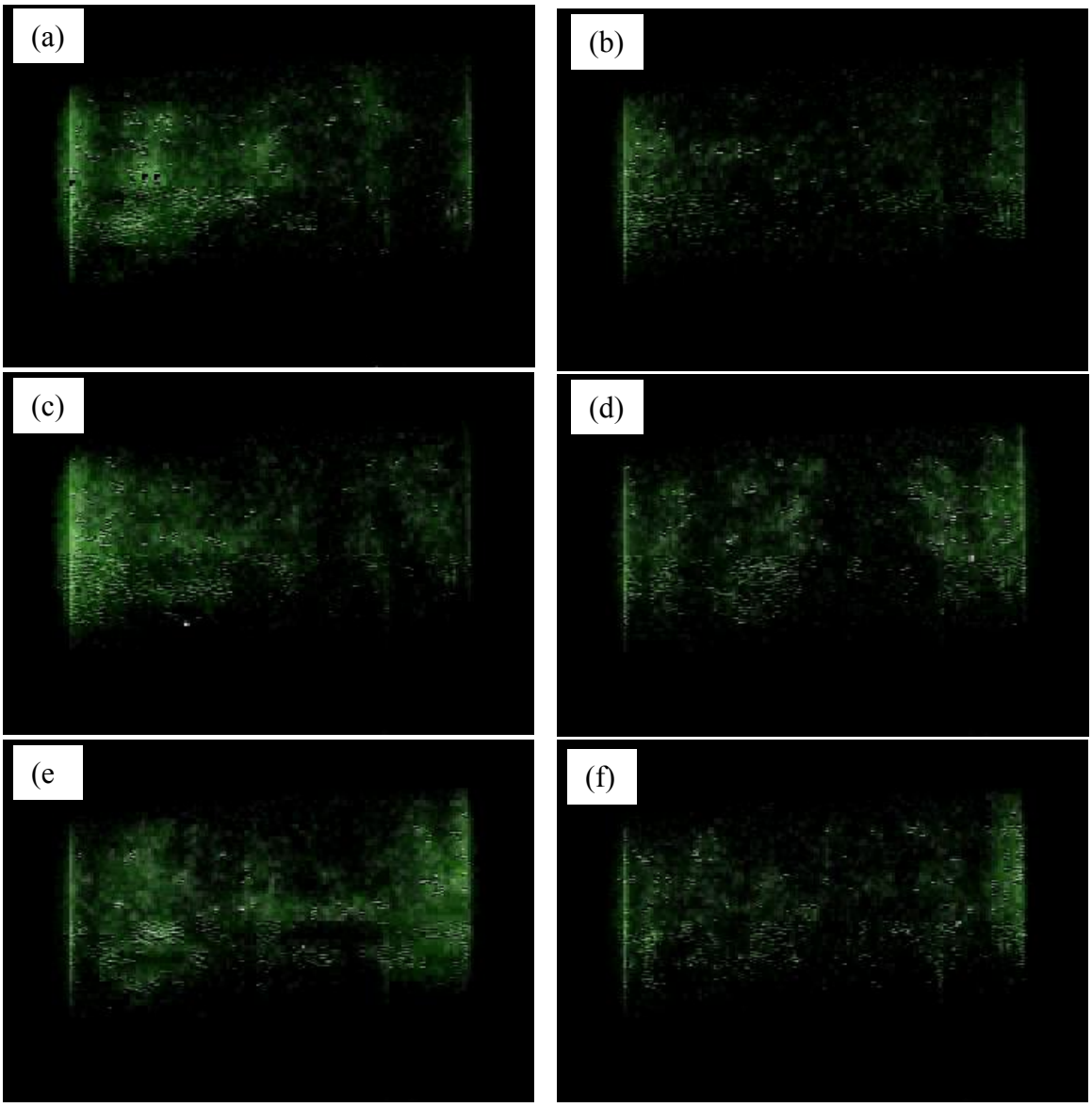

Figure 4.47. Selected frames from video of flow in riser under "very light" solids loading conditions. Particles are FCC catalyst. Illumination is with pulsed Nd:YAG laser.

5. Experimental Results

Representative results were presented in Section 4 in discussion of the diagnostic techniques. This section provides additional data and comparisons. The experimental results presented here are grouped by particle type. Results are presented first for experiments involving FCC catalyst and subsequently for experiments involving glass beads. DP and GDT data are presented for both. EIT data are presented for FCC catalyst only because glass beads produced excessive static electricity which made EIT measurements too noisy to provide accurate data. CARPT data (presented in Section 4.7) are presented for glass beads only because the radioactive tracer particle was matched to the size and density of glass beads. It was not possible to create a radioactive tracer particle with sufficient source strength that matched the size and density of FCC particles.

5.1 FCC Catalyst

Figure 5.1 shows pressure data plotted against height z in the riser (non-dimensionalized using riser inner diameter D) for multiple experiments and the run conditions listed in Table 5.1. It was found that riser conditions are sensitive to the overall solids inventory in the CFB and that solids inventory gradually drops during CFB operation because some particles (mostly fine particles, which are generated by attrition) are carried to the baghouse filter. Therefore, experiments were performed for less than 30 minutes each, and particles were added between runs to keep the CFB particle inventory stable. However, even with care taken to keep the CFB inventory and inlet conditions identical for each experiment, variations in operating conditions as seen in Figure 5.1 are apparent. Such difficulties are common with CFBs but have been little addressed in the literature (Merrow, 1986). These variations were taken into consideration in the EIT uncertainty analysis presented in Section 4.5.

Table 5.1. Test Conditions for FCC. Uncertainty includes run-to-run variations.

Case Number	Superficial Gas Velocity at Top of Riser U_g (m/s)	Solids Flux G_s (kg/m^2·s)
1 (low gas, low solids)	5.2 ± 0.1	68.4 ± 7.0
2 (high gas, low solids)	7.0 ± 0.1	67.3 ± 3.2
3 (high gas, high solids)	7.0 ± 0.1	82.3 ± 2.8
4 (low gas, high solids)	5.2 ± 0.1	83.8 ± 3.7

EIT and GDT data were recorded at a single height during each run, so axial profiles were developed by acquiring data at one height, stopping the flow, moving the diagnostics, and repeating to obtain data at the next axial location for each of the experimental conditions. Conditions were returned to the same nominal values for each run. Acquisition of an axial profile could take several days (again, nominally identical conditions exhibited some run-to-run differences).

The complete set of radial solids profiles obtained from EIT and GDT is shown in Figure 5.2, and the data are presented in Table 5.2. EIT and GDT show very good agreement over the full range of flow conditions, as discussed in Section 4.5. Recall that both the EIT and GDT reconstructions used the same form of polynomial and were constrained to positive coefficients, and that all data are time-averaged. GDT profiles taken at additional riser heights are shown in Figure 5.3. These are all single samples, and there are no corresponding EIT data, so the data are shown as single curves without uncertainties.

The profiles from GDT and EIT at all flow conditions and measurement heights were integrated to determine cross-sectionally averaged solids volume fraction values. These values are shown in Table 5.2 and plotted as a function of height in Figure 5.4. Eq. (4.5.7) was also used to estimate the cross-sectionally averaged solids volume fraction from DP measurements. The error bars shown in Figure 5.4 correspond to the values used to produce the uncertainty envelopes in Figure 5.2. The DP method overestimates average solids volume fractions near the base of the riser, where the solids volume fraction is the largest. This discrepancy is typically attributed to the acceleration of particles, which is not accounted for by the hydrostatic assumption, and therefore this discrepancy is presumed to result from these limitations in interpretation of the DP values, rather than in the EIT or GDT data. The last term of Eq. (4.5.6) accounts for vertical accelerations using a one-dimensional assumption. However, this term is negligible here, which suggests that three-dimensional effects are responsible for the observed discrepancy.

The present data show similar trends to those of Schlichthaerle and Werther (1999), even though the present solids fluxes are much higher and the axial region scanned extends much further up the riser. Equation (4.5.6) shows that in cases of low solids flux the DP-determined solids loading should be accurate and therefore agree with that measured by GDT. The Schlichthaerle and Werther data indicate that even at low solids flux the effect of solids loading gradients is still important at the base of the riser. Louge and Chang (1990) also present data showing similar behavior at even higher solids fluxes (up to 600 $kg/m^2 \cdot s$).

The disagreements between the data from the DP method and those obtained using EIT and GDT near the base of the riser can be attributed to two sources. First, any forces not accounted for in Eq. (4.5.6), such as friction, would result in an error, although such forces are usually assumed to be negligible (Louge, 1997). Second, the DP method relies on a pressure difference across a relatively large distance (30.5 cm) and thus represents a large spatial average, whereas the measurement volume of EIT is smaller and that of GDT is even smaller. The impact of spatial averaging could be explored in future work by taking many GDT measurements between two pressure ports in small increments (e.g., 2 cm apart) and integrating to obtain the average solids volume fraction. A similar procedure with EIT is not possible with the current setup because the many flanges and ports restrict the EIT ring to certain positions, but this could be done by adding an extended riser section without ports. The difference between EIT and GDT does not exceed a solids volume fraction value of 0.03 in most cases and may also be attributable to the difference in measurement volumes and the aforementioned bias in the EIT measurement.

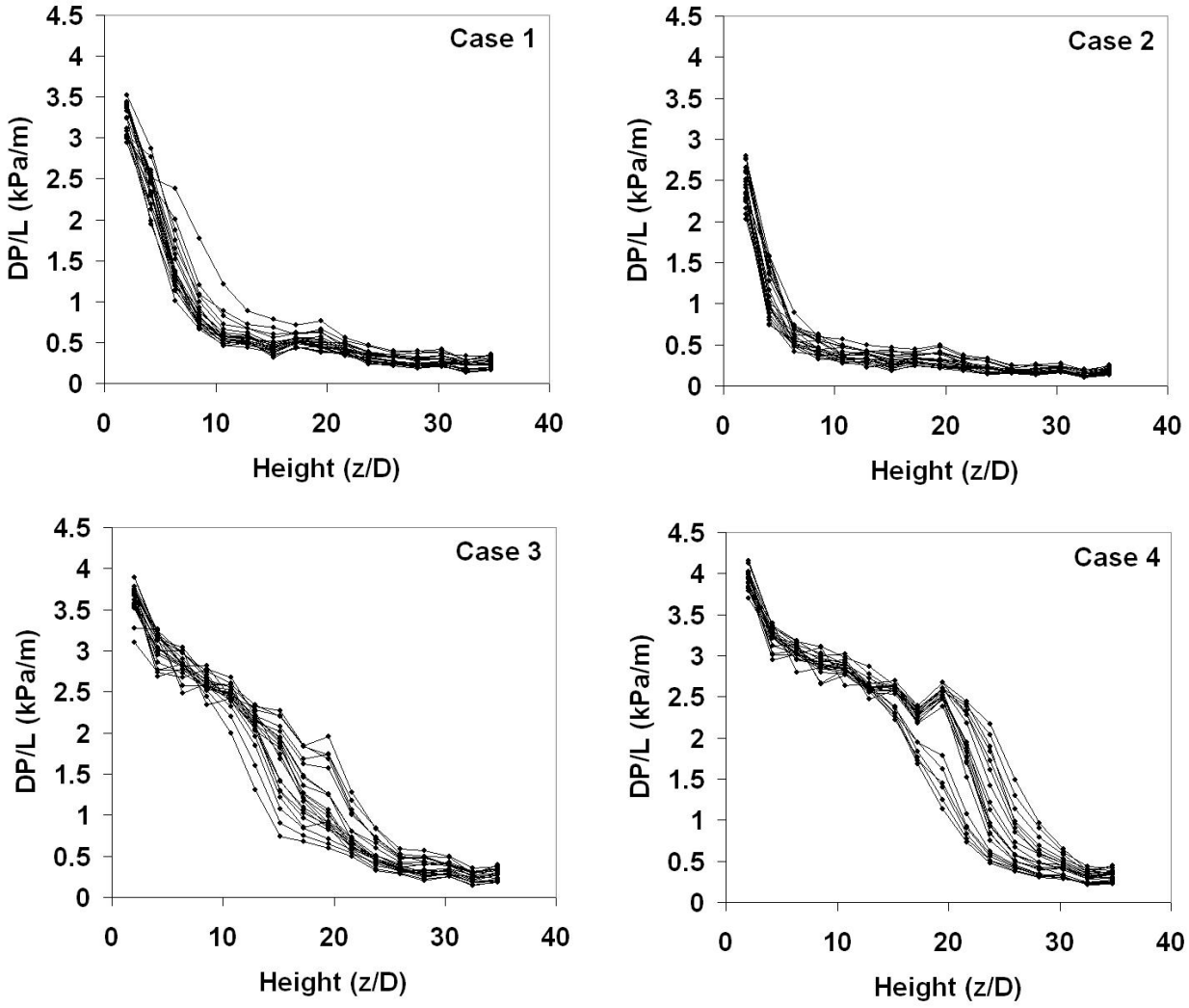

Figure 5.1. Differential pressure measured as a function of height along the riser for experiments with FCC catalyst. The conditions for the four cases shown are presented in Table 5.1; the multiple traces show repeat runs under nominally identical conditions.

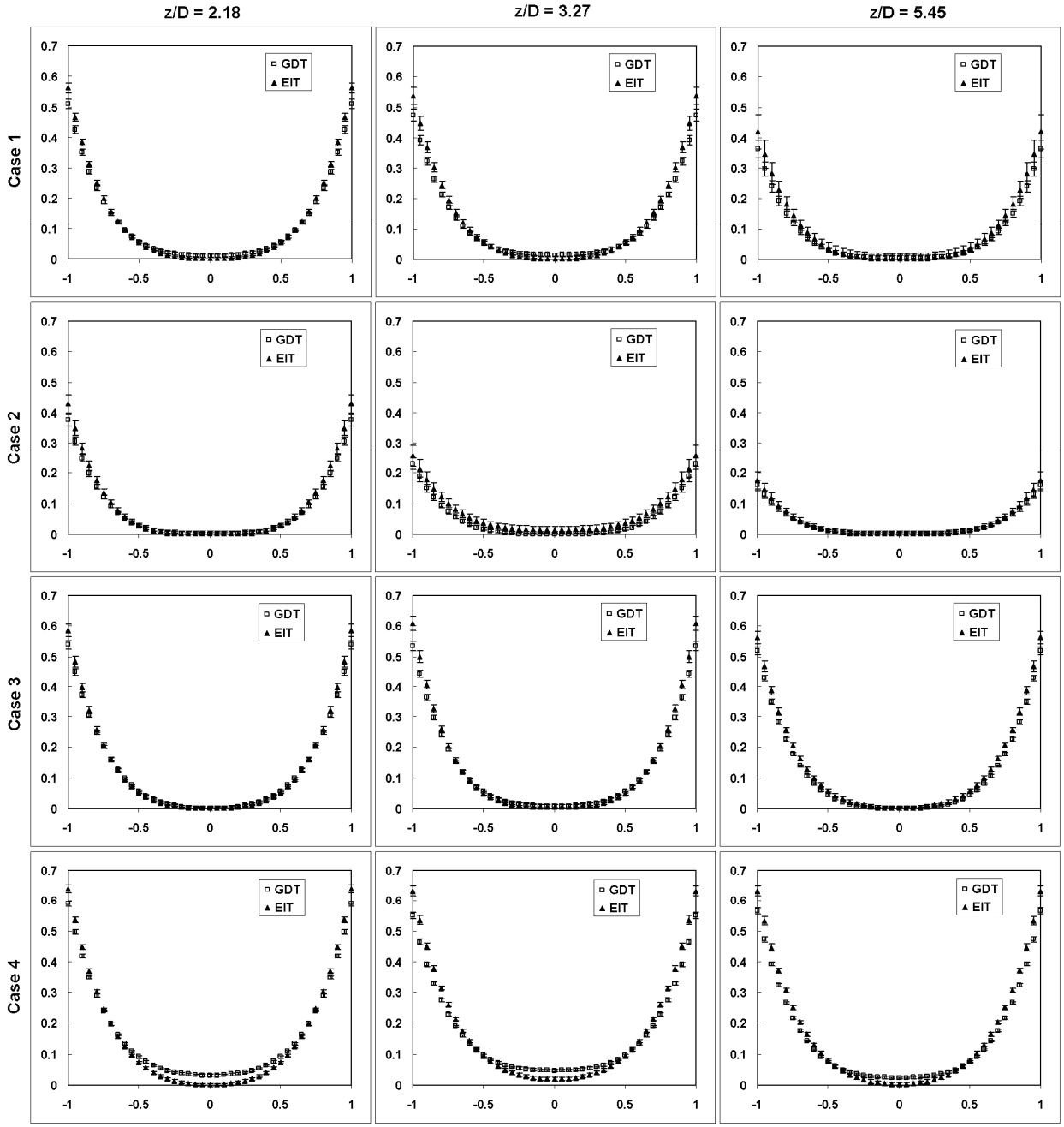

Figure 5.2. a) FCC catalyst solids volume fraction profiles obtained by EIT and GDT for riser axial locations *z/D* = 2.18, 3.27, and 5.45, for each of the 4 experimental conditions given in Table 5.1. Axes are solids volume fraction of FCC catalyst vs. dimensionless riser radius.

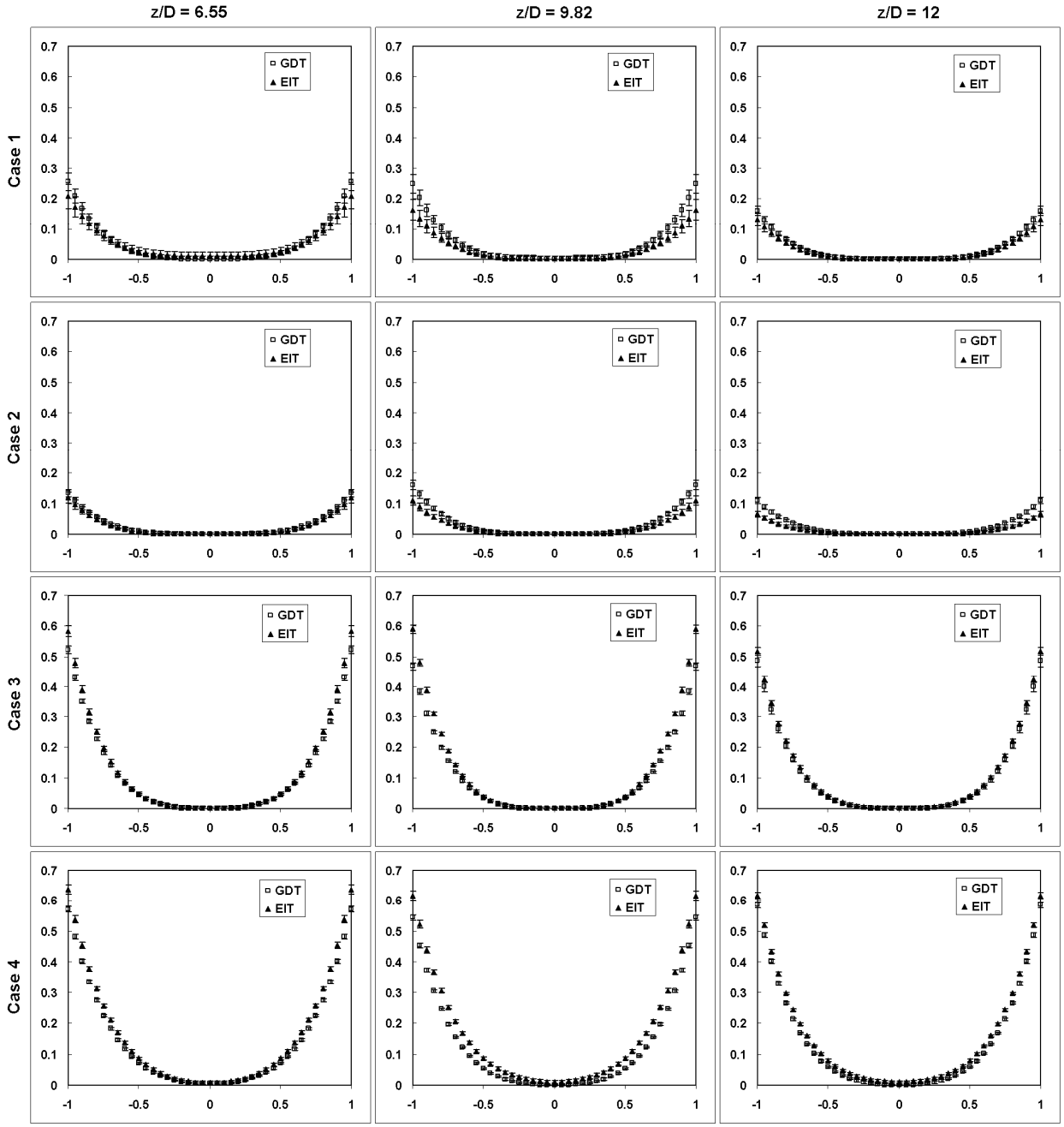

Figure 5.2. b) FCC catalyst solids volume fraction profiles obtained by EIT and GDT for riser axial locations *z/D* = 6.55, 9.82, and 12.00, for each of the 4 experimental conditions given in Table 5.1. Axes are solids volume fraction of FCC catalyst vs. dimensionless riser radius.

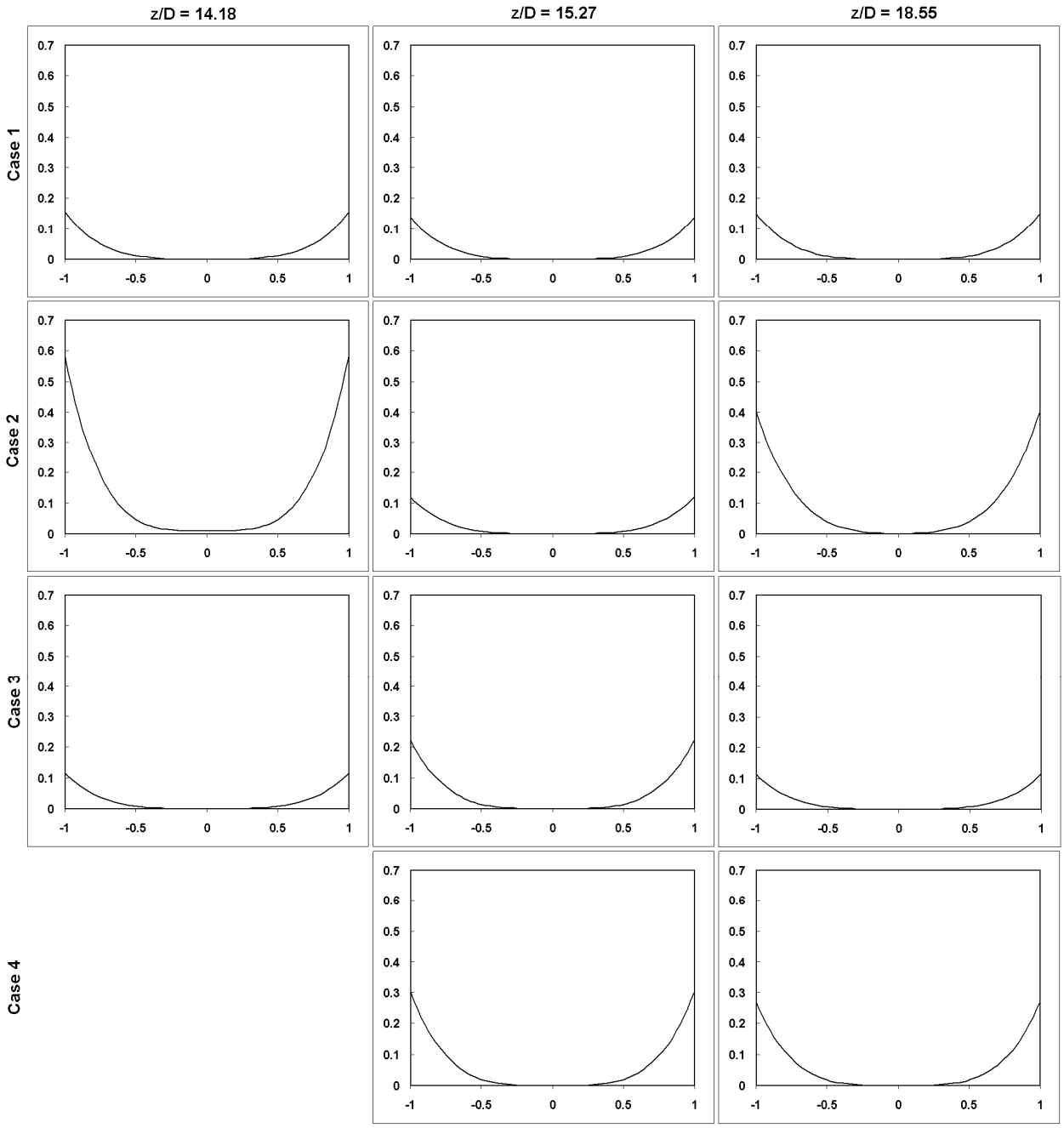

Figure 5.3. a) FCC catalyst solids volume fraction profiles at higher riser locations than Figure 5.2, obtained by GDT only, for z/D = 14.16, 15.27, and 18.55.

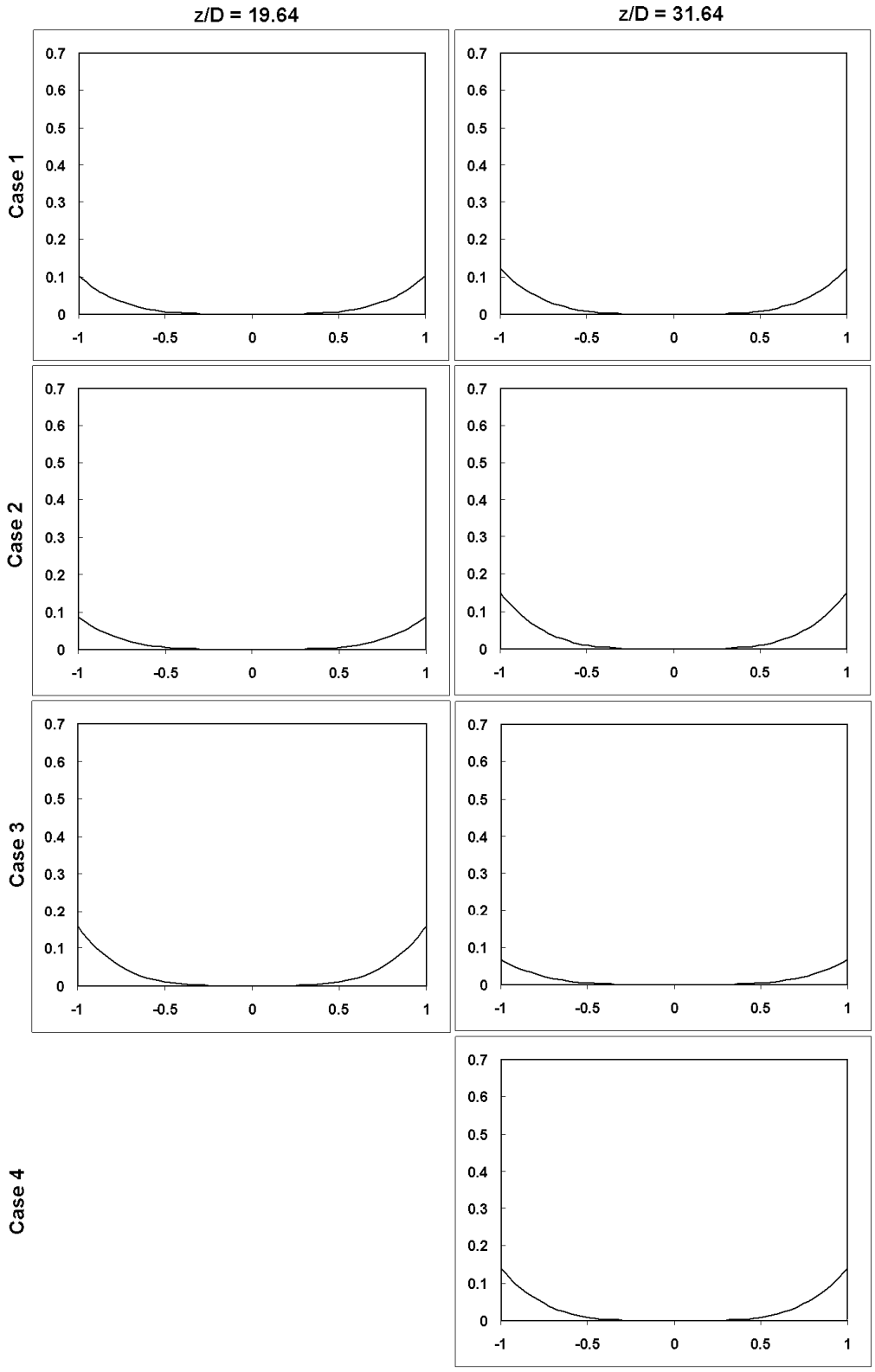

Figure 5.3. b) FCC catalyst solids volume fraction profiles at higher riser locations than Figure 5.2, obtained by GDT only, for z/D = 19.64 and 31.64.

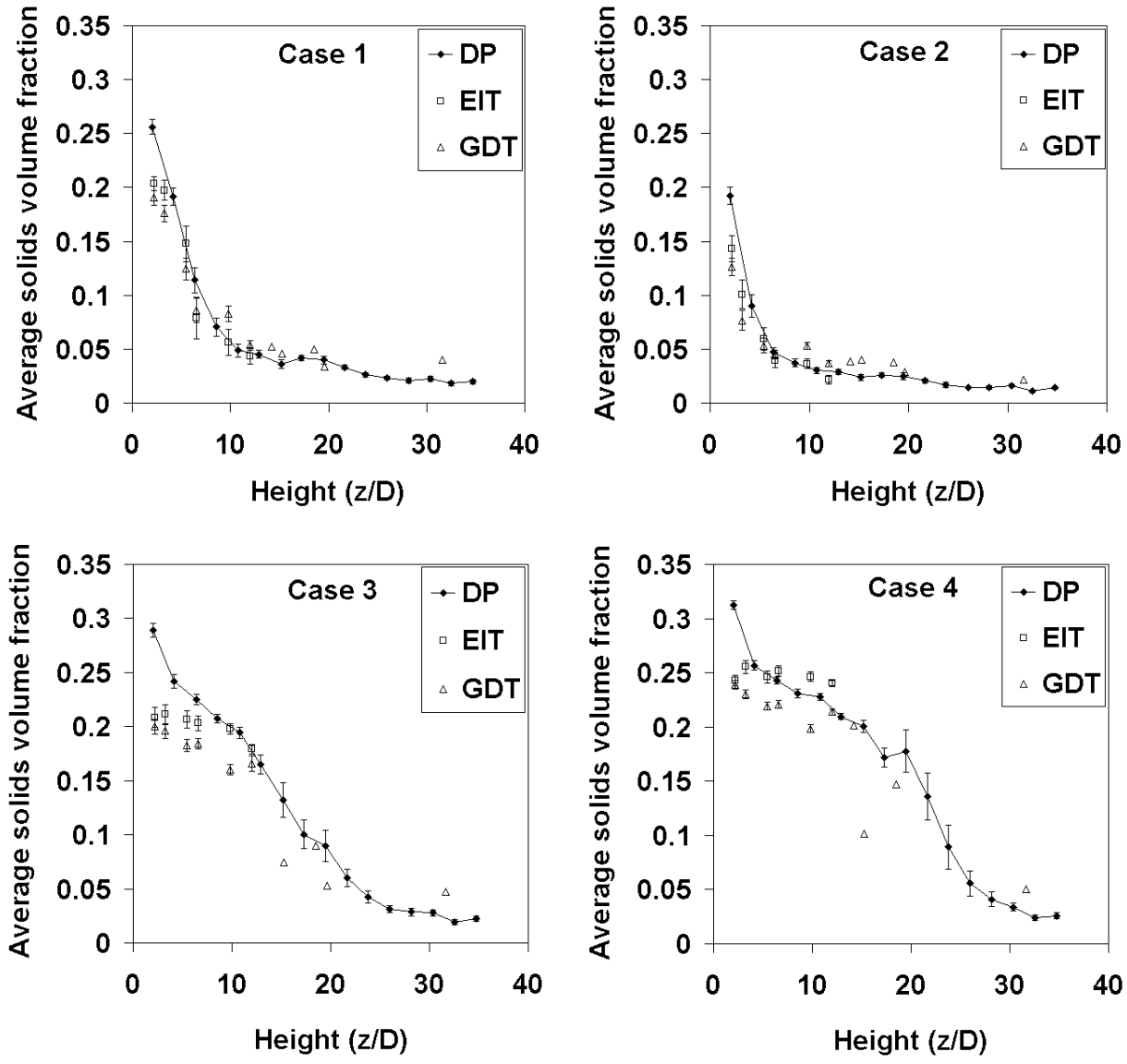

Figure 5.4. Cross-sectionally averaged solids volume fraction vs. dimensionless riser height for DP, EIT, and GDT.

Table 5.2. Results for each case in Table 5.1 at heights measured above the top of the riser engagement section: cross-sectionally averaged solids volume fractions from DP (Eq. (4.5.7)), GDT and EIT, coefficients for average GDT and EIT profiles, and average R^2 values.

Height (z/D)	$(1 - \phi)_{DP}$		$(1 - \phi)$	$f(r)$ coefficients			R^2
				a_0	a_2	a_4	
Case 1							
2.18	0.251 ± 0.007	GDT	0.191 ± 0.007	0.010	0.086	0.414	0.949
		EIT	0.203 ± 0.006	0	0.096	0.466	0.938
3.27	0.218 ± 0.008	GDT	0.176 ± 0.008	0.014	0.051	0.408	0.918
		EIT	0.197 ± 0.010	0	0.110	0.427	0.951
5.45	0.146 ± 0.010	GDT	0.124 ± 0.010	0.003	0.009	0.352	0.950
		EIT	0.148 ± 0.016	0	0.047	0.373	0.905
6.55	0.110 ± 0.011	GDT	0.086 ± 0.011	0.001	0.004	0.251	0.939
		EIT	0.079 ± 0.019	0.010	0.017	0.181	0.670
9.82	0.058 ± 0.007	GDT	0.083 ± 0.007	0	0	0.249	0.928
		EIT	0.056 ± 0.012	0	0.011	0.056	0.697
12	0.047 ± 0.005	GDT	0.054 ± 0.005	0	0	0.161	0.903
		EIT	0.044 ± 0.007	0	0	0.131	0.641
Case 2							
2.18	0.184 ± 0.008	GDT	0.126 ± 0.008	0	0.008	0.368	0.909
		EIT	0.143 ± 0.012	0	0	0.430	0.901
3.27	0.132 ± 0.009	GDT	0.077 ± 0.009	0	0	0.230	0.832
		EIT	0.101 ± 0.014	0.013	0.039	0.204	0.788
5.45	0.065 ± 0.007	GDT	0.053 ± 0.007	0	0	0.159	0.907
		EIT	0.059 ± 0.010	0	0.004	0.172	0.735
6.55	0.047 ± 0.004	GDT	0.045 ± 0.004	0.001	0	0.133	0.794
		EIT	0.040 ± 0.007	0	0	0.119	0.577
9.82	0.033 ± 0.003	GDT	0.053 ± 0.003	0	0	0.160	0.833
		EIT	0.037 ± 0.005	0	0	0.110	0.624
12	0.029 ± 0.003	GDT	0.037 ± 0.003	0	0	0.110	0.834
		EIT	0.022 ± 0.004	0	0	0.065	0.571

Table 5.2 continued

Height (z/D)	$(1 - \phi)_{DP}$		$(1 - \phi)$	$f(r)$ coefficients			R^2
				a_0	a_2	a_4	
Case 3							
2.18	0.285 ± 0.007	GDT	0.200 ± 0.007	0	0.123	0.416	0.927
		EIT	0.209 ± 0.009	0	0.080	0.505	0.941
3.27	0.262 ± 0.007	GDT	0.196 ± 0.007	0.008	0.077	0.449	0.935
		EIT	0.211 ± 0.009	0.005	0.030	0.574	0.960
5.45	0.232 ± 0.006	GDT	0.182 ± 0.006	0	0.057	0.462	0.978
		EIT	0.207 ± 0.008	0	0.116	0.447	0.936
6.55	0.223 ± 0.005	GDT	0.184 ± 0.005	0	0.062	0.460	0.969
		EIT	0.203 ± 0.007	0	0.053	0.530	0.917
9.82	0.200 ± 0.005	GDT	0.160 ± 0.005	0	0.026	0.442	0.946
		EIT	0.198 ± 0.005	0	0.009	0.581	0.952
12	0.177 ± 0.007	GDT	0.166 ± 0.007	0	0.022	0.465	0.975
		EIT	0.179 ± 0.004	0	0.041	0.474	0.571
Case 4							
2.18	0.308 ± 0.004	GDT	0.239 ± 0.004	0.031	0.131	0.428	0.953
		EIT	0.243 ± 0.005	0	0.179	0.460	0.949
3.27	0.280 ± 0.004	GDT	0.230 ± 0.004	0.047	0.093	0.409	0.940
		EIT	0.255 ± 0.006	0.019	0.191	0.422	0.964
5.45	0.249 ± 0.004	GDT	0.219 ± 0.004	0.023	0.093	0.449	0.977
		EIT	0.246 ± 0.005	0.003	0.202	0.427	0.947
6.55	0.242 ± 0.003	GDT	0.221 ± 0.003	0.004	0.169	0.398	0.976
		EIT	0.252 ± 0.005	0.007	0.210	0.420	0.921
9.82	0.229 ± 0.003	GDT	0.198 ± 0.003	0	0.101	0.444	0.963
		EIT	0.246 ± 0.005	0.011	0.206	0.399	0.956
12	0.217 ± 0.003	GDT	0.214 ± 0.003	0	0.114	0.470	0.990
		EIT	0.240 ± 0.003	0.010	0.167	0.440	0.954

5.2 Glass Beads

Table 5.3 lists the run conditions for experiments performed using glass beads as the solid phase. The solids flux data in Table 5.3 were derived from solids collection using the diverter valve (see Section 4.6). Note that the glass bead cases were previously discussed in Section 4.7, where the solids fluxes listed were determined by tracking the radioactive particle during its flow through the angled standpipe into the base of the riser and converting its time of flight to a solids flux value, assuming packed-bed conditions in the standpipe. The solids flux values determined by the two techniques (diverter valve and time of flight) agreed to within the uncertainty of the diverter valve technique for all of the cases.

Figure 5.5 shows pressure data plotted against riser height for multiple experiments and the run conditions listed in Table 5.3. In general, there was less variation between nominally identical runs than with FCC catalyst as seen in Figure 5.1. GDT profiles for these experiments are shown in Figure 5.6. Note that the profiles show non-zero solids loadings near the riser center at the lowest riser height for all three cases. Figure 5.7 shows average solids volume fraction vs. riser height as in Figure 5.4 for FCC catalyst. As in Figure 5.3, these are single samples and there are no corresponding EIT data, so the data are shown as single curves without uncertainties.

Table 5.3. Test Conditions for glass beads. Uncertainty includes run-to-run variations.

Case Number	Superficial Gas Velocity U_g (m/s)	Solids Flux G_s (kg/m^2·s)
Case 1	5.49 ± 0.11	103 ± 26
Case 2	7.71 ± 0.13	134 ± 11
Case 3	5.56 ± 0.12	126 ± 15

Cases 1 and 3 were similar in that the same superficial gas velocity was supplied to the riser flow. However, Case 1 had reduced fluidization air supplied to the standpipe feeding solids from the downcomer to the engagement section relative to the more typical operating conditions of Case 3. Additionally, fluidization air was introduced through only three ports in Case 1. These modifications reflected an attempt to ensure that the standpipe was run as a packed bed to facilitate the time-of-flight mass-flux measurement technique. Because of the reduced fluidization, Case 1 exhibited regular slugging (slug period on the order of 10s of seconds). Case 2 was a faster, well-fluidized case, and like Case 2 was "normal" in terms of riser configuration.

Uncertainty estimates for both U_g and G_s here really reflect a measure of repeatability (as with, for example, the DP data). This is partly why the uncertainty in G_s is so much lower for Cases 2 and 3: significantly more G_s data were collected for these cases. Each ensemble of G_s data has significant scatter, even in a single CFB run in which many (~20) G_s measurements were made.

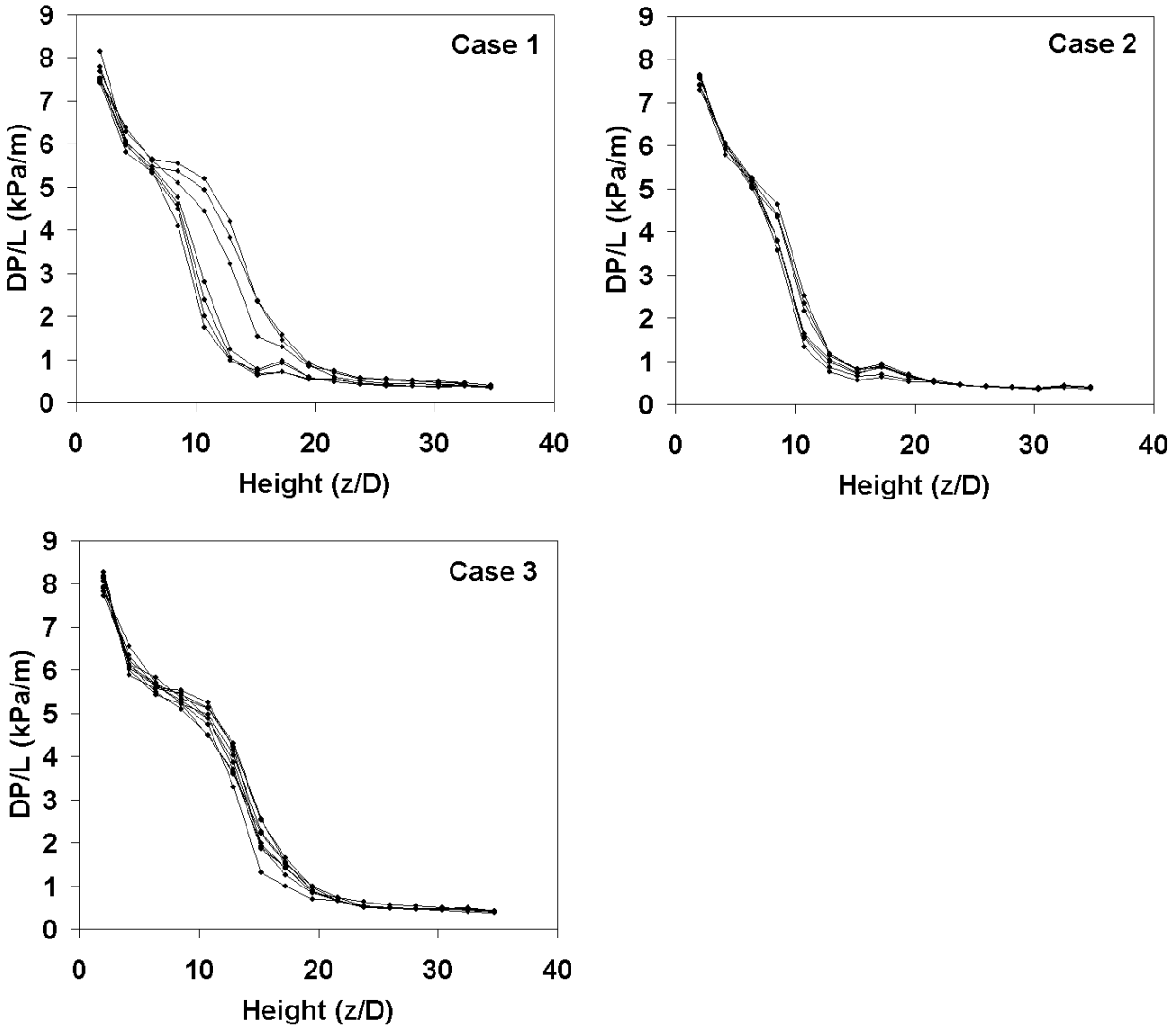

Figure 5.5. Differential pressure measured as a function of height along the riser for experiments with glass beads. The conditions for the three cases shown are presented in Table 5.3; the multiple traces show repeat runs under nominally identical conditions.

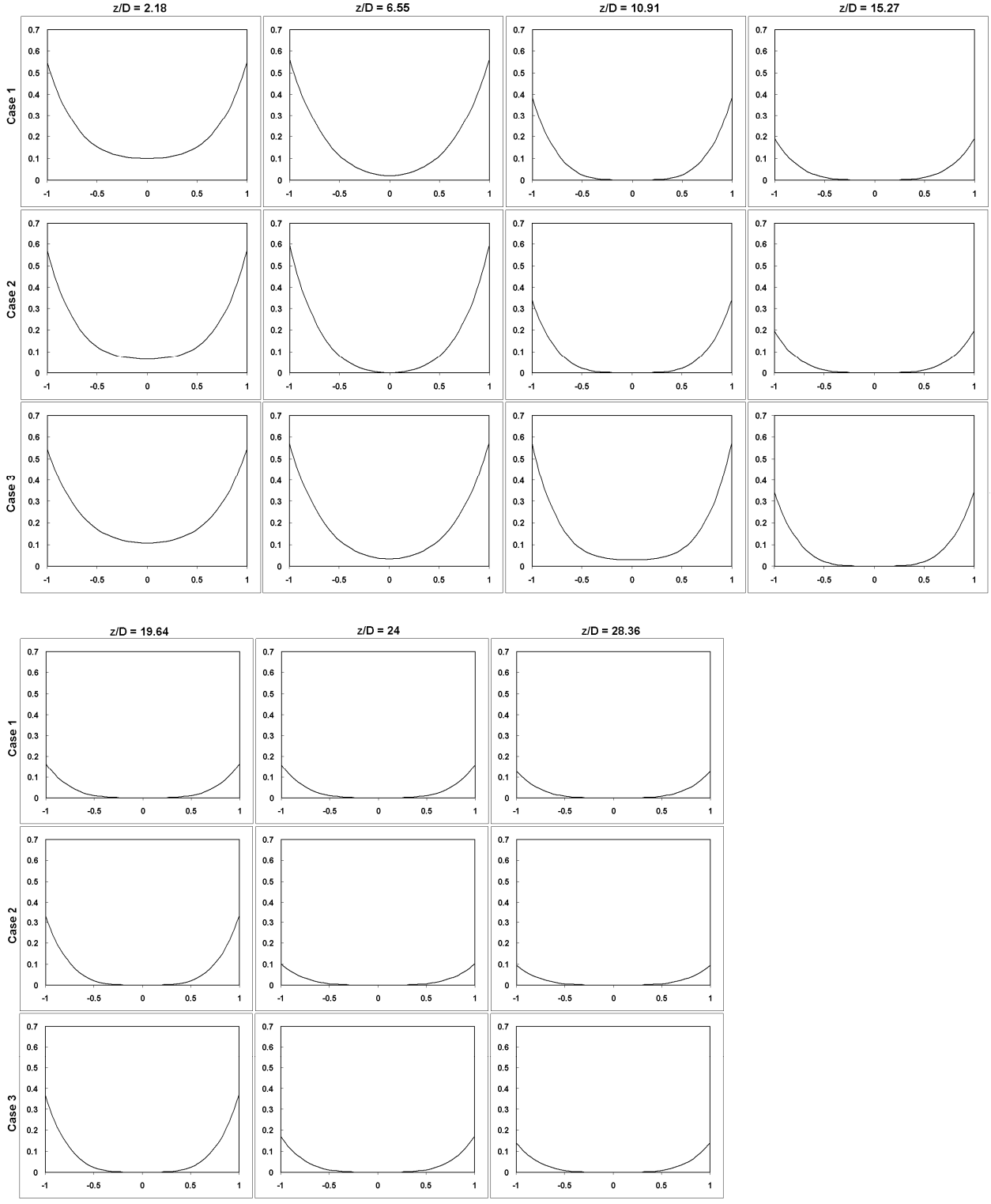

Figure 5.6. Complete set of glass bead solids volume fraction radial profiles obtained by GDT for different axial locations in the riser and for each of the three experimental conditions listed in Table 5.3. Axes are solids volume fraction of glass beads vs. dimensionless riser radius.

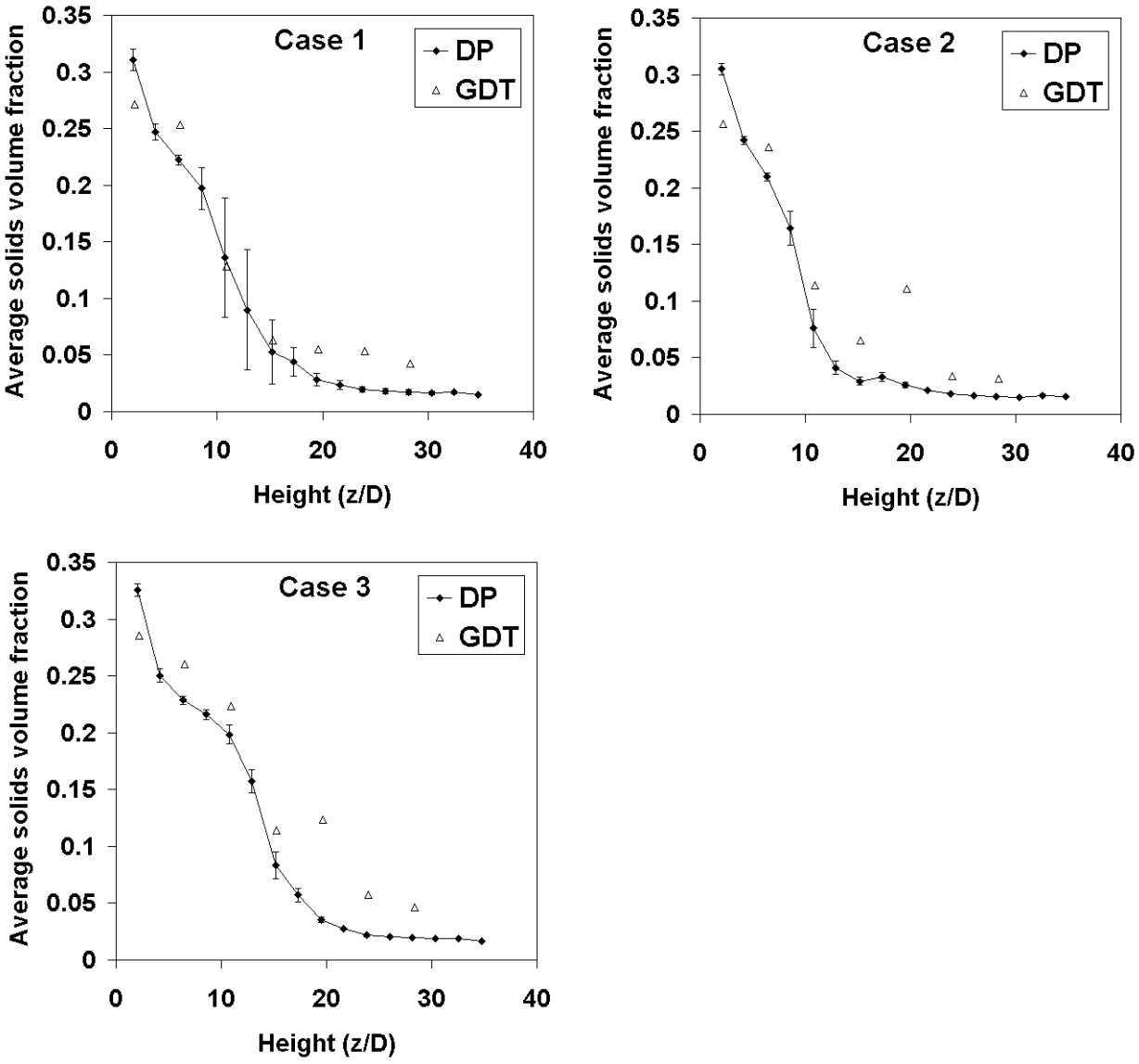

Figure 5.7. Average glass bead solids volume fraction vs. dimensionless riser height for DP and GDT; conditions for the cases are defined in Table 5.3.

6. Simulations

6.1 Overview

The gas-solid-riser experiment discussed in previous sections is briefly reviewed to emphasize details of particular relevance to computational modeling. The commercial gas-particle flow-simulation code *Arena-flow* is discussed with emphasis on the numerical method and its appropriateness for performing simulations of the gas-solid-riser experiment. The simplified geometry used in the simulations, consisting of the 45º standpipe, the engagement section, and the riser tube, and the reasons for these simplifications are discussed. The results from four baseline cases using fluid catalytic cracking (FCC) particles are presented. Important *Arena-flow* modeling parameters are identified, and the sensitivity of the baseline results to these parameters is investigated. Additional results are presented for glass beads, which are larger and denser than FCC particles.

6.2 Modeling Requirements for the Gas-Solid-Riser Experiment

The gas-solid-riser experiment, shown in Figure 6.1, is briefly reviewed. See Trujillo et al. (2001a) for more details. Motive air enters the engagement section via a vertical pipe (8.5-cm ID), a small amount of fluidization air enters the annular base of the engagement section (26.6-cm ID), and solid particles enter the engagement section from the right via the standpipe (7.6-cm ID). The motive air entrains some of the fluidized particles and transports them through the contraction at the top of the engagement section into the riser tube (14-cm ID). The gas-solid flow travels up the riser tube (5.77-m height) and exits the riser tube into the disengagement section, a large-diameter cylinder. The air exits the top of the disengagement section into two cyclones, the diplegs of which penetrate deeply into the downcomer (29-cm ID). The particles drain out of the base of the disengagement section via a dogleg into the downcomer. The downcomer is filled to a large fraction of its height with fluidized particles, which descend slowly. A slide valve between the downcomer and the standpipe controls the rate of solids circulation. The air from the cyclones and the downcomer is vented to a HEPA-filter bag house. Additional fluidization air is supplied along the standpipe and the dogleg. Humidified, filtered air at a pressure slightly above ambient is used in all experiments. Air flow rates, both motive and fluidization, are well characterized. Typical gas superficial velocities in the riser tube are 5-8 m/s.

Two types of solid particles are used in the experiments. Fluid catalytic cracking (FCC) particles, shown in Figure 6.2, are used for most of the experiments (Trujillo et al., 2001a). These particles can be approximately described by a log-normal size distribution with the 10% and 90% cutoffs occurring at diameters of 30 μm and 180 μm, respectively. The particles are porous and have a particle mass density of 1275 kg/m^3. Based on their size distribution and mass density, these particles are classified as belonging to Geldart Group A (Geldart, 1973). Glass beads, shown in Figure 6.3, are used in some of the experiments. These particles can be approximately described

by a normal size distribution with the 10% and 90% cutoffs occurring at diameters of 120 μm and 180 μm, respectively. The particles are solid and have a particle mass density of 2.5 g/cm^3. Based on their size distribution and mass density, these particles are classified as belonging to Geldart Group B (Geldart, 1973). Thus, both types of particles are fairly spherical but rather polydisperse.

Several experimental diagnostics are routinely applied to the gas-solid-riser experiment (Trujillo et al., 2001b; O'Hern et al., 2003; Tortora et al., 2003; Trujillo et al., 2004). Pressure is measured at a large number of locations throughout the system. The pressure measurements are performed differentially: pressure differences are measured between adjacent locations. These pressure differences are then summed to determine the pressure differences between nonadjacent locations. Most pressure taps are covered with porous metal to prevent particles from reaching the pressure gauges. This has the effect of applying a low-pass temporal filter to the pressure signals prior to their measurement. Vertical pressure profiles along the height of the riser tube are often interpreted using the hydrostatic assumption to estimate vertical distributions of solids volume fraction averaged over the riser-tube cross section. Profiles of solids volume fraction are measured using gamma-density tomography (GDT). A cesium-137 source provides gamma photons that are partially attenuated as they pass through the gas-solid flow. A traversable linear array of sodium-iodide scintillation detectors on the opposite side of the riser tube determines the transmitted fraction of the gamma photons at many lateral positions. A tomographic algorithm reconstructs the spatial distribution of material within the cross-section of the riser tube. The entire GDT apparatus can be translated vertically along the majority of the riser height. In practice, measurements are made at several locations. Because of the time required to accumulate sufficient gamma photons, the data recorded by GDT are essentially time-averaged (like the pressure measurements). Moreover, the GDT system has only one viewing angle. Therefore, an axisymmetric assumption (perhaps with tilt allowed) is made to convert the GDT measurements into profiles of solids volume fraction. Electrical-impedance tomography (EIT) has also been applied in a limited number of experiments, with results that are generally in harmony with the GDT and pressure measurements. Solids mass flux in the riser tube has been measured using a variety of sampling and optical probes, with limited success. The installation of a diverter system in the dogleg (see Figure 6.1) has enabled more reliable measurements of the average solids mass flux. Typical solids mass fluxes in the riser tube are in the range of 50-100 kg/m^2·s.

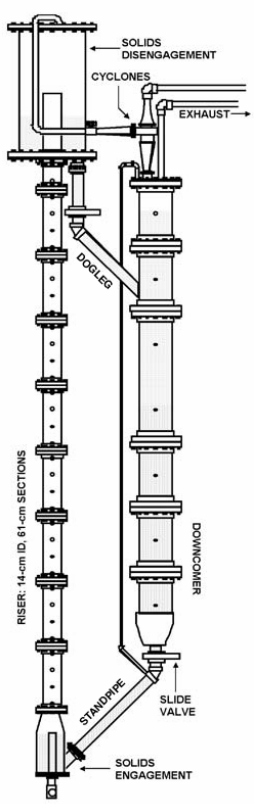

Figure 6.1. Schematic diagram of gas-solid-riser experiment.

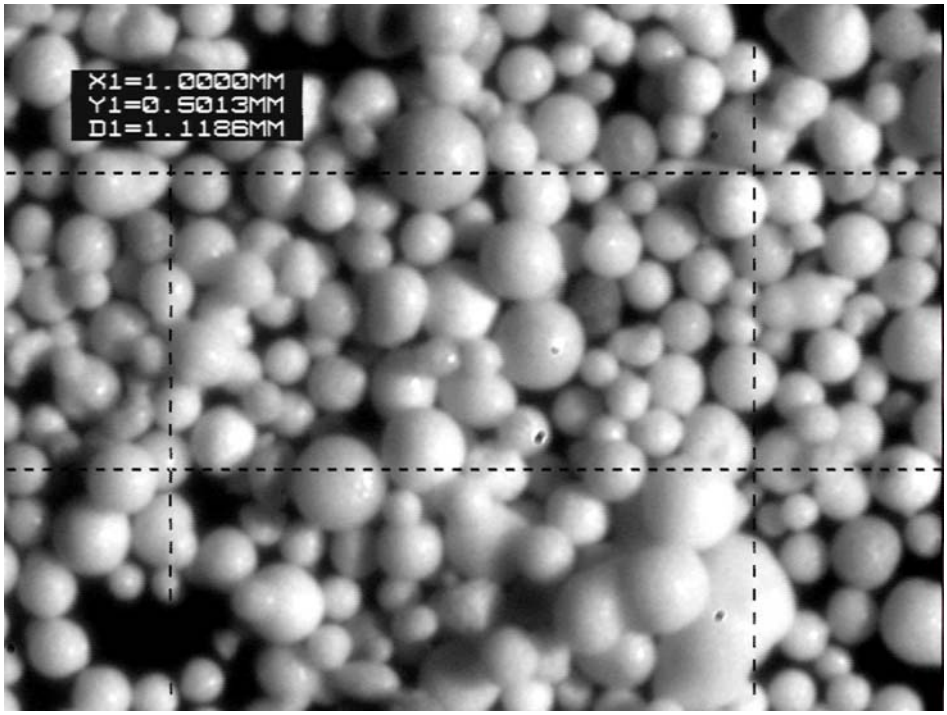

Figure 6.2. FCC particles used in many experiments. The center rectangle (dashed lines) is 1 mm x 0.5 mm.

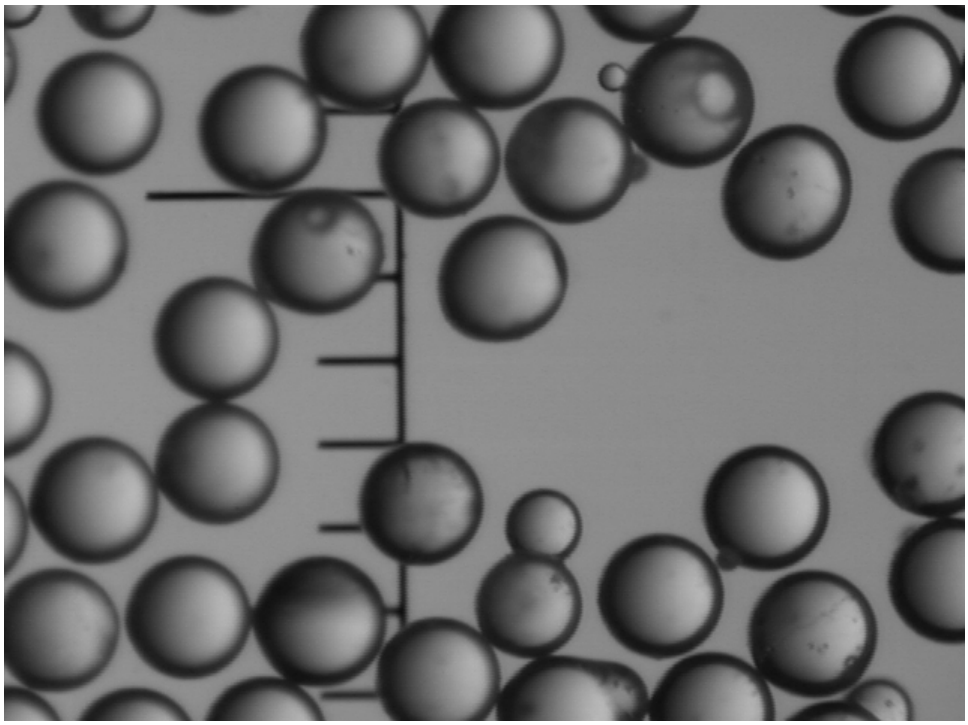

Figure 6.3. Glass beads are used in some experiments.

Typical experiments are performed as follows. A motive air flow rate is selected that produces a prescribed gas superficial velocity in the riser cross section, and the slide valve is opened to a prescribed position. A period of time is allowed for the starting transient to decay, and data are acquired. Typically, two values of gas superficial velocity and two values of solids mass flux are examined, yielding four combinations referred to below as the "baseline cases." In the experiments below, the gas superficial velocities are 5.3 m/s and 7.4 m/s, denoted "low" and "high," respectively. Measurements of the solids mass flux have proved more uncertain, but the "low" and "high" values are on the order of 50 kg/m^2·s and 100 kg/m^2·s, respectively. Figure 6.4 shows the pressure along the height of the riser for the four cases discussed above, and Figure 6.5 shows the corresponding solid-volume-fraction profiles measured at a height of 3.8 m using GDT. Increasing the gas superficial velocity while holding the solids mass flux fixed decreases both the vertical pressure gradient and the solids volume fraction. Increasing the solids mass flux while holding the gas superficial velocity fixed increases the vertical pressure gradient and the solids volume fraction. This is in harmony with the expectation that most of the vertical pressure gradient is produced by the weight of the particles. The pressure profiles are generally observed to have a sharp bend (a "knee") connecting two fairly linear regions. The solid-volume-fraction profiles indicate fairly large values adjacent to the walls and fairly low values near the axis (a core-annular type of profile).

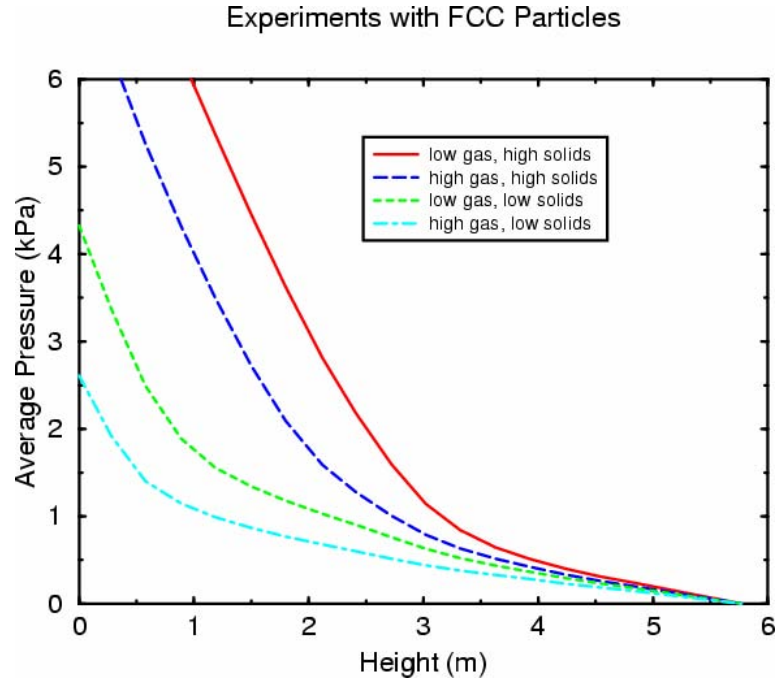

Figure 6.4. Experimental average pressure distributions with FCC particles for the four baseline cases.

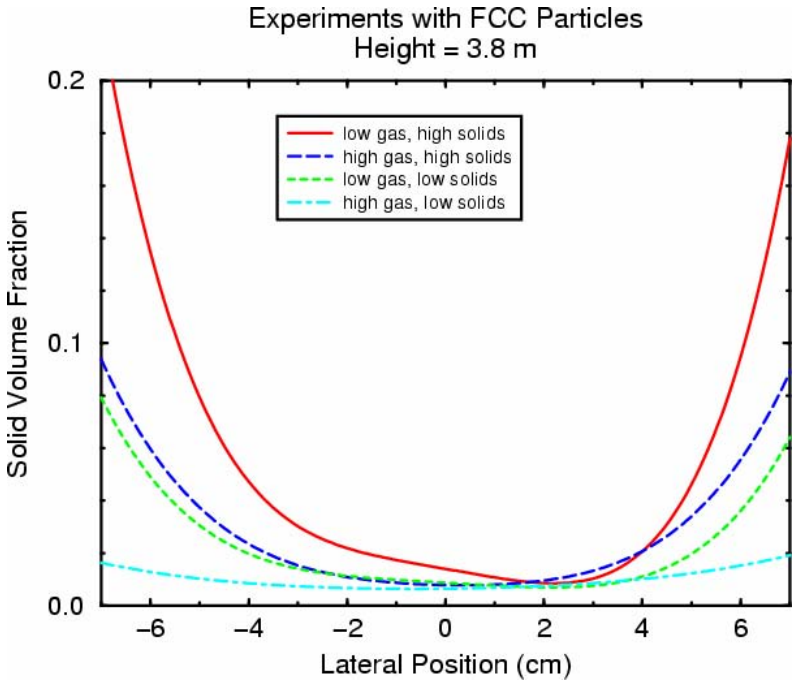

Figure 6.5. Experimental average solid-volume-fraction profiles with FCC particles for the four baseline cases.

Several modeling requirements arise from the above characteristics of the gas-solid-riser experiment.

1. The model must be able to treat complicated geometries. The flow geometry is quite complicated (see Figure 6.1) and includes the standpipe, engagement section, motive-air tube, riser tube, disengagement section, dogleg, downcomer, slide valve, and cyclone/venting system, as well as numerous taps for injecting fluidization air. Although not all of these components must be modeled in detail to investigate the flow in the riser tube, the model must represent the geometric complexity of the standpipe, motive-air tube, engagement section, and riser tube.

2. The model must be able to treat multiple injection locations for air (the standpipe, motive-air tube, and fluidization annulus in the engagement section).

3. The model must also be capable of allowing solid particles to enter and to exit the domain at multiple locations (the end of the standpipe and the top of the riser tube).

4. The model must represent particle loadings that range from dilute in the upper part of the riser tube to dense in the engagement section (a fluidized bed) and standpipe, as well as intermediate particle loadings.

5. The model must represent polydisperse particle-size distributions and should represent particle mass-density distributions, as well.

6. The model must contain appropriate representations of particle-gas, particle-wall, and particle-particle interactions.

7. The model must accept (complicated) geometry from some standard CAD or solid-modeling software.

8. The model must have extensive post-processing capabilities, including visualization, data output along slices and lines, and time-averaging, so that computational and experimental results can be compared.

9. The model must be capable of simulating the experiment with reasonable wall-clock times (say, less than a month).

6.3 Description of the *Arena-flow* Gas-Particle Simulation Code

The commercial gas-particle flow-simulation code *Arena-flow* meets all of the above requirements (Williams et al., 2002; 2003; 2004). *Arena-flow* treats complicated geometries with multiple locations for gas and particles to enter and exit. Particles can have fairly arbitrary distributions of size and mass density, particle loadings from dilute through dense are treated, and various models characterizing particle-gas, particle-wall, and particle-particle interactions are available. *Arena-flow* accepts complicated geometric information from stereolithography ("stl") files and uses the General Mesh Viewer (GMV) software for post-processing (Ortega,

1995). An advanced numerical method for gas-particle flows enables *Arena-flow* to simulate this type of flow with reasonable times (Andrews et al., 1996; Snider et al., 1998; Snider, 2001).

The multiphase particle-in-cell (MP-PIC) numerical method implemented in *Arena-flow* is specifically formulated for dense particle flows (Andrews et al., 1996; Snider et al., 1998; Snider, 2001). In this method, the carrier gas is treated as a continuum fluid (an Eulerian representation), whereas the particle phase is treated both as a continuum medium and as discrete entities (a Lagrangian representation). More specifically, particles are represented by discrete particle "clouds" that move and interact with the carrier gas and the walls of the domain in a Lagrangian manner, but interact with other particles by having their properties mapped to the Eulerian grid and then back to the particles. As a result, the MP-PIC numerical method is capable of treating gas-solid flows that range from dilute through dense. Moreover, the Lagrangian representation facilitates the direct incorporation of distributions of particle properties (e.g., size and mass density).

In the simulations below, the fluid phase is incompressible, both phases are isothermal, no interphase mass transfer is allowed, and agglomeration and fragmentation of particles are neglected. These restrictions are not inherent to the method but are representative of the gas-solid-riser flow: they can be removed for other applications (Snider et al., 2004). Fluid and particle quantities are denoted by the subscripts f and p, respectively.

The motion of the fluid is described by the corresponding continuity and momentum equations. The fluid continuity equation is given by

$$\frac{\partial \theta_f}{\partial t} + \nabla \cdot \left(\theta_f \mathbf{u}_f \right) = 0 \,, \tag{6.3.1}$$

where θ_f and $\mathbf{u}_f$ are the volume fraction and the velocity of the fluid, respectively. The fluid momentum equation is given by

$$\frac{\partial \left(\theta_f \mathbf{u}_f \right)}{\partial t} + \nabla \cdot \left(\theta_f \mathbf{u}_f \mathbf{u}_f \right) = -\frac{1}{\rho_f} \nabla p - \frac{1}{\rho_f} \mathbf{F} + \theta_f \mathbf{g} + \theta_f \left(\frac{\mu_f + \mu_t}{\rho_f} \right) \nabla^2 \mathbf{u}_f \,, \tag{6.3.2}$$

where ρ_f is the fluid mass density, p is the fluid pressure, $\mathbf{g}$ is the gravitational acceleration, μ_f is the fluid absolute viscosity, μ_t is a turbulent viscosity from an algebraic turbulence model, and $\mathbf{F}$ is the momentum transfer rate per unit volume from the fluid to the particles (Snider, 2001).

The motion of the particle phase is described in terms of particle "clouds" that represent the underlying particle probability distribution function (Andrews et al., 1996; Snider et al., 1998; Snider, 2001; Williams et al., 2002). Each particle cloud represents a fixed number N_p of identical particles, all of which have position $\mathbf{x}_p$, velocity $\mathbf{u}_p$, mass density ρ_p, volume V_p, and effective spherical radius

$$R_p = \left(3V_p / 4\pi \right)^{1/3} . \tag{6.3.3}$$

By virtue of the Lagrangian representation of the particles, mass is inherently conserved, so no particle continuity equation is solved. Nevertheless, on the Eulerian grid, the fluid and particle volume fractions are conserved according to

$$\theta_f + \theta_p = 1\,, \tag{6.3.4}$$

where θ_p is the particle volume fraction. The particle momentum equation is given by

$$\frac{d\mathbf{u}_p}{dt} = D_p\left(\mathbf{u}_f - \mathbf{u}_p\right) - \frac{1}{\rho_p}\nabla p + \mathbf{g} - \frac{1}{\theta_p \rho_p}\nabla \tau_p\,, \tag{6.3.5}$$

where D_p characterizes the fluid-particle drag and τ_p is the interparticle stress. Several models for fluid-particle drag are considered (Snider et al., 1998; Snider, 2001; Williams et al., 2002), including the Stokes relation, the Gidaspow model (Gidaspow, 1994), and the Ergun relation. The latter two models include the effects of finite Reynolds number and of the close-packed particle volume fraction θ_{cp}.

An isotropic interparticle stress model is used to describe collisions between particles, where the off-diagonal elements of the stress tensor are set equal to zero. In this approach, the interparticle stress is given by

$$\tau_p = \frac{P_s \theta_p^{\beta}}{\max\left(\theta_{cp} - \theta_p, 0\right) + \varepsilon}\,, \tag{6.3.6}$$

where P_s is a stress scale with units of pressure, β is a positive exponent (typically $2 \le \beta \le 5$), and $\varepsilon = 10^{-8}$ is included to prevent singular behavior if the solids volume fraction should exceed the close-packed particle volume fraction (e.g., during a fluctuation).

A sophisticated particle-wall interaction model is employed to describe reflections of particles from walls (Williams et al., 2003). This model allows for fairly general combinations of specular and diffuse particle reflections, the properties of which can depend on the incident velocity and angle of the particle.

A finite-volume method on a staggered Eulerian grid is used for the continuum equations. The details of this method have been reported elsewhere (Andrews et al., 1996; Snider et al., 1998; Snider, 2001; Williams et al., 2002). In brief, the fluid and the particles are implicitly coupled through the interphase momentum transfer. To determine this quantity, the fluid velocity is interpolated to particle positions, and the resulting force on particles is interpolated back to the grid. Conservative three-dimensional interpolation operators are employed (Snider, 2001). Similarly, because of the Lagrangian particle motion, volume is conserved, and advection-based numerical diffusion is absent. To ensure the satisfaction of fluid continuity when volume is conserved, a pressure-velocity error equation is formed from the fluid continuity equation and the momentum equations, and a SIMPLE type of solution is used to solve this equation (Snider et al., 2004).

The numerical method outlined above is implemented in *Arena-flow* in a transient, three-dimensional manner. Geometry specification is achieved via CAD drawings, and the *Arena-flow* grid generator transforms the geometry to control volumes (Snider et al., 2004). The resulting grid is body-fitted: numerical walls follow the physical geometry. Because of the Lagrangian nature of particle motion, the surface triangles and their associated unit normal vectors from the Eulerian mesh are used to ensure that the particles remain within the domain (Snider et al., 2004). Because the numerical solution is transient, averaging can be enabled after a prescribed amount of time. Simulation results are viewed with the GMV software package (Ortega, 1995).

6.4 Geometry for the Gas-Solid-Riser Simulations

The MP-PIC gas-particle flow-simulation code *Arena-flow* is used to simulate the gas-solid-riser experiment described above. Figure 6.6 shows the computational domain used in the simulations. The dimensions correspond to the experimental system described above (e.g., the riser tube has an inner diameter of 14 cm and a height of 5.77 m). The model in Figure 6.6 contains only a portion of the full experimental flow system: the standpipe, motive-air tube, engagement section, and riser tube are included, but the disengagement section, cyclones, dogleg, downcomer, and slide valve are not included. These latter components are not included for two reasons. First, the large-diameter disengagement section acts as a constant-pressure reservoir into which the gas and particles from the riser tube are exhausted. Second, the standpipe acts primarily as a particle supply for the engagement section and has relatively little effect on the flow behavior in the riser. These assumptions are examined in more detail below. Figure 6.7 shows portions of the computational mesh used for the simulations. Additional mesh-refinement simulations are performed on a mesh produced by dividing all elements in the riser tube in half along both cross-sectional directions (i.e., four times the original number of elements in the riser tube). No significant differences are observed between the original mesh and the refined mesh.

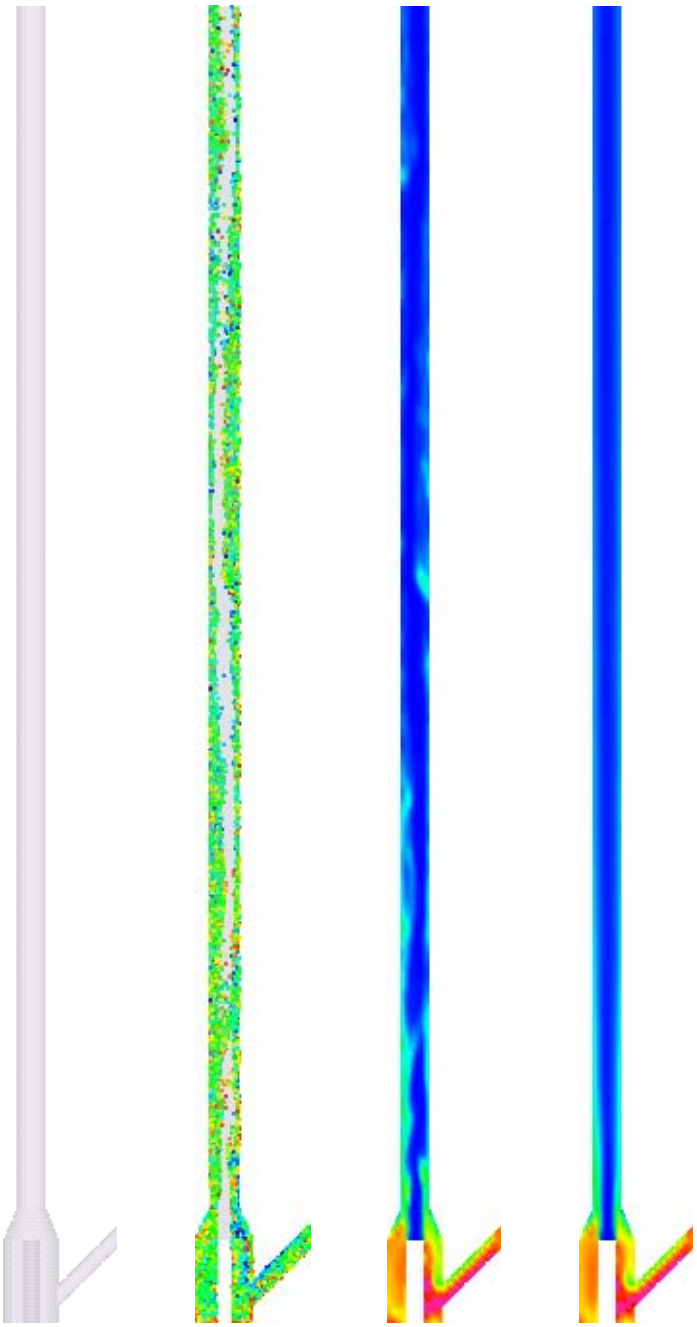

Figure 6.6. Domain, particles, instantaneous solids volume fraction, and average solids volume fraction.

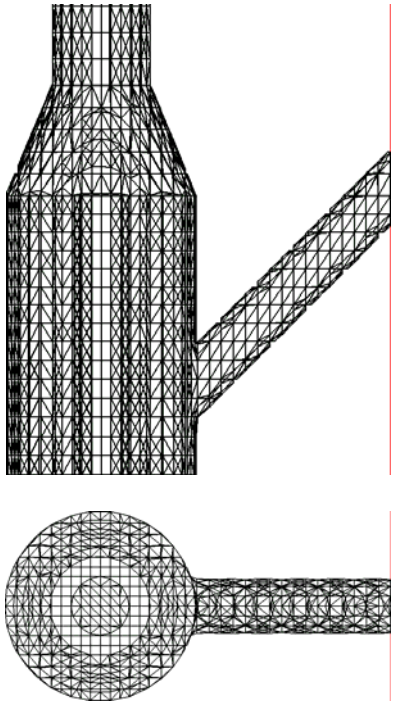

Figure 6.7. Computational mesh: side and top views.

6.5 Simulation Results for FCC Baseline Cases

The following physical and numerical parameters are used in the baseline simulations, with any departures for particular cases identified. The gas is ambient air, with a mass density of 1.093 kg/m^3 and an absolute viscosity of 1.9×10^{-5} Pa·s, and the particles are FCC catalyst with properties given above. The interparticle stress employs a close-packed particle volume fraction of 0.68, a particle-to-wall momentum-loss factor of 0.1, a specular-incident-angle coefficient of 1, and diffuse coefficient of 0 (Williams et al., 2002; Williams et al., 2003). A Gidaspow-type particle-fluid drag law is used, which includes particle-Reynolds-number and particle-volume-fraction effects (Gidaspow, 1994; Williams et al., 2002: Snider et al., 2004). The gravitational acceleration is downward with a value of 9.8 m/s^2. The time step is restricted to be no greater than 0.0015 m/s.

There are four non-wall boundaries that require boundary conditions. At the top end of the riser tube, the pressure is set equal to 0 (these simulations are incompressible, so the ambient pressure is subtracted from all pressures), and particles are deleted when they cross this plane. At the top of the motive-air tube, the gas velocity is set equal to a constant value in the vertical direction to produce a gas superficial velocity in the (empty) riser tube of either 5.3 m/s ("low" gas flow) or 7.4 m/s ("high" gas flow), and particles are not permitted to cross this plane. On the annular region at the bottom of the engagement section, the gas velocity is set equal to a constant vertical value, typically 0.06 m/s (above minimum fluidization), and particles are not permitted to cross this plane.

The elliptical boundary at the right side of the standpipe is more complicated because particles are introduced in this region. A small constant horizontal gas superficial velocity u_f is prescribed at this boundary. In all computational cells adjacent to this boundary, the particle volume fraction is constrained to have a certain value θ_p, and the particle velocity is constrained to be 95% of the of the gas phase velocity, which yields an average particle volume flux in the standpipe of

$$\theta_p u_p = \frac{0.95\theta_p u_f}{\theta_f} = \frac{0.95\theta_p u_f}{1-\theta_p} . \tag{6.3.7}$$

The solids mass flux in the riser tube is simply the above volume flux multiplied by the particle mass density and the ratio of the standpipe elliptical area to the riser-tube cross-sectional area. Typically, riser-tube values around 50 kg/m^2·s ("low" solids flow) and 100 kg/m^2·s ("high" solids flow) are used in the simulations and are achieved by prescribing u_f values of 0.20 m/s and 0.25 m/s and θ_p values of 0.35 and 0.45, respectively. The prescribed value of θ_p is maintained by adding particles to a cell whenever the cell value falls below the prescribed value.

The following initial conditions are used. The gas is initially at rest, and the gas-flow boundary conditions are instantaneously applied at the first time step. Motionless particles are resident in the engagement section at near to the close-packed particle volume fraction and in the standpipe at a volume fraction comparable to the boundary condition described above.

Results are acquired at fixed intervals of 0.05 s throughout a total simulation time of 30 s, yielding 600 time planes. Two flux planes are placed in the domain to quantify the solids mass flux for comparison to the nominal value indicated above. One of these planes is just below the top end of the riser tube, and the other is just to the left of the right end of the standpipe. The solids mass fluxes from these planes are found to be statistically the same regarding long-time averages. Because the flux plane near the top of the riser tube illustrates the starting transient and its decay, results from this flux plane are reported below. A simulation of 30 s of riser operation requires approximately one week of run time on a high-end workstation. Figures 6.6 and 6.8 through 6.10 show *Arena-flow* simulation results for the baseline case of low gas flow and high solids flow. The other combinations of gas superficial velocity and solids mass flow are qualitatively similar.

Figure 6.6 shows results on a thin slice through the axis of the computational domain. Particle positions colored by particle diameter (blue and red denote diameters of 30 μm and 180 μm, respectively) are shown at a time of 30 s. The temporal variations inherent in the flow are evident and are captured by the Lagrangian particles. In particular, the gas travels upward along a sinuous path, with wisps of particles occasionally spanning from one side of the riser tube to the other. The smaller particles are located preferentially on the right side of the engagement section (the side connected to the standpipe). Figure 6.6 also shows the instantaneous solids volume fraction at 30 s and the solids volume fraction averaged over 5-30 s (blue and red correspond to values of 0 and 0.6, respectively). Again, the temporal variations in this flow are evident: wisps of particles are blown up the riser tube in a coherent fashion (this behavior is even more obvious in animations).

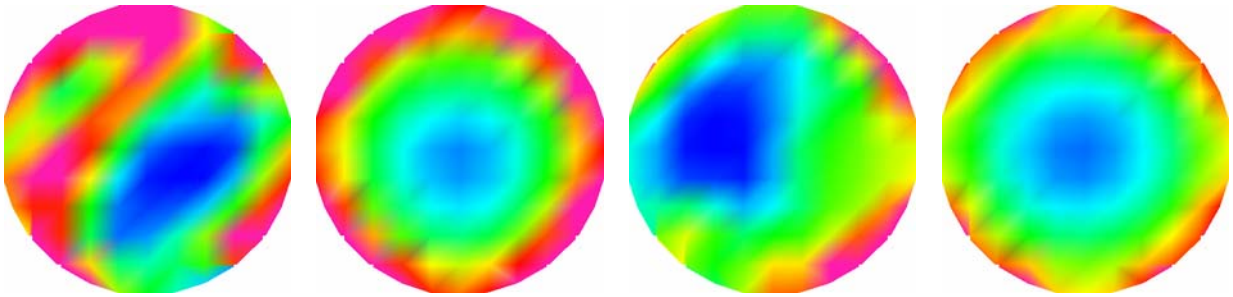

Figure 6.8. Difference between instantaneous and average solid-volume-fraction profiles.

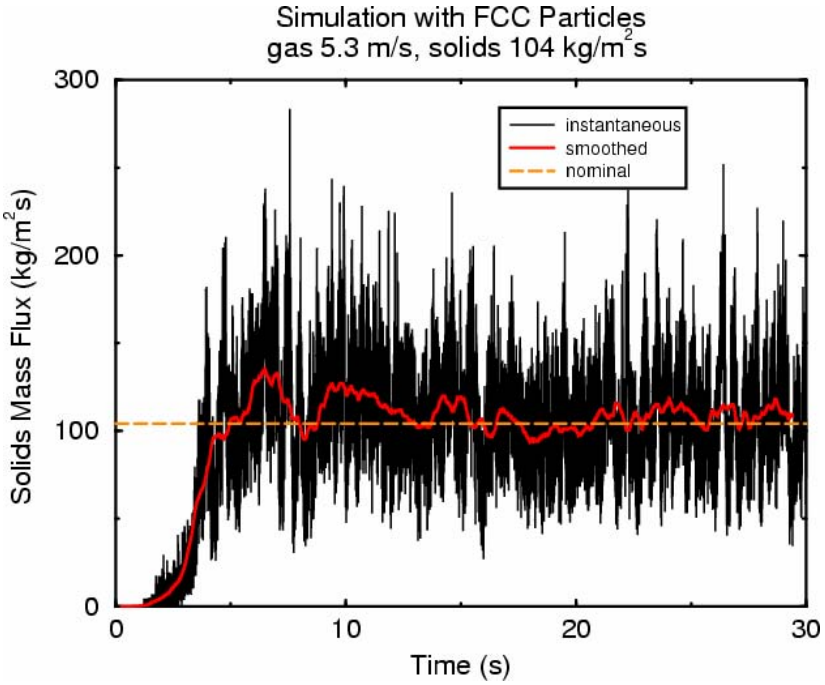

Figure 6.9. Computational solids mass flux with FCC particles for low gas flow and high solids flow.

Figure 6.8 shows results corresponding to those of Figure 6.6, but in a cross-section at heights of 2.0 m and 3.8 m above the engagement section. The color distribution has been rescaled from that of Figure 6.6 to illustrate the radial dependence of the solids volume fraction more clearly (blue and red correspond to values of 0 and 0.1, respectively). Plots of the instantaneous solids volume fraction at 30 s and the corresponding average over 5-30 s are shown at these two vertical locations. The decrease in solids volume fraction with height is clearly evident. The average solid-volume-fraction profiles are nearly axisymmetric (a slight imprint of the Cartesian mesh is evident), whereas the instantaneous profiles are strongly asymmetric, especially at the lower height. Nevertheless, both exhibit the core-annular nature of the flow: the air travels preferentially near the center of the riser tube, whereas the particles are located preferentially adjacent to the riser-tube wall.

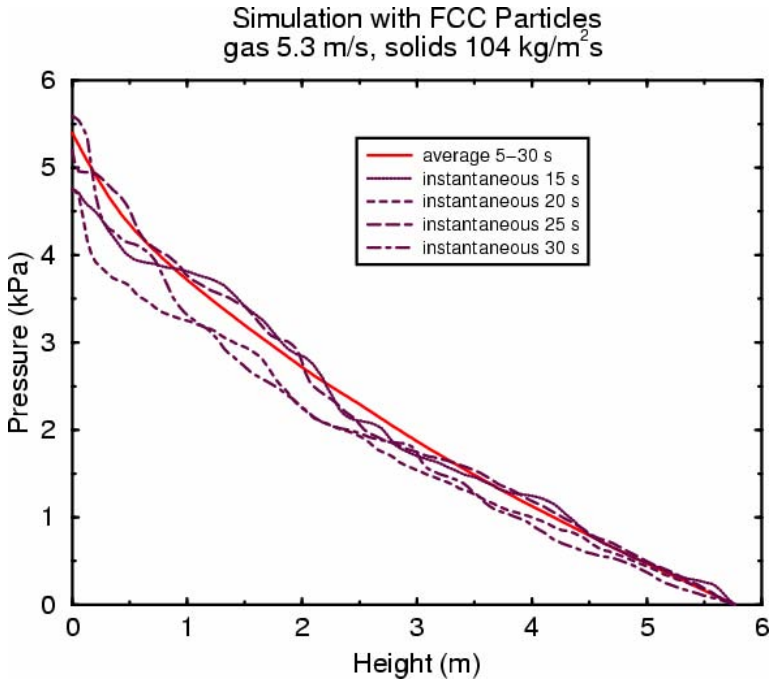

Figure 6.10. Computational pressure distributions with FCC particles for low gas flow and high solids flow.

Figure 6.9 shows the solids mass flux crossing the flux plane just below the top of the riser tube. The fluctuations in the instantaneous curve arise from two sources. First, discrete particles cross the flux plane, which produces discrete jumps in the solids mass flow. Second, the flow itself has a large degree of unsteadiness, as shown in Figures 6.6 and 6.8. When a wisp of solids crosses the flux plane, it produces a large but brief increase in the solids mass flux. A smoothed version of the instantaneous curve is generated by applying a running average with a duration of 1000 time steps. After about 5-15 s, the time required for flow transients to decay in the riser, this running average oscillates about the nominal solids mass flux produced by the boundary condition on the right side of the standpipe. This nominal value is shown for reference in the figure.

Figure 6.10 shows the pressure distribution along the height of the riser. Both the average value over 5-30 s and instantaneous values at 15, 20, 25, and 30 s are shown. The pressure at the height of 5.77 m (the top of the riser tube) is always equal to 0 by virtue of the boundary condition applied at this surface. The pressure grows slightly faster than linearly with distance below the top of the riser tube. The maximum pressure difference is 5 kPa (less than 6% of ambient pressure), indicating that the incompressible assumption is reasonably well satisfied. This pressure difference from the bottom to the top of the riser tube is in reasonable agreement (20%) with a value estimated from the weight of the solids suspended in the riser tube. The pressure fluctuations at a given height are typically 20% or less of the corresponding average value. Although not shown, pressure variations within the cross-section are extremely small compared to those along the height.

Figure 6.11 shows the average pressure for the four baseline combinations of gas superficial velocity and solids mass flux in the riser tube. If the gas superficial velocity is increased while the solids mass flux is held constant, the pressure gradient decreases in magnitude. Similarly, if the solids mass flux is decreased while the gas superficial velocity is held constant, the pressure gradient decreases in magnitude. These two trends are explained as follows. The pressure gradient is strongly correlated to the weight of suspended solids, which is reduced either by increasing the particle velocity by increasing the gas velocity or by decreasing the rate at which particles are injected into the riser by decreasing the solids mass flux.

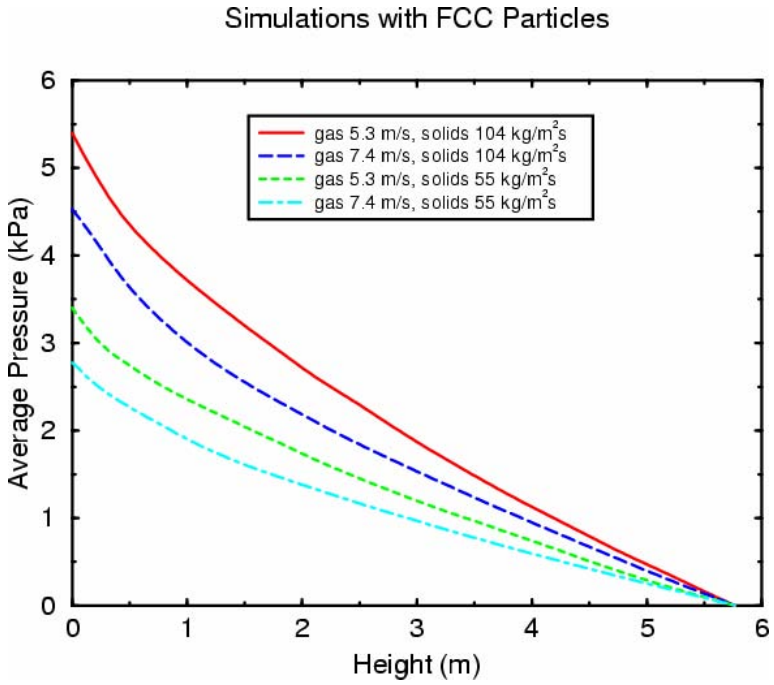

Figure 6.11. Computational average pressure distributions with FCC particles for the four baseline cases.

Figure 6.12 shows profiles of average solids volume fraction for the four baseline cases at a height of 3.8 m. In all four cases, the solids volume fraction is highest at the riser-tube walls and lowest near the axis. The effects of gas superficial velocity and solids mass flux are the same as for the previous figure: the larger the vertical pressure gradient, the larger the solids volume fraction. More specifically, decreasing the superficial gas velocity and increasing the solids mass flux both act to increase the solids volume fraction.

The simulation results in Figures 6.11 and 6.12 can be compared directly with the experimental results in Figures 6.3 and 6.4. The same overall trends and magnitudes are observed in both data sets. However, the experimental pressure profiles all exhibit a knee at heights in the range of 0.5 to 3 m, depending on flow conditions. The computational pressure distributions show enhanced upward concavity in the first 1 m but do not have knees. The experimental and computational solid-volume-fraction profiles are in qualitative agreement. However, in the lower portion of the riser tube, the experimental values are typically larger than the computational values. This

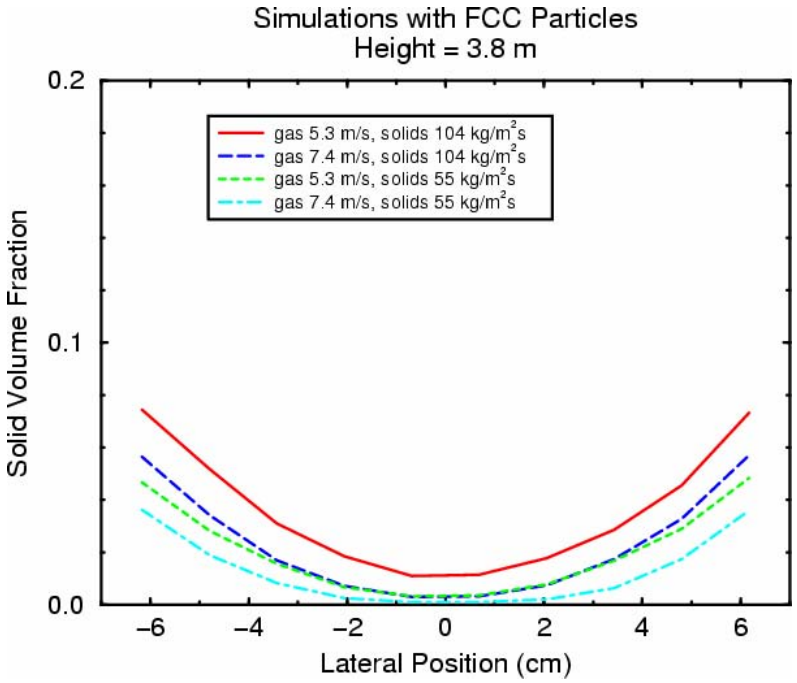

Figure 6.12. Computational average solid-volume-fraction profiles with FCC particles for the four baseline cases.

observation is in accord with the fact that the experimental pressure gradient in the lower portion of the riser tube is significantly larger than the computational pressure gradient in this region. Moreover, the computational solid-volume-fraction profiles are generally flatter than the corresponding experimental profiles, which exhibit rather large values near the riser-tube walls and quite small values near the riser-tube axis.

6.6 Sensitivity of FCC Results to Model Parameters

As previously discussed, although the computational and experimental results are in qualitative agreement, there are certain systematic differences between the two sets of results. In brief, the experimental results indicate larger solid-volume-fraction values in the lower portion of the riser tube, a larger difference between the near-wall and near-axis solid-volume-fraction values, and a knee roughly halfway up the riser tube, at which location the pressure and solid-volume-fraction vertical variations change significantly. Thus, it is important to assess the sensitivity of the computational results to the numerical method employed. More specifically, the effects of the following factors on the computational results are investigated, where, for each factor, simulations are performed at the low and high gas flow rates and at the high solids flow rate.

1. Standpipe boundary condition. The computational model uses a boundary condition to represent the standpipe. Simulations are performed in which the gas velocity at this boundary is halved and the particle volume fraction is correspondingly increased to maintain the same solids mass flux. No significant change in the computational results is observed in the riser tube.

2. Motive-air velocity profile. To ascertain the effect of the motive air's velocity profile, simulations are performed in which half the motive-air tube is blocked while maintaining the same total motive air flow rate. While cross-sectional profiles are distorted within the first 1 m of the riser tube (total height of 5.77 m), this perturbation quickly "heals" and does not significantly affect the flow in the remainder of the riser tube.

3. Fluidization air. Simulations are performed wherein the fluidization velocity is varied by ±50% from the nominal value. Although the fluidized bed in the engagement section expands or contracts correspondingly by a slight amount, no significant difference is seen in the riser tube.

4. Particle mass density. Simulations are performed in which the particle mass density is decreased by 20% but the particle volume flux in the standpipe is increased correspondingly to keep the solids mass flux constant. No significant change is observed in the riser tube.

5. Particle-gas interaction. Simulations are performed using the three different drag laws discussed above. Some effects are seen in the fluidized bed (wherein these drag laws differ the most), but no significant change is seen in the riser tube.

6. Particle-wall and particle-particle interaction parameters. Simulations with various combinations of these parameters, including fully specular and fully diffuse wall reflections and minimum and maximum particle-particle momentum transfer, are performed. Fully specular walls yield only slightly smaller pressure gradients than fully diffuse walls. Although there are slight changes and the trends are in the expected directions, the changes are much smaller than the difference between the experimental and computational results in all cases.

7. Polydisperse particle-size distribution. Simulations are performed in which the broad particle size distribution (30-180 μm) is replaced with a narrow distribution around the mean value (100-110 μm). It is emphasized that this replacement is made for sensitivity assessment only, not because of uncertainty in the experimental particle size distribution. Although slight changes in the fluidized bed are observed that result from the greater difficulty in fluidizing monodisperse particles, no significant change is seen in the riser tube.

8. Particle mean size. Simulations are performed in which the original particle size distribution (30-180 μm) is replaced by alternate distributions with larger mean sizes (100-180 μm and 160-180 μm). It is emphasized that this replacement is made for sensitivity assessment only, not because of uncertainty in the experimental particle size distribution. Unlike the previous factors, the simulation results are observed to depend significantly on the particle mean size. As the particle mean size is increased while holding the gas superficial velocity and the solids mass flux constant, several changes are observed: the gradient and concavity of the vertical pressure variation both increase (see Figure 6.13), the solid-volume-fraction values adjacent to the riser-tube walls increase (see Figure 6.14), and the particle velocities near the riser-tube walls become negative (see Figure 6.15).

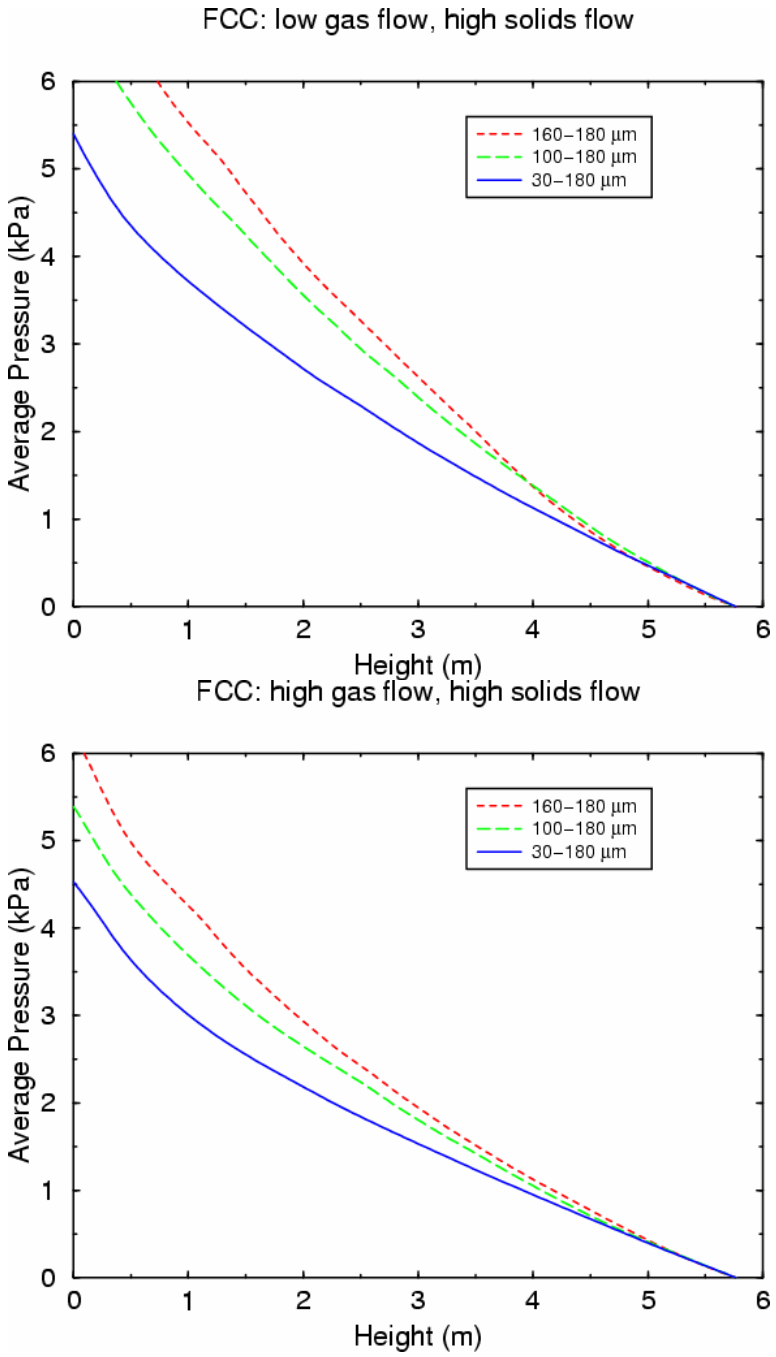

Figure 6.13. Average vertical pressure variation increases as particle mean size increases.

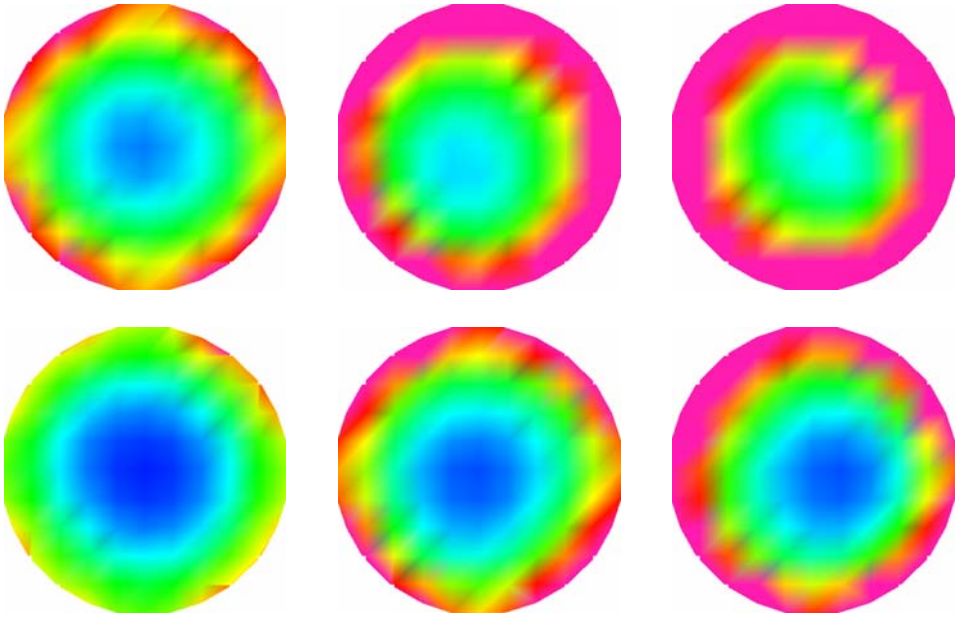

Left to right: 30-180 μm, 100-180 μm, 160-180 μm.
Top: low gas flow. Bottom: high gas flow. Blue: 0.0. Red: 0.1.

Figure 6.14. Average solids volume fraction near the wall increases as particle mean size increases.

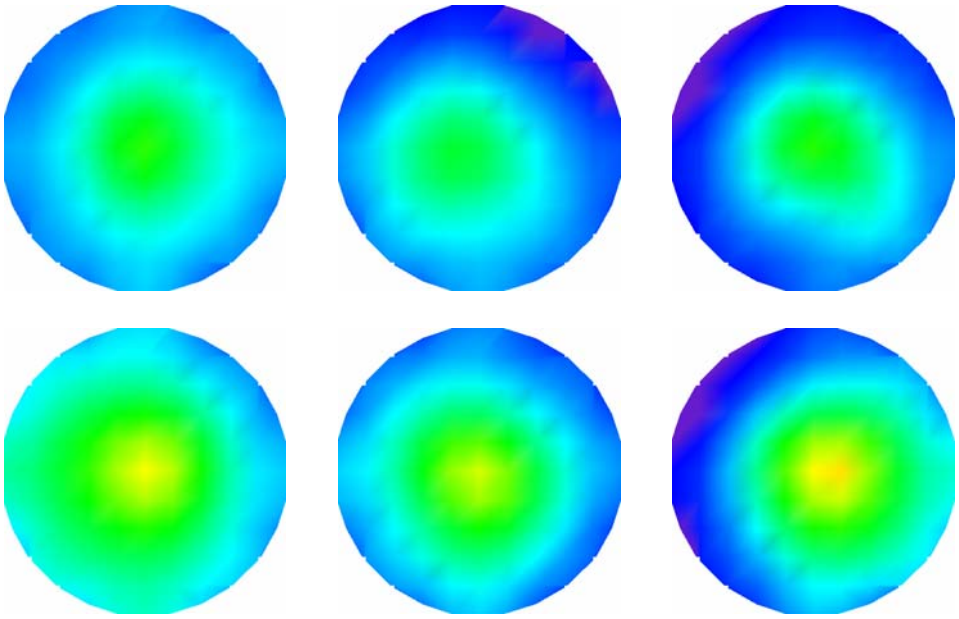

Left to right: 30-180 μm, 100-180 μm, 160-180 μm.
Top: low gas flow. Bottom: high gas flow. Purple: negative.

Figure 6.15. Average particle velocity near the wall becomes negative as particle mean size increases.

6.7 Glass Baseline Cases and Results

The baseline cases discussed above for FCC particles are simulated using glass beads. Figure 6.3 shows a photograph of typical glass beads. There are three principal differences between the glass beads and FCC particles. First, glass beads have a particle mass density of 2500 kg/m^3, compared to 1275 kg/m^3 for FCC particles. Second, glass beads have a particle size distribution in the range of 120-180 μm, compared to 30-180 μm for FCC particles. Thus, glass beads are heavier and lack the fines that are present in the FCC particles. Third, the close-packed particle volume fraction is 0.59, compared to 0.68 for FCC particles. Since these differences make glass beads more difficult to fluidize than FCC particles, the fluidization velocity at the base of the engagement section is increased from 0.06 m/s to 0.24 m/s. Approximately the same values of gas superficial velocity and solids mass flux are employed in the baseline cases: 5.3 m/s and 7.4 m/s (low and high gas flow), and 50 kg/m^2·s and 100 kg/m^2·s (low and high solids flow). It is noted in passing that increasing the particle mass density while holding the solids mass flux fixed decreases the solids volume flux.

Figure 6.16 shows the average pressure distributions with glass beads for the four baseline combinations of gas superficial velocity and solids mass flux in the riser tube. If the gas superficial velocity is increased while the solids mass flux is held constant, the pressure gradient decreases in magnitude. Similarly, if the solids mass flux is decreased while the gas superficial velocity is held constant, the pressure gradient decreases in magnitude. These two trends are as observed with FCC particles. However, the pressure gradient with glass beads is significantly greater than with FCC particles at corresponding conditions.

Figure 6.17 shows profiles of average solids volume fraction with glass beads for the four baseline cases at a height of 3.8 m. In all four cases, the solids volume fraction is highest at the riser-tube walls and lowest near the axis. The effects of gas superficial velocity and solids mass flux are the same as for the previous figure: the larger the vertical pressure gradient, the larger the solids volume fraction. More specifically, decreasing the superficial gas velocity and increasing the solids mass flux both act to increase the solids volume fraction. Again, this trend is as observed with FCC particles. However, the solids volume fraction with glass beads is appreciably greater than with FCC particles at corresponding conditions.

The glass-bead computational results in Figures 6.16 and 6.17 can be compared directly with the experimental results as they become available. Some sensitivity simulations are performed with glass beads and are in harmony with those previously discussed for FCC particles. More specifically, the computational results depend strongly on the gas superficial velocity in the riser tube and the solids mass flux in the riser tube but are rather insensitive to other parameters. Of course, the particle mean size and the particle mass density are clearly important, as indicated by the differences between FCC particles and glass beads (e.g., Figures 6.11 and 6.12 and 6.16 and 6.17).

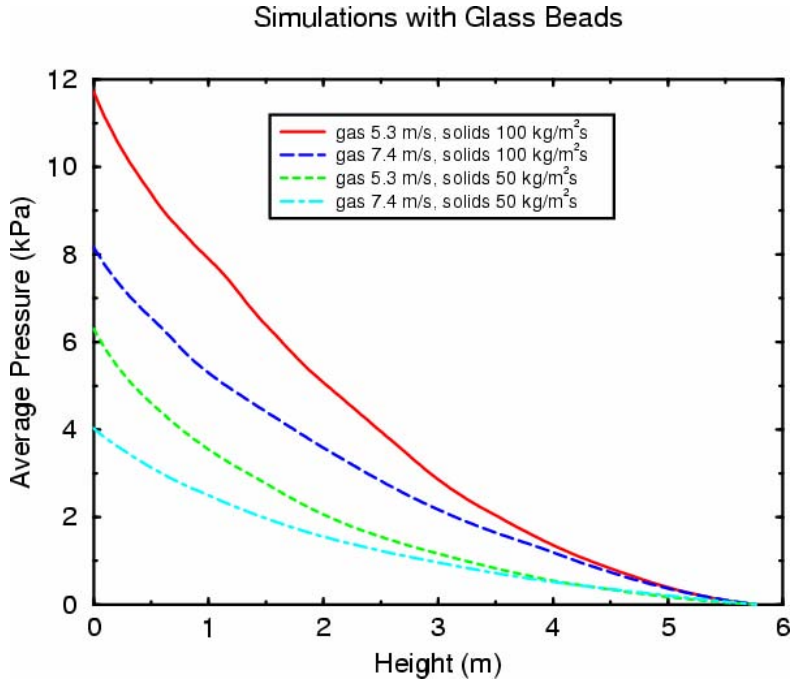

Figure 6.16. Computational average pressure distributions with glass beads for the four baseline cases.

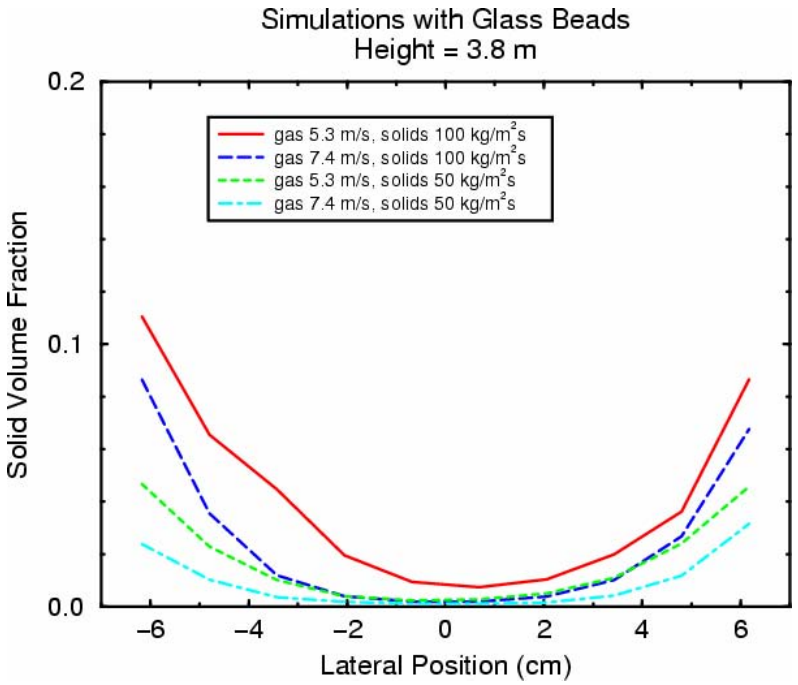

Figure 6.17. Computational average solid-volume-fraction profiles with glass beads for the four baseline cases.

6.8 Summary

The above investigation demonstrates that the *Arena-flow* results are robust and rather insensitive to values selected for most numerical parameters (e.g., the parameters governing particle-particle and particle-wall interactions). Moreover, the above results are well correlated in terms of four parameters: the gas superficial velocity in the riser tube, the solids mass flux in the riser tube, the particle mean size, and the particle mass density. It is possible that the latter two parameters can be combined into a single parameter (e.g., terminal velocity), but this has not been investigated. The computed variations of the pressure and solids volume fraction in the vertical and radial directions and in time and the dependence of these quantities on the gas superficial velocity and solids mass flux are in semi-quantitative agreement with the experimentally observed trends.

Curiously, increasing the particle mean size in the computations improves their agreement with the experiments. This improvement seems related to the increase in average solids volume fraction and the occurrence of negative values of the average particle velocity near the riser-tube walls that are observed when the particle mean size is increased. It is not suggested that the experimental particle size distribution is incorrect—the particle sizes can be verified visually and measured quantitatively with several techniques. Rather, these observations indicate that accurate modeling of the gas flow and the particle interactions in the near-wall region of a vertical tube is essential for obtaining good agreement with experimental results.

Based on these observations, the Arena-flow, LLC staff have recently developed a new code called *Barracuda* for computing gas-particle flows (Williams, 2006). *Barracuda* offers several improvements over the original *Arena-flow* software for computing riser flows. First, *Barracuda* implements gas-compressibility effects that are not included in *Arena-flow*. Second, the solver in *Barracuda* is much faster than the solver in *Arena-flow*, allowing a riser simulation to be performed in less than a day, rather than 6-8 days. Third, *Barracuda* includes an improved gas-turbulence model that produces more accurate pressure drops along the height of the riser. Fourth, *Barracuda* includes temperature and heat-transfer effects in the gas and particle phases, which are not included in *Arena-flow*. Fifth, the particle-stress formulation in *Barracuda* incorporates accurate information about the static and dynamic coefficients of friction of the particle phase. It is anticipated that these enhancements will improve the already-reasonable level of agreement between computation and experiment.

7. Conclusions

Sandia National Laboratories fabricated and operated a circulating fluidized bed (CFB) facility for the Multiphase Fluid Dynamics Research Consortium (MFDRC). The system has been operated with FCC catalyst and glass beads as the solid material, flowing with air as the fluidization and motive gas. Numerous design improvements implemented over the course of the program allowed the CFB to be operated smoothly and with relatively repeatable flow conditions. Specific improvements included the addition of an air bypass line to the particle return leg, better fluidization at the base of the downcomer, improved cyclone return diplegs, and addition of a reliable solids flux measurement system.

Diagnostics used on the CFB included pressure measurements throughout the flow loop, gamma-densitometry tomography (GDT), electrical-impedance tomography (GDT), solids flux suction probe, fiber-optic voidage probe, bulk solids flux via diversion to a weigh chamber, computer aided radioactive particle tracking (CARPT), and optical techniques. Some of these techniques, though in common usage in CFB research, were shown to have problems when used to measure high-accuracy data sets, as needed for validating and improving computational models.

This report summarizes key aspects of the experimental facility, diagnostics, and data. Wherever possible, "lessons learned" are included. Data sets acquired during the program are included in this report. Radial profiles of solids volume fraction as a function of axial location in the riser show that the core-annular flow regime is found in this flow for all of the flow conditions examined. The area-averaged solids loading decreases with increasing height along the riser, with the dense-to-dilute transition occurring at various axial locations depending on the flow conditions. EIT and GDT results were generally in good agreement for both radial profiles and area-averaged solids loading, but the average solids loading determined from pressure measurements generally gave higher values than those obtained by EIT and GDT low in the riser. This is thought to be due to three-dimensional flow effects near the base of the riser.

Major accomplishments of this program include:

1. **Circulating Fluidized Bed (CFB) operational:** A gas-solid CFB was developed and operated that was of sufficient size and could be operated under conditions that were industrially relevant. Most of the diagnostics were focused on the riser section of the CFB.

2. **Gamma-Densitometry Tomography (GDT):** A GDT system was designed and assembled for use on the riser, including a tall vertical traverse for axial movement along the riser. GDT was applied to measure radial profiles of the solids volume fraction under different flow conditions.

3. **Electrical-Impedance Tomography (EIT):** EIT was developed and validated against GDT. The good agreement between EIT and GDT is remarkable given the fact that the systems are independent from one another and determine solids volume fractions by measuring totally different material properties. This suggests that, where feasible, EIT

can be used in place of GDT, which is advantageous because EIT is safer, less expensive, and potentially faster.

4. **Computer Aided Radioactive Particle Tracking (CARPT):** Previous CARPT implementations had been in bubble columns or in gas-solid risers operating under low solids flux conditions. The implementation of the WUStL CARPT system in these experiments extended CARPT to higher solids flux conditions. Detailed reporting of these results is done elsewhere; the data included here are intended only to demonstrate that the technique was successfully implemented in this application.

5. **Data sets:** Tables 5.1 and 5.3 show the test conditions examined (combinations of gas and solids flux for FCC and glass beads, respectively). For each of these conditions, extensive pressure measurements were made around the CFB loop and axial and radial profiles of solids volume fraction were measured. Data sets can be used to test computational models. Readers interested in obtaining full data sets should contact one of the Sandia authors.

6. ***Arena-flow*™ simulations:** *Arena-flow*™ was applied to simulate the riser flow and to examine the sensitivity of varying parameters in the computational models. The simulations produced results that were in good general agreement with the experimental data.

Future work with this experimental facility is dependent on funding. We hope to continue acquiring data for different particle types and flow conditions. In addition, the facility can be reconfigured for examination of different flow geometries, for example different inlet conditions, effect of internals, different exit conditions, etc. As the data acquired in this facility are applied to validate and improve theoretical and computational models, we expect that other specific test cases will be identified that could best be run in this facility. In addition, we are open to collaboration when a testbed with this capability is needed for testing of new designs or diagnostics.

Appendix A. FIDAP Simulations for Electric Impedance Tomography

A.1. Overview

A FIDAP model of the 16-electrode electrical-impedance-tomography (EIT) system for the gas-solid riser is presented. This model relies on the analogy between electrostatics and heat conduction. An extrapolation technique is presented that enables electrical currents to be determined extremely accurately from results on a single coarse mesh. This technique forms an essential part of the EIT reconstruction method herein that uses DAKOTA to optimize the permittivity distribution and FIDAP to determine the corresponding electrode currents to compare to experimental measurements. Representative simulations indicate that the voltage field and electrode currents depend rather weakly on the conditions in the riser tube and that the experimental measurements must have a low uncertainty to enable different conditions to be distinguished.

A.2. Introduction

In support of the gas-solid-riser experiment to characterize turbulent, dense, gas-solid flows (O'Hern et al., 2004; Williams et al., 2004), an electrical-impedance-tomography (EIT) system is being used to characterize the material distribution in cross sections at selected vertical locations along the riser tube. In the gas-solid-riser experiment, gas and particles are injected at the base of the riser tube (14-cm ID, 5.7-m height) and flow vertically upward until reaching the disengagement section at the top. The gas is clean, humidified air. Two types of particles have been used: fluid catalytic cracking (FCC) particles (diameters of 30-180 μm, particle density of 1275 kg/m^3) and glass particles (diameters of 120-180 μm, particle density of 2500 kg/m^3). The riser tube is fabricated out of acrylic. Since all of these materials are dielectrics, EIT can be used to probe the material distribution during flow.

The EIT system operates as follows. In brief, 16 rectangular electrodes are placed adjacent to the exterior surface of the riser tube at equal azimuthal intervals, and a grounded cylindrical shield of somewhat larger diameter than the riser tube encloses the electrode region. An AC voltage is applied to one electrode (the "injection" electrode), the remaining electrodes are grounded, and the currents flowing through these electrodes are measured (the currents to the shield and from the injection electrode are not measured). Each of the 16 electrodes is successively selected as the injection electrode. A numerical algorithm is used to "reconstruct" the permittivity distribution from the measured currents. A constitutive relation between the flow permittivity (capacitance) and the volume fractions and permittivities of the flow components is then used to convert the permittivity distribution into a material distribution. The best form of such a constitutive relationship appears to be problem-dependent and is the subject of ongoing research (Tortora et al., 2005).

The numerical reconstruction used in EIT has two main components. First, the currents that result from applying the injection voltage to each electrode in succession must be determined for a prescribed permittivity distribution. This is sometimes called the "forward" problem. In the present implementation, the computational fluid dynamics code FIDAP (Fluent, Inc., 1998) solves the forward problem using the analogy between low-frequency electrical response of capacitive materials and steady heat conduction. This analogy is described below. Second, the prescribed permittivity field must be "adjusted" in an attempt to minimize the difference between the computed and experimental electrode currents in the least-squares sense. This is sometimes called the "backward" problem. In the present implementation, the optimization code DAKOTA solves the backward problem (Eldred et al., 2002ab, 2003). Essentially, DAKOTA supplies FIDAP with a set of parameters describing the permittivity distribution, FIDAP computes the electrode currents, DAKOTA adjusts the parameters, and these iterations are continued until the best agreement possible is obtained between experiment and computation.

For EIT to be successful, it is therefore essential that the computed and experimental currents be of high accuracy. The sections below focus on how high-accuracy currents can be achieved from FIDAP simulations on relatively coarse meshes. Use of a coarse mesh is highly desirable because of speed considerations: DAKOTA typically calls FIDAP many times to optimize the permittivity distribution for a single experimental data set. The following sections describe the governing equations, their implementation in FIDAP, and an extrapolation technique that allows highly accurate currents to be determined from coarse-mesh simulations.

A.3. Governing Equations

The Maxwell equations describe general electrodynamic phenomena (Jackson, 1975). These equations are given below.

$$\nabla \cdot \mathbf{D} = \rho \,, \tag{A.1}$$

$$\nabla \times \mathbf{H} = \mathbf{J} + \frac{\partial \mathbf{D}}{\partial t} \,, \tag{A.2}$$

$$\nabla \cdot \mathbf{E} + \frac{\partial \mathbf{B}}{\partial t} = 0 \,, \tag{A.3}$$

$$\nabla \cdot \mathbf{B} = 0 \,. \tag{A.4}$$

In the capacitive situation under consideration, the domain consists of linear dielectric materials and perfect conductors (surfaces of constant voltage). All of these conductors are grounded except one, which has a voltage of amplitude V_E and frequency f (angular frequency $\omega = 2\pi f$). The frequencies considered here are extremely low: $fL << c$, where c is the speed of light in vacuum (3×10^8 m/s) and L is a length scale representing the geometry.

Under these conditions, the Maxwell equations simplify considerably. Since there are no magnetic or electromagnetic phenomena, the magnetic field vectors **B** and **H** are zero. Thus, Equation (A.4) is identically satisfied, and Equation (A.3) simplifies considerably in that the electric field **E** must be the gradient of a potential (the voltage V):

$$\mathbf{E} = -\nabla V \ . \tag{A.5}$$

Since the nonconducting materials are linear dielectrics, the displacement **D** and the electric field **E** are linearly related:

$$\mathbf{D} = \tilde{\varepsilon}\varepsilon_0 \mathbf{E} \ , \tag{A.6}$$

where $\varepsilon_0 = 8.854\times10^{-12}$ F/m is the permittivity of vacuum and $\tilde{\varepsilon} \geq 1$ is the relative permittivity of a dielectric medium. These relations, together with that fact that there is no free charge ($\rho = 0$), allow Equations (A.1) and (A.2) to be simplified considerably:

$$\nabla \cdot (\tilde{\varepsilon} \nabla V) = 0 \ , \tag{A.7}$$

$$\mathbf{J} = \tilde{\varepsilon}\varepsilon_0 \nabla \left(\frac{\partial V}{\partial t} \right). \tag{A.8}$$

Equation (A.8) assumes that the permittivity distribution does not change during the time of interest. The voltage V and the resulting charge flux **J** are oscillatory in time (and 90° out of phase) in this application, which allows a final simplification (quantities with tildes are nondimensional):

$$\mathbf{x} \equiv L\tilde{\mathbf{x}} \ , \ \nabla \equiv L^{-1}\tilde{\nabla} \ , \tag{A.9}$$

$$V \equiv \tilde{v} V_E \cos(\omega t) \ , \ \mathbf{J} \equiv \tilde{j}(\varepsilon_0 \omega V_E / L) \sin(\omega t) \ , \tag{A.10}$$

$$\tilde{\nabla} \cdot (\tilde{\varepsilon} \tilde{\nabla} \tilde{v}) = 0 \ , \tag{A.11}$$

$$\tilde{\mathbf{j}} = -\tilde{\varepsilon} \tilde{\nabla} \tilde{v} \ . \tag{A.12}$$

Equations (A.11) and (A.12) are mathematically analogous to the equations of steady heat conduction, with the normalized voltage $\tilde{v}$, the normalized charge flux $\tilde{\mathbf{j}}$, and the relative permittivity $\tilde{\varepsilon}$ directly corresponding to the temperature, the heat flux, and the thermal conductivity, respectively.

A.4. FIDAP MODEL

The computational fluid dynamics code FIDAP (Fluent, Inc., 1998) can solve the equations describing steady heat conduction as well equation sets describing more complicated phenomena (e.g., fluid flow). Since Equations (A.11) and (A.12) are linear in the normalized voltage, only one "iteration" is required to determine the voltage field in the domain and the corresponding currents to the electrodes. FIDAP can treat multiple regions with different properties (e.g.,

permittivity). These properties can be constant in space (the default situation), or they can vary spatially (a user-defined Fortran subroutine is required in this case). FIDAP treats geometries of two and three dimensions. For convenience and clarity, the examples shown below are two-dimensional with a constant permittivity in each distinct geometrical region.

The geometry of the gas-solid riser is considered. Figure A.1 shows a schematic diagram of the riser tube, and Table A.1 delineates the geometric dimensions of the riser tube and the EIT electrode system. The riser tube has an ID of 5.5 inch (14 cm) and a wall thickness of 0.5 inch (1.27 cm) and is made out of acrylic ($\tilde{\varepsilon} = 2.76$). The 16 electrodes are mounted at equal azimuthal intervals around the exterior of the riser tube. In all examples below, the "large" electrodes, which are only slightly larger than the "small" electrodes, are used (see Table A.1). A hollow metal grounded shield with height equal to that of the electrodes and diameter slightly larger than the riser-tube OD, encloses the electrodes. The region between the shield's inner surface and the riser tube's outer surface is partially filled with air ($\tilde{\varepsilon} = 1$) and partially filled with acrylic support rings (see Table A.1). The region outside the shield is filled with air, and the region inside the riser tube contains the gas-solid flow ($\tilde{\varepsilon} \geq 1$).

Two two-dimensional computational domains are developed based on the riser-tube geometry. Figure A.2 shows these computational domains. The semicircular domain is appropriate only for purely radial permittivity distributions in the flow region: symmetry is imposed on the flat edge. The circular domain, however, can handle general two-dimensional distributions of permittivity. The outer radius of both computational domains corresponds to the inner radius of the shield. The electrode numbers used in later plots are exhibited. In the following examples, Electrode 0 always receives the applied voltage although this is not required for the circular domain. The materials in the flow, tube, and air/ring regions have the permittivity values indicated above (see Table A.1). Since the air/ring region is filled with two materials (see Figure A.1 and Table A.1), a parallel-capacitor approximation is used to select an effective permittivity for this region ($\tilde{\varepsilon} = 1.78$). If a more accurate value is known, it can be used without difficulty. The two-dimensional approximation employed here is somewhat marginal because of the shortness of the electrodes; however, this approach is not restricted to two-dimensional geometries.

Four computational meshes are examined for each domain. Figure A.3 shows these meshes. The labels refer to the degree of refinement employed to develop the mesh. More specifically, the meshes labeled "1" are the most coarse, and the meshes labeled "2", "3", and "4" are developed from the previous mesh by dividing the meshing length scale by the label number. In other words, the elements in Mesh 4 are roughly 1/4 the length and 1/16 the area of those in Mesh 1.

Three permittivity values are considered in the flow region. The value $\tilde{\varepsilon} = 1$ is referred to as "empty" because it corresponds to air alone in the riser tube (i.e., no solid particles). The values $\tilde{\varepsilon} = 2$ and $\tilde{\varepsilon} = 4$ are referred to as "half-full" and "full" because they approximately correspond to filling the riser tube with glass particles ($\tilde{\varepsilon} = 7$) to volume fractions that are half of randomly close packed and completely randomly close packed, respectively (Tortora et al., 2005).

Figure A.3 shows the permittivity distributions and the resulting voltage distributions determined by FIDAP on Mesh 4 for these three cases. Because all non-injection electrodes and the shield

are grounded, the voltage falls rapidly to small values away from the injection electrode. Somewhat surprisingly, the voltage distribution is almost independent of the flow permittivity. Figure A.3 also shows the normalized current per unit height flowing through each electrode for these cases:

$$\frac{\tilde{I}}{\tilde{H}} = \left(\frac{I}{\varepsilon_0 \omega V_E L} \right) \Bigg/ \left(\frac{H}{L} \right) = \int (\tilde{\mathbf{j}} \cdot \hat{\mathbf{n}}) d\tilde{l} \,, \tag{A.13}$$

where I is the current and H is the electrode height in the direction perpendicular to Figures A.1 and A.2. Three different plots are used to illustrate the effect of flow permittivity more clearly. As the flow permittivity is increased from 1 to 4, the current flowing out of Electrode 0 (the injection electrode) increases by about 11%. Since the permittivity is analogous to thermal conductivity, this result is not surprising. The injection current, however, is not measured in the experiments, so this dependence cannot be used to facilitate reconstruction. Surprisingly, the current to the nearest-neighbor electrodes is seen to decrease by only 4% as the permittivity is increased from 1 to 4. These currents, though measured experimentally, are only weakly sensitive to material distribution in the flow region. Electrode 8, located oppositely to Electrode 0 (the injection electrode), is the electrode whose current exhibits the greatest sensitivity to the flow permittivity: the current to Electrode 8 is almost proportional to the flow permittivity. However, the current to Electrode 8 is at most 0.6% of the current from Electrode 0. This disparity in magnitude means that the experimental measurements must be of high accuracy and precision to resolve this dependence.

A.5. Extrapolation Technique

The FIDAP ("uncorrected") electrode and shield currents for all three values of flow permittivity on all four semicircular meshes are shown in Tables A.2-A.4. Upon close scrutiny of these values, certain trends become apparent. All comparisons below are for the same flow permittivity.

1. The electrode currents increase by 2.4% from Mesh 1 to Mesh 2 and by 1.1% from Mesh 2 to Mesh 4. Given the fact that the currents to nearest-neighbor electrodes vary by only 4% as the flow permittivity varies from 1 to 4, even Mesh 4 is not refined enough.

2. The net current flowing into the domain should be zero but is appreciably nonzero. The net current does decrease with mesh refinement but rather slowly, similar to the above.

3. When the electrode currents from one mesh are divided by the electrode currents from another mesh, these ratios are equal to high precision. This is true even for Mesh 1. These ratios are almost identical for all flow permittivity values.

4. The shield current changes by 0.036% from Mesh 1 to Mesh 4 and is thus well resolved.

Upon reflection, the probable cause of these observations is the fact that the voltage field is weakly singular at the corners of the electrodes: the charge flux becomes infinite at the corner because the voltage gradient becomes infinite, but the current is finite because the singularity is integrable. Mesh refinement only improves the representation of the charge flux near the electrode corners. Since the electrodes and the mesh sections around them are identical, mesh refinement improves the computed current at each electrode by the same fraction. On the other hand, the shield (in two dimensions) has no corners. Thus, its current is virtually independent of mesh refinement.

These observations can be used to develop an extrapolation strategy that yields highly accurate currents even on coarse meshes. Denote the electrode currents computed on a particular mesh by $\{\tilde{I}_k\}$, where $k = 0,...,15$, and denote the shield current by $\tilde{I}_s$. Note that the injection current $\tilde{I}_0$ is of opposite sign from all the other currents (unlike in Tables A.2-A.4 and Figure A.3). Assume that the infinitely refined electrode currents are $\{C\tilde{I}_k\}$, where C is a constant, and that the infinitely refined shield current is $\tilde{I}_s$ (no factor of C). At infinite refinement, the currents must sum to zero:

$$C(\tilde{I}_0 + \tilde{I}_1 + \ldots + \tilde{I}_{15}) + \tilde{I}_s = 0 . \tag{A.14}$$

The electrode and shield currents can then be "extrapolated" to infinite refinement:

$$\tilde{I}_k^{\text{ext}} = C\tilde{I}_k , \; C = \frac{-\tilde{I}_s}{\tilde{I}_0 + \tilde{I}_1 + \ldots + \tilde{I}_{15}} ; \; \tilde{I}_s^{\text{ext}} = \tilde{I}_s . \tag{A.15}$$

Again, recall that the injection current $\tilde{I}_0$ is of opposite sign to the rest of the currents.

As well as showing the "uncorrected" currents from FIDAP, Tables A.2-A.4 also show the "extrapolated" currents from Equation (A.15) for all meshes and for all values of the flow permittivity. To reiterate, each set of extrapolated currents for a given mesh uses only the uncorrected currents on the same mesh. As can be seen from close scrutiny of these tables, the extrapolated currents are almost independent of mesh refinement. The extrapolated currents on Meshes 1 and 4 differ by only 0.2% for all three flow permittivities, indicating that even the most coarse mesh can produce highly accurate values. By way of contrast, the uncorrected currents on Mesh 1 and Mesh 4 differ from the corresponding extrapolated values by 4.6% and 1.3%, respectively. These errors are probably unacceptably large, given the modest effect of flow permittivity on electrode current.

Table A.1. EIT geometry (all lengths in inches) and parameters.

Region	Description
Riser tube interior (flow)	$r < 2.75$
Riser tube wall	$2.75 < r < 3.25$
Electrode rings	$3.25 < r < 4.4375$, $1.25 < \lvert z \rvert < 2.25$
Shield	$4.4375 < r < 4.58775$, $\lvert z \rvert < 2.25$
Electrodes: 16 "large"	$3.25 < r < 3.4370$, $\lvert z \rvert < 2.25$, $\Delta\theta = 8.824°$, $\Delta\phi = 22.5°$
Electrodes: 16 "small"	$3.25 < r < 3.4279$, $\lvert z \rvert < 2.25$, $\Delta\theta = 8.308°$, $\Delta\phi = 22.5°$
Permittivity of air	$\tilde{\varepsilon} = 1$
Permittivity of tube	$\tilde{\varepsilon} = 2.76$
Permittivity of air/ring	$\tilde{\varepsilon} = 1.78 = ((1.25)(1) + (2.25 - 1.25)(2.76))/(2.25)$
Permittivity of flow	$\tilde{\varepsilon} = 1$ (empty), $\tilde{\varepsilon} = 2$ (half-full), $\tilde{\varepsilon} = 4$ (full)

Table A.2. Uncorrected and extrapolated currents when riser tube is "empty" ($\tilde{\varepsilon} = 1$).

Elec.	Uncor. Current Mesh 1	Uncor. Current Mesh 2	Uncor. Current Mesh 3	Uncor. Current Mesh 4	Extrap. Current Mesh 1	Extrap. Current Mesh 2	Extrap. Current Mesh 3	Extrap. Current Mesh 4
0	6.13756	6.28739	6.33127	6.35412	6.42118	6.42936	6.43387	6.43627
1	1.61652	1.65753	1.66995	1.67643	1.69122	1.69496	1.69701	1.69810
2	0.14389	0.14767	0.14876	0.14932	0.15054	0.15100	0.15117	0.15125
3	0.04446	0.04559	0.04592	0.04609	0.04651	0.04662	0.04666	0.04669
4	0.02393	0.02453	0.02471	0.02480	0.02503	0.02509	0.02511	0.02512
5	0.01645	0.01686	0.01698	0.01704	0.01721	0.01725	0.01726	0.01727
6	0.01303	0.01335	0.01345	0.01350	0.01363	0.01365	0.01367	0.01367
7	0.01144	0.01173	0.01181	0.01185	0.01197	0.01199	0.01200	0.01201
8	0.01098	0.01125	0.01132	0.01136	0.01149	0.01150	0.01151	0.01151
shield	2.49745	2.49674	2.49661	2.49655	2.49745	2.49674	2.49661	2.49655

Table A.3. Uncorrected and extrapolated currents when riser tube is "half-full" ($\tilde{\varepsilon} = 2$).

Elec.	Uncor. Current Mesh 1	Uncor. Current Mesh 2	Uncor. Current Mesh 3	Uncor. Current Mesh 4	Extrap. Current Mesh 1	Extrap. Current Mesh 2	Extrap. Current Mesh 3	Extrap. Current Mesh 4
0	6.41708	6.57337	6.61911	6.64291	6.71404	6.72179	6.72632	6.72874
1	1.60044	1.64078	1.65300	1.65939	1.67450	1.67782	1.67978	1.68083
2	0.19900	0.20409	0.20557	0.20633	0.20821	0.20870	0.20889	0.20899
3	0.07858	0.08055	0.08113	0.08142	0.08221	0.08237	0.08244	0.08248
4	0.04561	0.04676	0.04710	0.04727	0.04773	0.04782	0.04786	0.04788
5	0.03214	0.03294	0.03317	0.03329	0.03363	0.03368	0.03371	0.03372
6	0.02570	0.02634	0.02652	0.02662	0.02688	0.02693	0.02695	0.02696
7	0.02266	0.02323	0.02339	0.02348	0.02371	0.02375	0.02377	0.02378
8	0.02178	0.02230	0.02246	0.02254	0.02278	0.02280	0.02282	0.02283
shield	2.49752	2.49682	2.49668	2.49663	2.49752	2.49682	2.49668	2.49663

Table A.4. Uncorrected and extrapolated currents when riser tube is "full" ($\tilde{\varepsilon} = 4$).

Elec.	Uncor. Current Mesh 1	Uncor. Current Mesh 2	Uncor. Current Mesh 3	Uncor. Current Mesh 4	Extrap. Current Mesh 1	Extrap. Current Mesh 2	Extrap. Current Mesh 3	Extrap. Current Mesh 4
0	6.79011	6.95504	7.00327	7.02834	7.10496	7.11208	7.11664	7.11909
1	1.55329	1.59218	1.60399	1.61015	1.62531	1.62813	1.62995	1.63094
2	0.26374	0.27034	0.27226	0.27325	0.27597	0.27644	0.27667	0.27678
3	0.12860	0.13180	0.13273	0.13321	0.13457	0.13478	0.13488	0.13493
4	0.08169	0.08374	0.08433	0.08464	0.08548	0.08563	0.08570	0.08573
5	0.06012	0.06161	0.06204	0.06227	0.06290	0.06300	0.06305	0.06307
6	0.04916	0.05039	0.05074	0.05092	0.05144	0.05152	0.05156	0.05158
7	0.04384	0.04493	0.04525	0.04541	0.04588	0.04595	0.04598	0.04600
8	0.04227	0.04329	0.04359	0.04374	0.04423	0.04426	0.04429	0.04431
shield	2.49761	2.49690	2.49677	2.49671	2.49761	2.49690	2.49677	2.49671

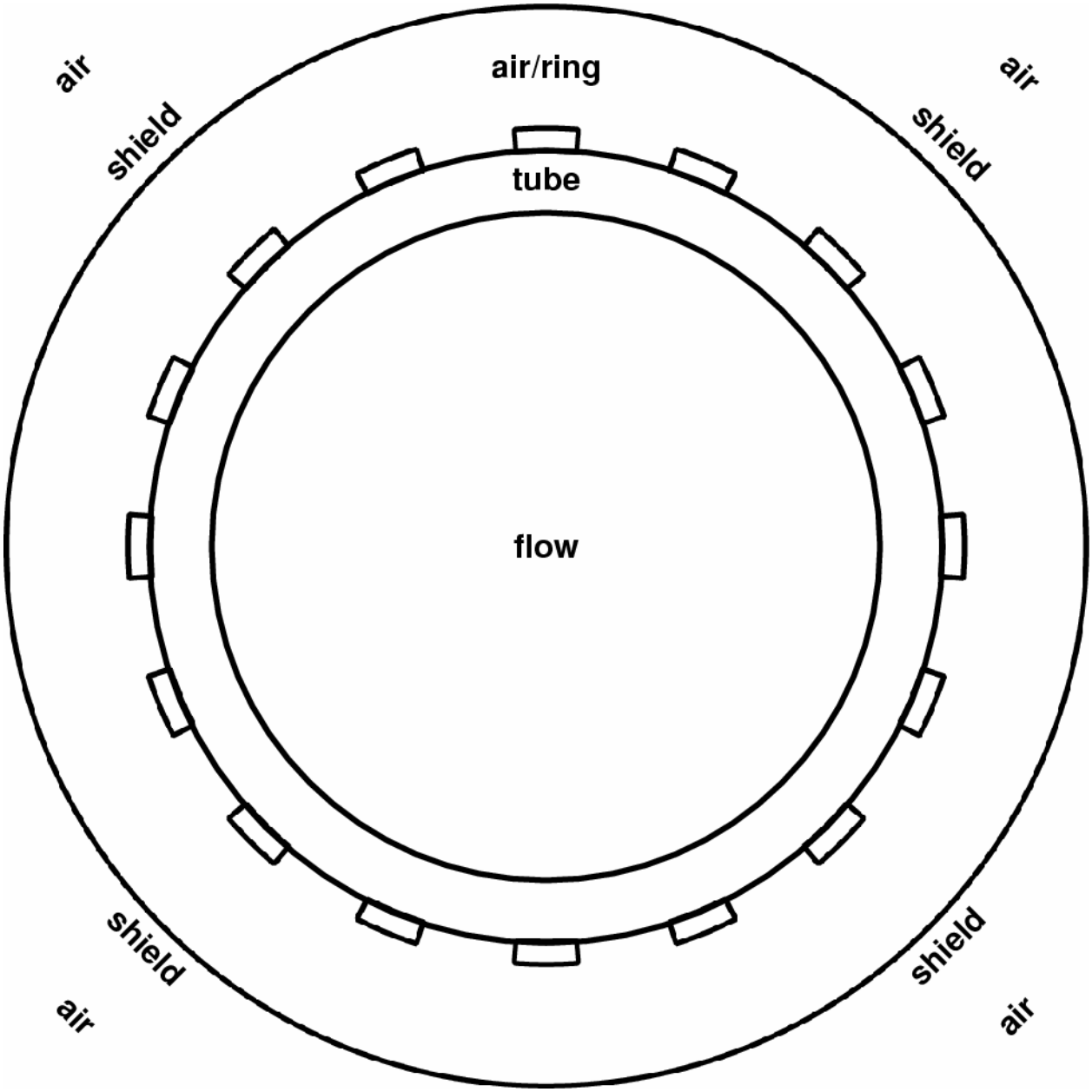

Figure A.1. Cross section of gas-solid-riser tube with EIT electrodes, ring, shield, and air.

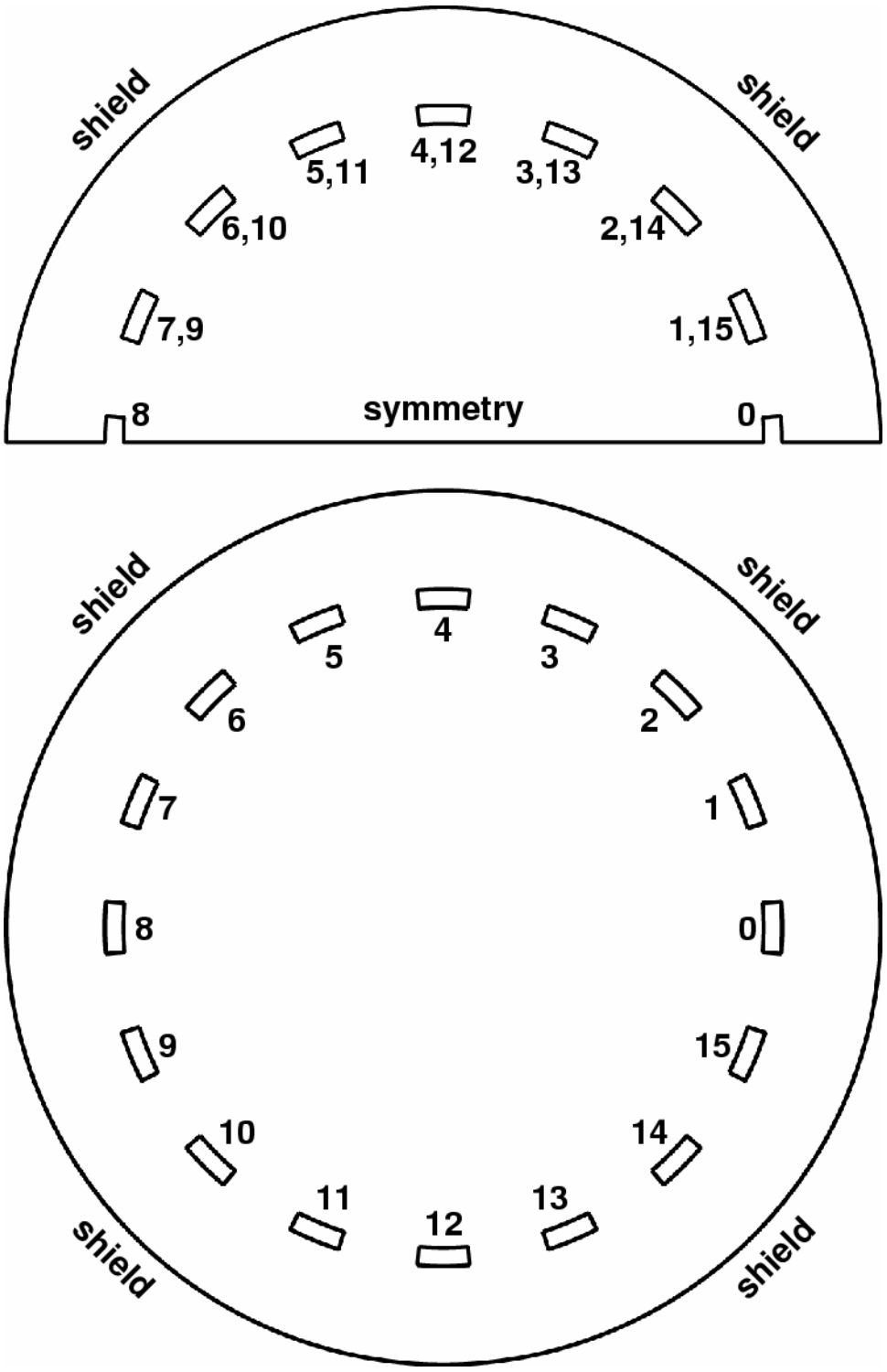

Figure A.2. FIDAP domains with electrode numbers for EIT simulations.

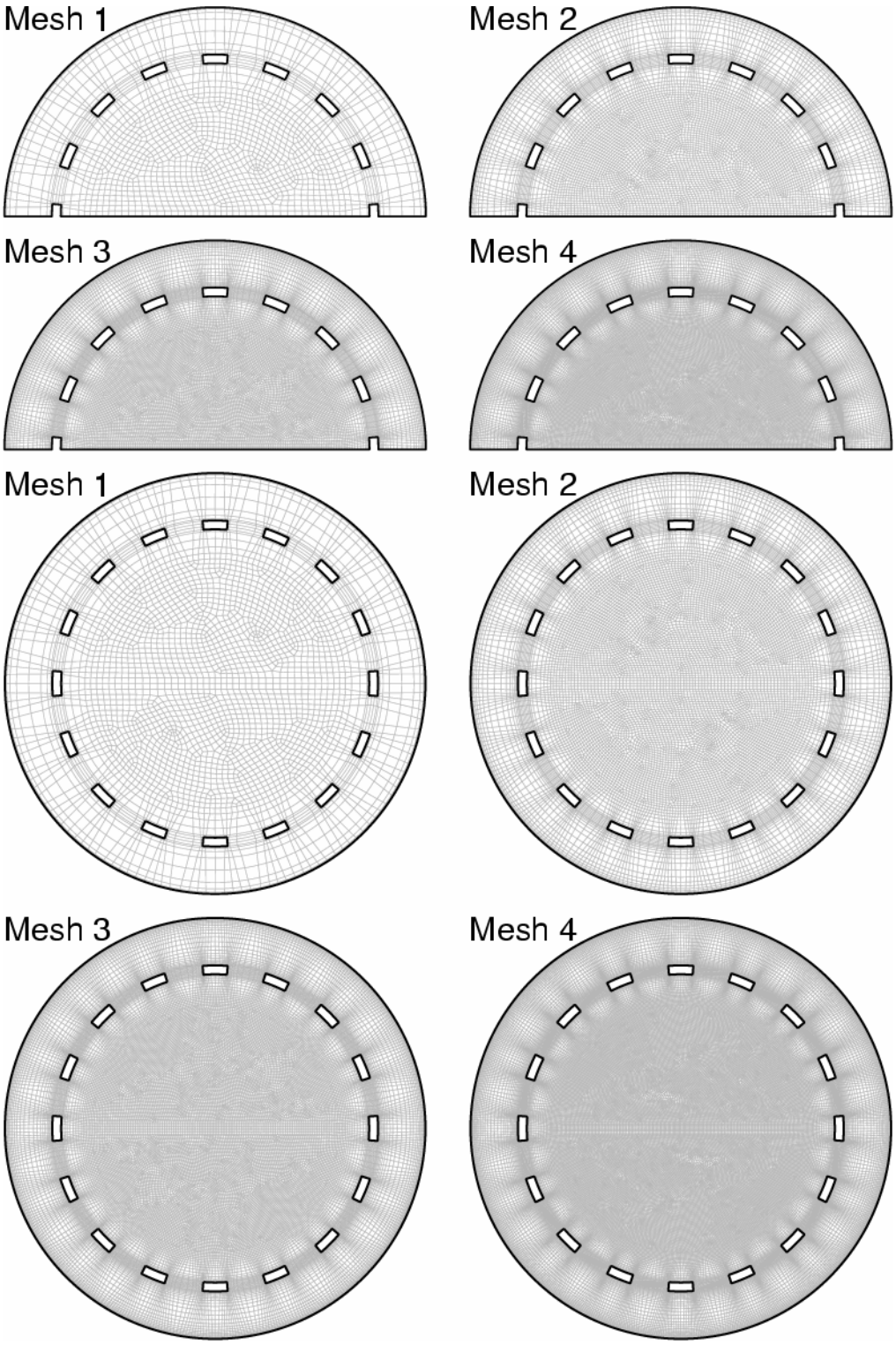

Figure A.3. FIDAP meshes for EIT simulations: 9-node quadrilaterals are used.

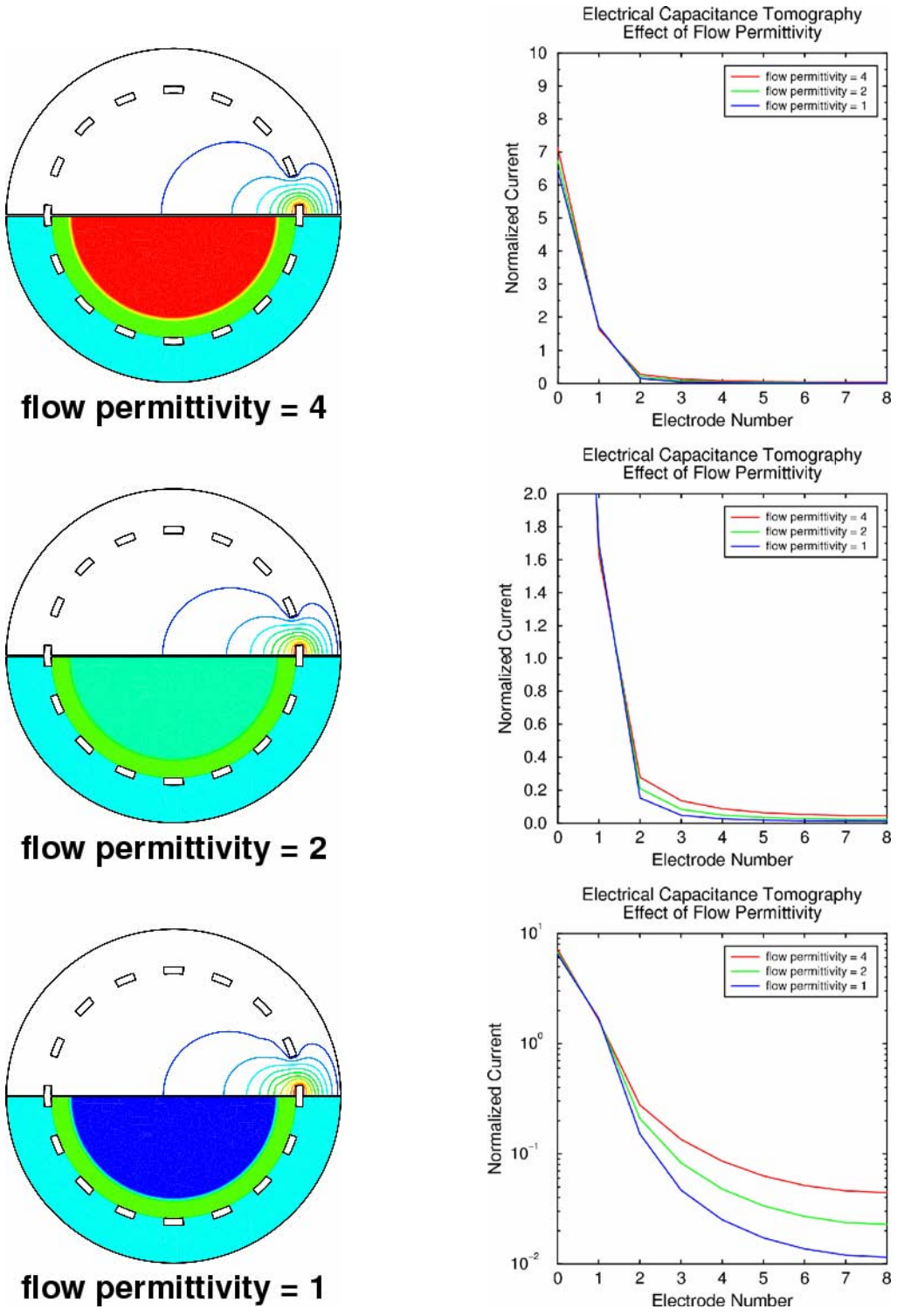

Figure A.4. Effect of flow permittivity on voltage distribution and electrode currents.

Appendix B: Detailed Simulation Results

This appendix contains additional computational results from the gas-particle flow-simulation code *Arena-flow* for the gas-solid-riser experiment. Each case is described in terms of the following parameters, the nominal values for each of which are given below. Departures from these values are noted.

Particle type:

FCC: 1275 kg/m^3, 30-180 μm, 0.68 close-packed particle volume fraction, porous
Glass: 2500 kg/m^3, 120-180 μm, 0.59 close-packed particle volume fraction, solid

Gas superficial velocity (from motive air) in the riser tube: U

Low Gas: 5.3 m/s
High Gas: 7.4 m/s

Solids mass flux in the riser tube: G

FCC Low Solids: 55 kg/m^2·s
FCC High Solids: 104 kg/m^2·s
Glass Low Solids: 50 kg/m^2·s
Glass High Solids: 100 kg/m^2·s

Gas velocity at the motive-air tube boundary: U_1

Low: 20.80 m/s
High: 28.65 m/s

Gas superficial velocity at the fluidization annulus boundary: U_3

FCC: 0.06 m/s
Glass: 0.24 m/s

Gas superficial velocity at the standpipe elliptical boundary: U_2

FCC Low Solids: 0.20 m/s
FCC High Solids: 0.25 m/s
Glass: 0.30 m/s

Solid volume fraction at the standpipe elliptical boundary: ε_2

FCC Low Solids: 0.35
FCC High Solids: 0.45
Glass Low Solids: 0.1429
Glass High Solids: 0.25

Six plots are presented for each case.

Solid volume fraction at a height of 3.8 m:	blue = 0.0, red = 0.1, FCC; 0.2 glass
Average particle velocity at a height of 3.8 m:	blue = 0 m/s, red = 8 m/s
Average gas velocity at a height of 3.8 m:	blue = 0 m/s, red = 10 m/s
Average solids volume fraction on axial slice:	blue = 0.0, red = 0.6
Average gas pressure versus height	
Mass flux versus time near top of riser tube	

FCC01: FCC, $U = 5.3$ m/s, $G = 104$ kg/m^2·s, $U_1 = 20.80$ m/s, $U_3 = 0.06$ m/s, $U_2 = 0.25$ m/s, $\varepsilon_2 = 0.45$.
Comments: FCC low-gas, high-solids baseline case (Case 2)

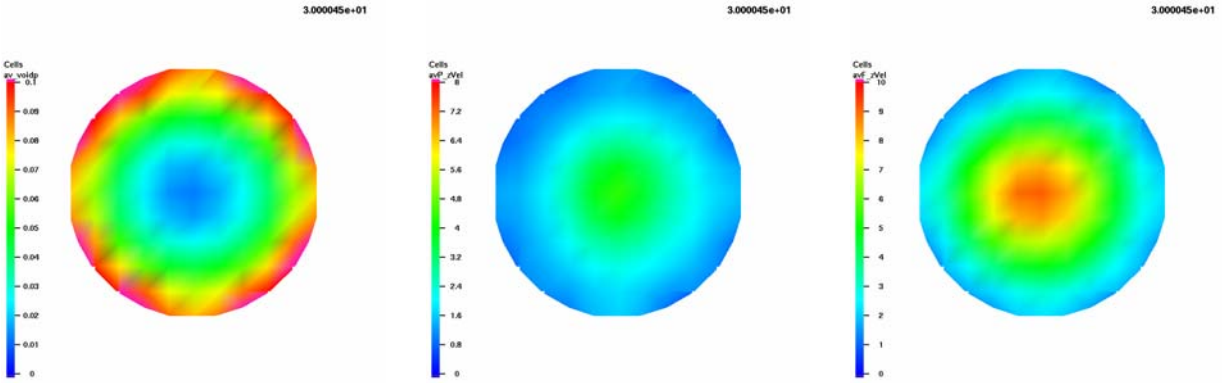

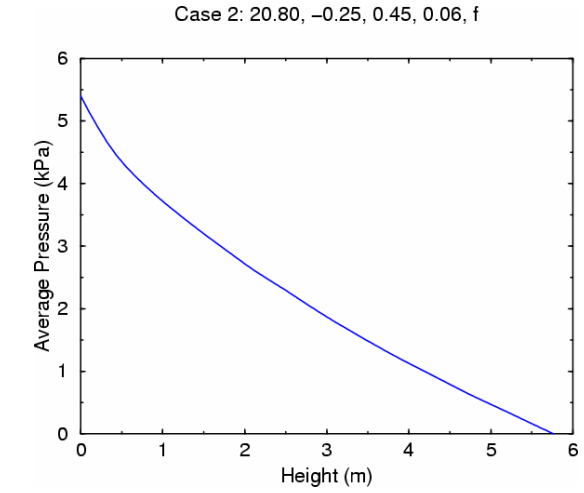

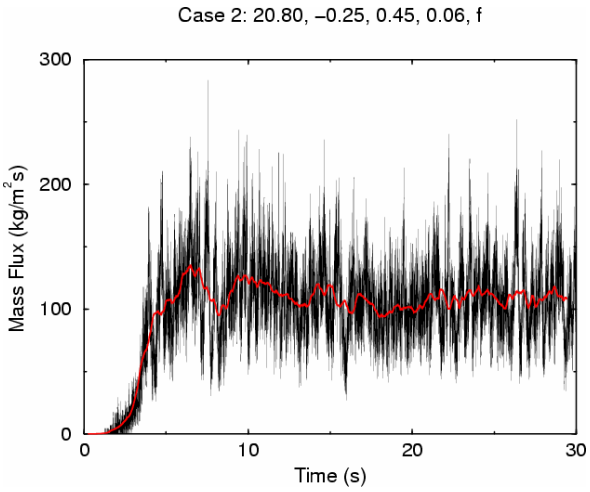

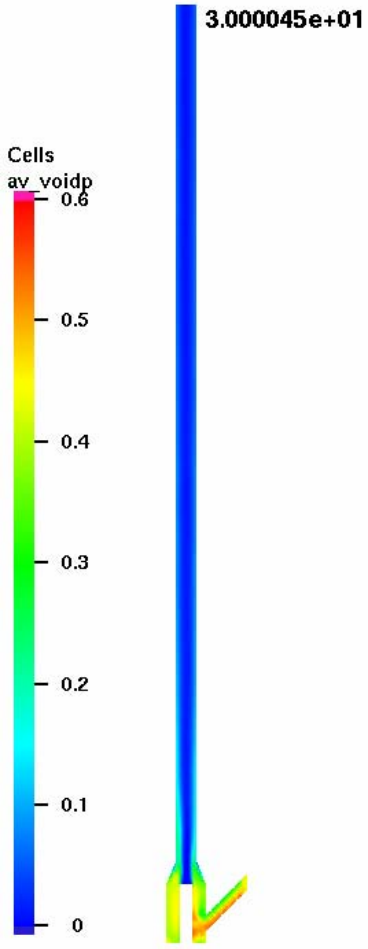

FCC02: FCC, $U = 5.3$ m/s, $G = 55$ kg/m^2·s, $U_1 = 20.80$ m/s, $U_3 = 0.06$ m/s, $U_2 = 0.20$ m/s, $\varepsilon_2 = 0.35$.
Comments: FCC low-gas, low-solids baseline case (Case 6)

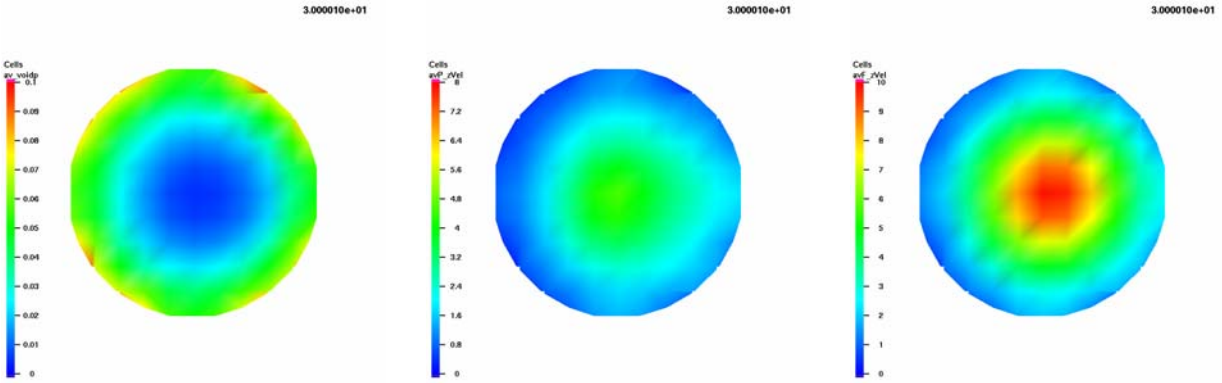

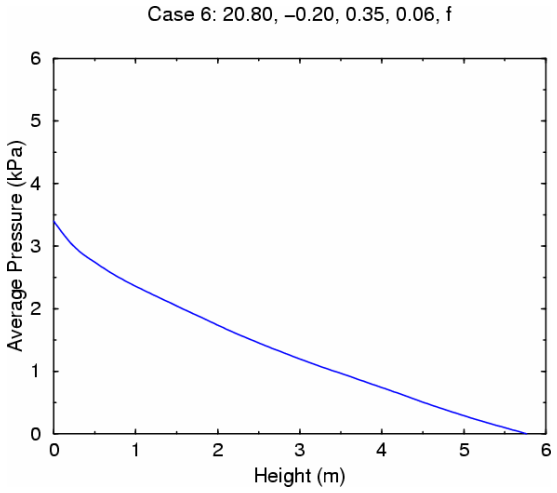

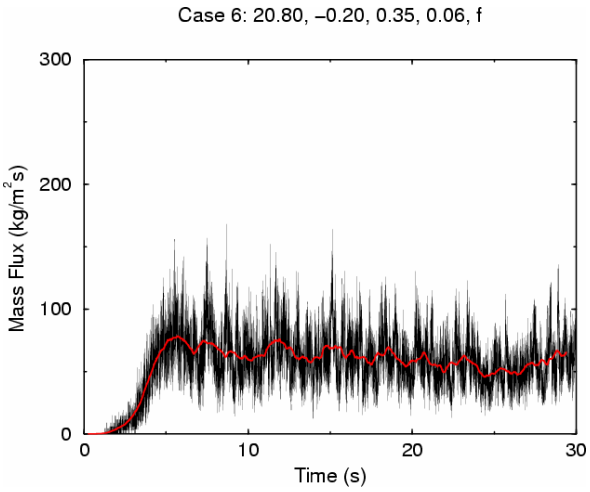

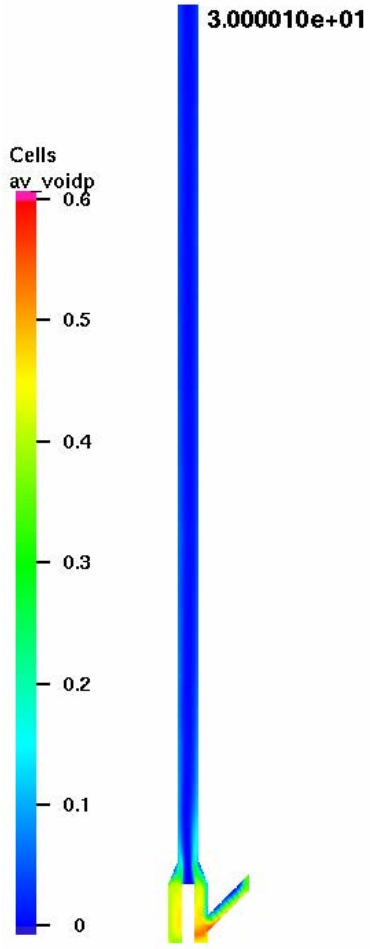

FCC03: FCC, $U = 5.3$ m/s, $G = 55$ kg/m^2·s, $U_1 = 20.80$ m/s, $U_3 = 0.06$ m/s, $U_2 = 0.1077$ m/s, $\varepsilon_2 = 0.50$.
Comments: Compare to FCC02 to assess standpipe boundary condition (Case 0)

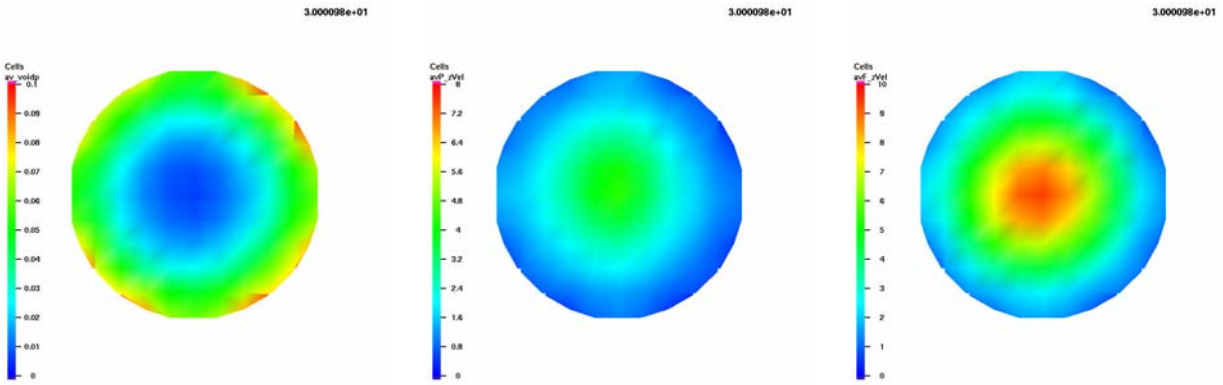

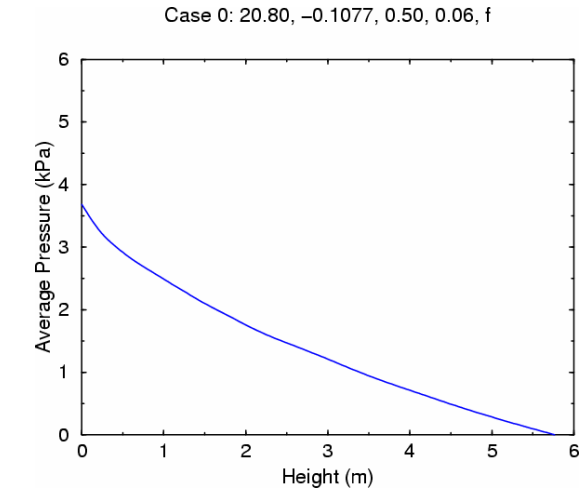

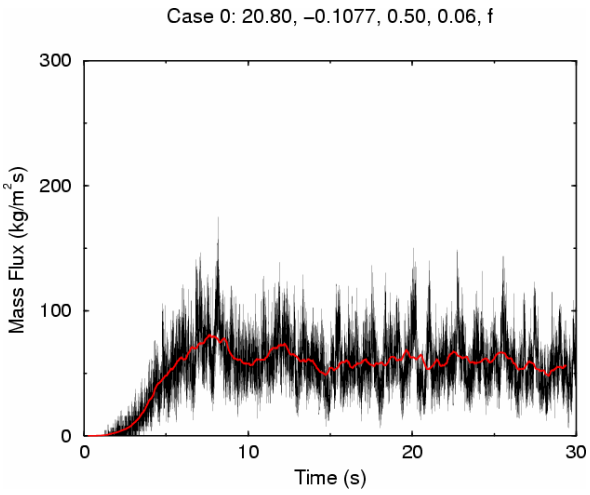

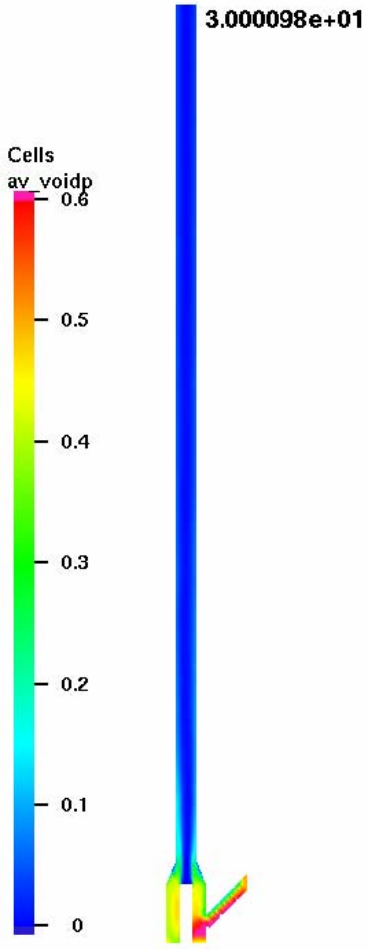

FCC04: FCC, $U = 5.3$ m/s, $G = 104$ kg/m^2·s, $U_1 = 41.60$ m/s, $U_3 = 0.06$ m/s, $U_2 = 0.25$ m/s, $\varepsilon_2 = 0.45$.
Comments: Compare to FCC01 to assess half-open motive-air tube (Case 1)

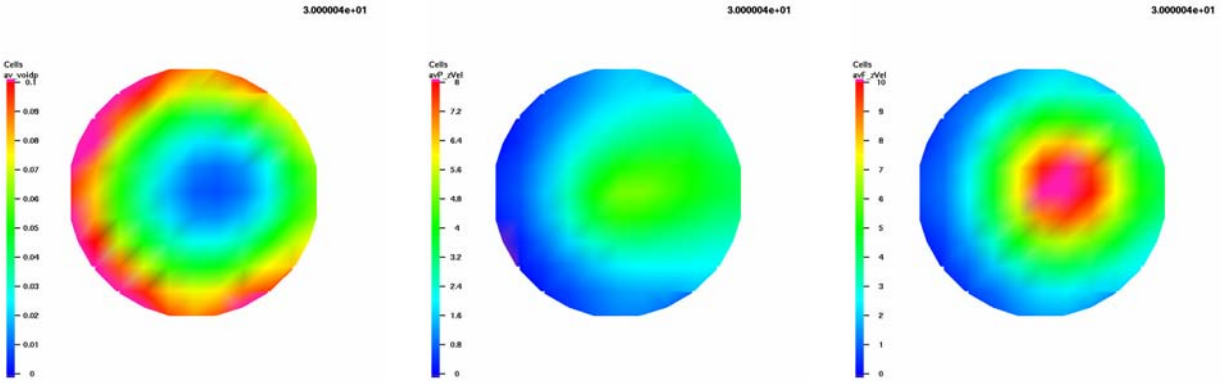

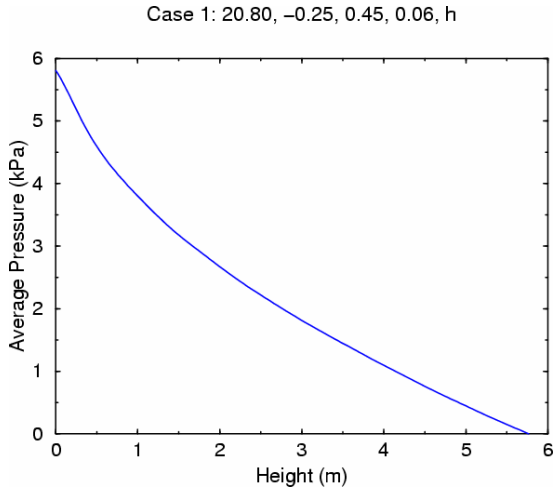

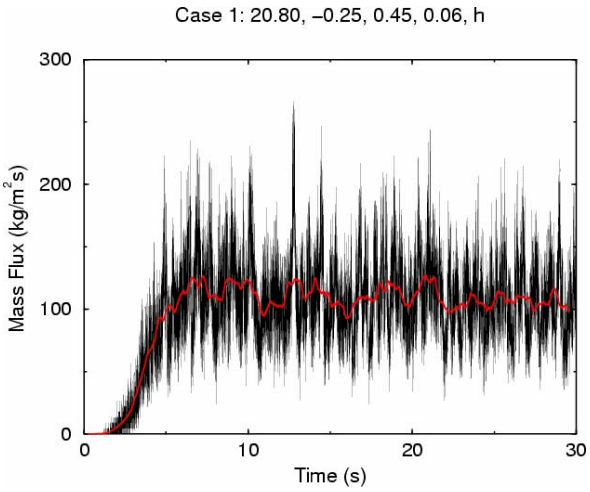

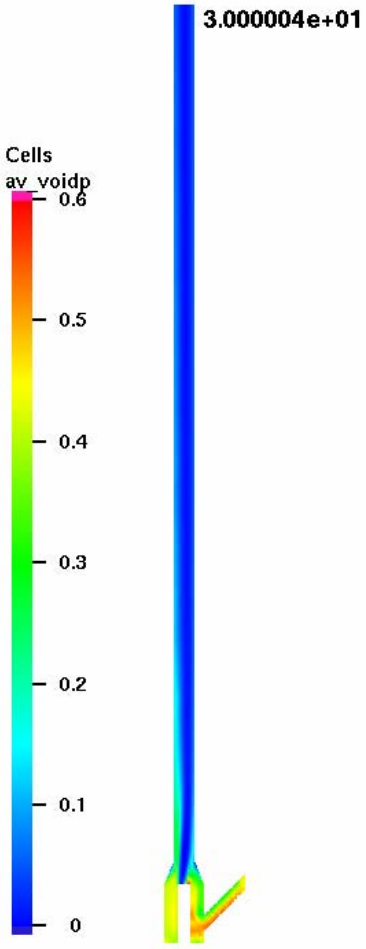

FCC05: FCC, $U = 5.3$ m/s, $G = 104$ kg/m^2·s, $U_1 = 20.80$ m/s, $U_3 = 0.03$ m/s, $U_2 = 0.25$ m/s, $\varepsilon_2 = 0.45$.
Comments: Compare to FCC01 to assess reduced fluidization velocity (Case A)

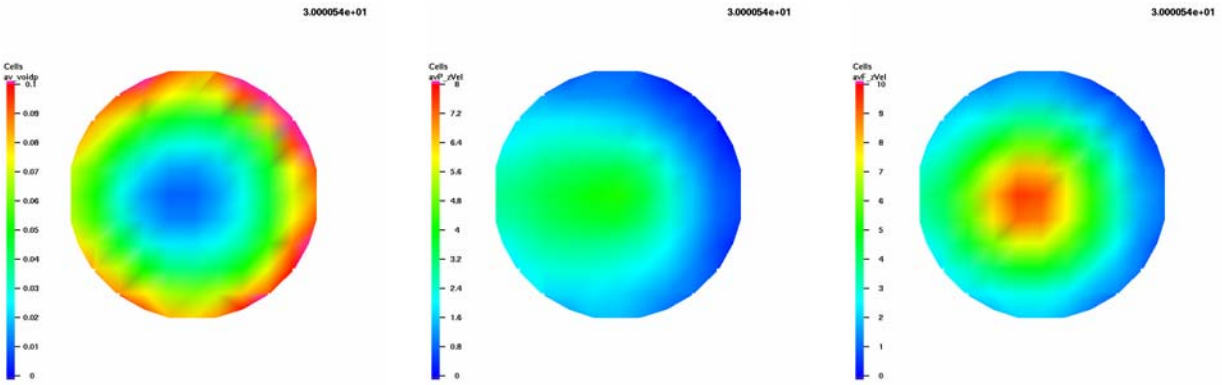

Case A: 20.80, –0.25, 0.45, 0.03, f

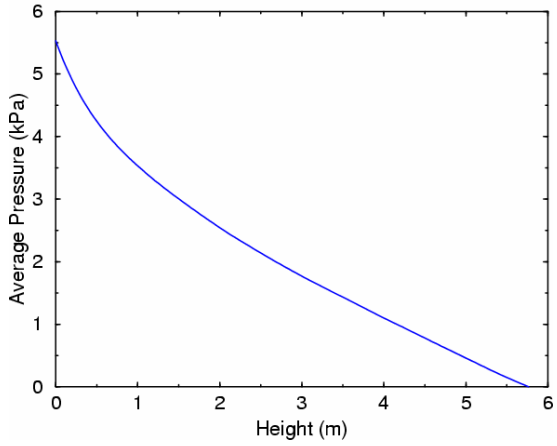

Case A: 20.80, –0.25, 0.45, 0.03, f

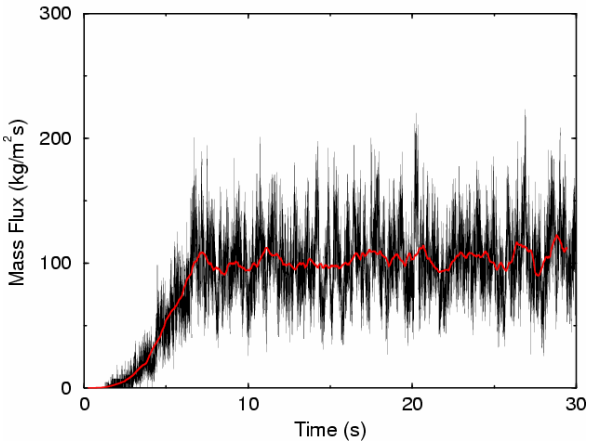

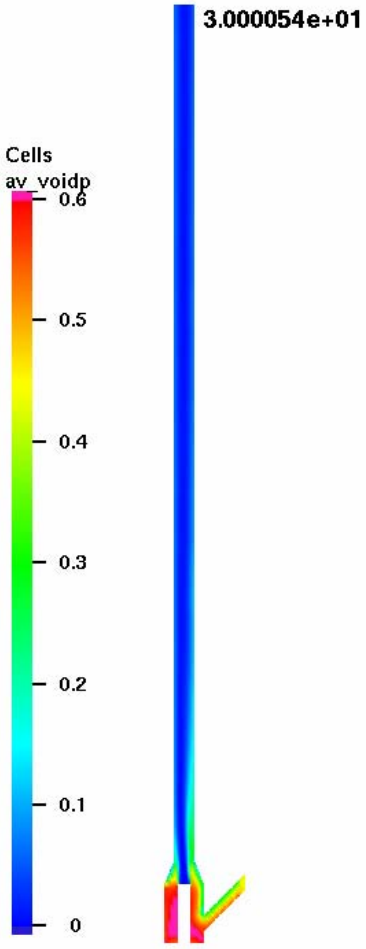

FCC06: FCC, $U = 5.3$ m/s, $G = 104$ kg/m^2·s, $U_1 = 20.80$ m/s, $U_3 = 0.09$ m/s, $U_2 = 0.25$ m/s, $\varepsilon_2 = 0.45$.
Comments: Compare to FCC01 to assess increased fluidization velocity (Case E)

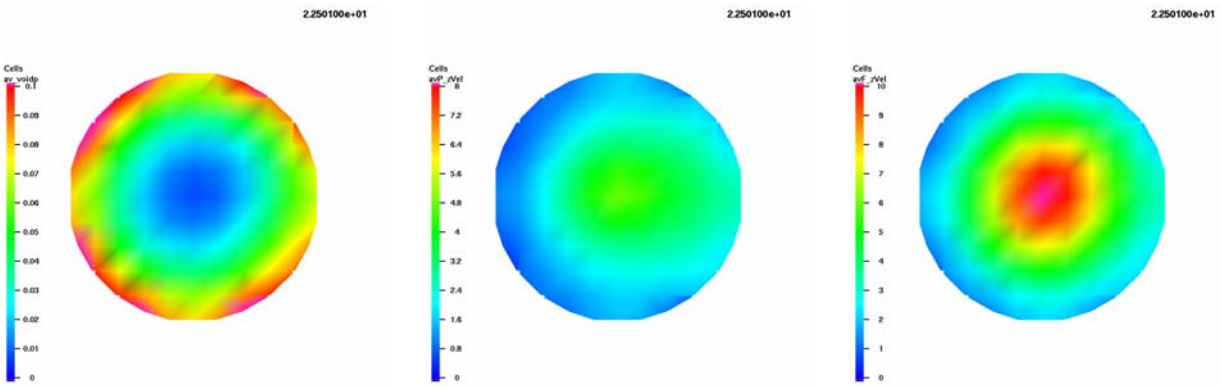

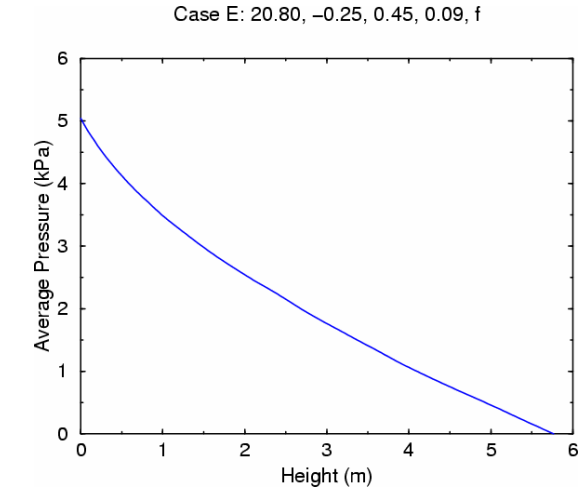

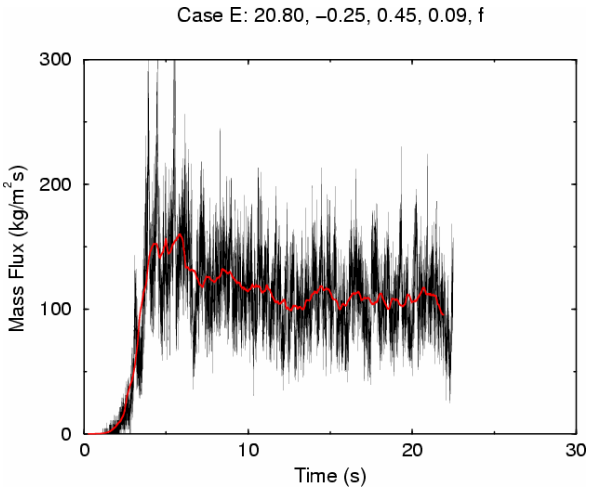

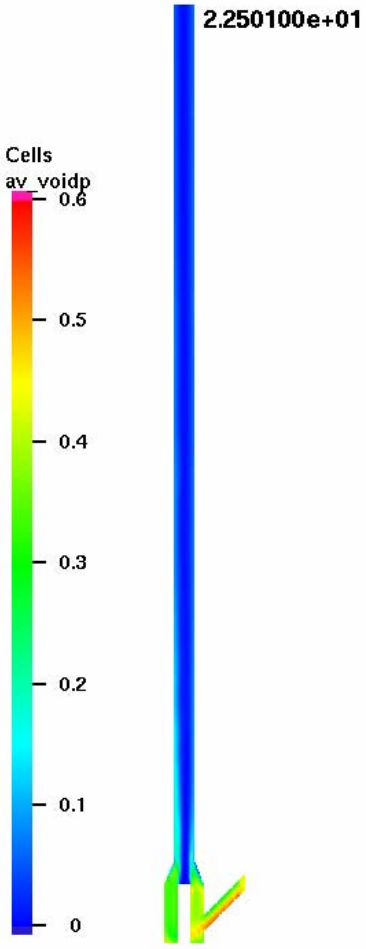

FCC07: FCC, $U = 5.3$ m/s, $G = 153$ kg/m^2·s, $U_1 = 20.80$ m/s, $U_3 = 0.06$ m/s, $U_2 = 0.30$ m/s, $\varepsilon_2 = 0.50$.
Comments: Compare to FCC01 and FCC02 to assess increased solids mass flux (Case 8)

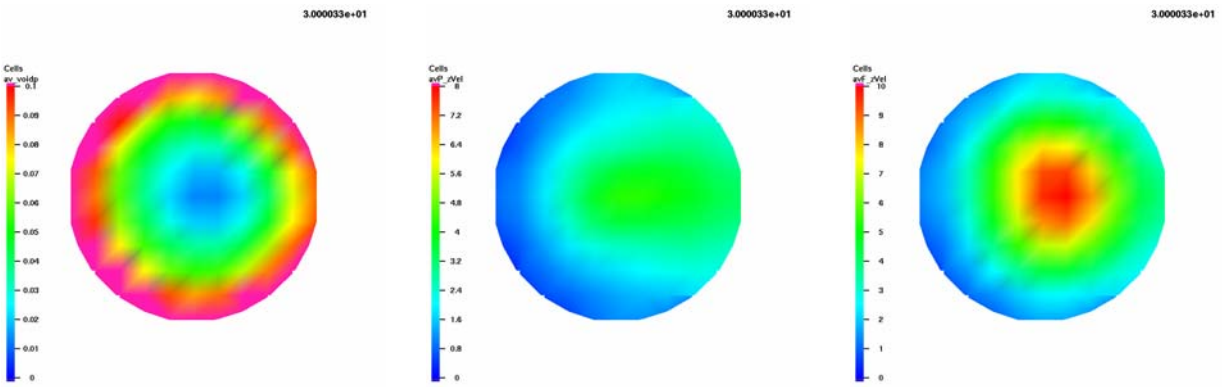

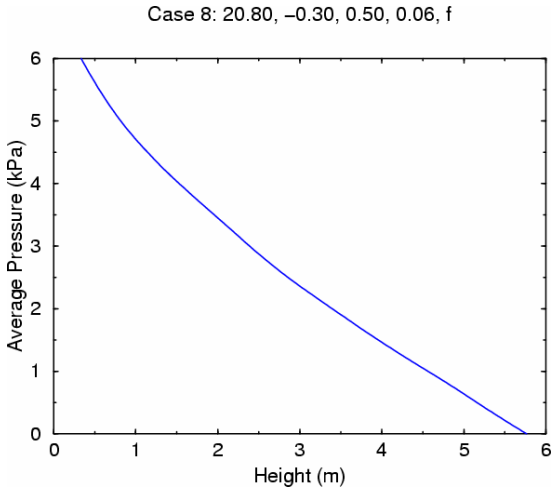

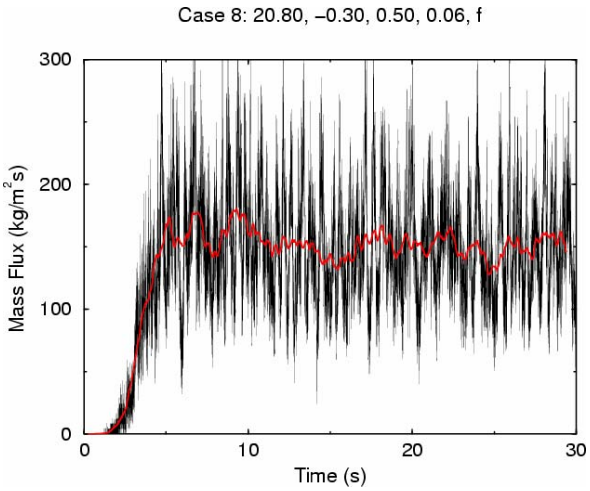

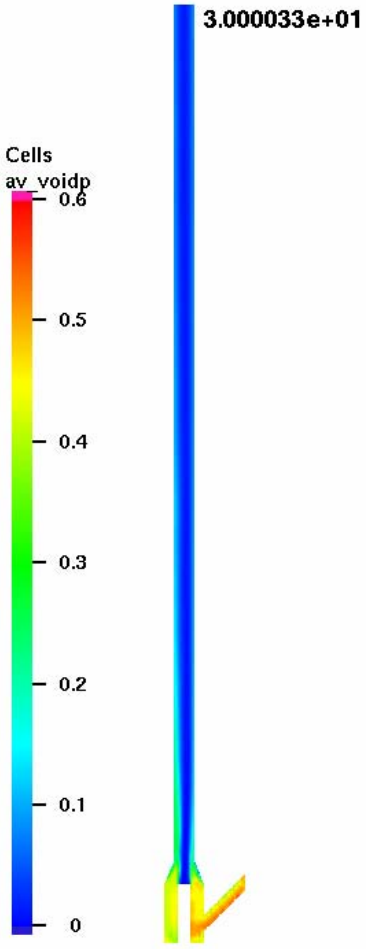

FCC08: FCC, $U = 5.3$ m/s, $G = 104$ kg/m^2·s, $U_1 = 20.80$ m/s, $U_3 = 0.06$ m/s, $U_2 = 0.3125$ m/s, $\varepsilon_2 = 0.45$.
Comments: Compare to FCC01 with reduced particle mass density of 1020 kg/m^3 (Case H)

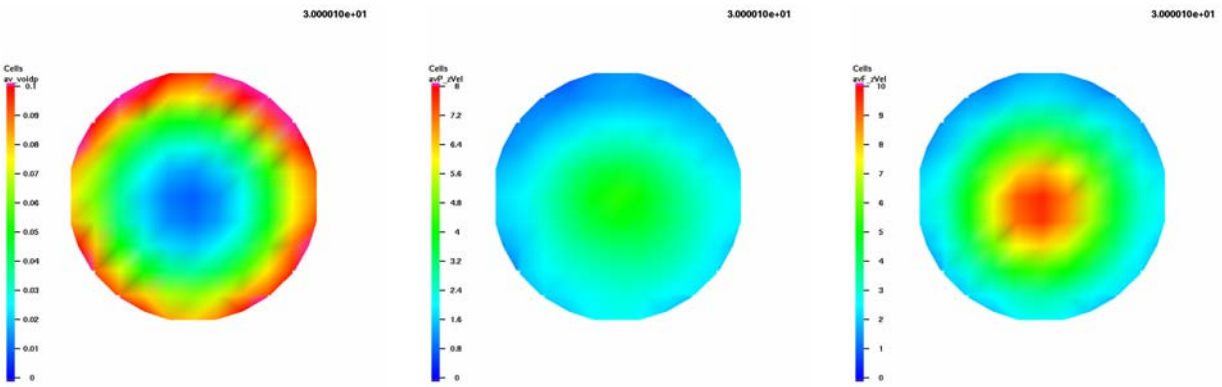

Case H: 20.80, –0.3125, 0.45, 0.06, f, l

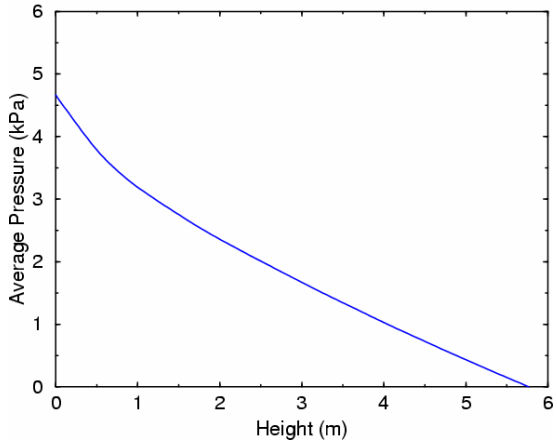

Case H: 20.80, –0.3125, 0.45, 0.06, f, l

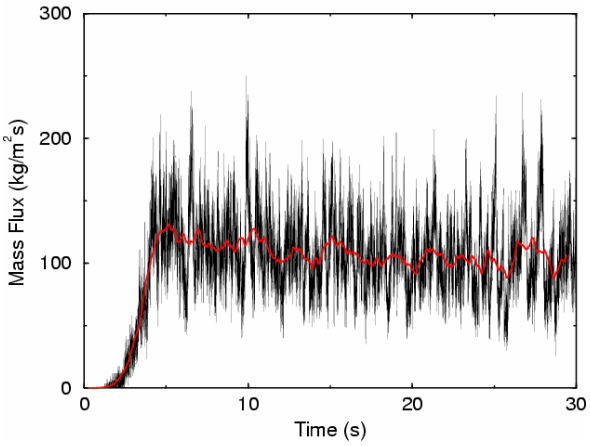

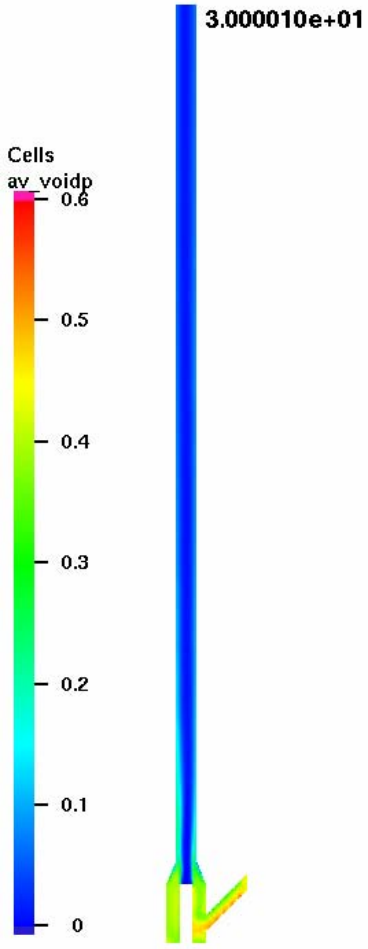

FCC09: FCC, $U = 5.3$ m/s, $G = 104$ kg/m^2·s, $U_1 = 20.80$ m/s, $U_3 = 0.06$ m/s, $U_2 = 0.25$ m/s, $\varepsilon_2 = 0.45$.
Comments: Compare to FCC01 to assess effect of drag model 2 instead of drag model 1 (Case C)

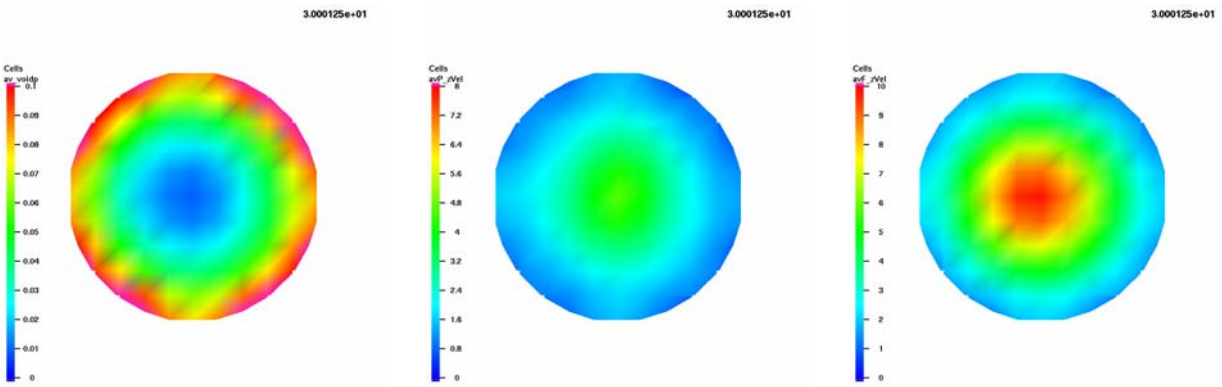

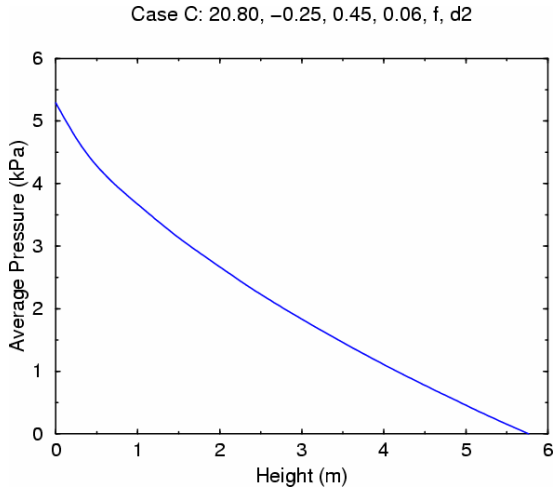

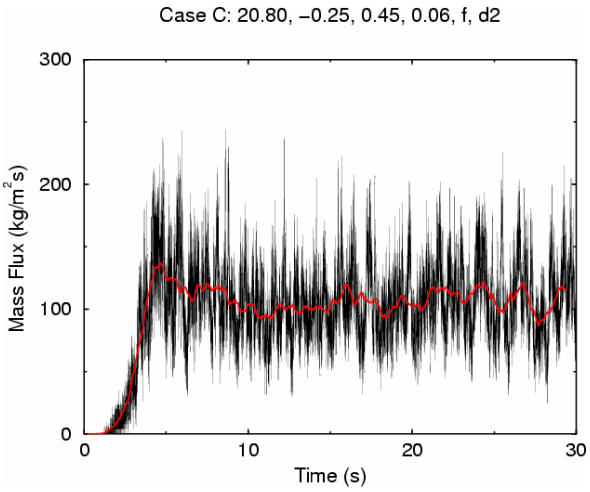

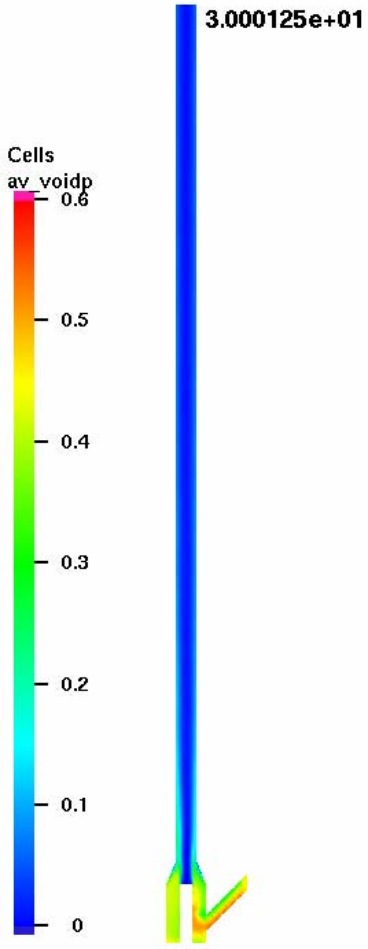

FCC10: FCC, $U = 5.3$ m/s, $G = 104$ kg/m^2·s, $U_1 = 20.80$ m/s, $U_3 = 0.06$ m/s, $U_2 = 0.25$ m/s, $\varepsilon_2 = 0.45$.
Comments: Compare to FCC01 to assess effect of drag model 3 instead of drag model 1 (Case K)

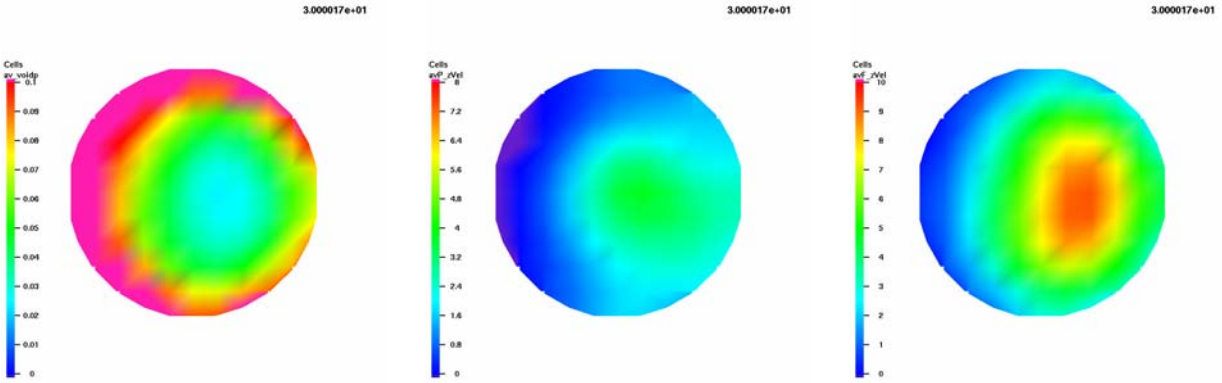

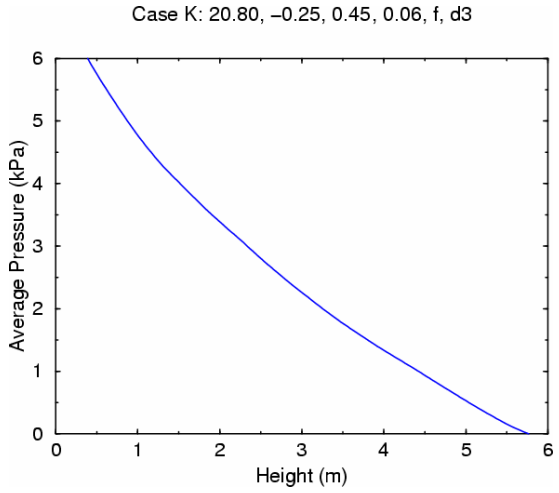

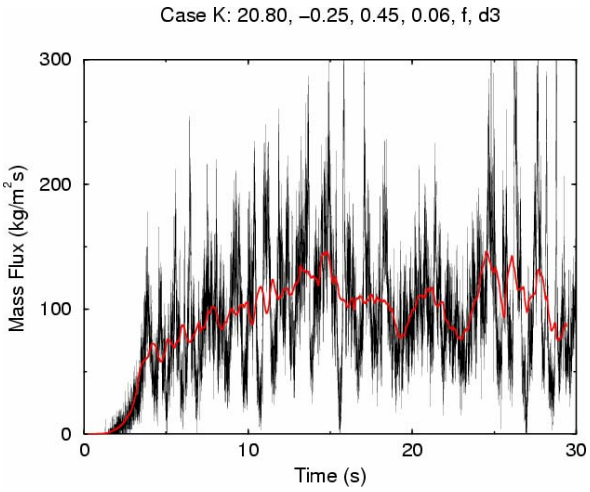

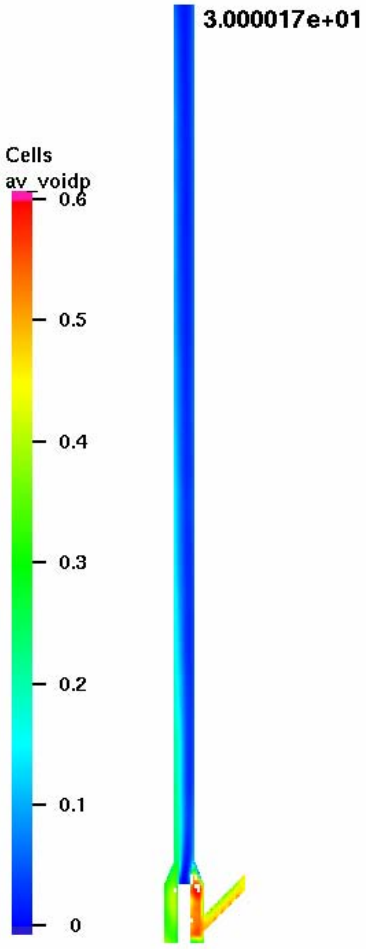

FCC11: FCC, $U = 5.3$ m/s, $G = 104$ kg/m^2·s, $U_1 = 20.80$ m/s, $U_3 = 0.06$ m/s, $U_2 = 0.25$ m/s, $\varepsilon_2 = 0.45$.
Comments: Compare to FCC01 to assess effect of increasing p-p interaction to 60% from 20% (Case M)

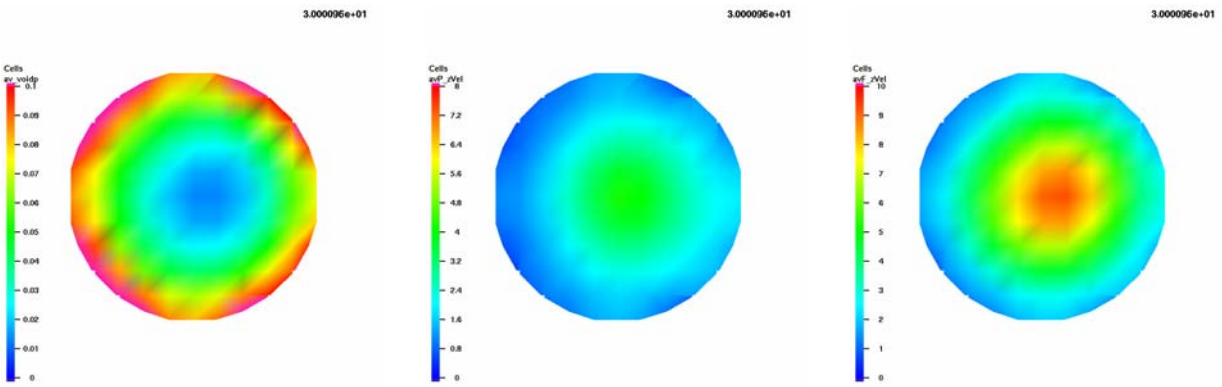

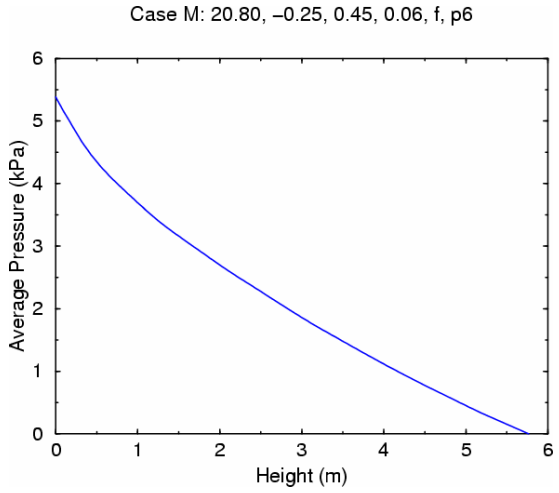

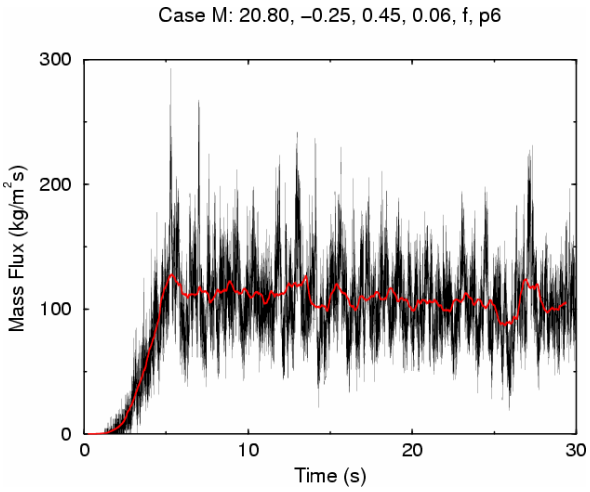

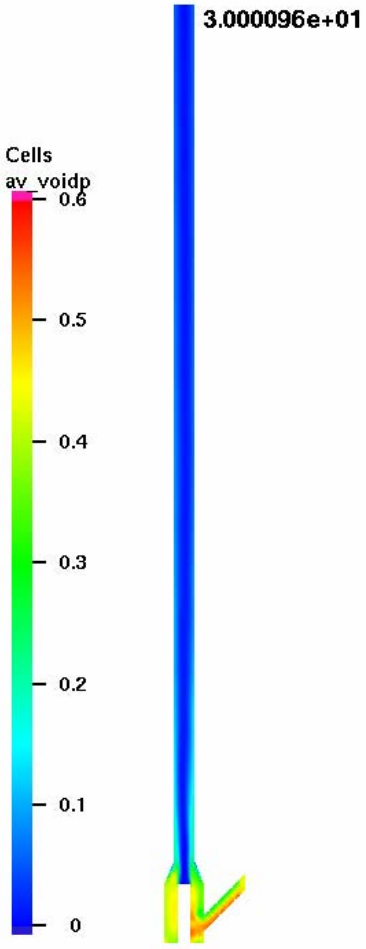

FCC12: FCC, $U = 5.3$ m/s, $G = 104$ kg/m^2·s, $U_1 = 20.80$ m/s, $U_3 = 0.06$ m/s, $U_2 = 0.25$ m/s, $\varepsilon_2 = 0.45$.
Comments: Compare to FCC01 to assess monodisperse particle size distribution of 100-110 µm (Case O)

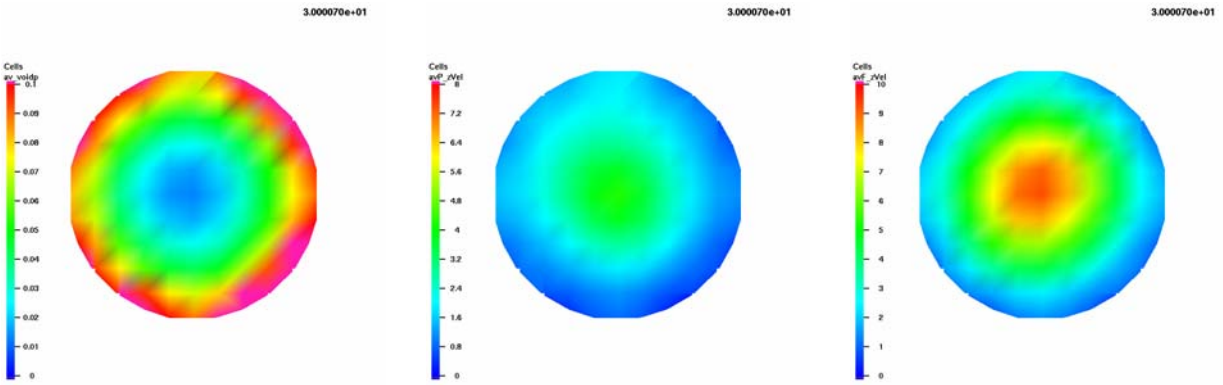

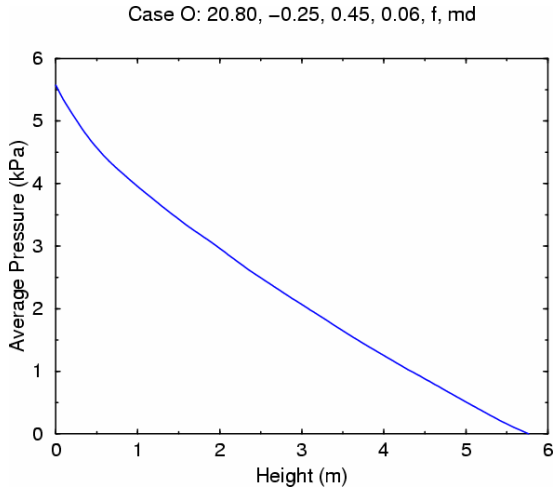

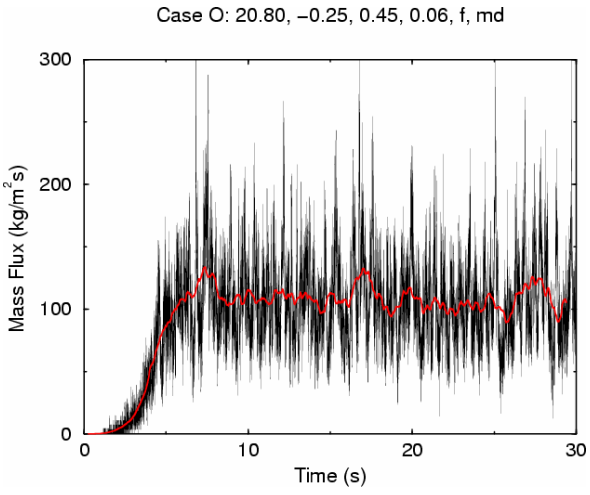

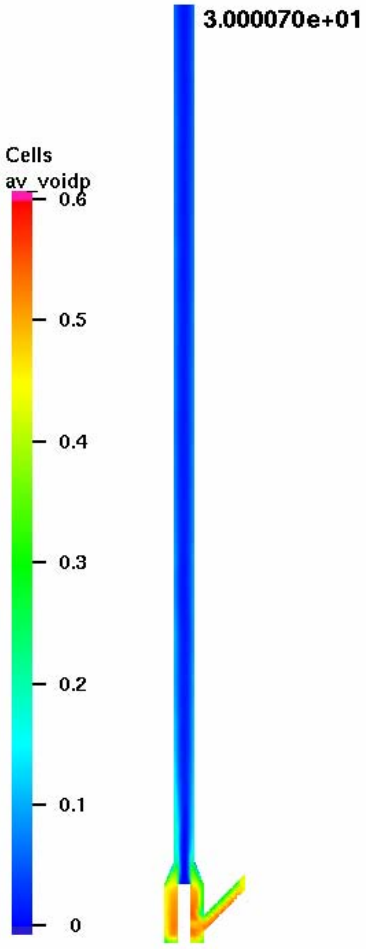

FCC13: FCC, $U = 5.3$ m/s, $G = 104$ kg/m^2·s, $U_1 = 20.80$ m/s, $U_3 = 0.06$ m/s, $U_2 = 0.25$ m/s, $\varepsilon_2 = 0.45$.
Comments: Compare to FCC01 to assess effect of specular walls (Case Q)

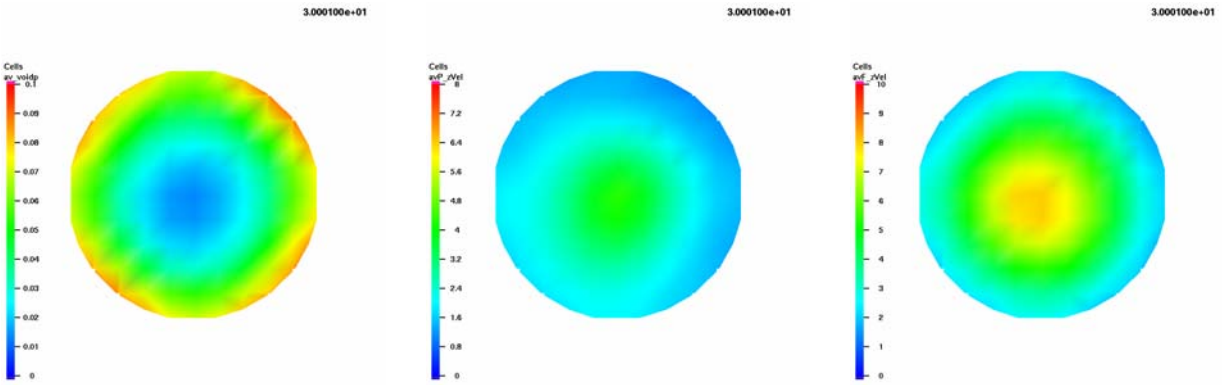

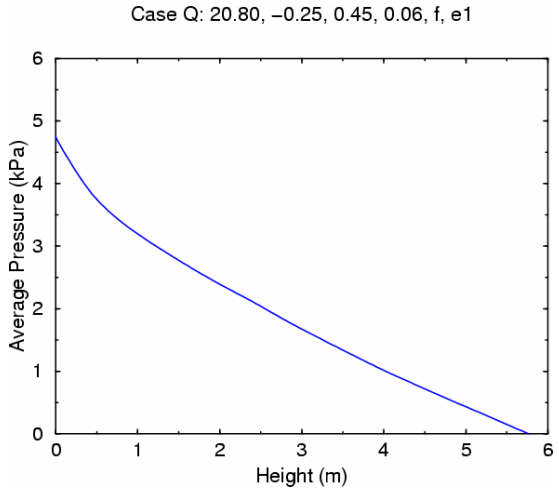

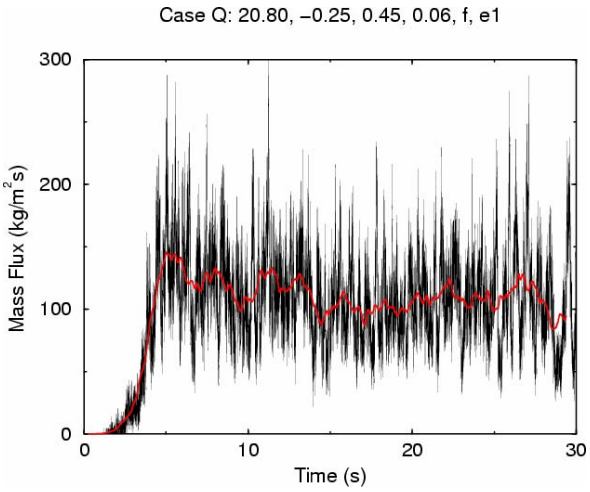

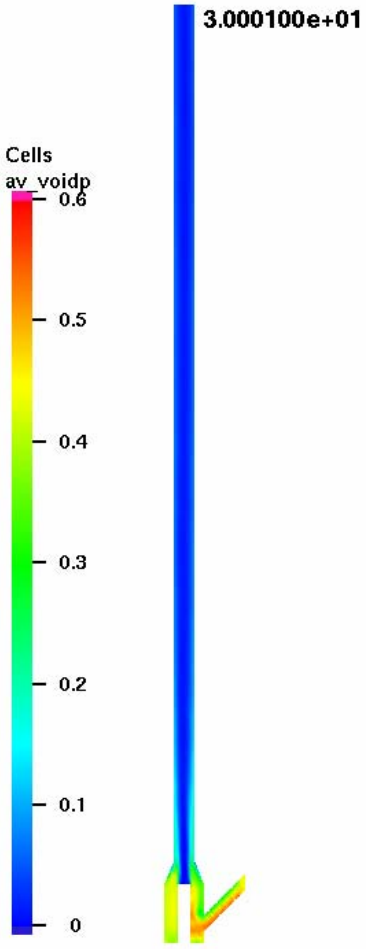

FCC14: FCC, $U = 5.3$ m/s, $G = 104$ kg/m^2·s, $U_1 = 20.80$ m/s, $U_3 = 0.06$ m/s, $U_2 = 0.25$ m/s, $\varepsilon_2 = 0.45$.
Comments: Compare to FCC01 to assess effect of diffuse walls (Case S)

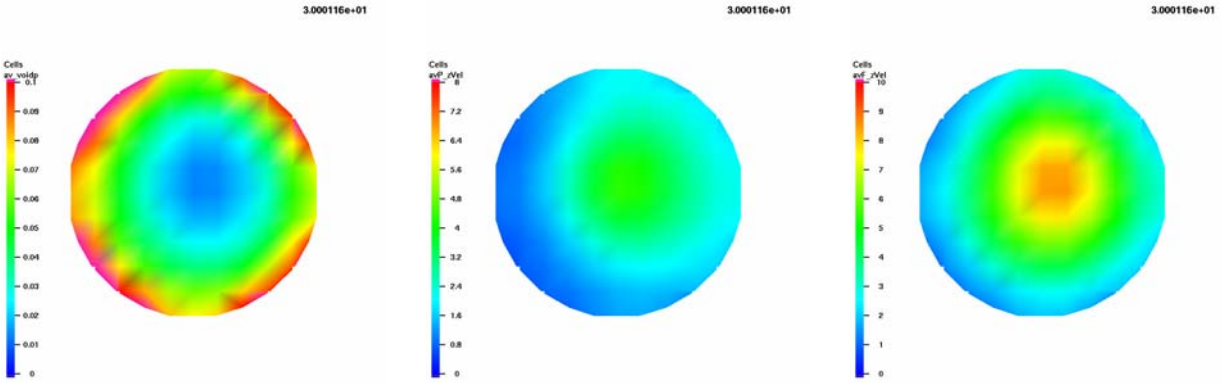

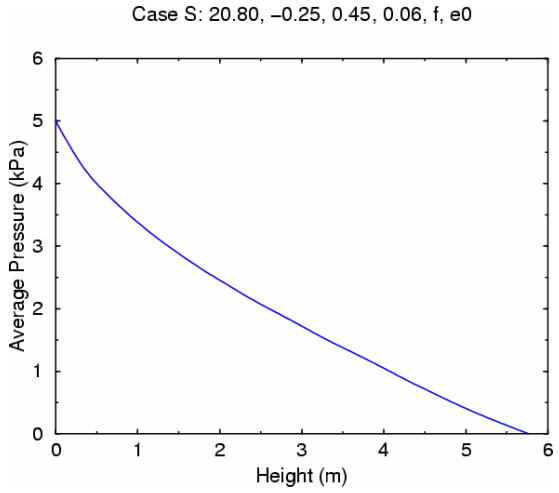

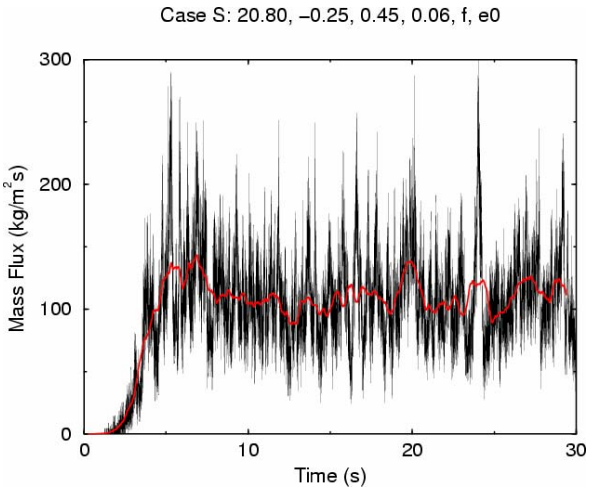

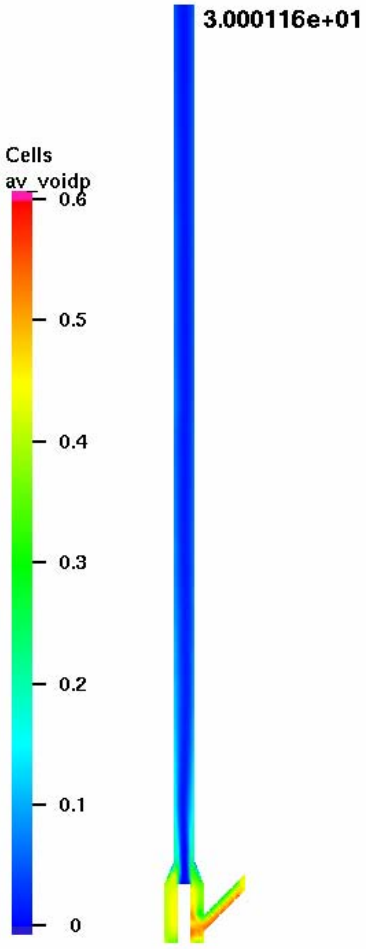

FCC15: FCC, $U = 5.3$ m/s, $G = 104$ kg/m^2·s, $U_1 = 20.80$ m/s, $U_3 = 0.06$ m/s, $U_2 = 0.25$ m/s, $\varepsilon_2 = 0.45$.
Comments: Compare to FCC01 to assess effect of increasing shear-stress exponent to 8 from 3 (Case Y)

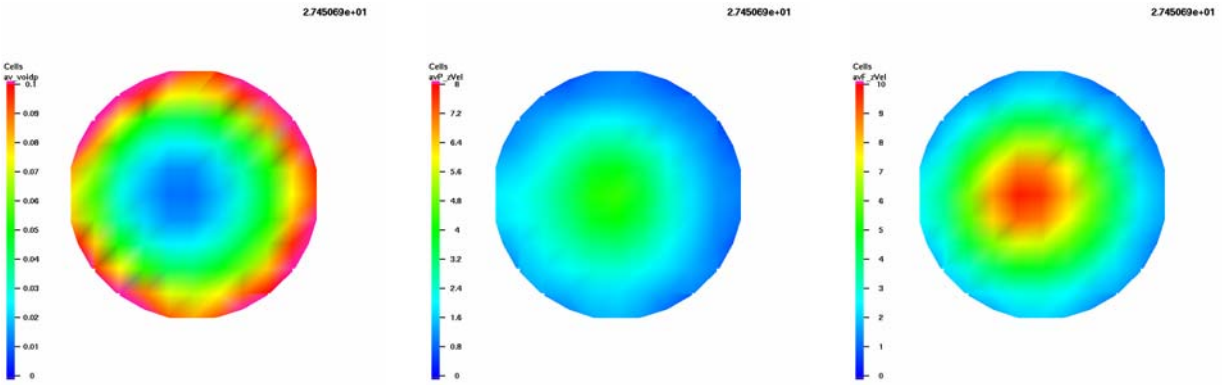

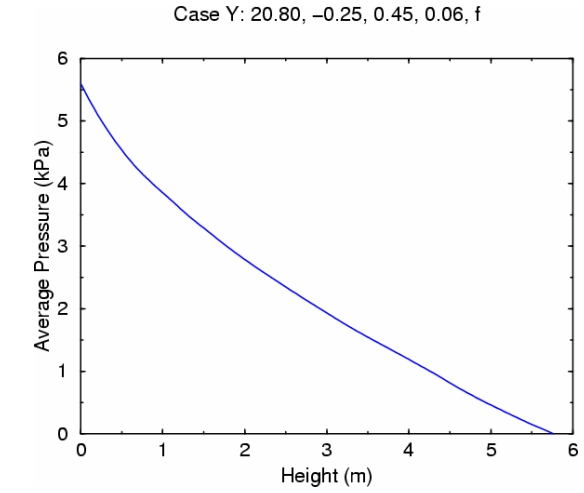

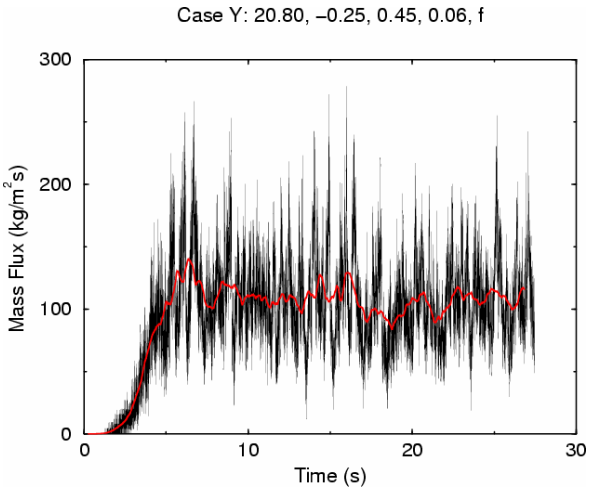

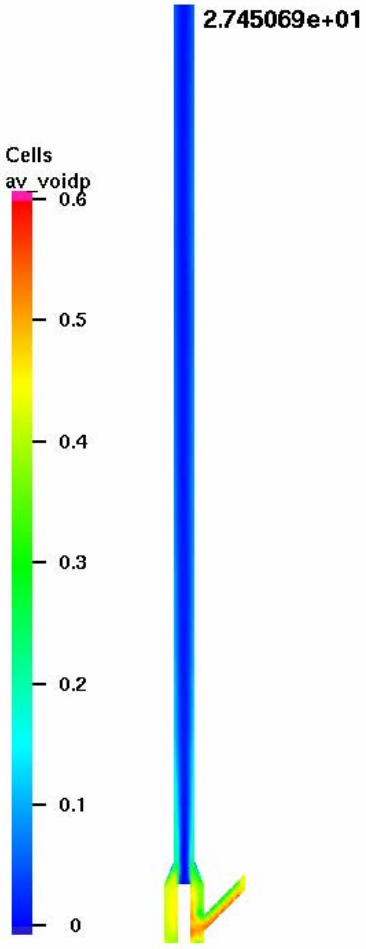

FCC16: FCC, $U = 5.3$ m/s, $G = 104$ kg/m^2·s, $U_1 = 20.80$ m/s, $U_3 = 0.06$ m/s, $U_2 = 0.25$ m/s, $\varepsilon_2 = 0.45$.
Comments: Compare to FCC01 to assess the effect of increasing close packing to 0.8 from 0.68 (Case ZA)

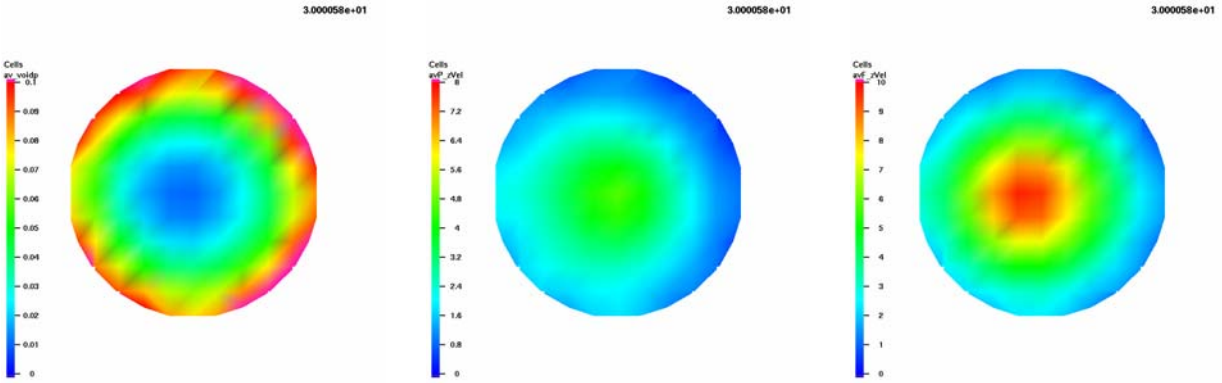

Case ZA: 20.80, –0.25, 0.45, 0.06, f

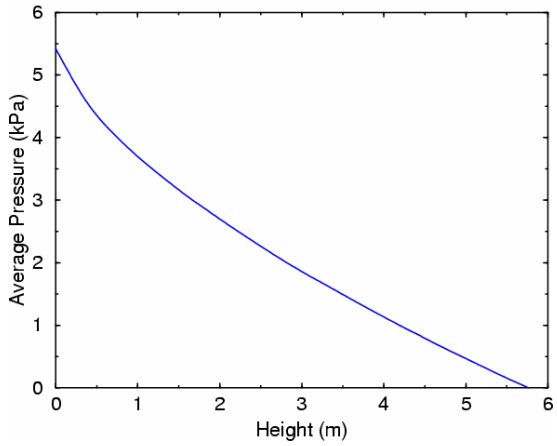

Case ZA: 20.80, –0.25, 0.45, 0.06, f

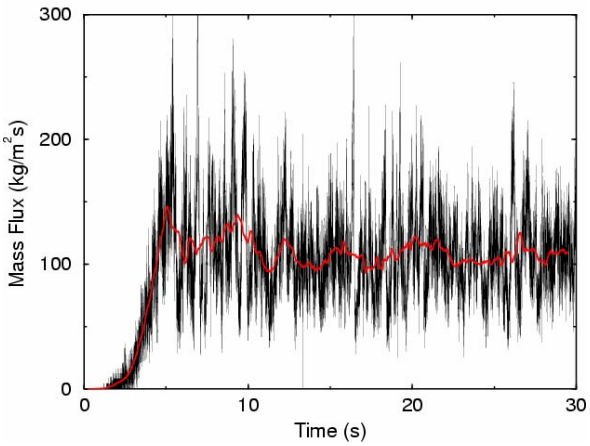

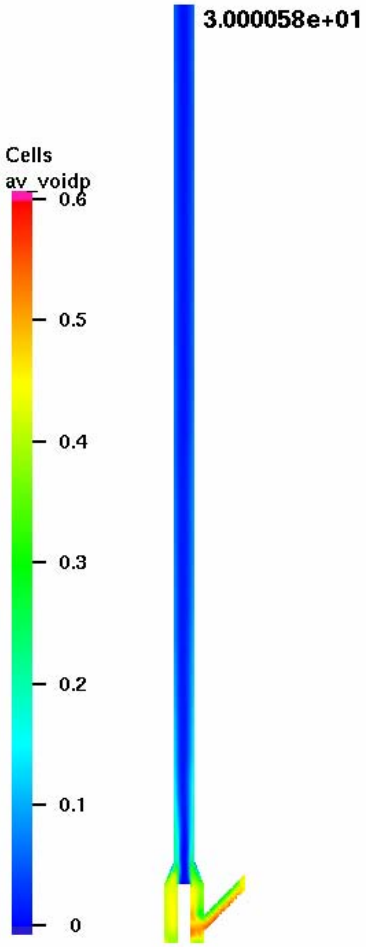

FCC17: FCC, $U = 5.3$ m/s, $G = 104$ kg/m^2·s, $U_1 = 20.80$ m/s, $U_3 = 0.06$ m/s, $U_2 = 0.25$ m/s, $\varepsilon_2 = 0.45$.
Comments: Compare to FCC01 and FCC18 to assess particle size distribution of 160-180 µm (Case ZC)

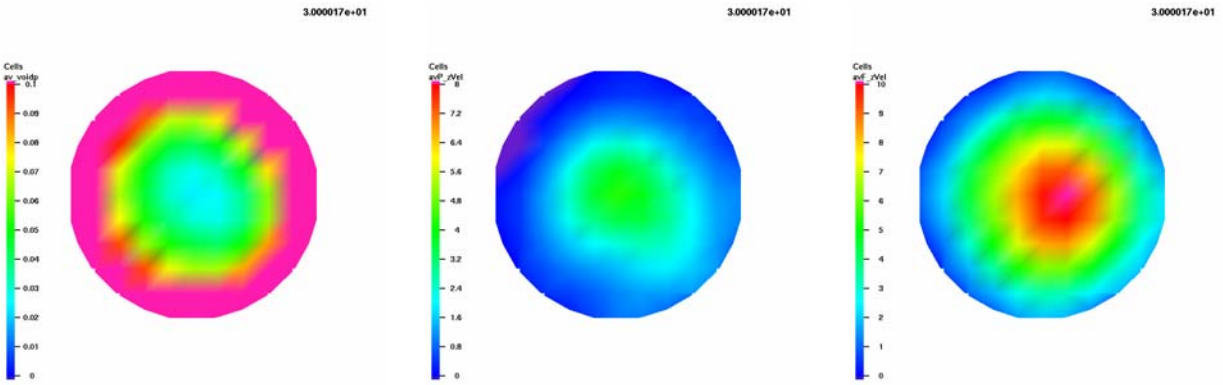

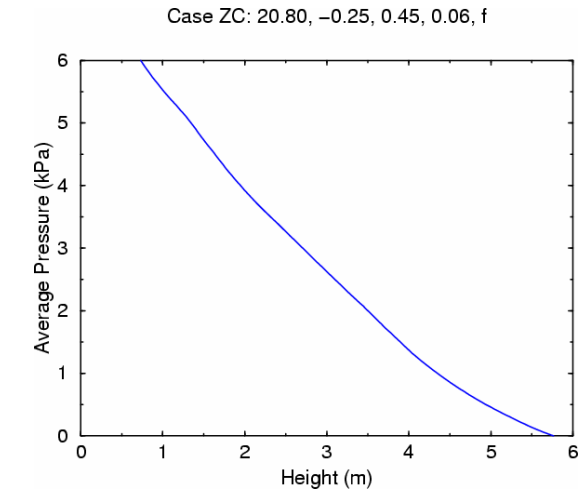

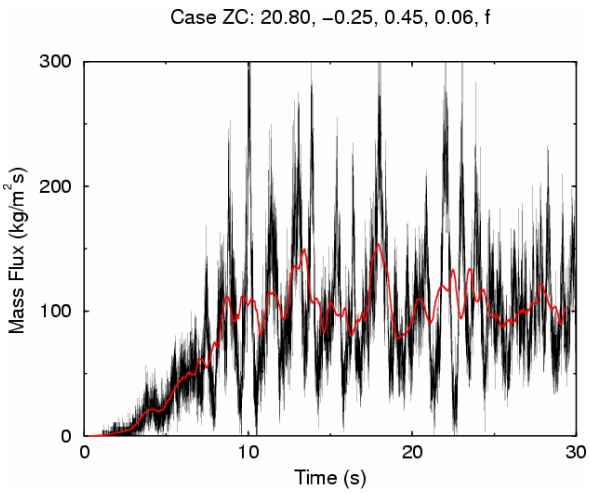

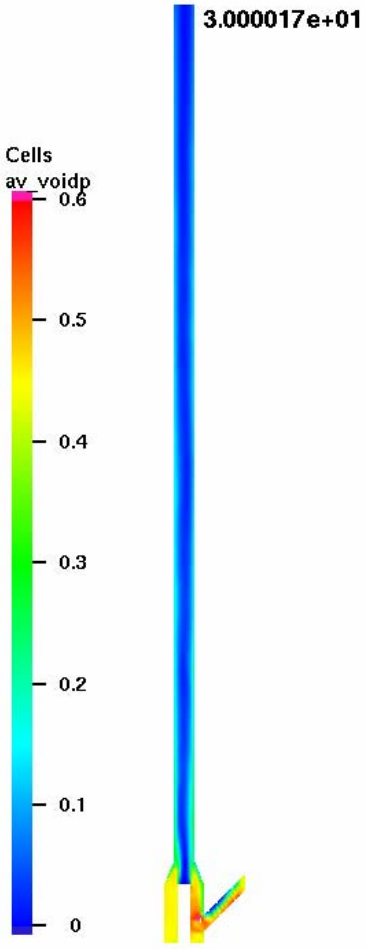

FCC18: FCC, $U = 5.3$ m/s, $G = 104$ kg/m^2·s, $U_1 = 20.80$ m/s, $U_3 = 0.06$ m/s, $U_2 = 0.25$ m/s, $\varepsilon_2 = 0.45$.
Comments: Compare to FCC01 and FCC17 to assess particle size distribution 100-180 μm (Case ZE)

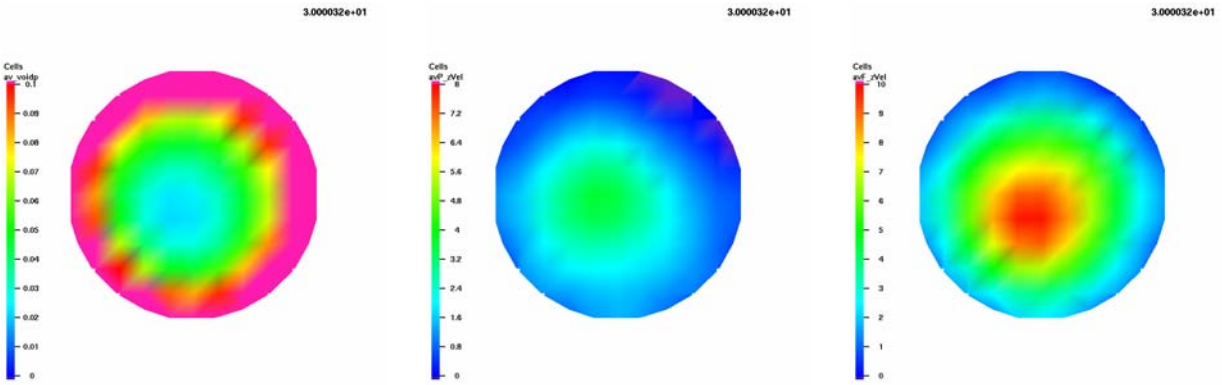

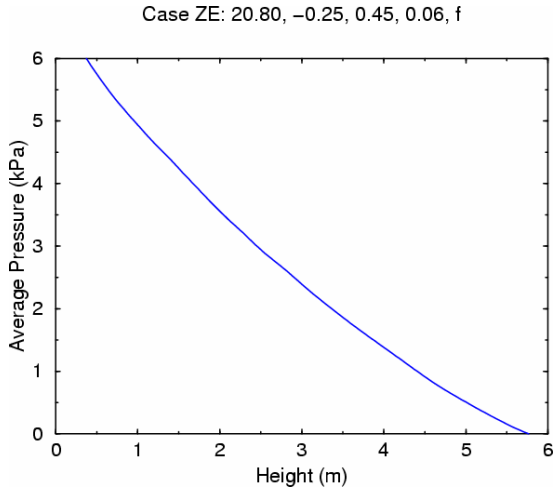

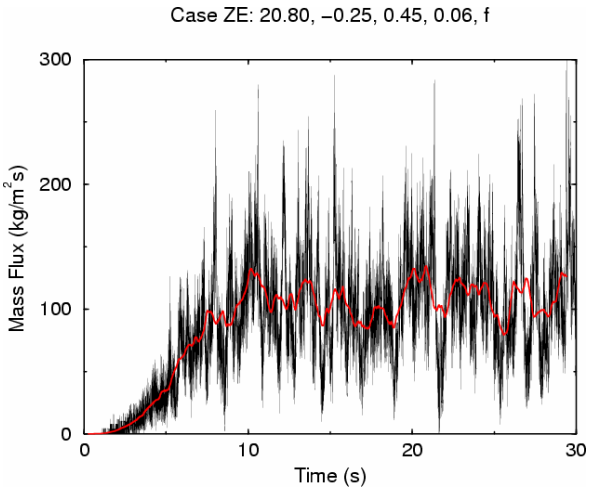

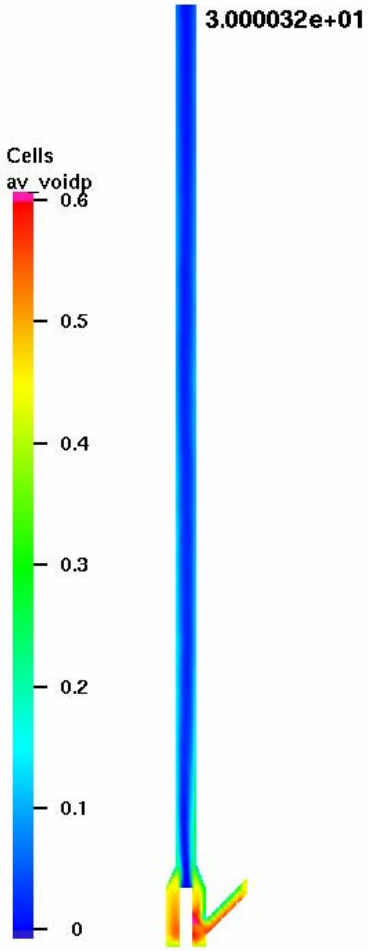

FCC19: FCC, $U = 5.3$ m/s, $G = 104$ kg/m^2·s, $U_1 = 20.80$ m/s, $U_3 = 0.06$ m/s, $U_2 = 0.25$ m/s, $\varepsilon_2 = 0.45$.
Comments: Compare to FCC01 to assess turning off turbulence model (Case ZG)

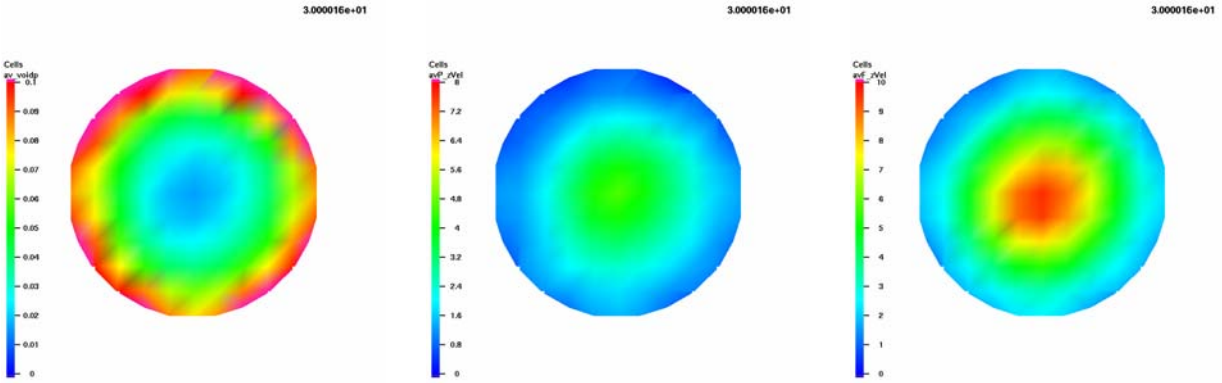

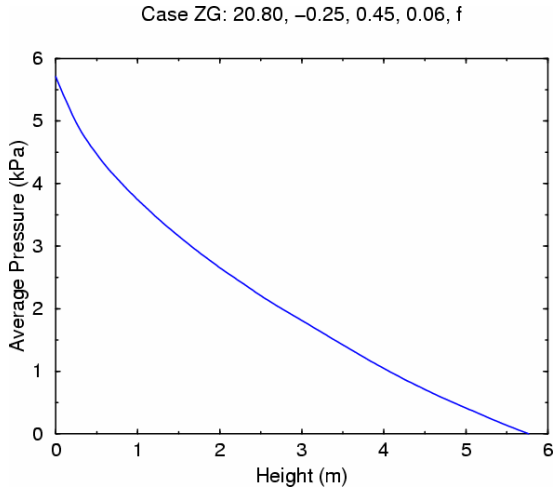

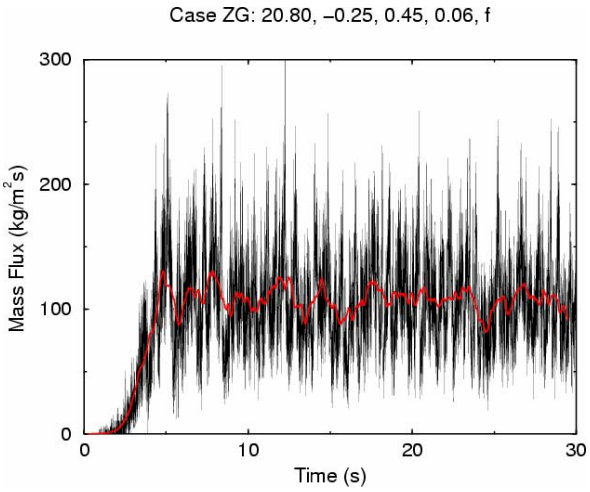

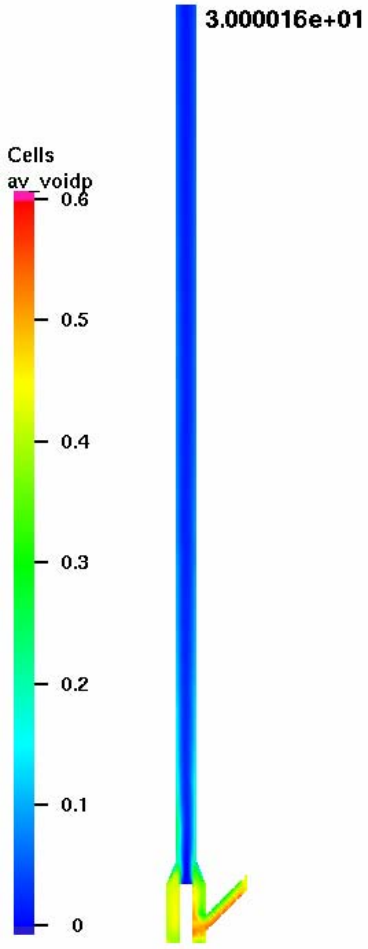

FCC21: FCC, $U = 7.4$ m/s, $G = 104$ kg/m^2·s, $U_1 = 28.65$ m/s, $U_3 = 0.06$ m/s, $U_2 = 0.25$ m/s, $\varepsilon_2 = 0.45$.
Comments: FCC high-gas, high-solids baseline case (Case 7)

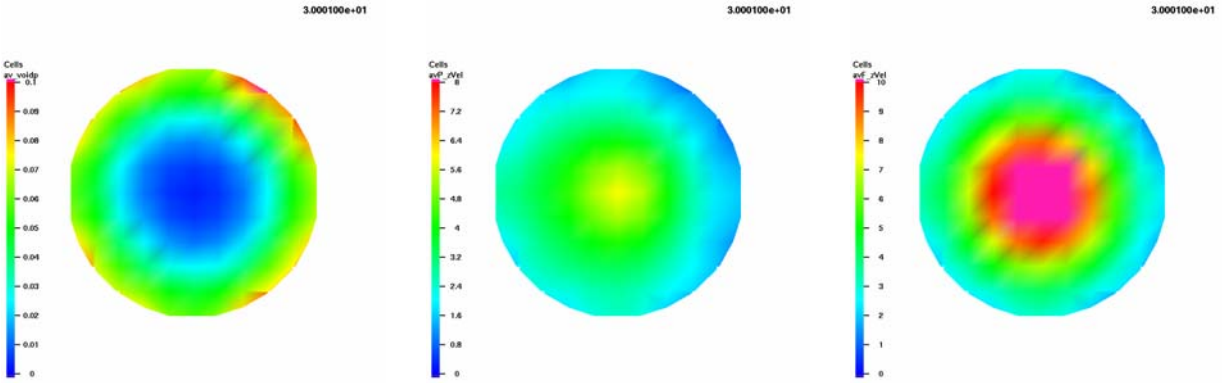

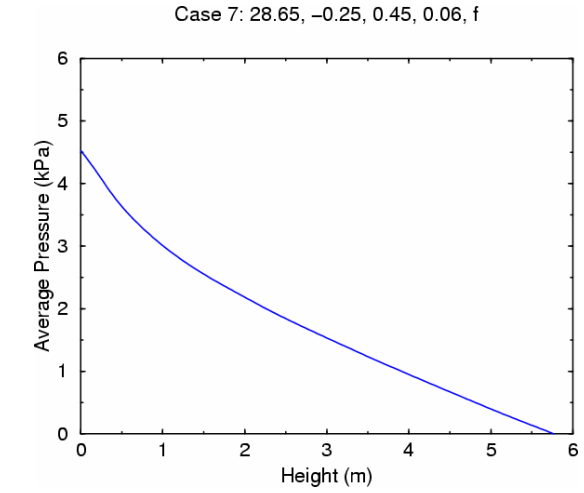

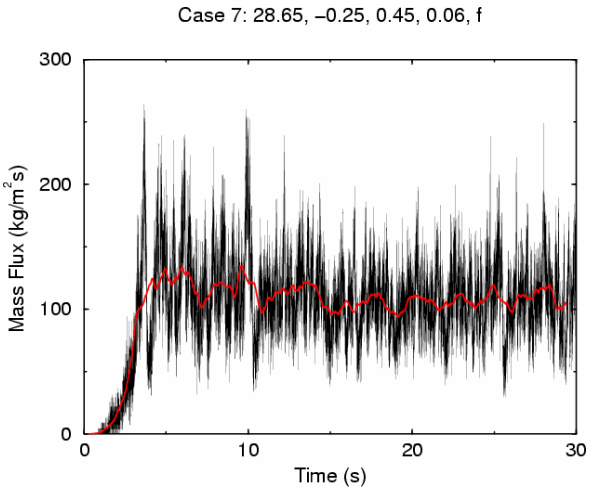

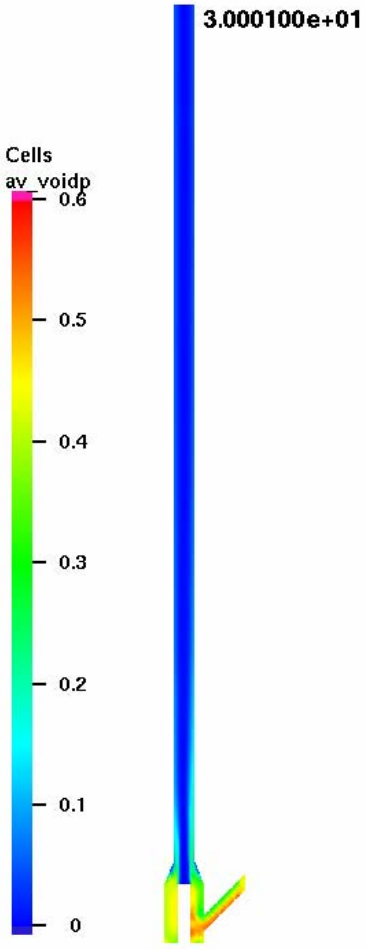

FCC22: FCC, $U = 7.4$ m/s, $G = 55$ kg/m^2·s, $U_1 = 28.65$ m/s, $U_3 = 0.06$ m/s, $U_2 = 0.20$ m/s, $\varepsilon_2 = 0.35$.
Comments: FCC high-gas, low-solids baseline case (Case 5)

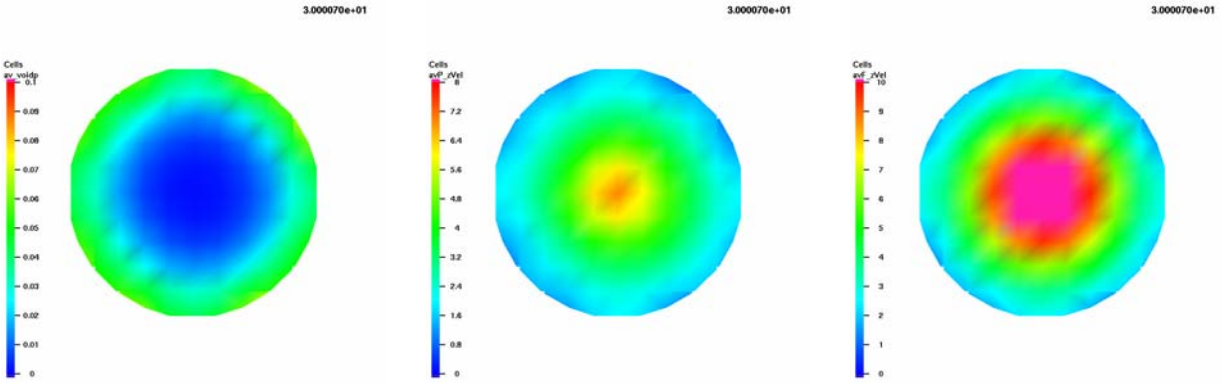

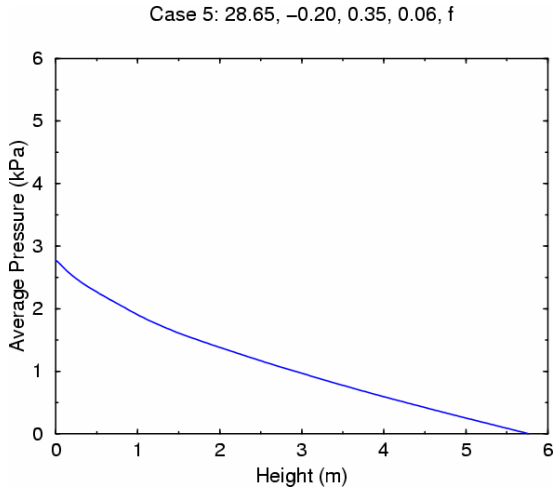

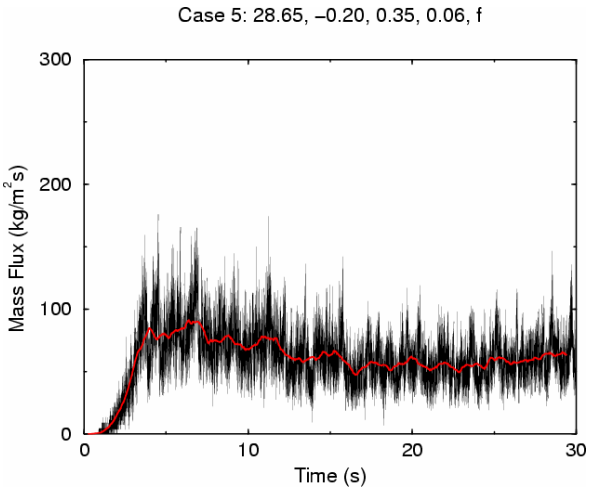

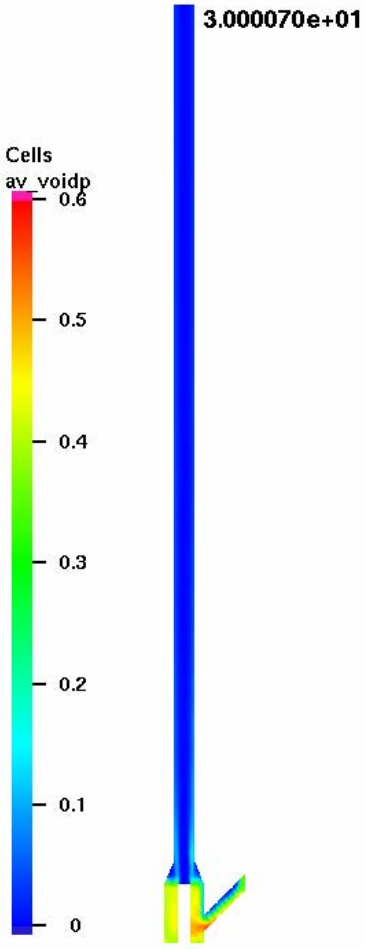

FCC23: FCC, $U = 7.4$ m/s, $G = 55$ kg/m^2·s, $U_1 = 28.65$ m/s, $U_3 = 0.06$ m/s, $U_2 = 0.1077$ m/s, $\varepsilon_2 = 0.50$.
Comments: Compare to FCC22 to assess standpipe boundary condition (Case 9)

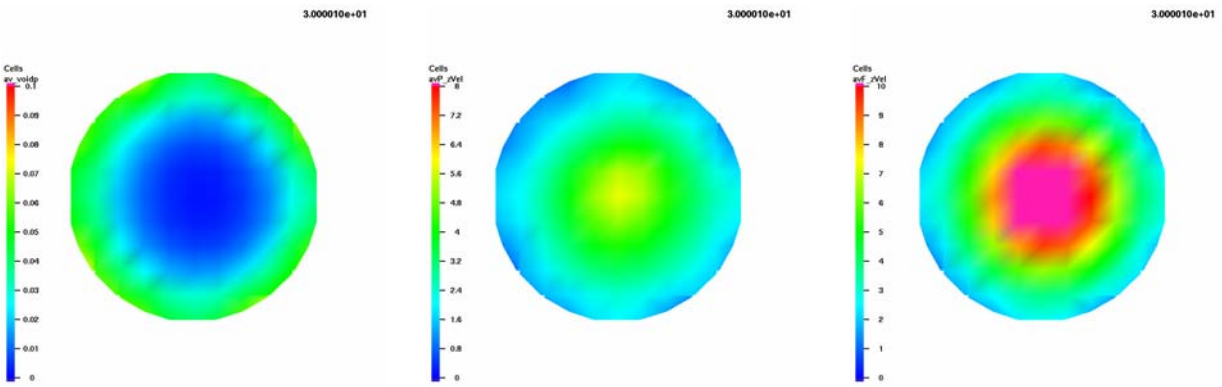

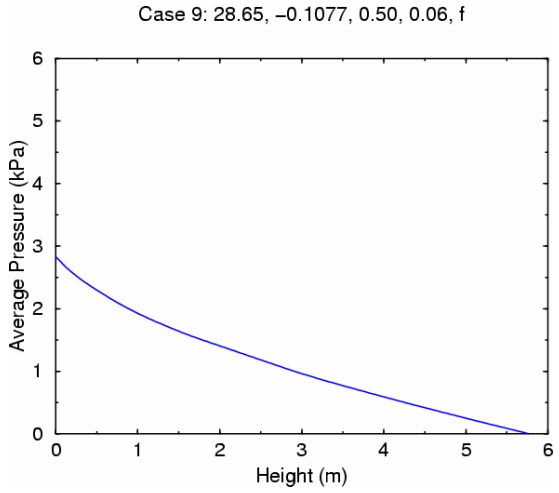

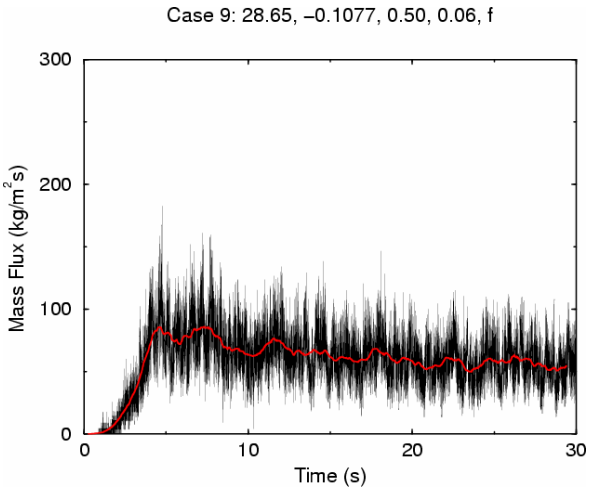

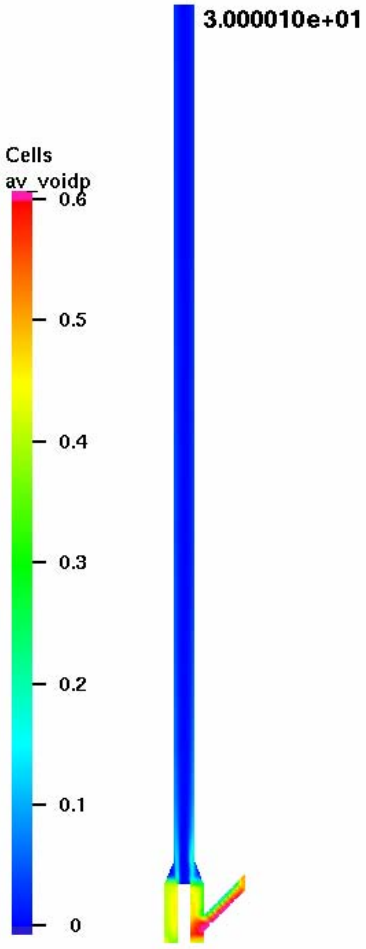

FCC24: FCC, $U = 7.4$ m/s, $G = 104$ kg/m^2·s, $U_1 = 41.60$ m/s, $U_3 = 0.06$ m/s, $U_2 = 0.25$ m/s, $\varepsilon_2 = 0.45$.
Comments: Compare to FCC21 to assess half-open motive-air tube (Case 3)

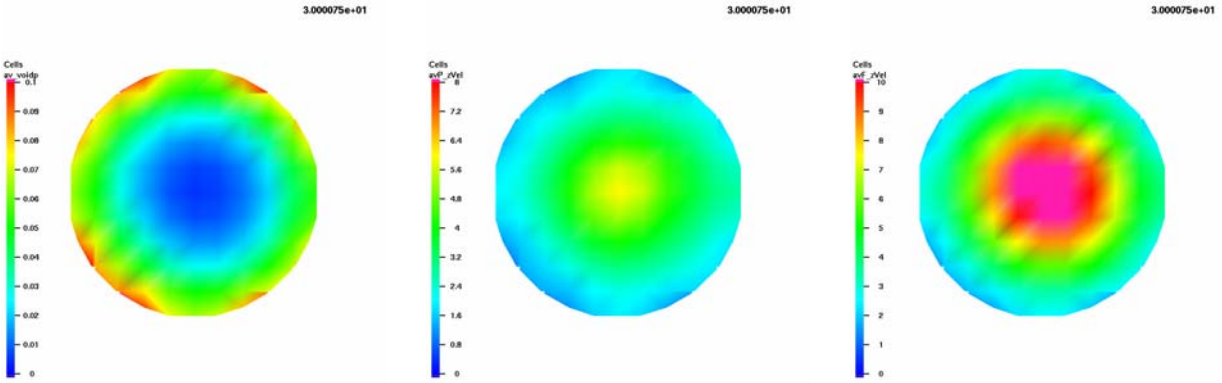

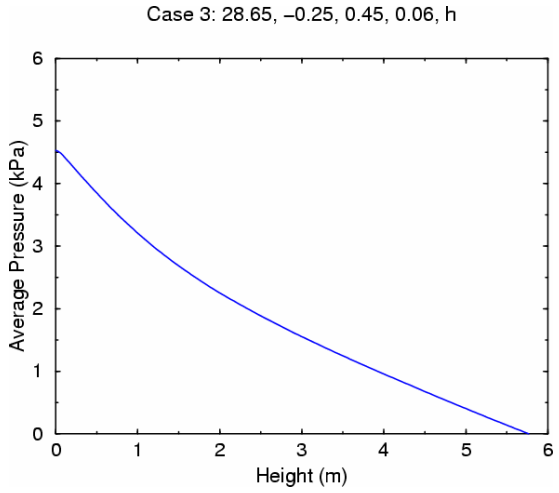

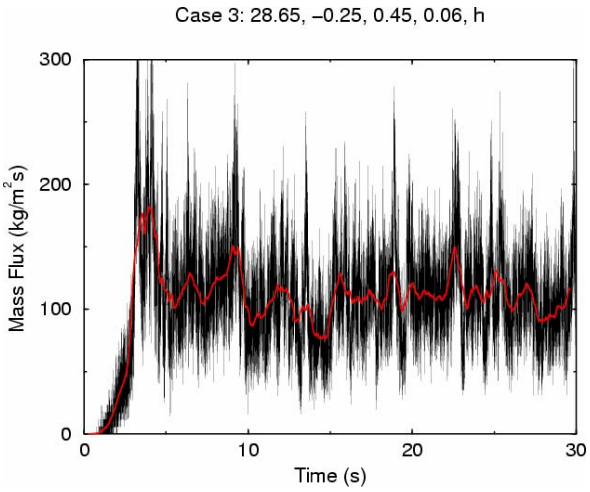

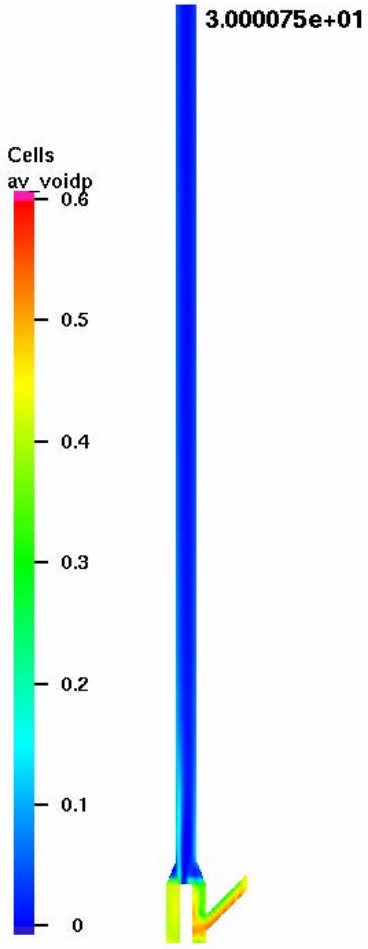

FCC25: FCC, $U = 7.4$ m/s, $G = 104$ kg/m^2·s, $U_1 = 28.65$ m/s, $U_3 = 0.03$ m/s, $U_2 = 0.25$ m/s, $\varepsilon_2 = 0.45$.
Comments: Compare to FCC21 to assess reduced fluidization velocity (Case B)

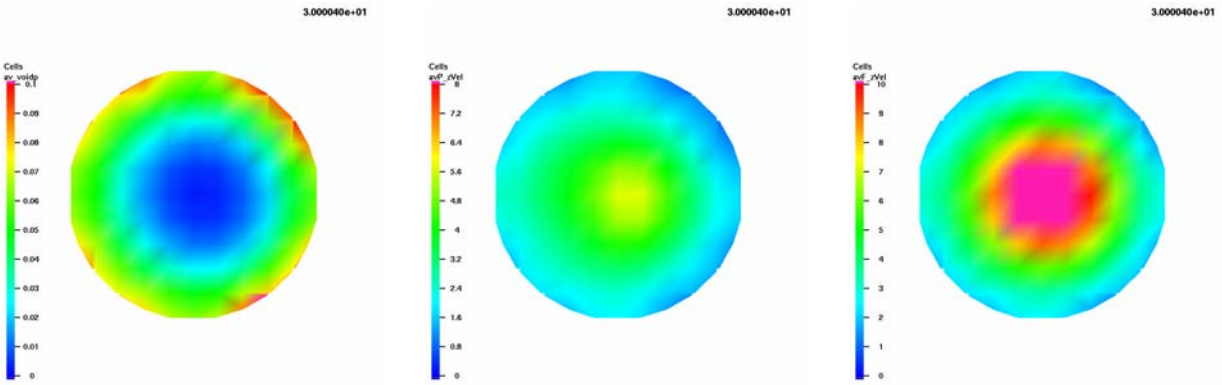

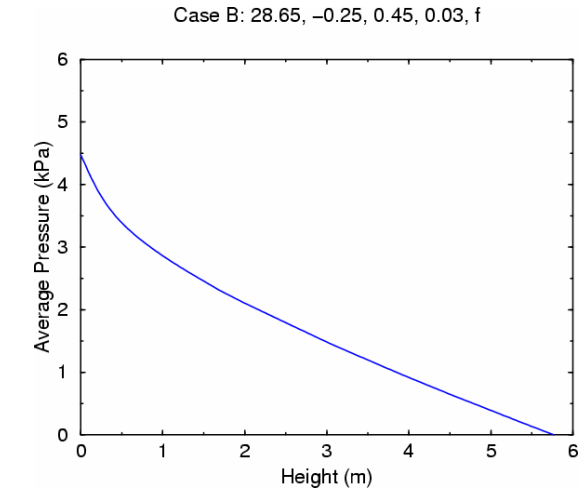

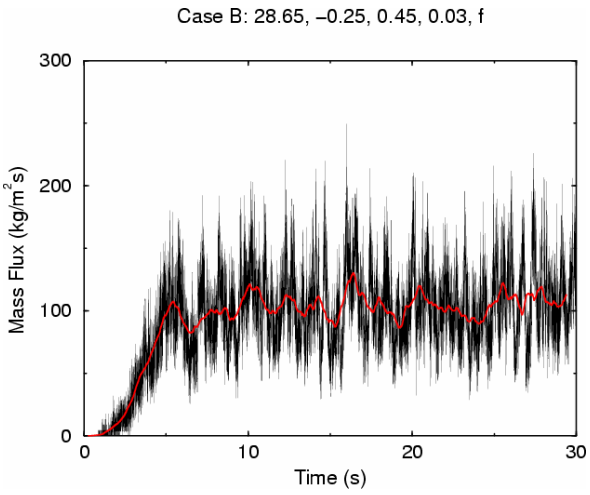

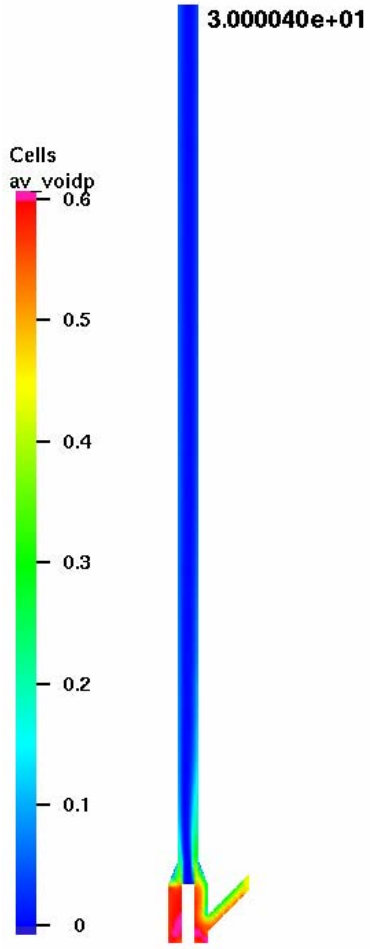

FCC26: FCC, $U = 7.4$ m/s, $G = 104$ kg/m^2·s, $U_1 = 28.65$ m/s, $U_3 = 0.09$ m/s, $U_2 = 0.25$ m/s, $\varepsilon_2 = 0.45$.
Comments: Compare to FCC21 to assess increased fluidization velocity (Case D)

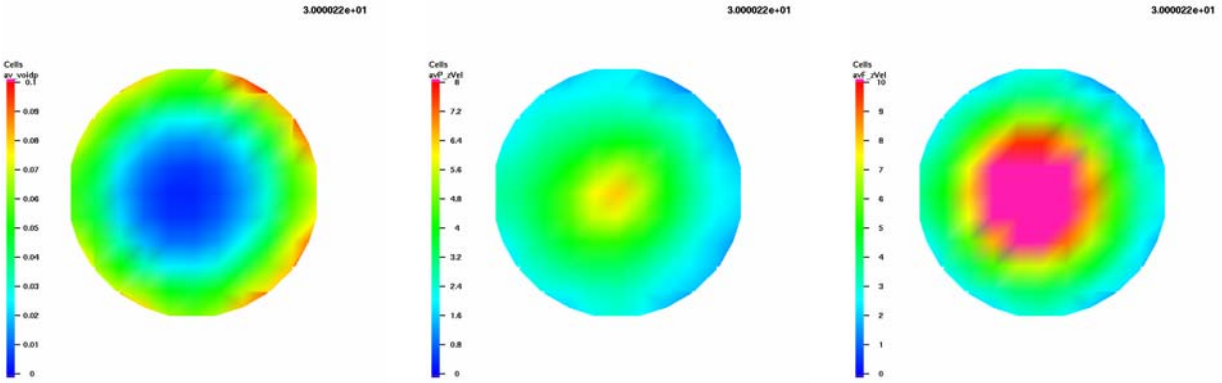

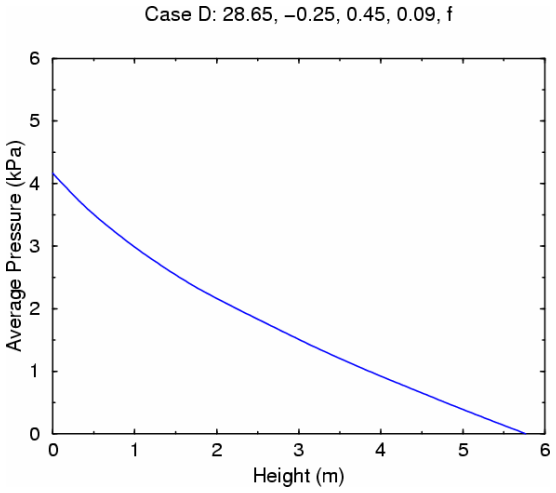

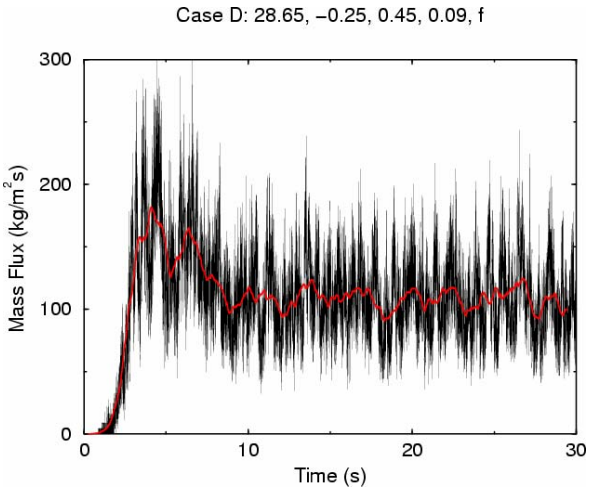

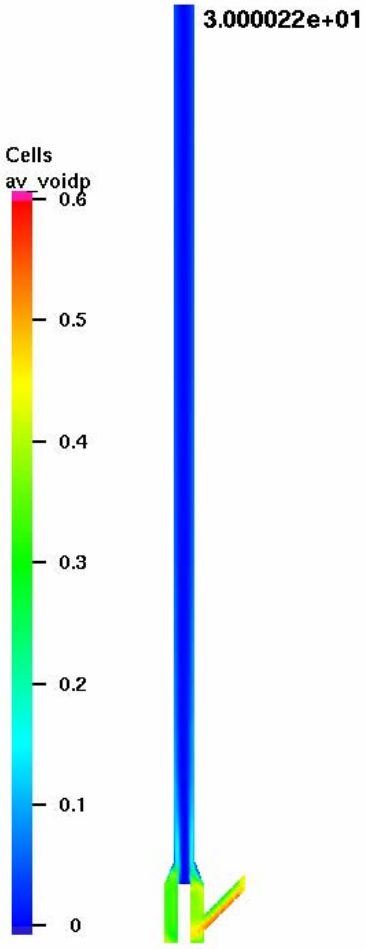

FCC27: FCC, $U = 7.4$ m/s, $G = 153$ kg/m^2·s, $U_1 = 28.65$ m/s, $U_3 = 0.06$ m/s, $U_2 = 0.30$ m/s, $\varepsilon_2 = 0.50$.
Comments: Compare to FCC21 and FCC02 to assess increased solids mass flux (Case 4)

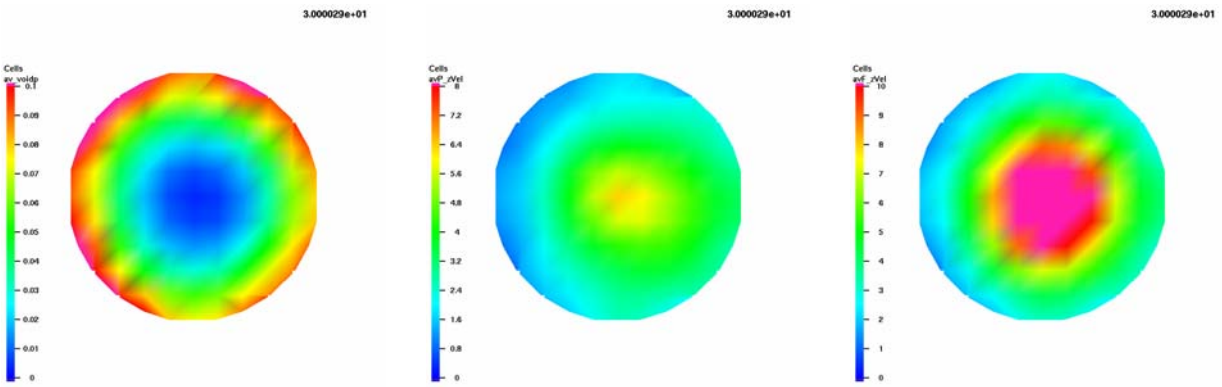

Case 4: 28.65, –0.30, 0.50, 0.06, f

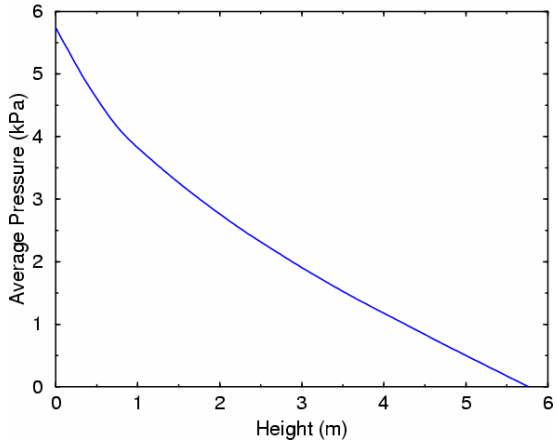

Case 4: 28.65, –0.30, 0.50, 0.06, f

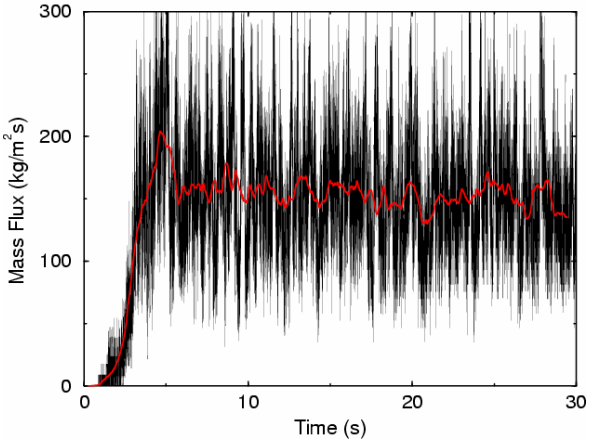

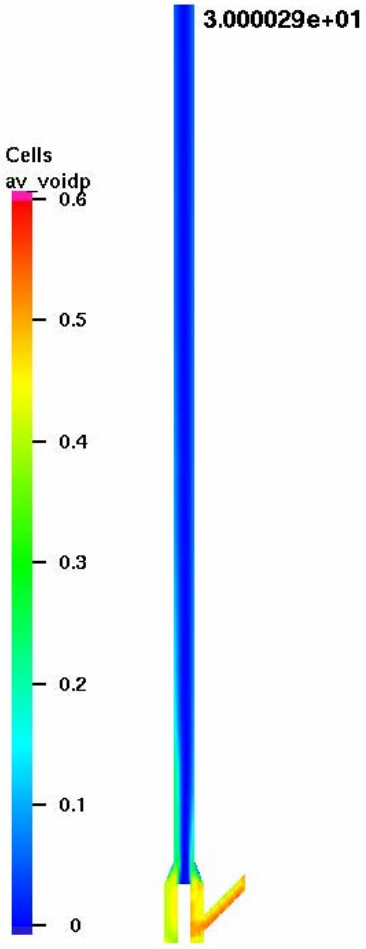

FCC28: FCC, $U = 7.4$ m/s, $G = 104$ kg/m^2·s, $U_1 = 28.65$ m/s, $U_3 = 0.06$ m/s, $U_2 = 0.3125$ m/s, $\varepsilon_2 = 0.45$.
Comments: Compare to FCC21 with reduced particle mass density of 1020 kg/m^3 (Case I)

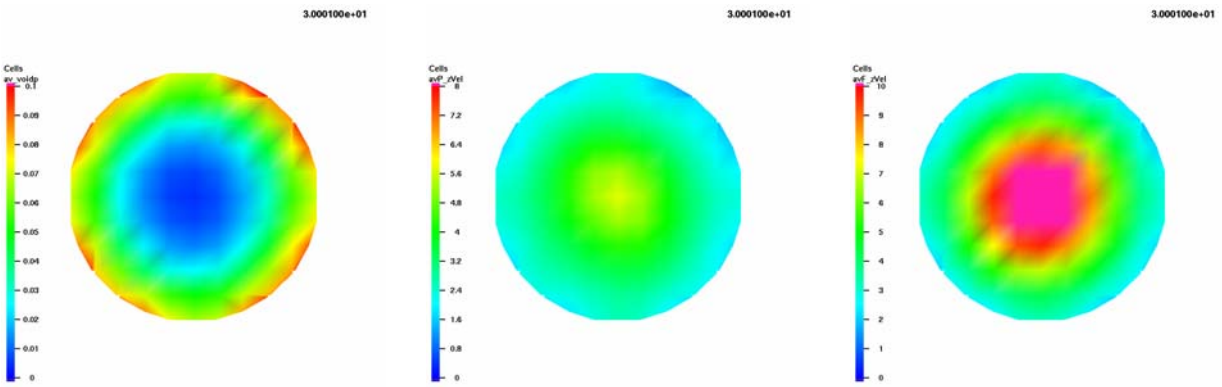

Case I: 28.65, –0.3125, 0.45, 0.06, f, l

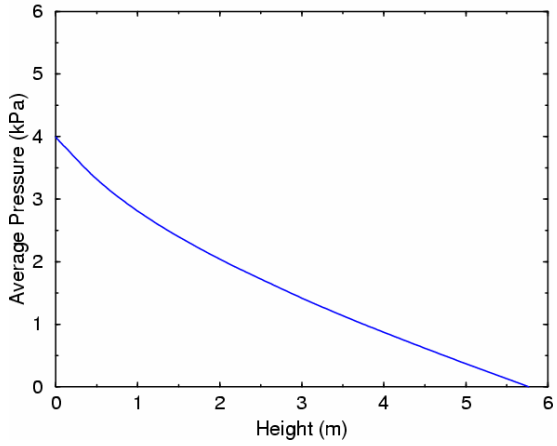

Case G: 28.65, –0.25, 0.45, 0.06, f, l

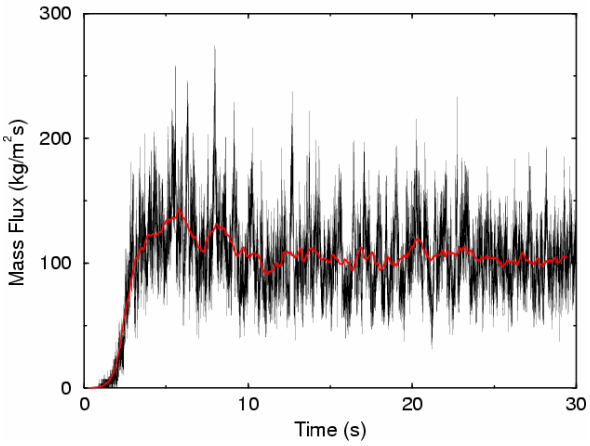

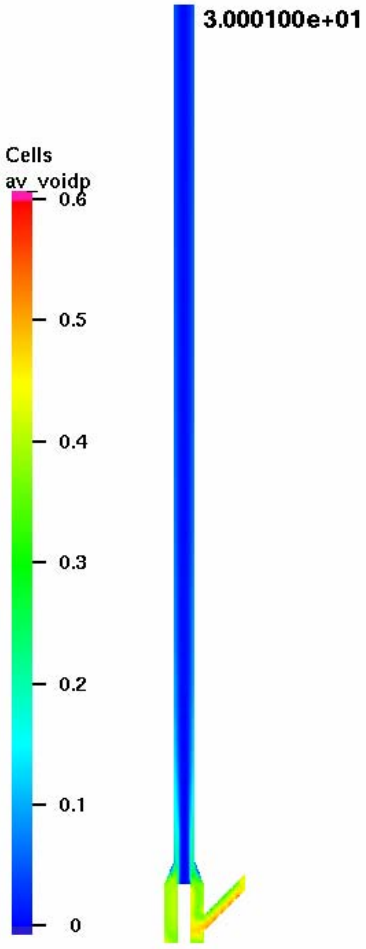

FCC29: FCC, $U = 7.4$ m/s, $G = 104$ kg/m^2·s, $U_1 = 28.65$ m/s, $U_3 = 0.06$ m/s, $U_2 = 0.25$ m/s, $\varepsilon_2 = 0.45$.
Comments: Compare to FCC21 to assess effect of drag model 2 instead of drag model 1 (Case J)

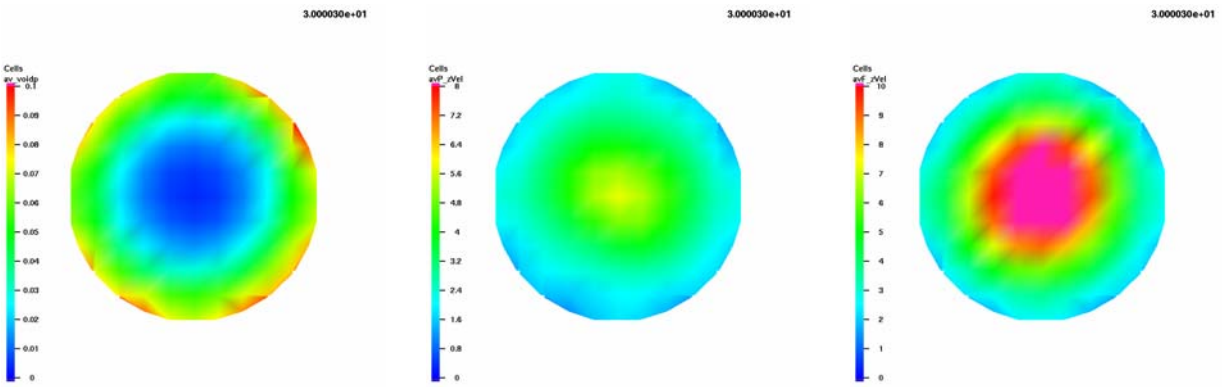

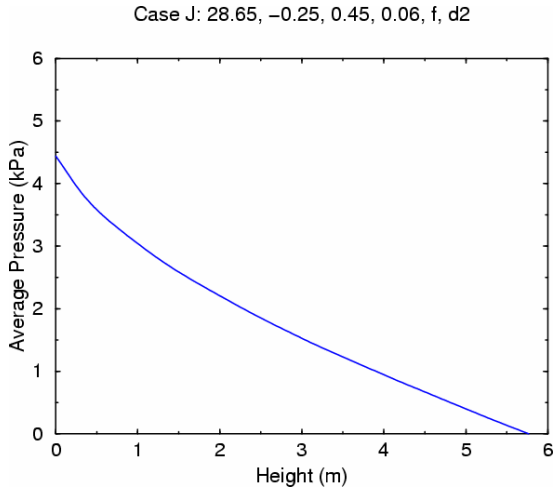

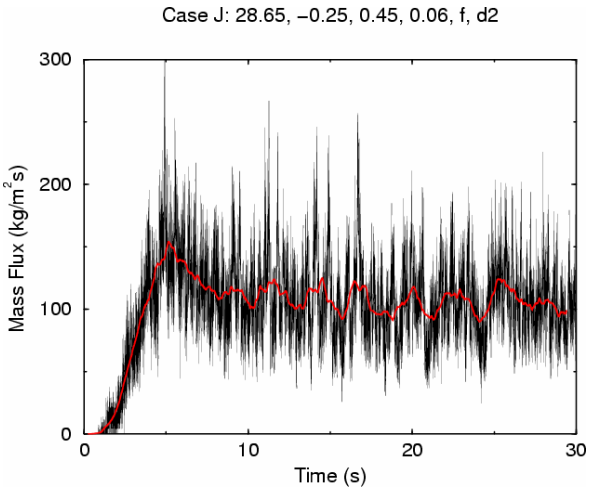

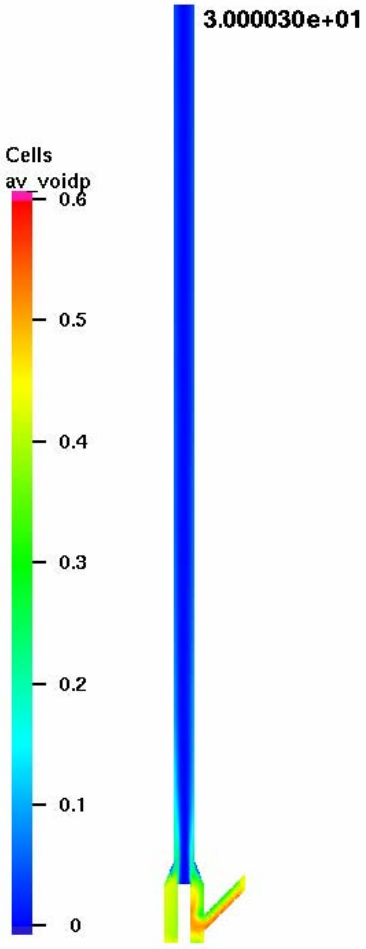

FCC30: FCC, $U = 7.4$ m/s, $G = 104$ kg/m^2·s, $U_1 = 28.65$ m/s, $U_3 = 0.06$ m/s, $U_2 = 0.25$ m/s, $\varepsilon_2 = 0.45$.
Comments: Compare to FCC21 to assess effect of drag model 3 instead of drag model 1 (Case L)

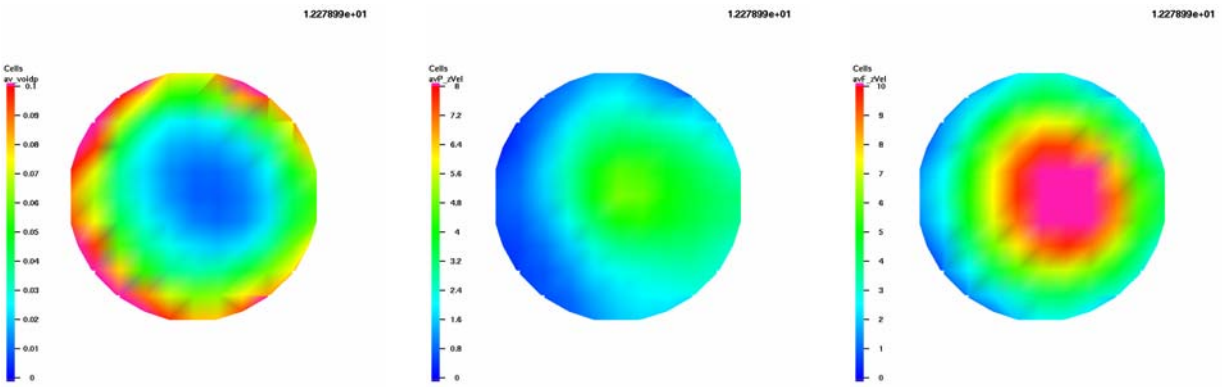

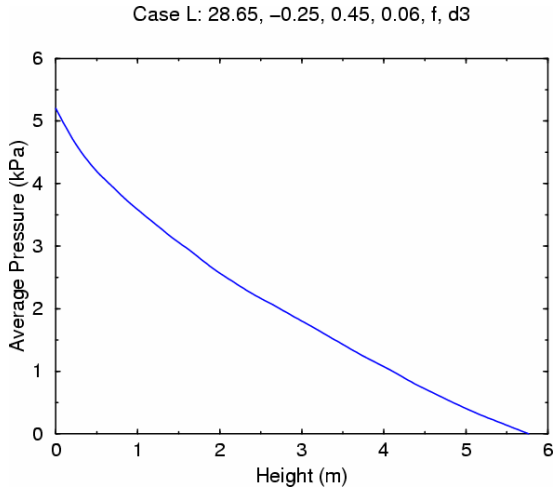

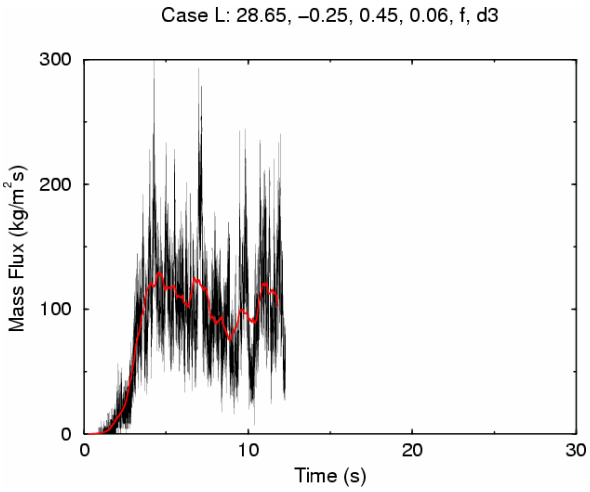

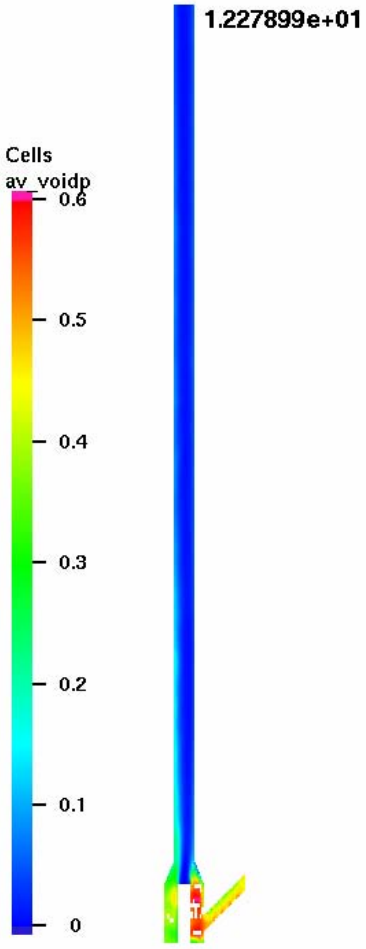

FCC31: FCC, $U = 7.4$ m/s, $G = 104$ kg/m^2·s, $U_1 = 28.65$ m/s, $U_3 = 0.06$ m/s, $U_2 = 0.25$ m/s, $\varepsilon_2 = 0.45$.
Comments: Compare to FCC21 to assess effect of increasing p-p interaction to 60% from 20% (Case N)

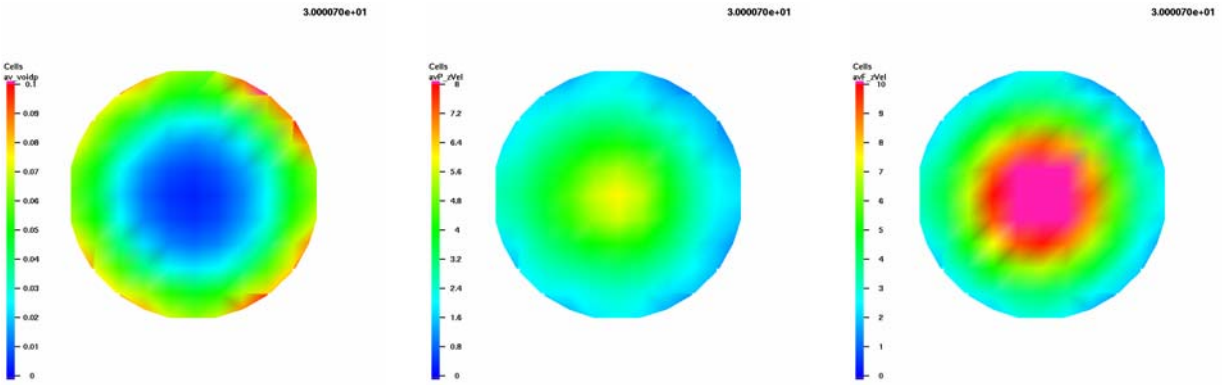

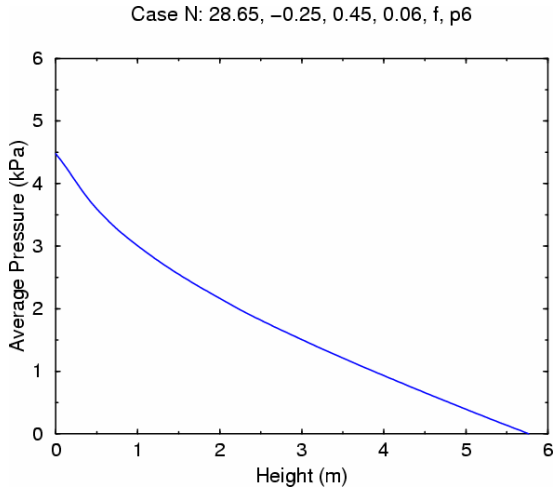

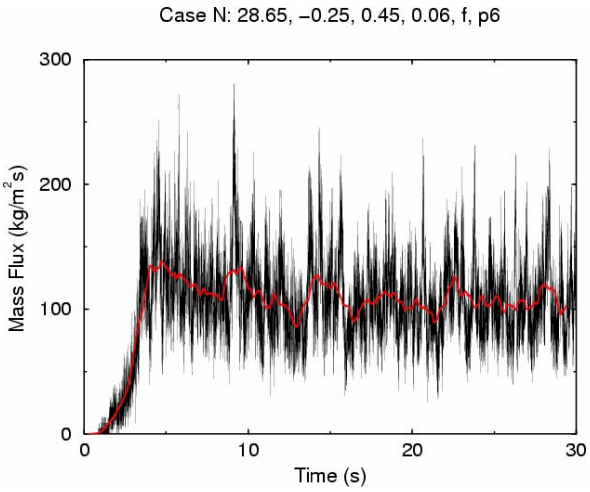

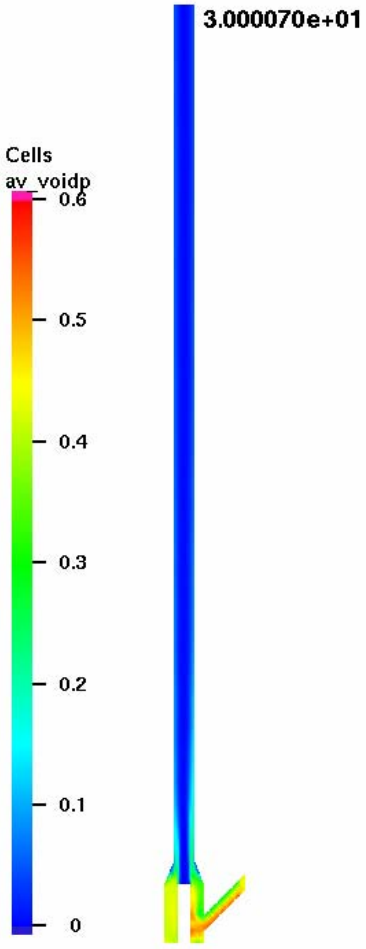

FCC32: FCC, $U = 7.4$ m/s, $G = 104$ kg/m^2·s, $U_1 = 28.65$ m/s, $U_3 = 0.06$ m/s, $U_2 = 0.25$ m/s, $\varepsilon_2 = 0.45$.
Comments: Compare to FCC21 to assess monodisperse particle size distribution of 100-110 µm (Case P)

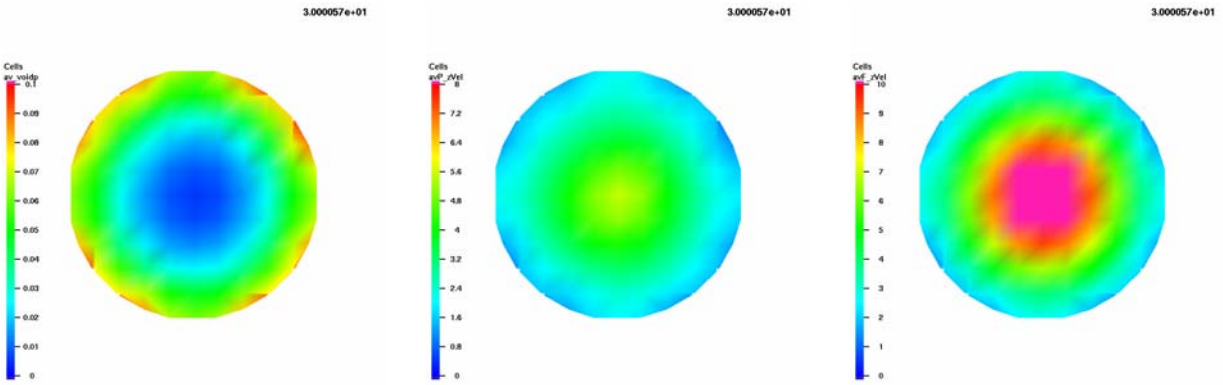

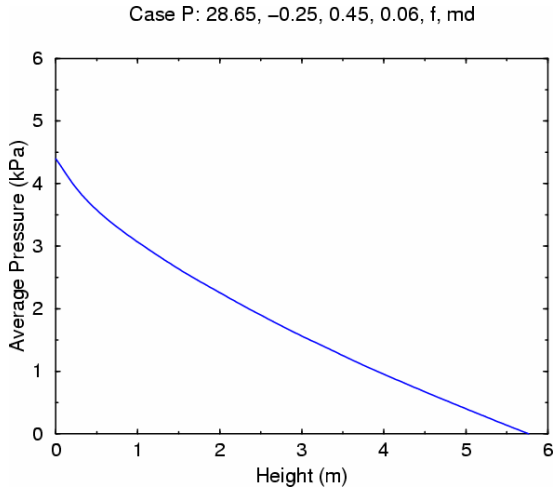

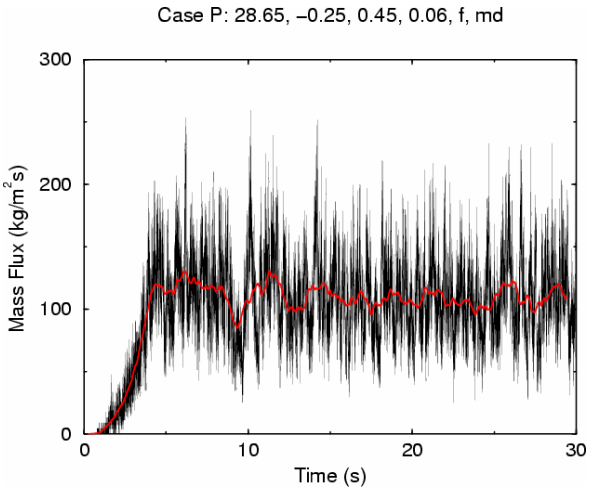

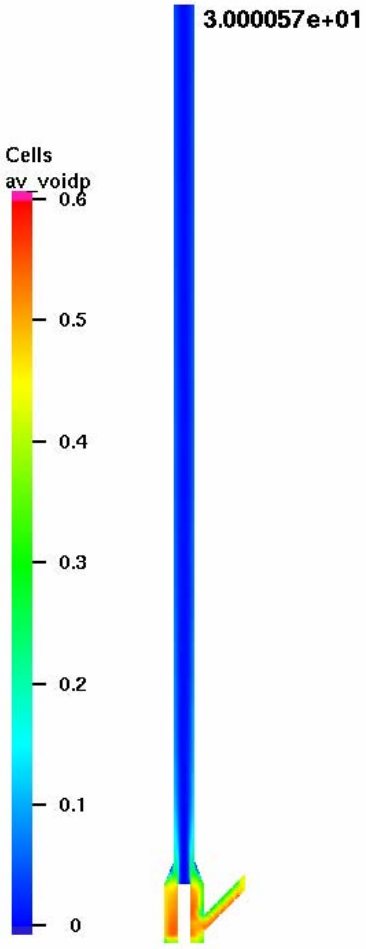

FCC33: FCC, $U = 7.4$ m/s, $G = 104$ kg/m^2·s, $U_1 = 28.65$ m/s, $U_3 = 0.06$ m/s, $U_2 = 0.25$ m/s, $\varepsilon_2 = 0.45$.
Comments: Compare to FCC21 to assess effect of specular walls (Case R)

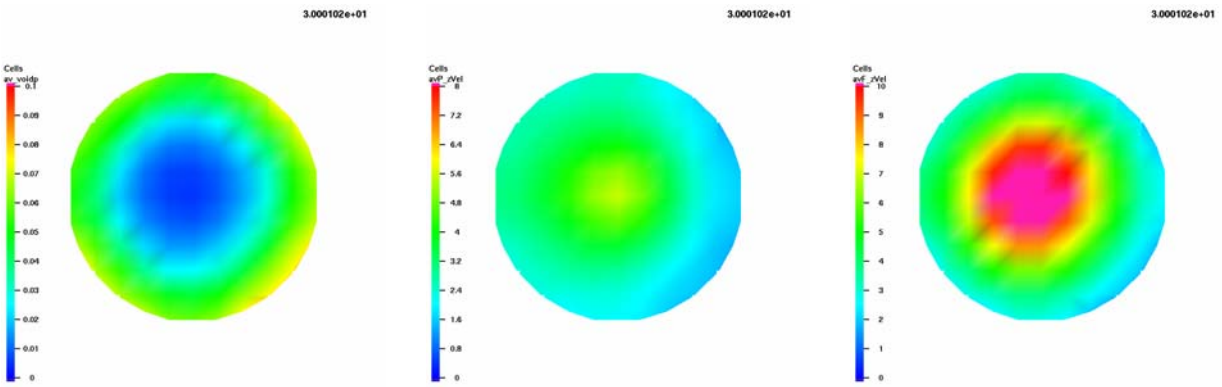

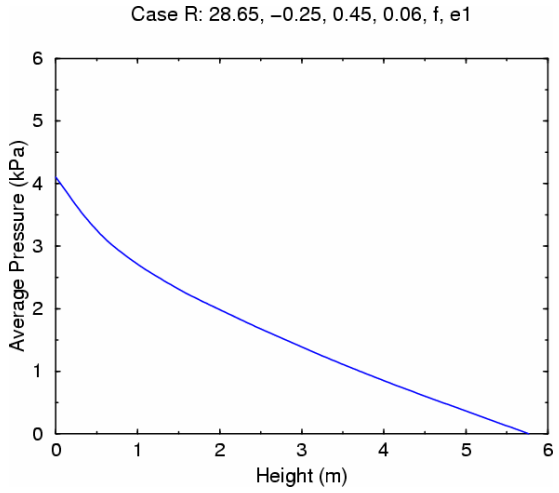

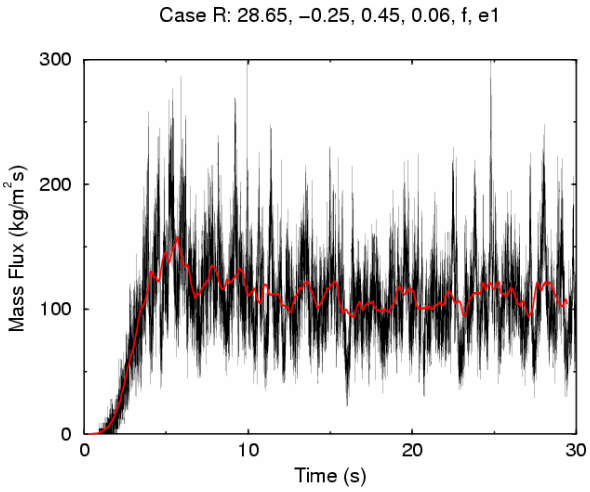

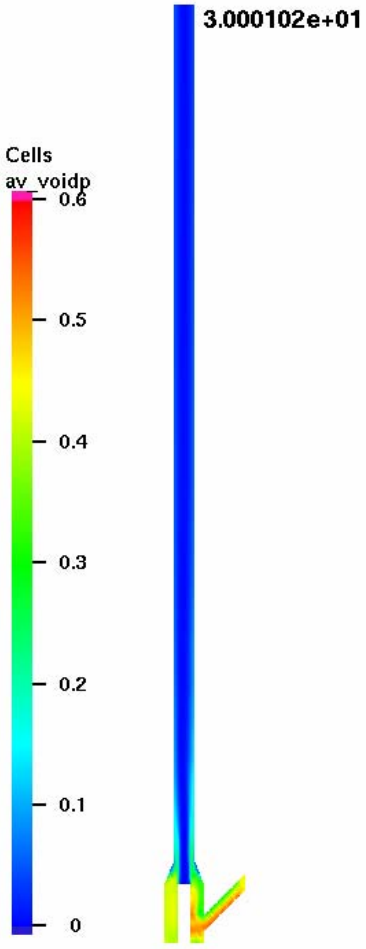

FCC34: FCC, $U = 7.4$ m/s, $G = 104$ kg/m^2·s, $U_1 = 28.65$ m/s, $U_3 = 0.06$ m/s, $U_2 = 0.25$ m/s, $\varepsilon_2 = 0.45$.
Comments: Compare to FCC21 to assess effect of diffuse walls (Case T)

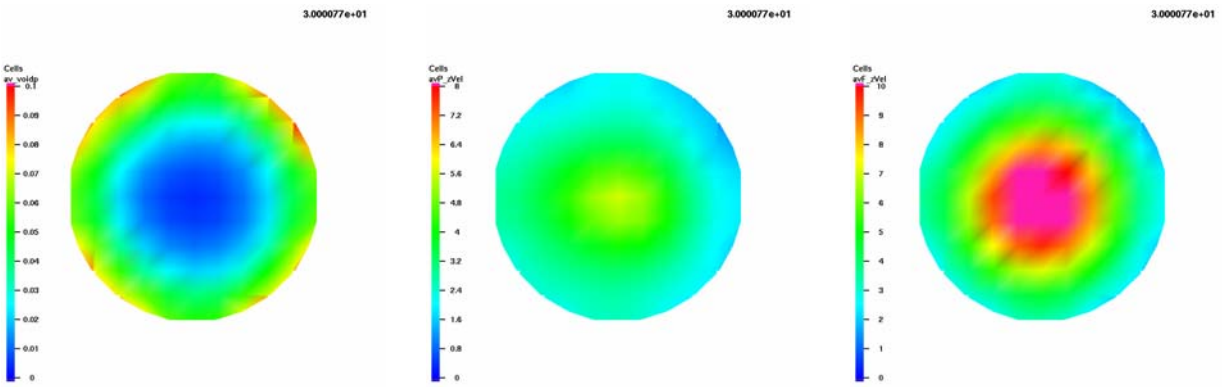

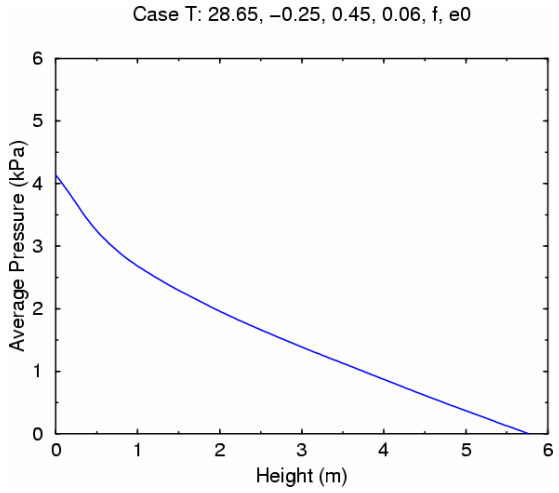

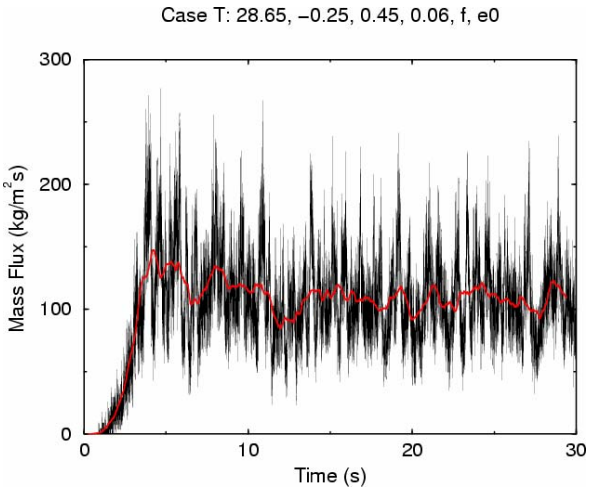

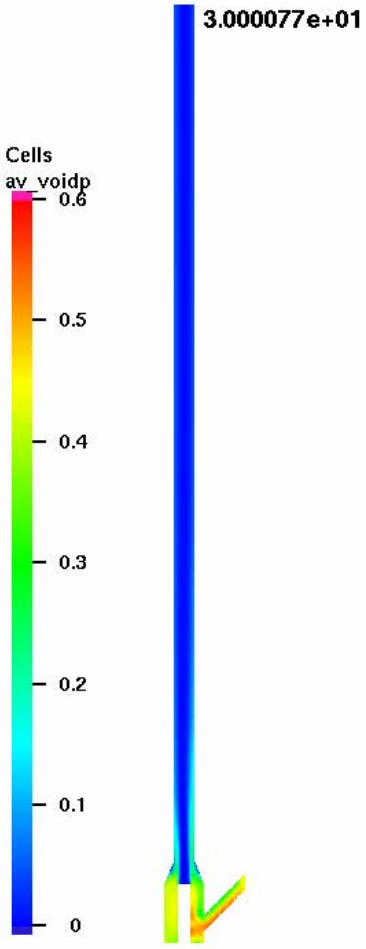

FCC35: FCC, $U = 7.4$ m/s, $G = 104$ kg/m^2·s, $U_1 = 28.65$ m/s, $U_3 = 0.06$ m/s, $U_2 = 0.25$ m/s, $\varepsilon_2 = 0.45$.
Comments: Compare to FCC21 to assess effect of increasing shear-stress exponent to 8 from 3 (Case Z)

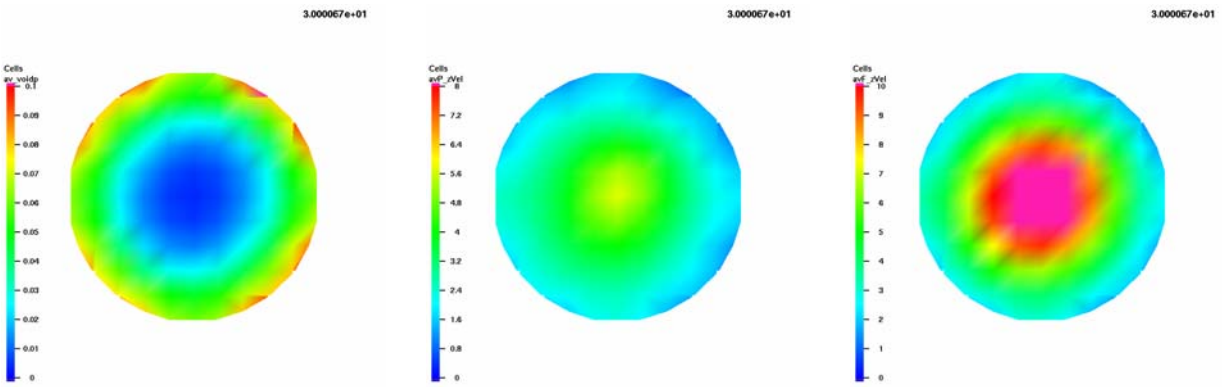

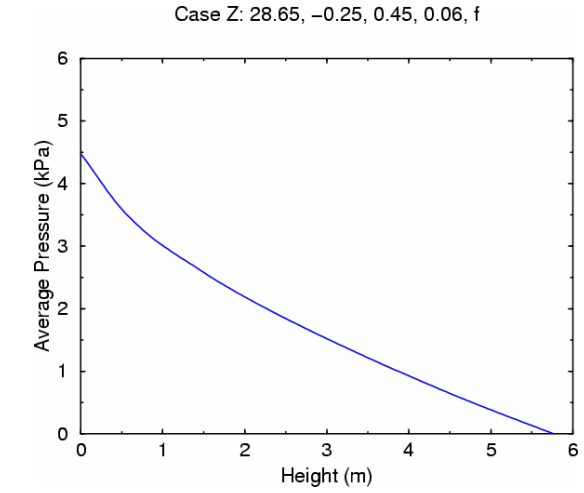

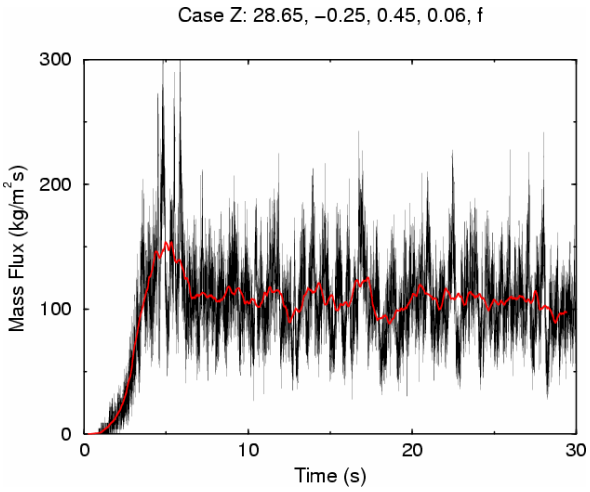

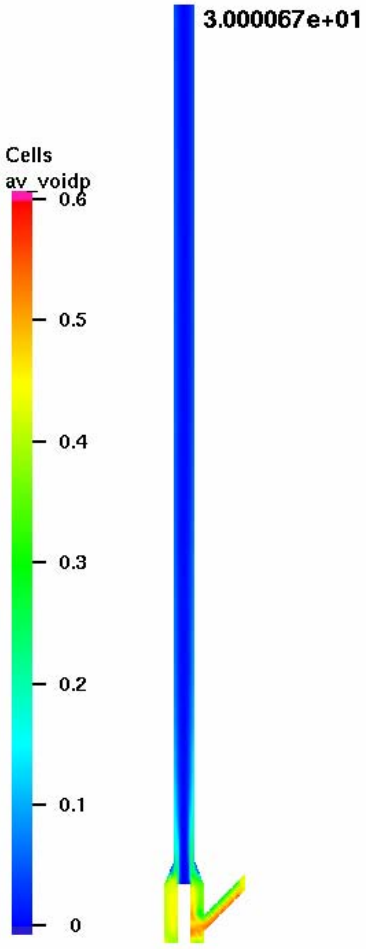

FCC36: FCC, $U = 7.4$ m/s, $G = 104$ kg/m^2·s, $U_1 = 28.65$ m/s, $U_3 = 0.06$ m/s, $U_2 = 0.25$ m/s, $\varepsilon_2 = 0.45$.
Comments: Compare to FCC21 to assess the effect of increasing close packing to 0.8 from 0.68 (Case ZB)

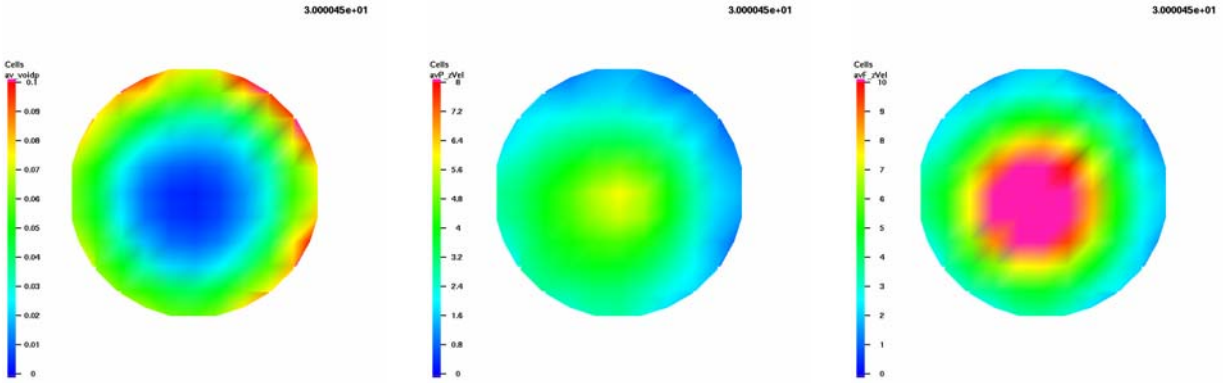

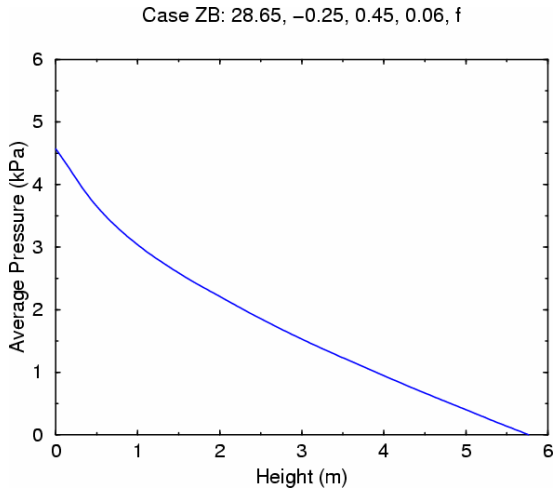

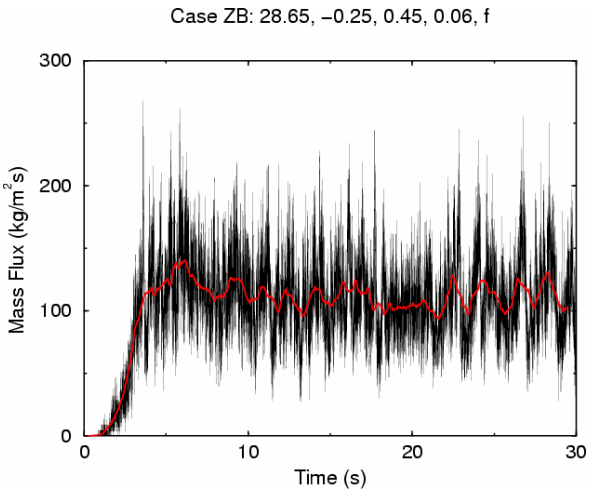

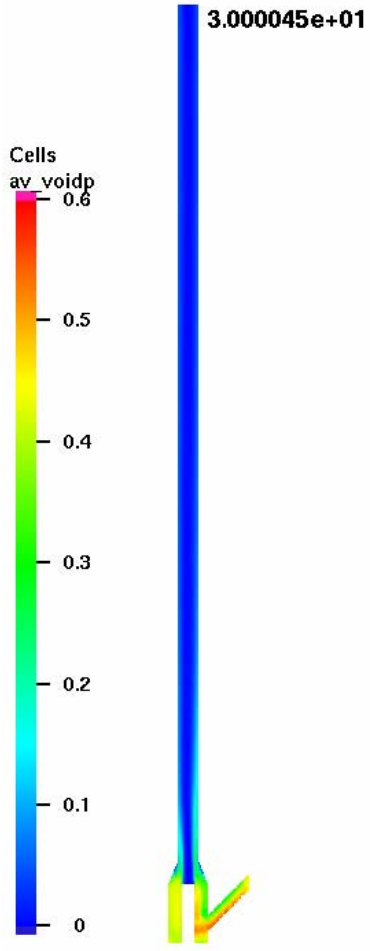

FCC37: FCC, $U = 7.4$ m/s, $G = 104$ kg/m^2·s, $U_1 = 28.65$ m/s, $U_3 = 0.06$ m/s, $U_2 = 0.25$ m/s, $\varepsilon_2 = 0.45$.
Comments: Compare to FCC21 and FCC38 to assess particle size distribution of 160-180 μm (Case ZD)

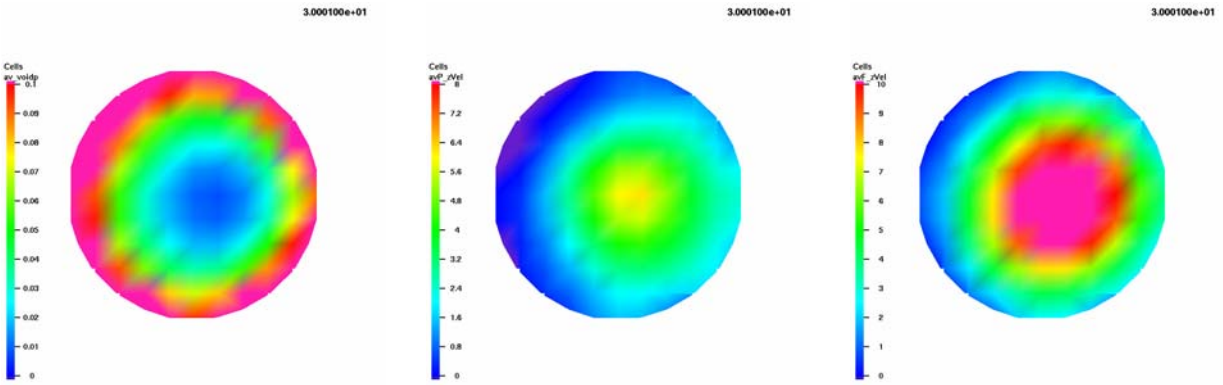

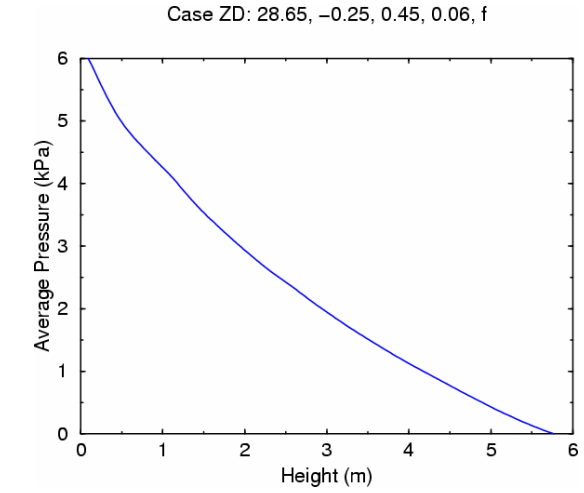

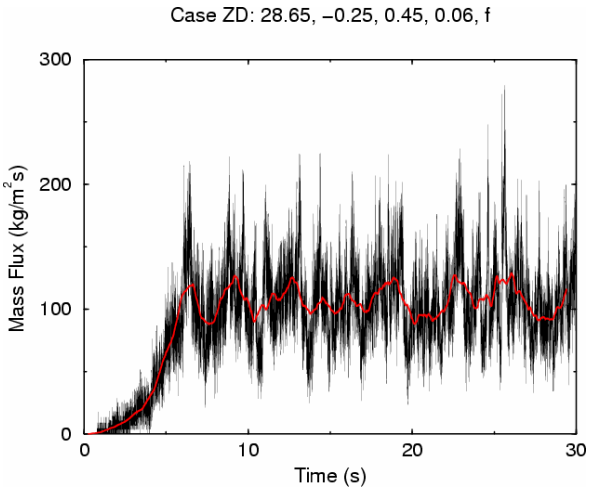

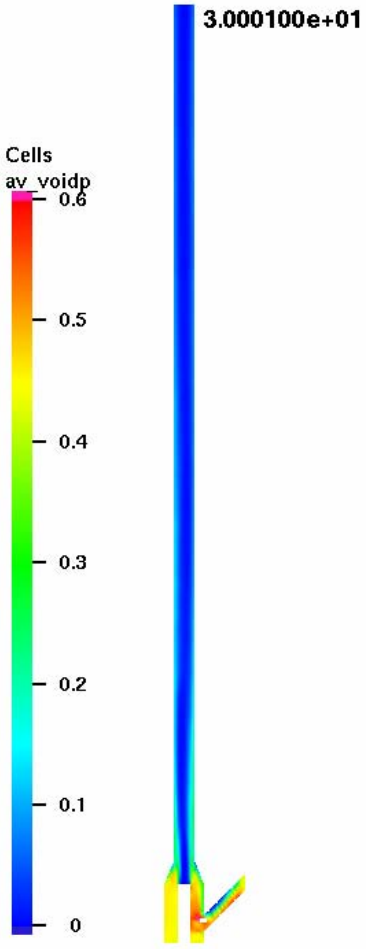

FCC38: FCC, $U = 7.4$ m/s, $G = 104$ kg/m^2·s, $U_1 = 28.65$ m/s, $U_3 = 0.06$ m/s, $U_2 = 0.25$ m/s, $\varepsilon_2 = 0.45$.
Comments: Compare to FCC21 and FCC37 to assess particle size distribution 100-180 μm (Case ZF)

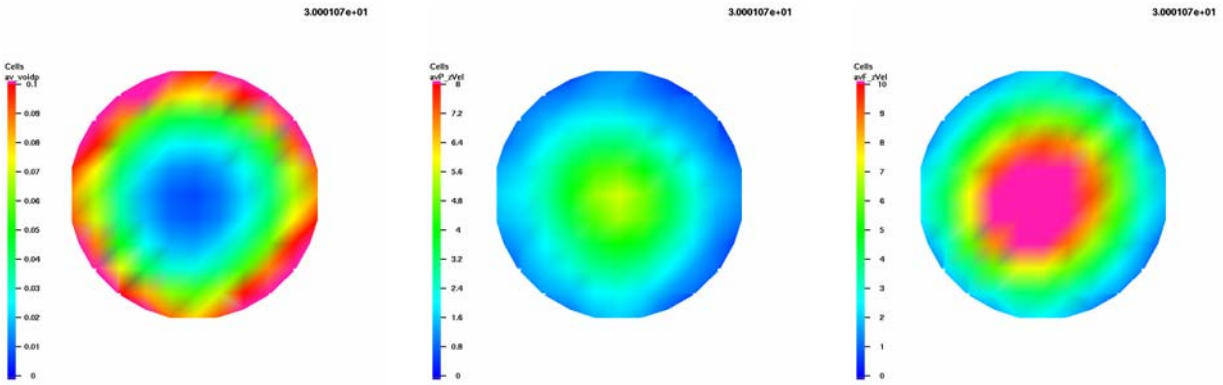

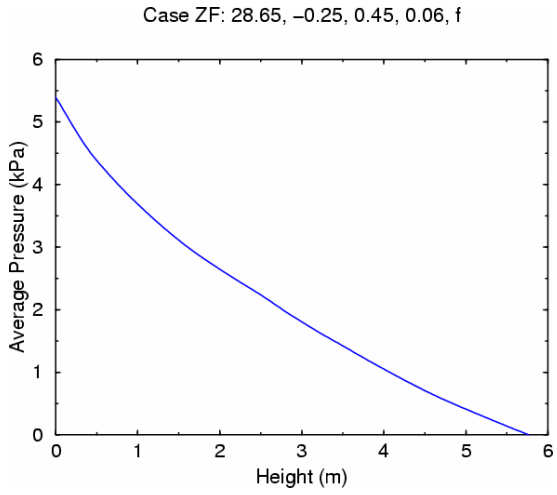

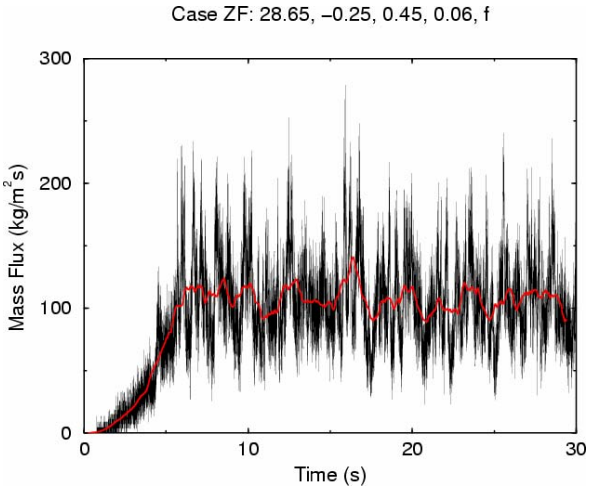

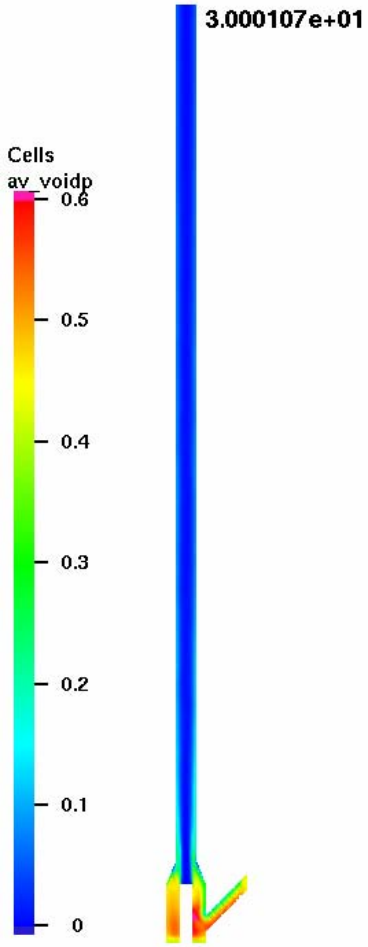

FCC39: FCC, $U = 7.4$ m/s, $G = 104$ kg/m^2·s, $U_1 = 28.65$ m/s, $U_3 = 0.06$ m/s, $U_2 = 0.25$ m/s, $\varepsilon_2 = 0.45$.
Comments: Compare to FCC21 to assess turning off turbulence model (Case ZH)

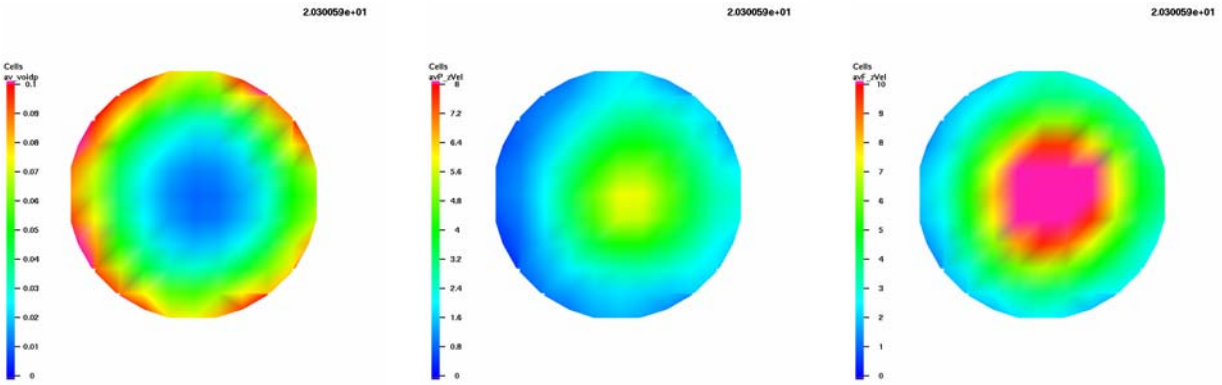

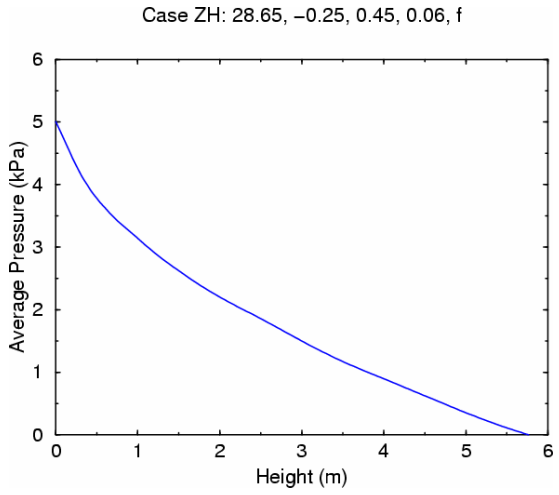

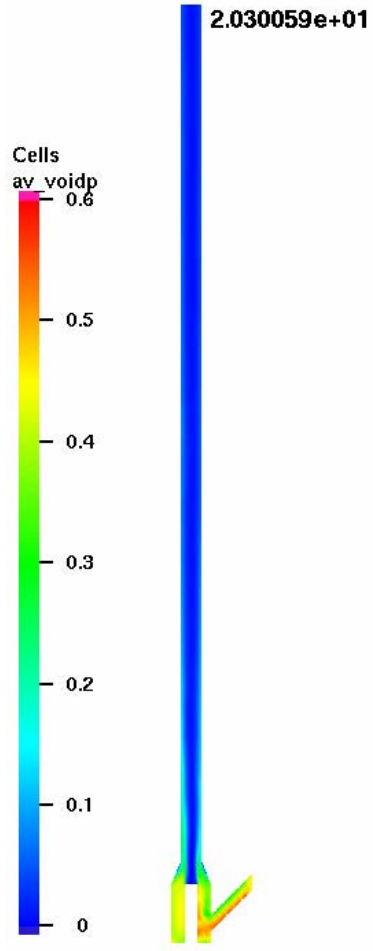

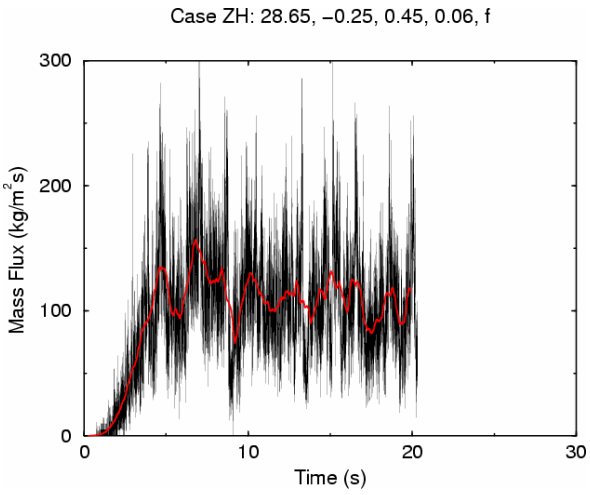

GLS01: Glass, U = 5.3 m/s, G = 100 kg/m^2·s, U_1 = 20.80 m/s, U_3 = 0.24 m/s, U_2 = 0.30 m/s, ε_2 = 0.25.
Comments: Glass low-gas, high-solids baseline case (Case 05)

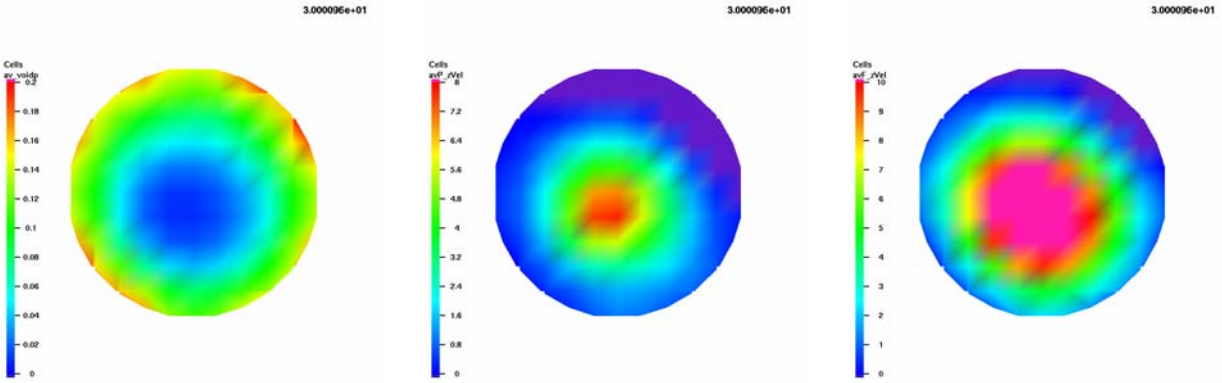

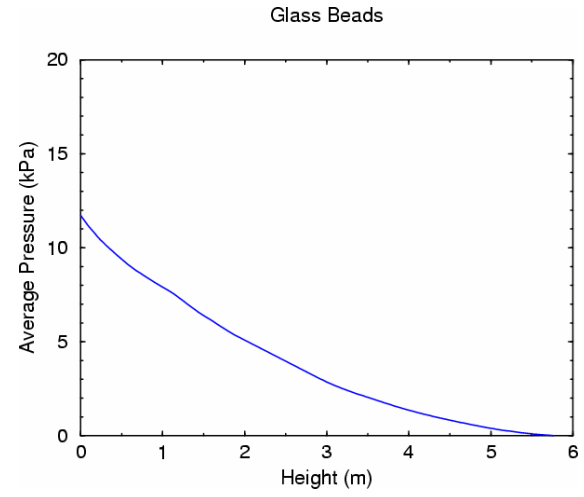

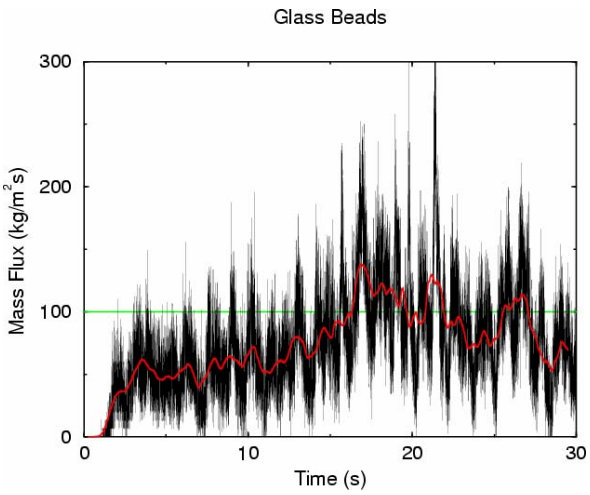

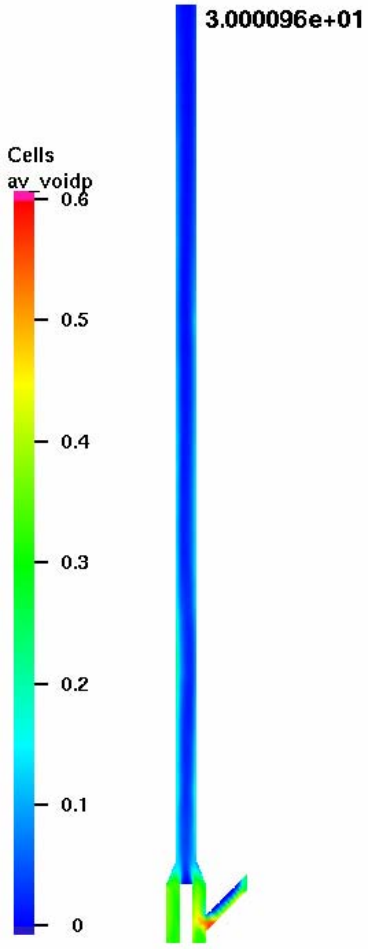

GLS02: Glass, $U = 5.3$ m/s, $G = 50$ kg/m^2·s, $U_1 = 20.80$ m/s, $U_3 = 0.24$ m/s, $U_2 = 0.30$ m/s, $\varepsilon_2 = 0.1429$.
Comments: Glass low-gas, low-solids baseline case (Case 06)

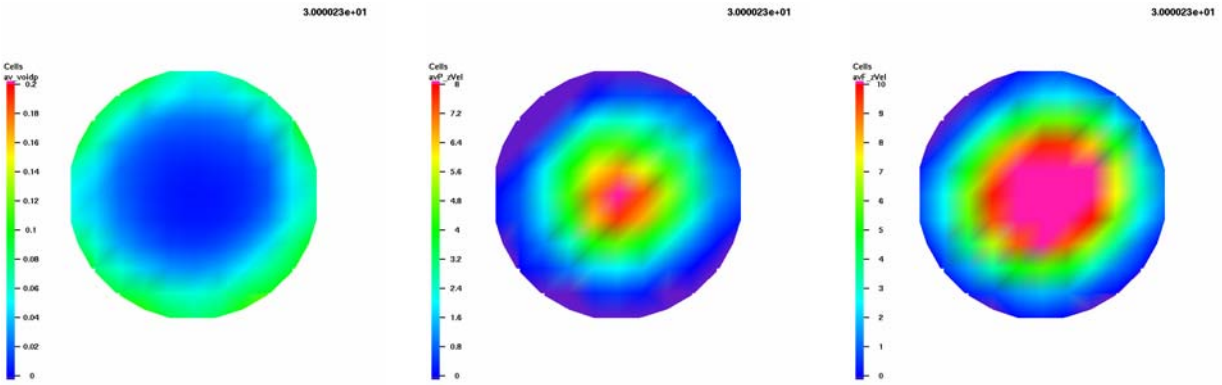

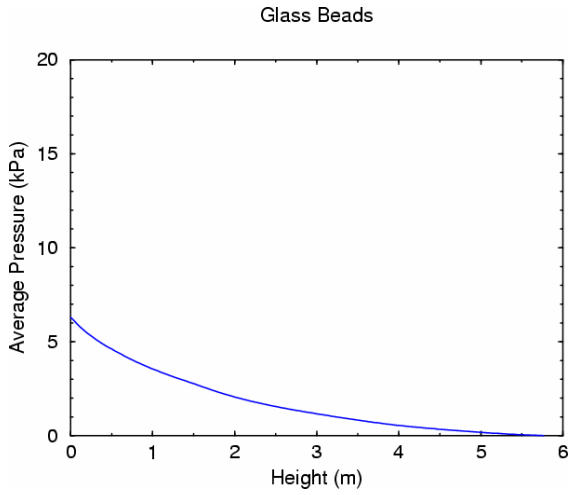

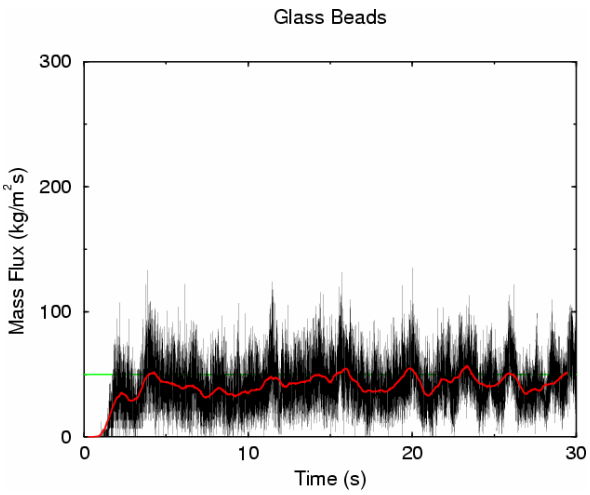

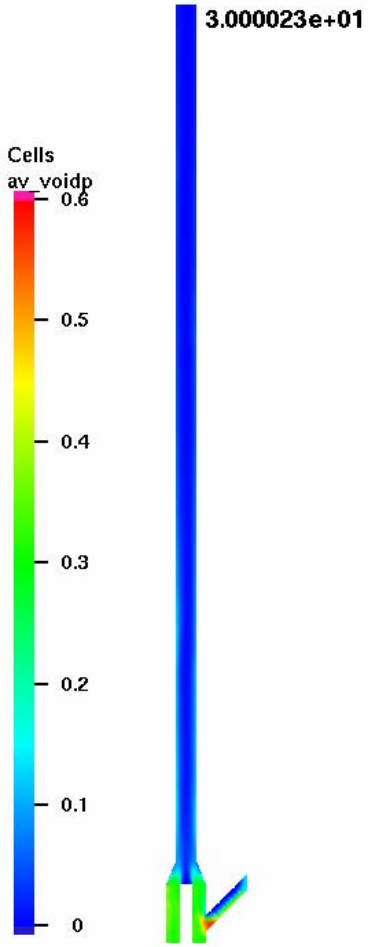

GLS03: Glass, $U = 5.3$ m/s, $G = 100$ kg/m^2·s, $U_1 = 20.80$ m/s, $U_3 = 0.12$ m/s, $U_2 = 0.30$ m/s, $\varepsilon_2 = 0.25$.
Comments: Compare to GLS01 to assess reduced fluidization (Case 02)

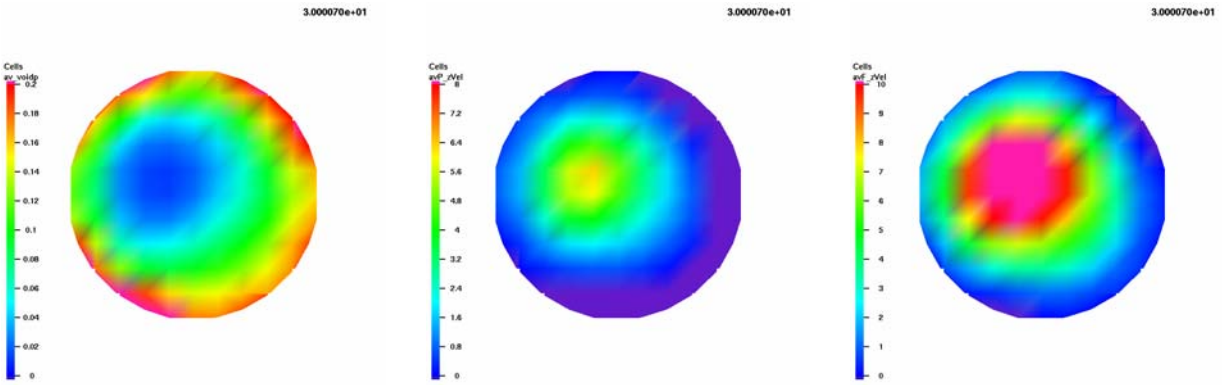

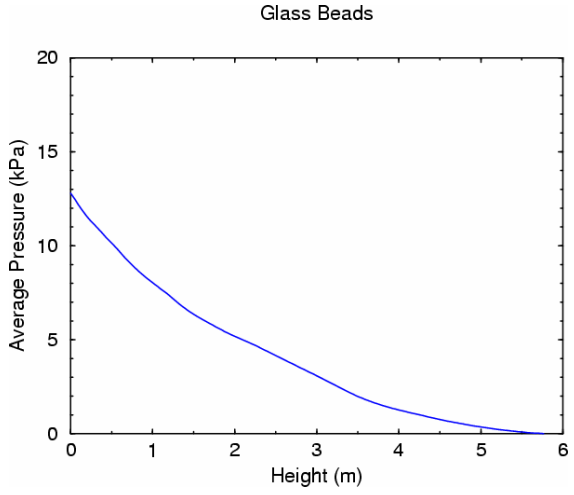

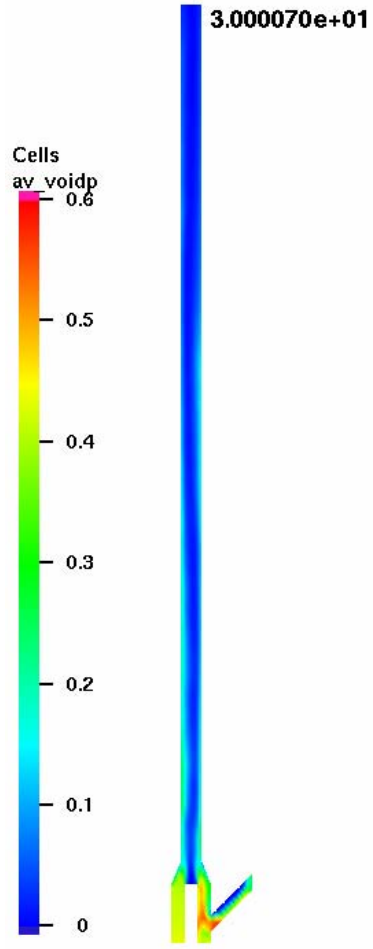

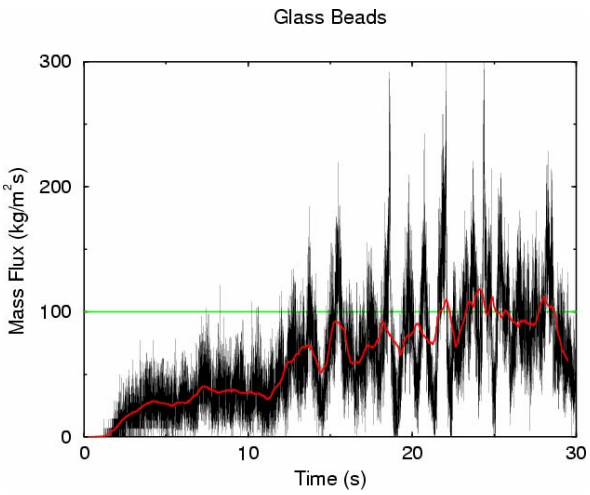

GLS04: Glass, $U = 5.3$ m/s, $G = 50$ kg/m^2·s, $U_1 = 20.80$ m/s, $U_3 = 0.12$ m/s, $U_2 = 0.30$ m/s, $\varepsilon_2 = 0.1429$.
Comments: Compare to GLS02 to assess reduced fluidization (Case 03)

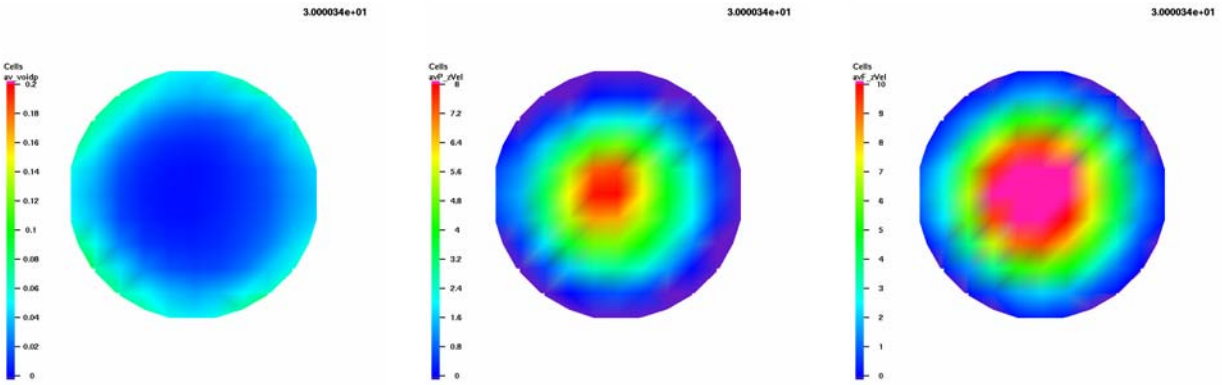

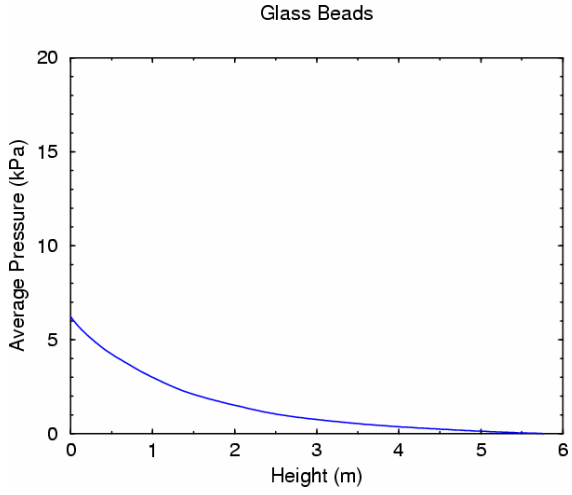

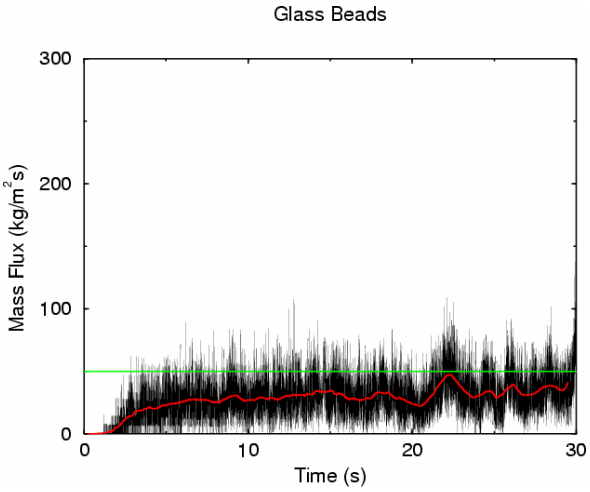

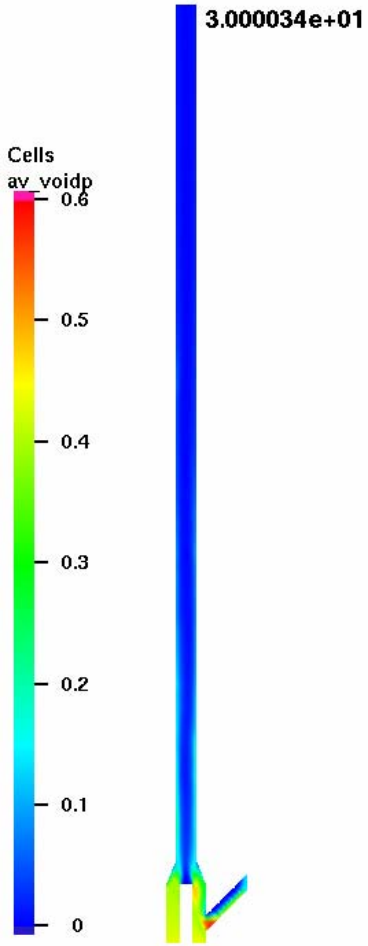

GLS05: Glass, $U = 5.3$ m/s, $G = 150$ kg/m^2·s, $U_1 = 20.80$ m/s, $U_3 = 0.12$ m/s, $U_2 = 0.30$ m/s, $\varepsilon_2 = 0.3333$.
Comments: Compare to GLS03 and GLS04 and GLS06 to assess solids mass flux (Case 04)

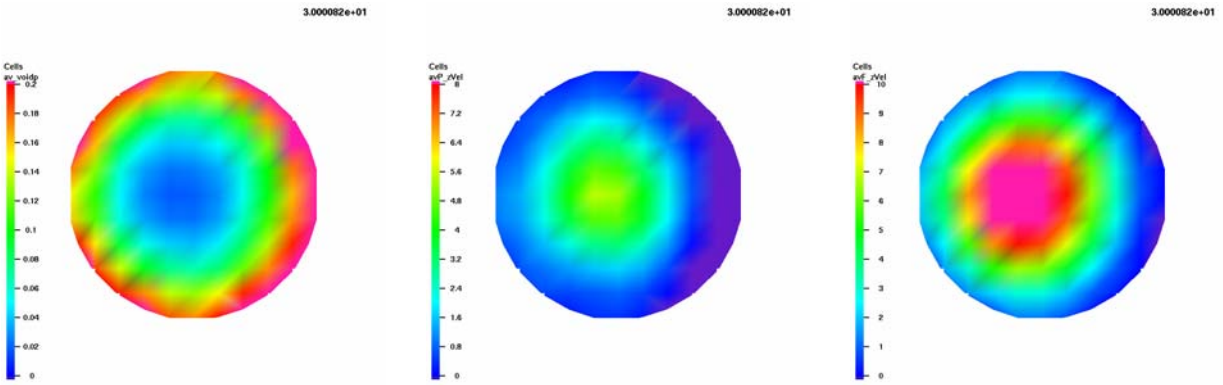

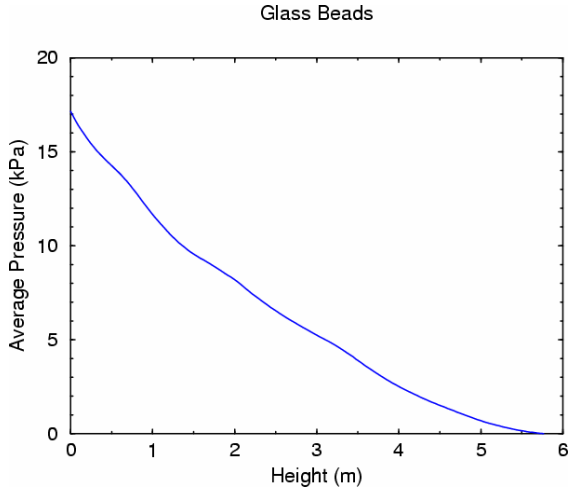

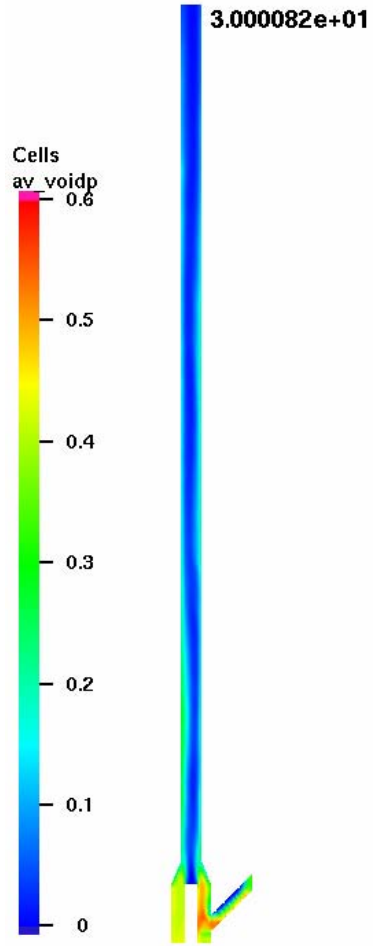

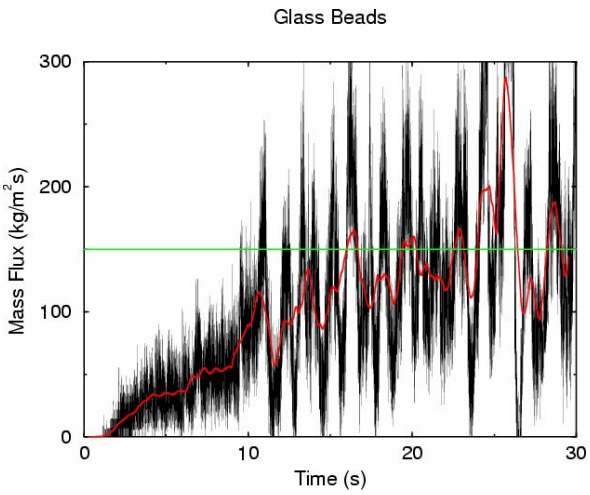

GLS06: Glass, $U = 5.3$ m/s, $G = 200$ kg/m^2·s, $U_1 = 20.80$ m/s, $U_3 = 0.12$ m/s, $U_2 = 0.30$ m/s, $\varepsilon_2 = 0.40$.
Comments: Compare to GLS03 and GLS04 and GLS05 to assess solids mass flux (Case 01)

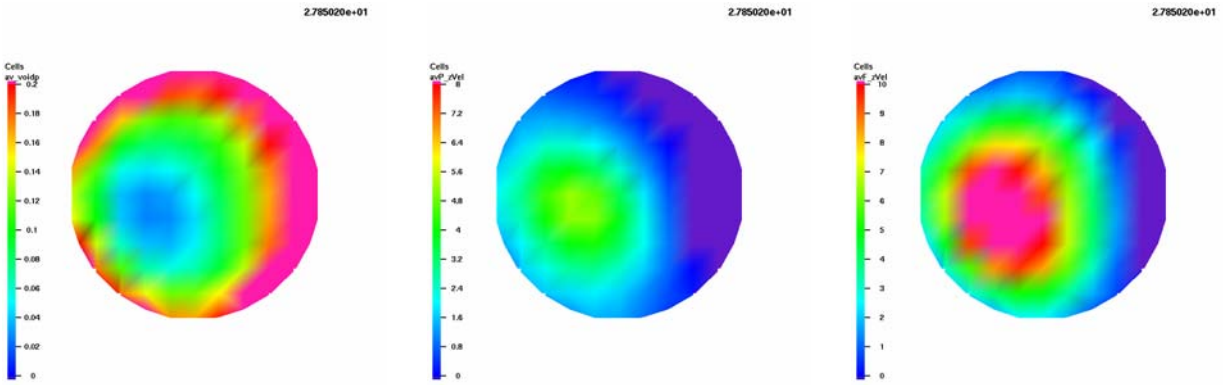

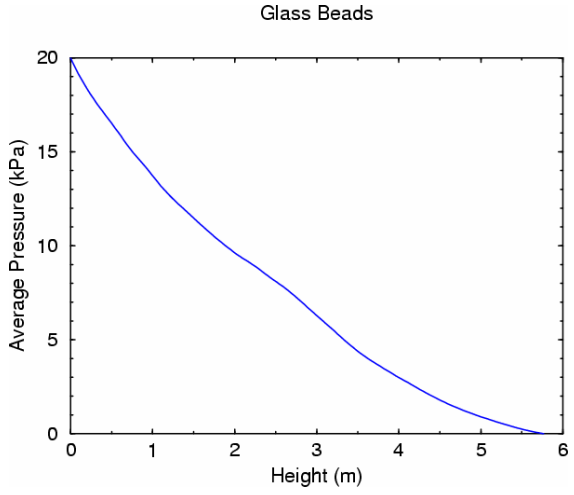

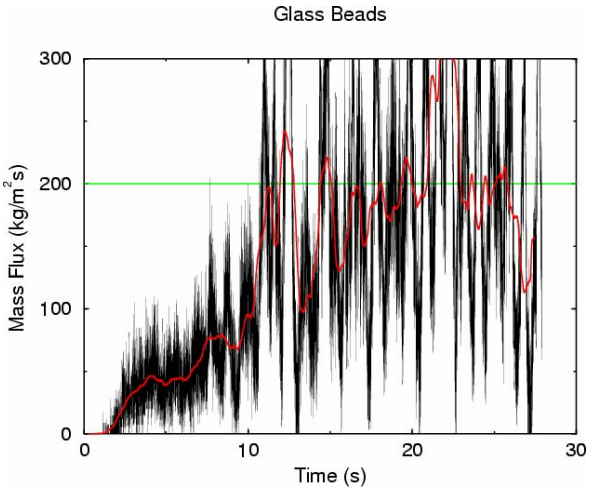

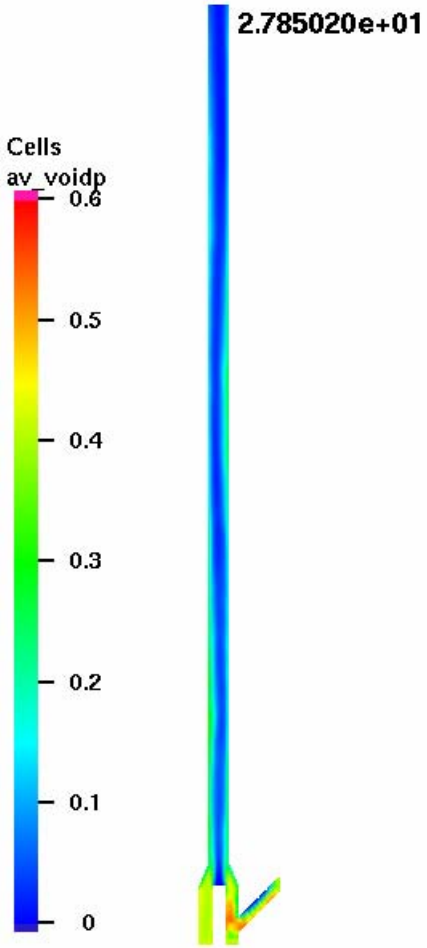

GLS11: Glass, $U = 7.4$ m/s, $G = 100$ kg/m^2·s, $U_1 = 28.65$ m/s, $U_3 = 0.24$ m/s, $U_2 = 0.30$ m/s, $\varepsilon_2 = 0.25$.
Comments: Glass high-gas, high-solids baseline case (Case 55)

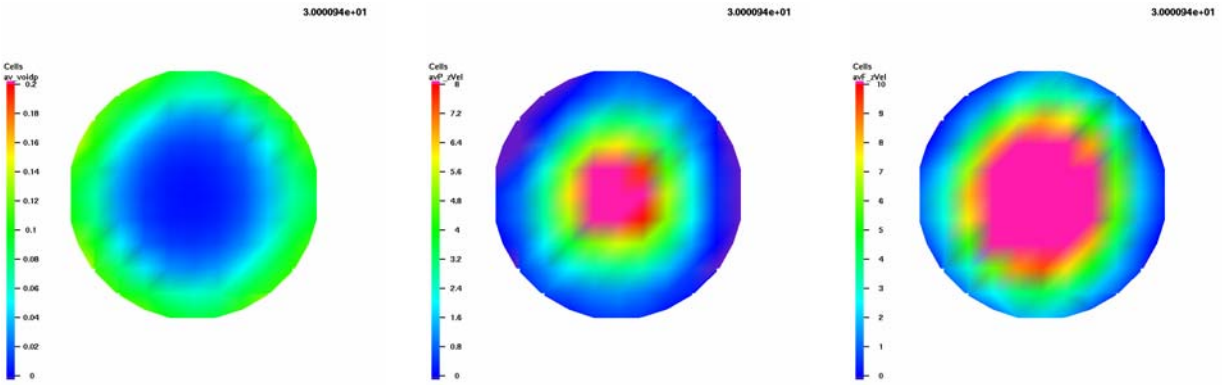

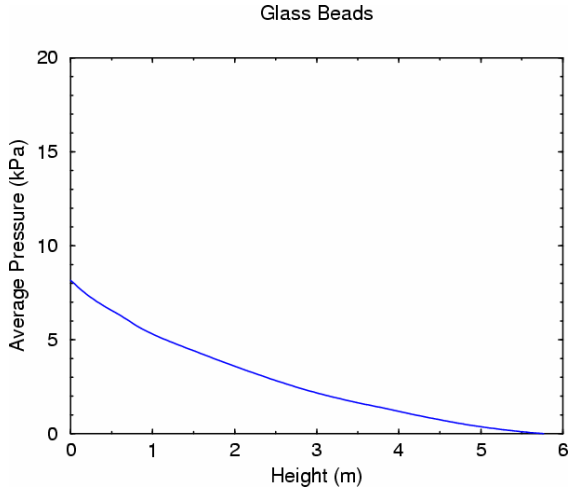

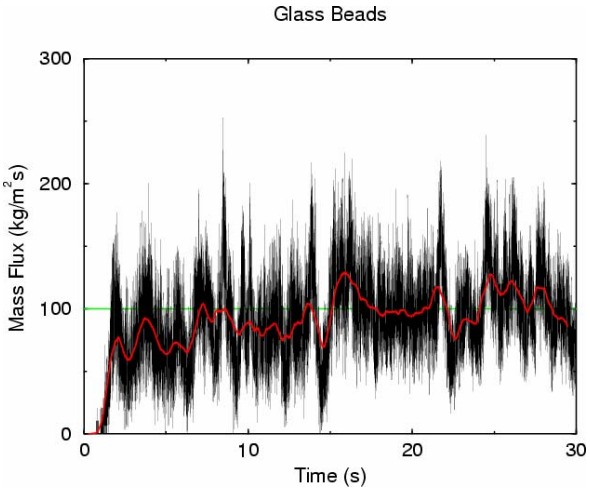

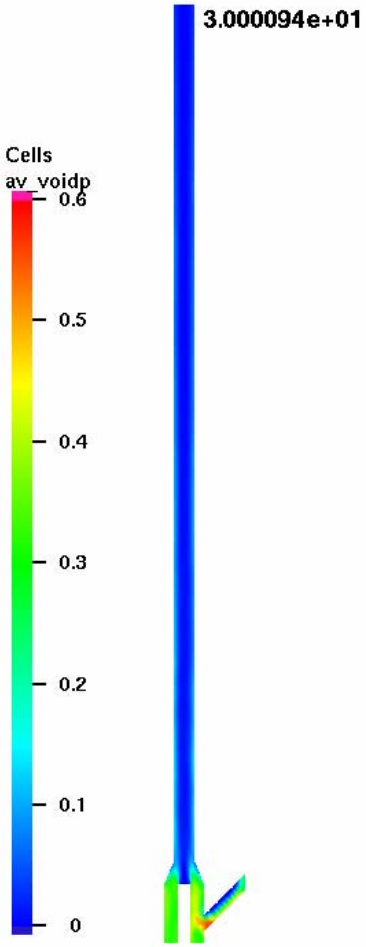

GLS12: Glass, $U = 7.4$ m/s, $G = 50$ kg/m^2·s, $U_1 = 28.65$ m/s, $U_3 = 0.24$ m/s, $U_2 = 0.30$ m/s, $\varepsilon_2 = 0.1429$.
Comments: Glass high-gas, low-solids baseline case (Case 56)

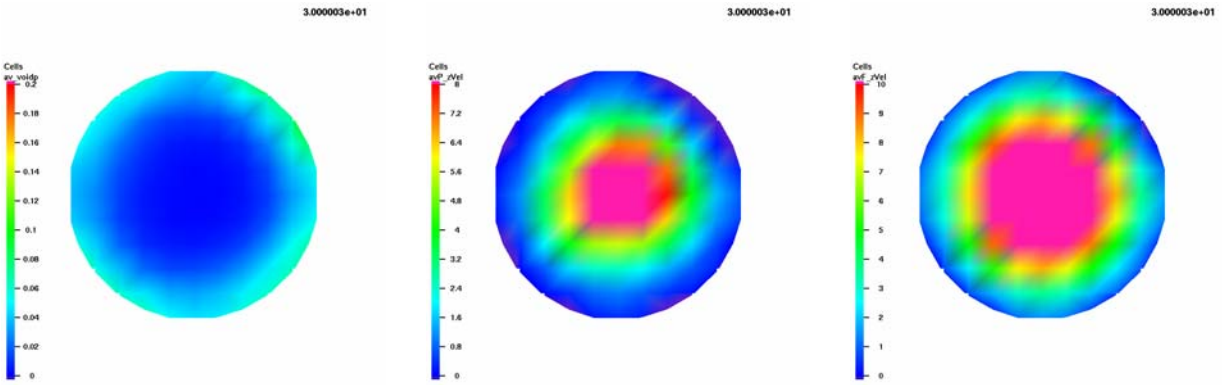

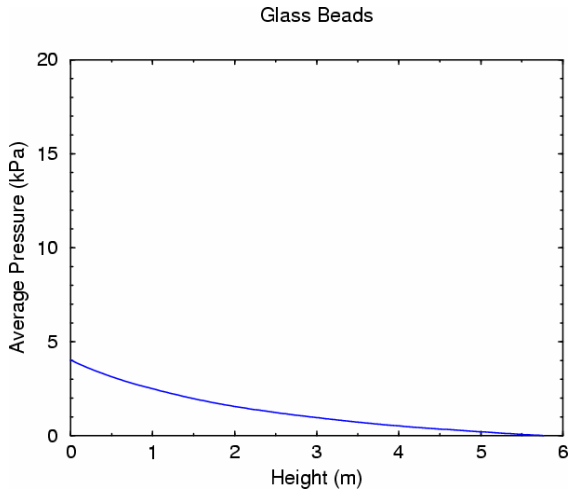

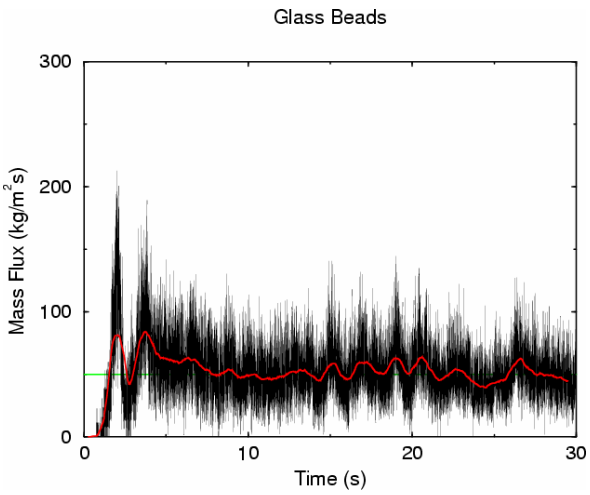

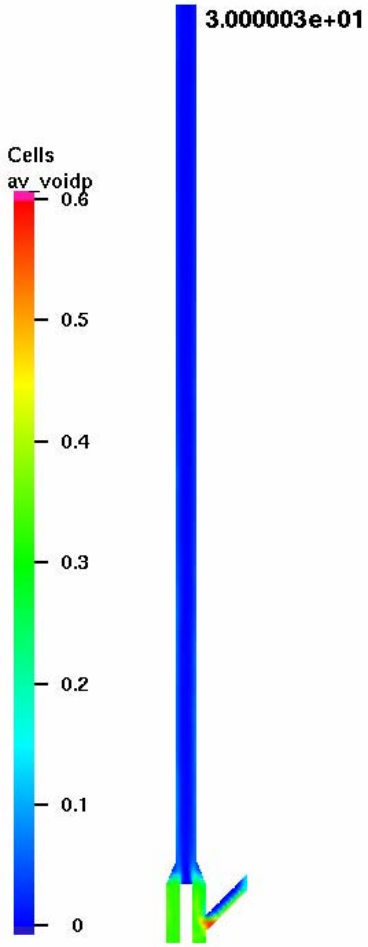

GLS13: Glass, $U = 7.4$ m/s, $G = 100$ kg/m^2·s, $U_1 = 28.65$ m/s, $U_3 = 0.12$ m/s, $U_2 = 0.30$ m/s, $\varepsilon_2 = 0.25$.
Comments: Compare to GLS11 to assess reduced fluidization (Case 52)

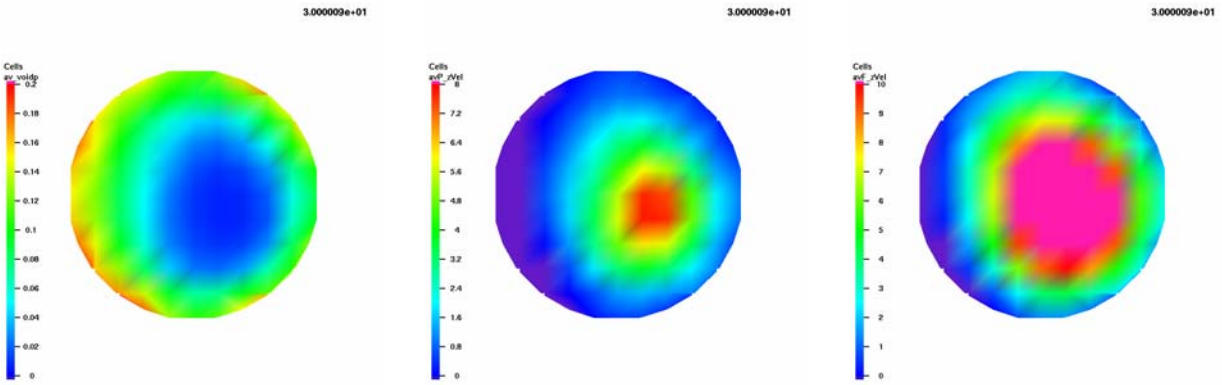

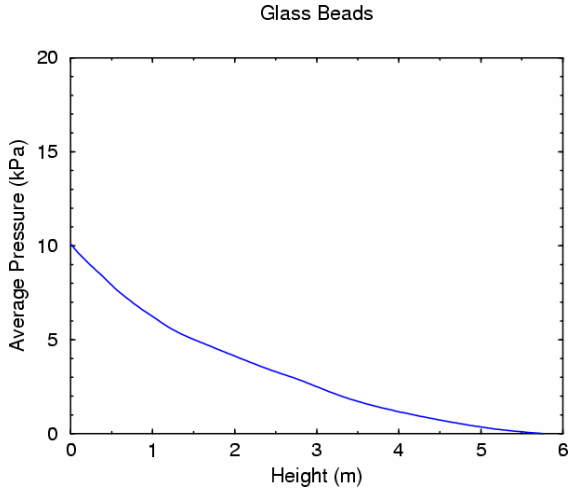

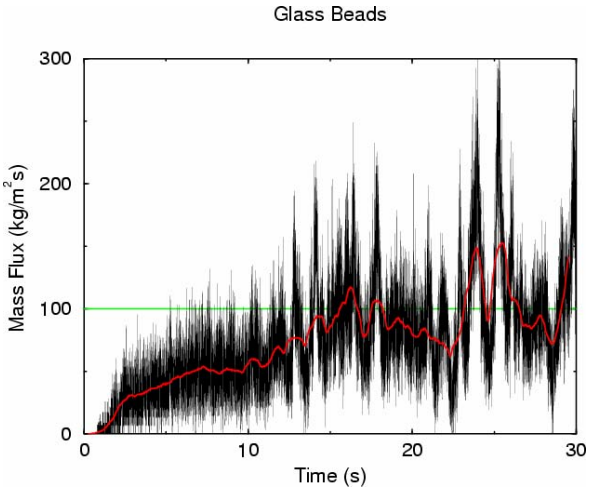

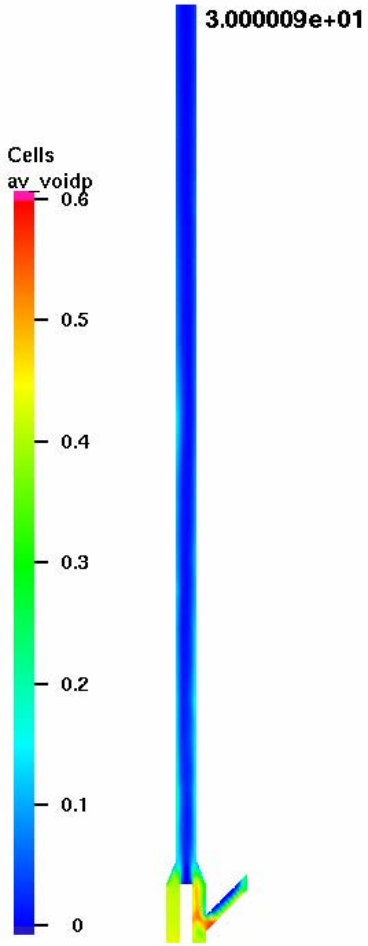

GLS14: Glass, $U = 7.4$ m/s, $G = 50$ kg/m^2·s, $U_1 = 28.65$ m/s, $U_3 = 0.12$ m/s, $U_2 = 0.30$ m/s, $\varepsilon_2 = 0.1429$.
Comments: Compare to GLS12 to assess reduced fluidization (Case 53)

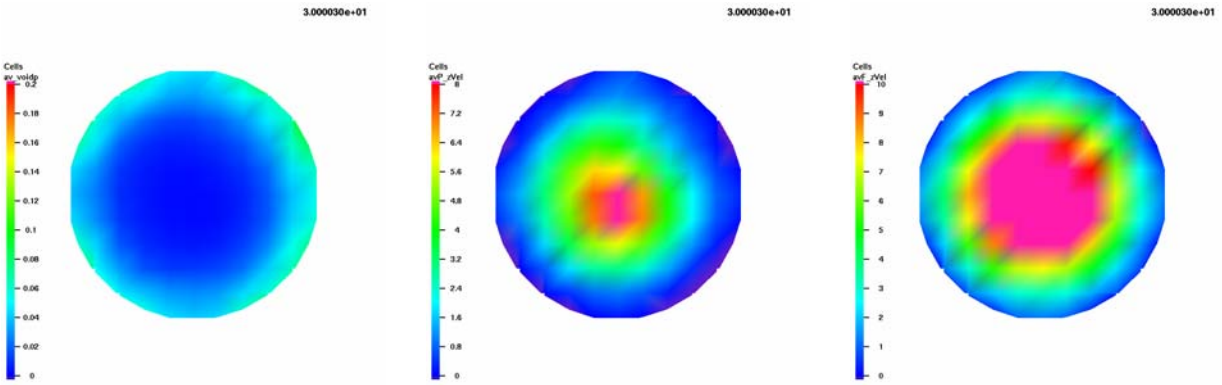

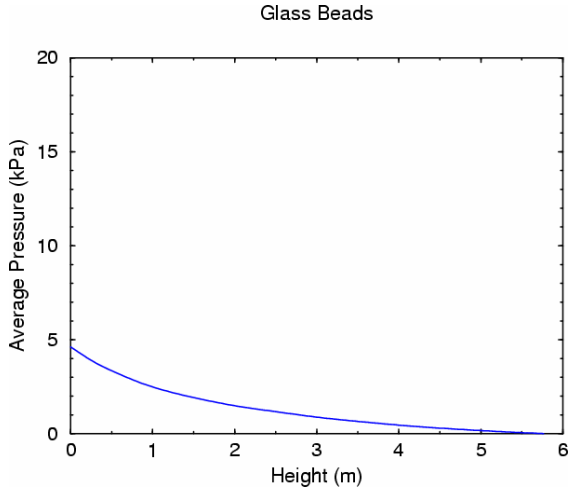

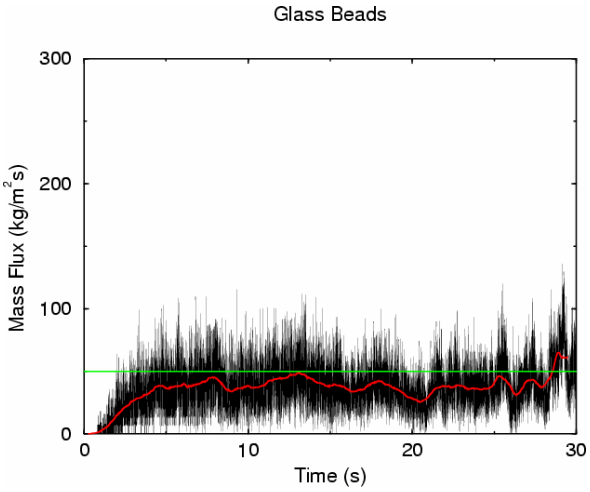

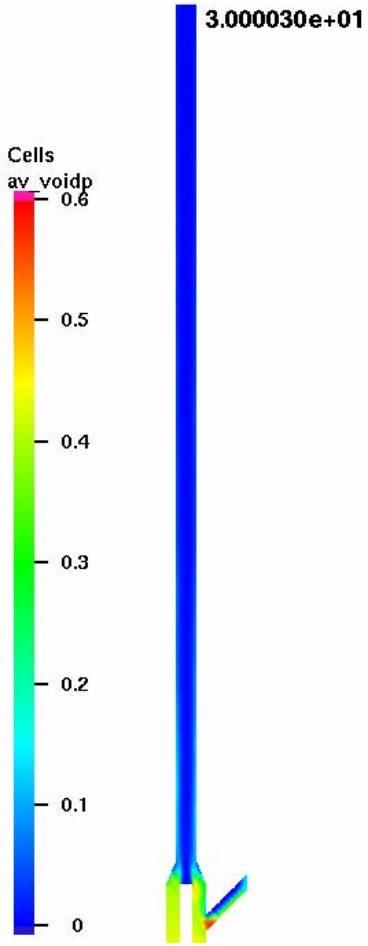

GLS15: Glass, $U = 7.4$ m/s, $G = 150$ kg/m^2·s, $U_1 = 28.65$ m/s, $U_3 = 0.12$ m/s, $U_2 = 0.30$ m/s, $\varepsilon_2 = 0.3333$.
Comments: Compare to GLS13 and GLS14 and GLS16 to assess solids mass flux (Case 54)

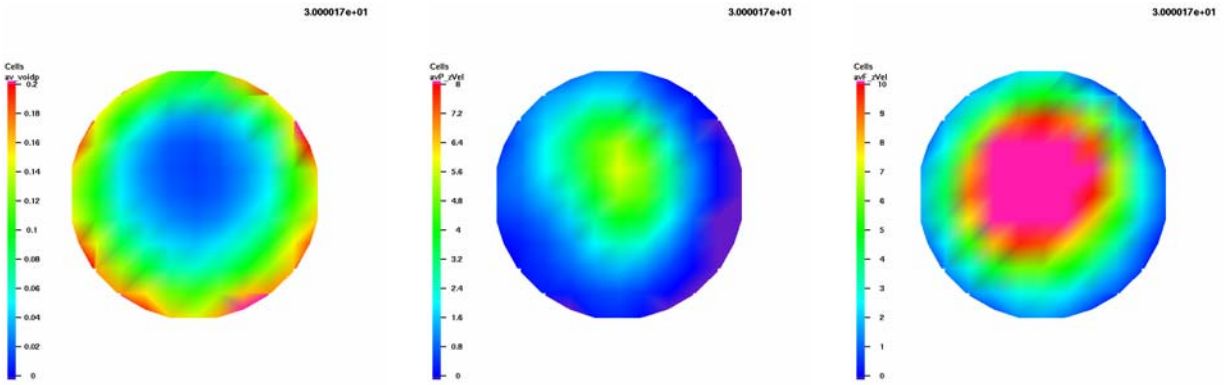

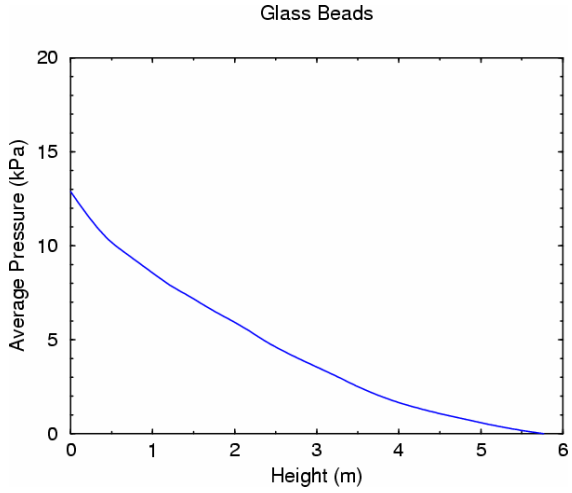

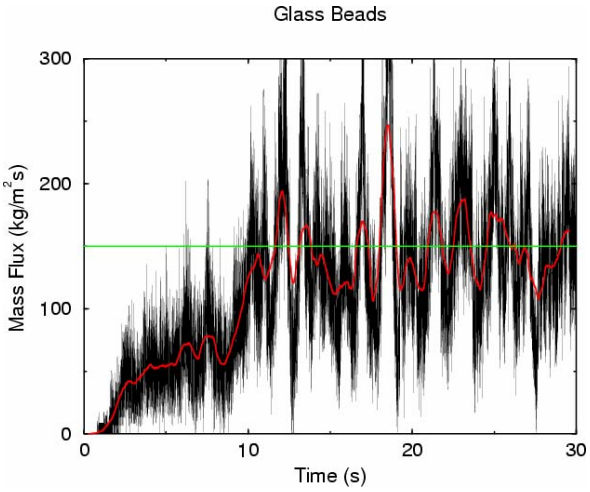

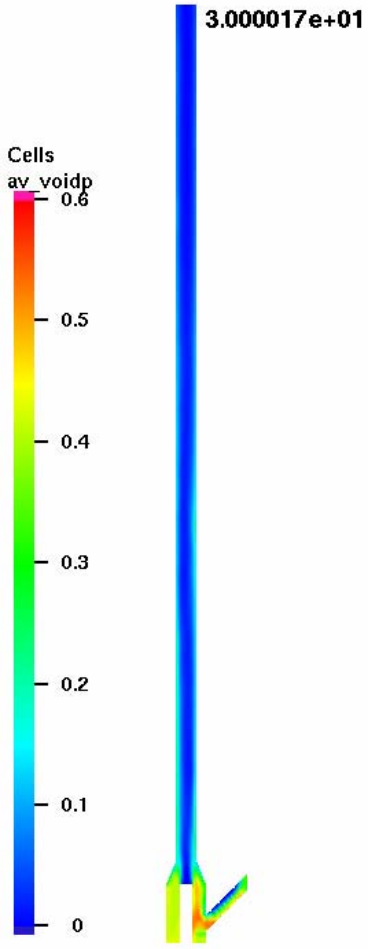

GLS16: Glass, $U = 7.4$ m/s, $G = 200$ kg/m^2·s, $U_1 = 28.65$ m/s, $U_3 = 0.12$ m/s, $U_2 = 0.30$ m/s, $\varepsilon_2 = 0.40$.
Comments: Compare to GLS13 and GLS14 and GLS15 to assess solids mass flux (Case 51)

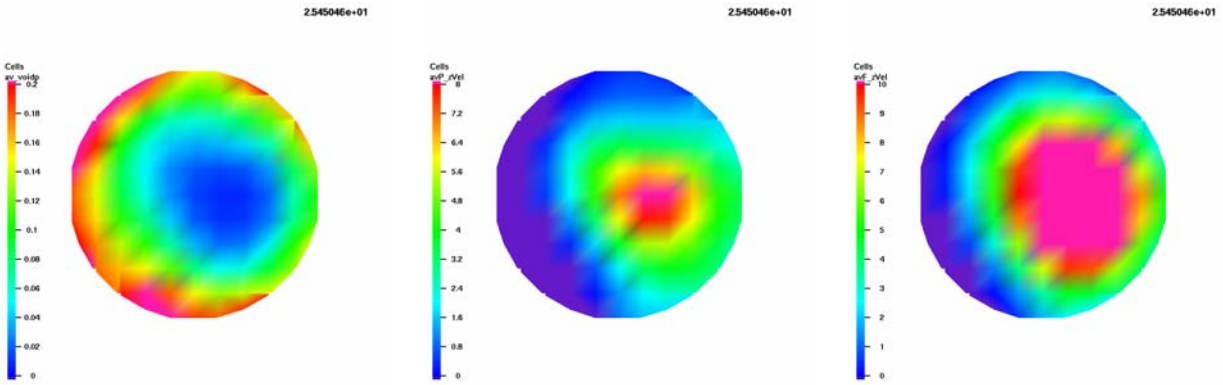

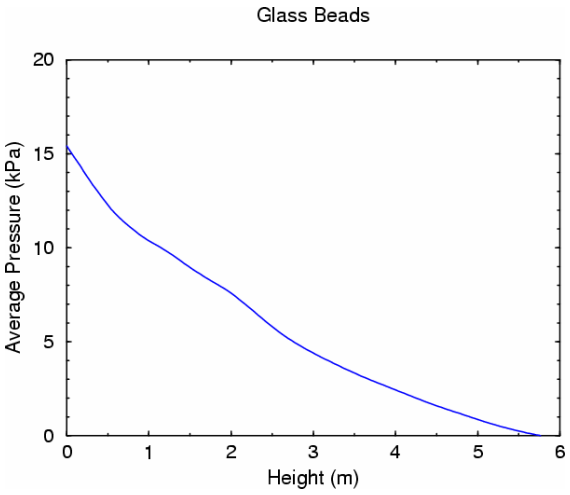

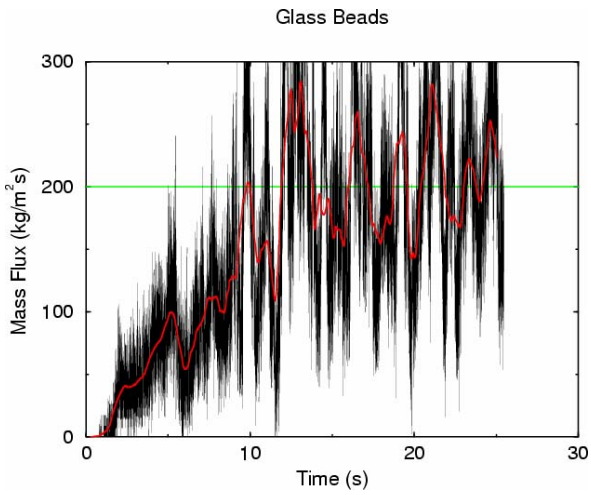

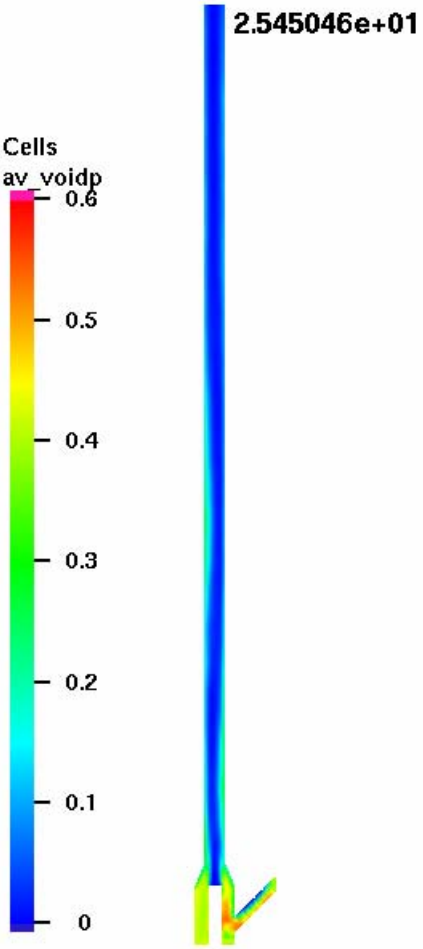

8. References

Andrews, M. J., and O'Rourke, P. J., 1996, "The Multiphase Particle-in-Cell (MP-PIC) Method for Dense Particle Flows," *International Journal of Multiphase Flow*, 22, 379-402.

Arena, U., Cammarota, A., and Pistone, L., 1985, "High Velocity Fluidization Behavior of Solids in a Laboratory Scale Circulating Bed," in *Circulating Fluidized Bed Technology: Proceedings of the First International Conference on Circulating Fluidized Beds*, edited by P. Basu, Pergamon, New York, NY, 119-125.

Avidan, A. A., 1997, "Fluid catalytic cracking," Chapter 13 of Circulating Fluidized Beds, J. R. Grace, A. A. Avidan, and T. M. Knowlton, editors, Blackie Academic and Professional, London, UK, 466-487.

Bachalo, W. D., 1994, "Experimental Methods in Multiphase Flows," *International Journal of Multiphase Flow*, 20(suppl.), 261-295.

Bares, J., 1988, "Electrical conductivity of packed particle beds," *IEEE Trans. Ind. App.* 24, 1050-1056.

Bartholomew, R. N., and Casagrande, R. M., 1957, "Measuring Solids Concentration in Fluidized Systems by Gamma-Ray Absorption," *Industrial and Engineering Chemistry*, 49(3), 428-431.

Berruti, F., Chaouki, J., Godfroy, L., Pugsley, T. S., and Patience, G. S., 1995, "Hydrodynamics of Circulating Bed Risers: A Review," *The Canadian Journal of Chemical Engineering*, 73, 579-601.

Bhusarapu, S. B., 2005, "Solids Flow Mapping in Gas-Solid Risers," Ph.D. dissertation, Chemical Engineering Department, Washington University in St. Louis.

Bhusarapu, S., Al-Dahhan, M., and Duduković, M. P., 2004a, "Quantification of solids flow in a gas-solid riser: single radioactive particle tracking," *Chemical Engineering Science*, 59(22-23), 5381-5386.

Bhusarapu, S., Fongarland, P., Al-Dahhan M. H., and Duduković, M. P., 2004b, "Measurement of Overall Solids Mass Flux in a Gas-Solid Circulating Fluidized Bed," *Powder Technology*, 148(2-3), 155-168.

Bhusarapu, S., Al-Dahhan, M., Duduković, M. P., Trujillo, S. M., and O'Hern, T. J., 2005, "Experimental Study of the Solids Velocity Field in Gas-Solid Risers," *Industrial & Engineering Chemistry Research*, 44, 9739-9749.

Bhusarapu, S., Al-Dahhan, M., and Duduković, M. P., 2006, "Solids Flow Mapping in a Gas–Solid Riser: Mean Holdup and Velocity Fields," *Powder Technology*, 163(1-2), 98-123.

Bi, H. T., and Grace, J. R., 1995, "Flow Regime Diagrams for Gas-Solid Fluidization and Upward Transport", *International Journal of Multiphase Flows*, 21, 1229-1236.

Bi, H. T., Ellis, N., Abba, I. A., and Grace, J. R., 2000, "A State-of-the-Art Review of Gas-Solid Turbulent Fluidization," *Chemical Engineering Science*, 55, 4789-4825.

Cassanello, M., Larachi, F., Legros, R., and Chaouki, J., 1999, "Solids Dynamics From Experimental Trajectory Time-Series of a Single Particle Motion in Gas-Spouted Beds," *Chemical Engineering Science*, 54, 2545-2554.

Ceccio, S. L., and George, D. L., 1996, "A Review of Electrical Impedance Techniques for the Measurement of Multiphase Flows," *ASME Journal of Fluids Engineering*, 118, 391-399.

Chaouki, J., Larachi, F., Duduković, M. P., eds., 1997, Non-Invasive Monitoring of Multiphase Flows, Elsevier, Amsterdam.

Chen, Y.-M., 2003, "Applications for Fluid Catalytic Cracking," Chapter 14 of Handbook of Fluidization and Fluid-Particle Systems, W.-C.Yang, editor., Marcel Dekker Inc., New York.

Cocco, R. A., Cleveland, J., Harner, R., and Chrisman, R., 1995, "Simultaneous In-situ Determination of Particle Loadings and Velocities in a Gaseous Medium," in *Developments in Fluidization and Fluid Particle Systems*, AIChE Symposium Series 308, edited by J. Chen, H. Arastoopour, L.-S. Fan, D. King, A. Weimer, and W.-C. Yang, American Institute of Chemical Engineers, New York, NY, 147-153.

Coronella, C. J., and Deng, J., 1998, "A Novel Method for Isokinetic Measurement of Particle Flux Within the Riser of a Circulating Fluidized Bed," *Powder Technology*, 99, 211-219.

Crowe, C. T., Troutt, R. and Chung, J. N., 1996, "Numerical Models For Two-Phase Turbulent Flows," *Annual Review of Fluid Mechanics*, 28, 11-43.

Crowe, C., Sommerfeld, M., and Tsuji, Y., 1997, Multiphase Flows with Droplets and Particles, CRC Press, Boca Raton, FL.

Cui, H., Mostoufi, N., and Chaouki, J., 2001, "Comparison of Measurement Techniques of Local Particle Concentration for Gas-Solid Fluidization," in *Fluidization X: Proceedings of the 10th Engineering Foundation Conference on Fluidization*, edited by M. Kwauk, J. Li and W.-C. Yang, Engineering Foundation, New York, 779-786.

Darwood, M. W., Davies, M., Godden, D., Jackson, P., James, K., and Stitt, E. H., 2003, "Development and Implementation of Gamma-ray Tomography for Field Applications," 3rd World Congress on Industrial Process Tomography, Banff, Canada.

Degaleesan, S., Roy, S., Kumar, S. B., and Duduković, M. P., 1996, "Liquid Mixing Based on Convection and Turbulent Dispersion in Bubble Columns," *Chemical Engineering Science*, 51(10), 1967-1976.

DOE/OIT, 1995, Technology Vision 2020: The Chemical Industry, http://www.chemicalvision2020.org/ and http://www.oit.doe.gov/chemicals/, Department of Energy Office of Industrial Technologies, Washington, DC.

Dry, R. J., and Beeby, C. J., 1997, "Applications of CFB Technology to Gas-Solid Reactions," Chapter 12 of Circulating Fluidized Beds, J. R. Grace, A. A. Avidan, and T. M. Knowlton, editors, Blackie Academic and Professional, London, UK, 441-465.

Du, L., Yao, J. Z., and Lin, W. G., 2005, "Experimental Study of Particle Flow in a Gas-Solid Separator With Baffles Using PDPA," *Chemical Engineering Journal*, 108, 59-67.

Dyakowski, T., Jeanmeure, L.F.C. and Jaworski, A.J., 2000, "Applications of Electrical Tomography for Gas-Solids and Liquid-Solids Flows – A Review," *Powder Technology*, 112, 174-192.

Eldred, M. S., Giunta, A. A., van Bloemen Waanders, B. G., Wojtkiewicz, S. F., Jr., Hart, W. E., and Alleva, M. P., 2002a, *DAKOTA, A Multilevel Parallel Object-Oriented Framework for Design Optimization, Parameter Estimation, Uncertainty Quantification, and Sensitivity Analysis. Version 3.0 Reference Manual*, Sandia report SAND2001-3515, Sandia National Laboratories, Albuquerque, NM.

Eldred, M. S., Giunta, A. A., van Bloemen Waanders, B. G., Wojtkiewicz, S. F., Jr., Hart, W. E., and Alleva, M. P., 2002b *DAKOTA, A Multilevel Parallel Object-Oriented Framework for Design Optimization, Parameter Estimation, Uncertainty Quantification, and Sensitivity Analysis. Version 3.0 Developers Manual*, Sandia report SAND2001-3514, Sandia National Laboratories, Albuquerque, NM.

Eldred, M. S., Giunta, A. A., van Bloemen Waanders, B. G., Wojtkiewicz, S. F., Jr., Hart, W. E., and Alleva, M. P., 2003, *DAKOTA, A Multilevel Parallel Object-Oriented Framework for Design Optimization, Parameter Estimation, Uncertainty Quantification, and Sensitivity Analysis. Version 3.1 Users Manual*, Sandia report SAND2001-3796, Sandia National Laboratories, Albuquerque, NM.

Ennis, B. J., Green, J., and Davies, R., 1994, "The Legacy of Neglect in the U.S.," *Chemical Engineering Progress* 90(4), 32-43.

Fan, L.-S., and Zhu, C., 1998, *Principles of Gas-Solid Flows*, Cambridge University Press, Cambridge, UK.

Figliola, R.S., and Beasley, D.E., 2000, Theory and Design for Mechanical Measurements, Third Edition, John Wiley & Sons, New York.

Fluent, Inc., 1998, *FIDAP User's Manuals*, version 8, Fluent, Inc., Lebanon, NH.

Geldart, D., 1973, "Types of Gas Fluidization," *Powder Technology*, 7, 285-292.

George, D. L., Torczynski, J. R., Shollenberger, K. A., and O'Hern, T. J., 2000a, *Quantitative Tomographic Measurements of Opaque Multiphase Flows*, Sandia report SAND2000-0443, Sandia National Laboratories, Albuquerque, NM.

George, D. L., Torczynski, J. R., Shollenberger, K. A., O'Hern, T. J., and Ceccio, S. L., 2000b, "Validation of Electrical Impedance Tomography for Measurements of Material Distribution in Two-Phase Flows," *International Journal of Multiphase Flow*, 26(4), 549-581.

George, D. L., Shollenberger, K. A., Torczynski, J. R., O'Hern, T. J., and Ceccio, S. L., 2001, "Three-Phase Material Distribution Measurements in a Vertical Flow Using Gamma-Density Tomography and Electrical-Impedance Tomography," *International Journal of Multiphase Flow*, 27, 1903-1930.

Georgakopoulos, D., Waterfall, R. C., and Yang, W. Q., 2001, "Towards the development of a multiple-frequency ECT system," 2*nd World Congress on Industrial Process Tomography*, Hannover, Germany, August 29-31, 2001.

Gidaspow, D., 1994, Multiphase Flow and Fluidization: Continuum and Kinetic Theory Descriptions with Application*s*, Academic Press: Harcourt Brace and Company, Boston, MA.

Goldstein, R. J., 1996, Fluid Mechanics Measurements, second edition, Taylor & Francis, Philadelphia, PA, USA.

Grace J. R., Avidan, A. A., and Knowlton, T. M., editors, 1997, Circulating Fluidized Beds, Blackie Academic and Professional, London, UK.

Grace, J. R., and Bi, H. T., 1997, "Introduction to Circulating Fluidized Beds," Chapter 1 of Circulating Fluidized Beds, J. R. Grace, A. A. Avidan, and T. M. Knowlton, editors, Blackie Academic and Professional, London, UK, 1-21.

Halow, J.S., Fasching, G.E., Nicoletti, P. and Spenik, J.L., 1993, "Observations of a Fluidized Bed Using Capacitance Imaging," *Chemical Engineering Science*, 48, 643-659.

Harris, B. J., and Davidson, J. F., 1992, "Velocity Profiles, Gas and Solids, in Fast Fluidized Beds," in *Fluidization VII: Proceedings of the 7th Engineering Foundation Conference on Fluidization*, O. E. Potter and D. J. Nicklin, editors, Engineering Foundation, New York, NY, 219-226.

Hartge, E.-U., Li, Y., and Werther, J., 1985, "Analysis of the Local Structure of the Two Phase Flow in a Fast Fluidized Bed," in *Circulating Fluidized Bed Technology: Proceedings of the First International Conference on Circulating Fluidized Beds*, edited by P. Basu, Pergamon, New York, NY, 153-160.

Horio, M., and Kuroki, H., 1994, "Three-Dimensional Flow Visualization of Dilutely Dispersed Solids in Bubbling and Circulating Fluidized Beds," *Chemical Engineering Science*, 49(15) 2413-2421.

Horio, M., 1997, "Hydrodynamics," Chapter 2 of Circulating Fluidized Beds, J. R. Grace, A. A. Avidan, and T. M. Knowlton, editors, Blackie Academic and Professional, London, UK, 21-78.

Huang, C., Lee, J., Schultz, W. W., and Ceccio, S. L., 2001, "Singularity Image Method for Electrical Impedance Tomography," in *Proceedings of the 2nd World Congress on Industrial Process Tomography*, Virtual Centre for Industrial Process Tomography, Leeds and Manchester, UK, 661-668.

Huang, S. M., Xie, C. G., Thorn, R., Snowden, D., and Beck, M. S., 1992, "Design of sensor electronics for electrical capacitance tomography," *IEEE Proceedings-G*, 139(1), 83-88.

Issangya, A. S., Bai, D., Grace, J. R., and Zhu, J., 1998, "Solids Flux Profiles in a High Density Circulating Fluidized Bed Riser," in *Fluidization IX: Proceedings of the 9th Engineering Foundation Conference on Fluidization*, edited by L.-S. Fan and T. M. Knowlton, Engineering Foundation, New York, NY, 197-204.

Jackson, J. D., 1975, *Classical Electrodynamics*, second edition, John Wiley & Sons, New York, NY, especially Appendix Tables 1-4.

Jackson, R., 2000, The Dynamics of Fluidized Particles, Cambridge University Press, Cambridge, UK.

Karim, K., Varma, R., Vesvikar, M., and Al-Dahhan, M.H., 2004, "Flow Pattern Visualization of a Simulated Digester," *Water Research*, 38, 3659–3670.

Karri, S. B. R., Knowlton, T. M., and Litchfield, J., 1995, "Increasing Solids Flow Rates Through a Hybrid Angled Standpipe Using a Bypass Line," in *Fluidization VIII: Proceedings of the 8th Engineering Foundation Conference on Fluidization*, edited by J.-F. Large and C. Laguérie, Engineering Foundation, New York, NY, 197-204.

Kashiwa, B. A., and VanderHeyden, W. B., 1998, private communication.

Kashiwa, B. A., and VanderHeyden, W. B., 2000, Toward a General Theory for Multiphase Turbulence – Part 1: Development and Gauging of the Model Equations, Los Alamos report LA-13773-MS, Los Alamos National Laboratory, Los Alamos, NM.

Khopkar, A. R., Rammohan, A. R., Ranade, V. V., and Duduković, M.P., 2005, "Gas-Liquid Flow Generated by a Rushton Turbine in Stirred Vessel: CARPT/CT Measurements and CFD Simulations," *Chemical Engineering Science*, 60, 2215–2229.

Knoll, G. F., 2000, Radiation Detection and Measurement, Third Edition, John Wiley and Sons, Inc., New York, NY, p. 122.

Knowlton, T., 2000, *PSRI Gas-Solid Flows Course Notes*, Particulate Solid Research, Inc., Chicago, IL.

Krohn, D. A., 1987, "Intensity Modulated Fiber Optic Sensors Overview," in *Fiber Optic and Laser Sensors IV: SPIE Proceedings Vol. 718*, edited by R. P. De Paula and E. Udd, Society of Photo-Optical Instrumentation Engineers, Bellingham, WA, 2-11.

Kunii, D., and Levenspiel, O., 1991, Fluidization Engineering, Butterworth-Heinemann, Boston, second edition.

Larachi, F., Kennedy, G.; Chaouki, J., 1994, "A γ-ray Detection System for 3-D Particle Tracking in Multiphase Reactors," *Nuclear Instruments and Methods Physics Research, Section A*, 338(2-3), 568-76.

Lee, Y. Y., 1997, "Design considerations for CFB boilers," Chapter 11 of Circulating Fluidized Beds, J. R. Grace, A. A. Avidan, and T. M. Knowlton, editors, Blackie Academic and Professional, London, UK, 417-438.

Lim, K. S., Zhu, J. X., and Grace, J. R., 1995, "Hydrodynamics of Gas-Solid Fluidization," *International Journal of Multiphase Flow*, 21(suppl.), 141-193.

Liu, X., Gao, S., and Li, J., 2005, "Characterizing particle clustering behavior by PDPA measurement for dilute gas-solid flow," *Chemical Engineering Journal*, 108, 193–202.

Louge, M., 1997, "Experimental Techniques," Chapter 9 of Circulating Fluidized Beds, J. R. Grace, A. A. Avidan, and T. M. Knowlton, editors, Blackie Academic and Professional, London, UK, 312-358.

Louge, M., and Chang, H., 1990, "Pressure and Voidage Gradients in Vertical Gas-Solid Risers," *Powder Technology*, 60, 197-201.

Louge, M., and Opie, M., 1990, "Measurements of the effective dielectric permittivity of suspensions," *Powder Technology,* 62(1), 85-94.

Makkawi, Y.T. and Wright, P.C., 2003, "The Voidage Function and Effective Drag Force For Fluidized Beds," *Chemical Engineering Science*, 58, 2035-2051.

Malcus, S., Cruz, E., Rowe, C., and Pugsley, T. J., 2002, "Radial Solid Mass flux Profiles in a High-Suspension Density Circulating Fluidized Bed," *Powder Technology*, 125, 5-9.

Mathiesen, V., Solberg, T., and Hjertager, B. H., 2000, "An experimental and computational study of multiphase flow behavior in a circulating fluidized bed," *International Journal of Multiphase Flow*, 26, 387-419.

Matsuno, Y., Yamaguchi, H., Oka, T., Kage, H., and Higashitani, K., 1983, "The Use of Optic Fiber Probes for the Measurement of Dilute Particle Concentrations: Calibration and Application to Gas-Fluidized Bed Carryover," *Powder Technology*, 36, 215-221.

Meredith, R. E., and Tobias, C. W., 1960, "Resistance to potential flow through a cubical array of spheres," *Journal of Applied Physics,* 31(7), 1270-1273.

Merrow, E. W., 1986, *A Quantitative Assessment of R&D Requirements for Solids Processing Technology*, note R-3216-DOE/PSSP, Rand Corporation, Santa Monica, CA.

Miller, A., and Gidaspow, D., 1992, "Dense, Vertical Gas-Solid Flow in a Pipe," *AIChE Journal*, 38(11), 1801-1815.

Mixon, W., and Xu, S., 2005, "Identify Liquid Maldistribution in Packed Distillation Towers by CAT-Scan Technology," AIChE Spring Meeting, presentation at Distillation Symposium.

Moran, J. C., and Glicksman, L. R., 2003, "Mean and fluctuating gas phase velocities inside a circulating fluidized bed," *Chemical Engineering Science*, 58(9), 1867-1878.

Mudde, R. F., Harteveld, W. K., van den Akker, H. E. A., van der Hagen, T. H. J. J., and van Dam, H., 1999, "Gamma Radiation Densitometry for Studying the Dynamics of Fluidized Beds," *Chemical Engineering Science*, 54, 2047-2054.

Nguyen, T., Nguyen, A., and Nieh, S., 1989, "An Improved Isokinetic Sampling Probe for Measuring Local Gas Velocity and Particle Mass Flux of Gas-Solid Suspension Flows," *Powder Technology*, 59, 183-189.

O'Hern, T. J., Trujillo, S. M., and Tortora, P. R., 2003, "Gamma Tomography System for Determination of Solids Loading in Gas-Solid Flows: Comparison with Axial Pressure Gradient Method," in *Proceedings of the 3rd World Congress on Industrial Process Tomography*, Virtual Centre for Industrial Process Tomography, Leeds and Manchester, UK, 438-444.

O'Hern, T. J., Trujillo, S. M., Oelfke, J. B., Tortora, P. R., and Ceccio, S. L., 2004, "Solids-Loading Measurements in a Gas-Solid Riser," paper HT-FED2004-56602, American Society of Mechanical Engineers, New York, NY.

Ortega, F. A., 1995, *GMV Version 2.9 General Mesh Viewer User's Manual*, Los Alamos report LAUR 95-2986, Los Alamos National Laboratory, Los Alamos, NM.

Pell, M., 1990, Gas Fluidization, Elsevier, Amsterdam.

Petrick, M., and Swanson, B. S., 1958, "Radiation Attenuation Method of Measuring Density of a 2-Phase Fluid," *Review of Scientific Instruments*, 29(12), 1079-1085.

Pugsley, T., Tanfara, H., Malcus, S., Cui, H., Chaouki, J. and Winters, C., 2003, "Verification of Fluidized Bed Electrical Capacitance Tomography Measurements with a Fibre Optic Probe," *Chemical Engineering Science*, 58, 3923-3934.

Qi, C., and Farag, I. H., 1993, "Lateral Particle Motion and Its Effect on Particle Concentration Distribution in the Riser of a CFB," *AIChE Symposium Series*, 89, 73-80.

Rammohan, A. R., Kemoun, A., Al-Dahhan, M. H., and Duduković, M. P., 2001, "A Lagrangian Description of Flows in Stirred Tanks Via Computer-Automated Radioactive Particle Tracking (CARPT)," *Chemical Engineering Science*, 56, 2629-2639.

Rao, S.M., Zhu, K., Wang, C.-H. and Sundaresan, S., 2001, "Electrical Capacitance Tomography Measurements on the Pneumatic Conveying Of Solids," *Industrial & Engineering Chemistry Research*, 40, 4216-4226.

Reh, L., and Li, J., 1990, "Measurement of Voidage in Fluidized Beds by Optical Probes," in *Circulating Fluidized Bed Technology III*, edited by P. Basu, M. Horio, and M. Hasatani, Pergamon, Oxford, 163-170.

Reinhardt, B., Cordonnier, A., and Florent, P., 1999, "Use of an Isokinetic Sampling Probe: Results in a Cyclone," *Powder Technology*, 101, 81-90.

Rhodes, M., 1998, Introduction to Particle Technology, John Wiley & Sons, Chichester, UK.

Rhodes, M. J., and Laussmann, P., 1992, "A Simple Non-Isokinetic Sampling Probe for Dense Suspensions," *Powder Technology*, 70, 141-151.

Rhodes, M. J., Wang, X. S., Cheng, H., Hirama, T., and Gibbs, B. M., 1992, "Similar profiles of solids flux in circulating fluidized-bed risers," *Chemical Engineering Science*, 47(7), 1635-1643.

Roco, M. C., 1993, Particulate Two-Phase Flow, Butterworth-Heinemann, Boston, MA.

Roy, S., Larachi, F., Al-Dahhan, M. H., and Duduković, M. P., 2002, "Optimal Design of Radioactive Particle Tracking Experiments for Flow Mapping in Opaque Multiphase Reactors," *Applied Radiation and Isotopes*, 56, 485-503.

Scaife, B. K. P., 1989, Principles of Dielectrics, Oxford University Press, New York.

Schlichthaerle, P., and Werther, J., 1999, "Axial Pressure Profiles and Solids Concentration Distributions in the CFB Bottom Zone," *Chemical Engineering Science*, 54, 5485-5493.

Scott, D. M., and Williams, R. A., eds., 1995, Frontiers in Industrial Process Tomography, Engineering Foundation, NY.

Shollenberger, K. A., Torczynski, J. R., Adkins, D. R., O'Hern, T. J., and Jackson, N. B., 1997, "Gamma-Densitometry Tomography of Gas Holdup Spatial Distribution in Industrial-Scale Bubble Columns," *Chemical Engineering Science*, 52(13), 2037-2048.

Sinclair Curtis, J., and van Wachem, B., 2004, "Modeling Particle-Laden Flows: A Research Outlook," *AIChE Journal,* 50(11), 2638-2645.

Snider, D. M., O'Rourke, P. J., and Andrews, M. J., 1998, "Sediment Flow in Inclined Vessels Calculated Using a Multiphase Particle-in-Cell Model for Dense Particle Flows," *International Journal of Multiphase Flow*, 24, 1359-1382.

Snider, D. M., 2001, "An Incompressible Three-Dimensional Multiphase Particle-in-Cell Model for Dense Particle Flows," *Journal of Computational Physics*, 170, 523-549.

Snider, D. M., Williams, K. A., and Johnson, R. A, 2004, "Multiphase Particle-in-Cell Simulations of Dense-Phase Flows in Cyclone Separators," paper HT-FED2004-56665, American Society of Mechanical Engineers, New York, NY.

Soo, S. L., editor, 1999, Instrumentation for Fluid-Particle Flow, Noyes Press, Park Ridge, NJ.

Srivastava, A., Agrawal, K., Sundaresan, S., Karri, S. B. R., and Knowlton, T. M., 1998, "Dynamics of Gas-Particle Flow in Circulating Fluidized Beds," *Powder Technology*, 100, 173-182.

Stitt, E. H., and James, K., 2003, "Process Tomography and Particle Tracking: Research and Commercial Diagnostic Tool," 3rd World Congress on Industrial Process Tomography, Banff, Canada.

Sundaresan, S., 2000, "Modeling the Hydrodynamics of Multiphase Flow Reactors: Current Status and Challenges," *AIChE Journal,* 46(6), 1102-1105.

Torczynski, J. R., O'Hern, T. J., Adkins, D. R., Jackson, N. B., and Shollenberger, K. A., 1997, "Advanced Tomographic Flow Diagnostics for Opaque Multiphase Fluids," Sandia report SAND97-1176, Sandia National Laboratories, Albuquerque, NM.

Tortora, P. R., 2004, "Electrical-impedance tomography for the quantitative measurement of solids distributions in gas-solid riser flows," Ph.D. Thesis, University of Michigan.

Tortora, P. R., Ceccio, S. L., Schultz, W. W., O'Hern, T. J., Torczynski, J. R., and Trujillo, S. M., 2003, "An Electrical-Impedance Tomography System for Collecting Validation-Quality Data from Gas-Solid Flows," in *Proceedings of the 3rd World Congress on Industrial Process Tomography*, Virtual Centre for Industrial Process Tomography, Leeds and Manchester, UK, 56-61.

Tortora, P. R., Ceccio, S. L., and Torczynski, J. R., 2005, *The Equivalent Electrical Permittivity of Gas-Solid Mixtures at Intermediate Solid Volume Fractions*, Sandia report SAND2005-4648, Sandia National Laboratories, Albuquerque, NM.

Trujillo, S. M., Shollenberger, K. A., O'Hern, T. J., Grasser, T. W., and Torczynski, J. R., 2001a, *A Gas-Solid Riser Experiment for Fundamental Studies of Turbulent Multiphase Flow*, Sandia report SAND2001-1158, Sandia National Laboratories, Albuquerque, NM.

Trujillo, S. M., O'Hern, T. J., Shollenberger, K. A., Torczynski, J. R., Tortora, P. R., and Ceccio, S. L., 2001b, "Baseline Measurements and Advanced Diagnostic Development in the Sandia/MFDRC Gas-Solid Riser," paper 410, in *Proceedings of the ICMF-2001*, edited by E. E. Michaelides, International Conference on Multiphase Flow.

Trujillo, S. M., O'Hern, T. J., Tortora, P. R., Oelfke, J. B., and Ceccio, S. L., 2004, "Solids Loading Measurements in a Gas-Solid Riser," paper HT-FED2004-56602, American Society of Mechanical Engineers, New York, NY.

van Beek, L. K. H., 1967, "Dielectric behaviour of heterogeneous systems," in *Progress in Dielectrics Volume 7* (Birks, J.B., editor), CRC Press, Cleveland, OH, 69-114.

van Breugel, J. W., Stein, J. J. M., and de Vries, R. J., 1969, "Isokinetic Sampling in a Dense Gas-Solids Stream," *Proceedings of the Institution of Mechanical Engineers*, 184(3c), 18-23.

Van engelandt, G. Heynderickx, G. J., and Marin, G. B., 2004, "Experimental Study of Gas-Solid Flow in Risers," *Proceedings of the 11th International Conference on Fluidization*, U. Arena, R. Chirone, M. Miccio, and P. Salatino, editors, Ischia, Italy, May.

van Santen, H., Kolar, Z. I., Mudde, R. F., and van den Akker, H. E. A., 1997, "Double Beam and Detector γ-radiation Attenuation Gauge for Studying Bubble Phenomena in Gas-Solid Fluidized Beds," *Applied Radiation and Isot*opes, 48(10), 1307-1312.

Vest, C. M., 1985, "Tomography for Properties of Materials That Bend Rays: A Tutorial," *Applied Optics*, 24, 4089-4094.

Wang, X. S., Rhodes, M. J., and Gibbs, B. M., 1995, "Influence of Temperature Distribution on Solids Flux Distribution in a CFB Riser," *Chemical Engineering Science*, 50(15), 2441-2447.

Warsito, W. and Fan, L.-S., 2003, "ECT Imaging of Three-Phase Fluidized Bed Based on Three-Phase Capacitance Model," *Chemical Engineering Science*, 58, 823-832.

Wei, F., Lu, F., Jin, Y., and Yu, Z., 1997, "Mass Flux Profiles in a High Density Circulating Fluidized Bed," *Powder Technology*, 91, 189-195.

Werther, J., 1999, "Measurement Techniques in Fluidized Beds," *Powder Technology*, 102, 15-36.

Williams, K. A., 2006, http://www.arena-flow.com/, January 13, 2006.

Williams, K. A., and Snider, D. M., 2002, *Arena-flow User's Manual*, Arena-flow, LLC, Albuquerque, NM.

Williams, K. A., and Snider, D. M., 2003, *Reflection Algorithm*, Technical Note 55, Arena-flow, LLC, Albuquerque, NM.

Williams, K. A., Snider, D. M., Torczynski, J. R., Trujillo, S. M., and O'Hern, T. J., 2004, "Multiphase Particle-in-Cell Simulations of Flow in a Gas-Solid Riser," paper HT-FED2004-56594, American Society of Mechanical Engineers, New York, NY.

Williams, P., and York, T., 1999, "Evaluation of integrated electrodes for electrical capacitance tomography," 1st World Congress on Industrial Process Tomography, Buxton, Greater Manchester, April 14-17, 1999.

Xu, G., Sun, G., and Gao, S., 2004, "Estimating radial voidage profiles for all fluidization regimes in circulating fluidized beds," *Powder Technology*, 139(2), 186-192.

Xu, S., and Pless, L., 2005, "Scan/Simulation Integrated Diagnostics for Distillation Improvement," AIChE Spring Meeting, presentation at Distillation Symposium.

Yang, W.-C., editor, 2003, Handbook of Fluidization and Fluid-Particle Systems, Marcel Dekker Inc., New York.

Zhang, D. Z., VanderHeyden, W. B., and Kashiwa, B.A., 1999, "Investigation of subgrid drag models for fluidized bed simulations," presented at the 52nd Annual Meeting of the American Physical Society, Division of Fluid Dynamics, New Orleans, LA.

Zhang, D. Z., and VanderHeyden, W. B., 2000, "Macroscopic equations for gas solid two-phase flows in fluidized beds," presented at the 53rd Annual Meeting of the American Physical Society, Division of Fluid Dynamics, Washington D.C.

Zhang, D. Z., and VanderHeyden, W. B., 2001a, "Modeling and Simulation of the Effects of Mesoscale Structures in Circulating Fluidized Beds," *Proceedings of 4th International Conference on Multiphase Flows*, New Orleans, LA.

Zhang, D. Z., and VanderHeyden, W. B., 2001b, "High-resolution three-dimensional numerical simulation of a circulating fluidized bed," *Powder Technology,* 116, 133-141.

Zhang, D. Z., and VanderHeyden, W. B., 2002, "The effects of mesoscale structures on the macroscopic momentum equations for two-phase flows," *International Journal of Multiphase Flow*, 28(5), 805-822.

Zhang, H., Johnston, P. M., Zhu, J.-X., de Lasa, H. I., and Bergougnou, M. A., 1998, "A Novel Calibration Procedure for a Fiber Optic Solids Concentration Probe," *Powder Technology*, 100, 260-272.

Zhang, H., and Zhu, J.-X., 2000, "Hydrodynamics in Downflow Fluidized Beds (2): Particle Velocity and Solids Flux Profiles," *Chemical Engineering Science*, 55, 4367-4377.

Zhang, W., Tung, Y. and Johnsson, F., 1991, "Radial voidage profiles in fast fluidized beds of different diameters," *Chemical Engineering Science*, 46(12), 3045-3052.

Zhang, W., Johnsson, F., and Leckner, B., 1995, "Fluid-Dynamic Boundary Layers in CFB Boilers," *Chemical Engineering Science*, 50(2), 201-210.

Zhou, J., Grace, J. R., Qin, S., Brereton, C. M. H., Lim, C. J., and Zhu, J., 1994, "Voidage Profiles in a Circulating Fluidized Bed of Square Cross-Section," *Chemical Engineering Science*, 49(19), 3217-3226.

DISTRIBUTION:

Muthanna Al-Dahhan
Washington University
Department of Chemical Engineering
One Brooking Drive, Campus Box 1198
St. Louis, MO 63130-4899

Sibashis Banerjee
Millennium Chemicals
6752 Bay Meadow Drive
Glen Burnie, MD 21060

Francine Battaglia
Iowa State University
Mechanical Engineering
3027 Black Engineering
Ames, IA 50011-2161

Satish Bhusarapu
Harper International Corporation
100 West Drullard Avenue
Lancaster, NY 14086

Jerry Boyle
National Energy Technology Laboratory
3610 Collins Ferry Road
P.O. Box 880, Mail Stop NO4
Morgantown, WV 26507-0880

Steven L. Ceccio
The University of Michigan
Mechanical Engineering & Applied Mechanics
2043 W. E. Lay Automotive Laboratory
1231 Beal Ave.
Ann Arbor, MI 48109-2121

Raymond A. Cocco
Particulate Solid Research, Inc.
4201 W. 36th St., Suite 200
Chicago, IL 60632

C. Stuart Daw
Oak Ridge National Laboratory
P. O. Box 2009, MS8088
One Bethel Valley Rd
Oak Ridge, TN 37831-8088

Thomas M. Dayton
AEA Technology
Engineering Software Inc.
Omega Corporate Center
1260 Omega Drive
Pittsburgh, PA 15205

Eduardo D'Azevedo
Oak Ridge National Laboratory
Computer Science & Mathematics Division, Mathematical Sciences Section
P. O. Box 2008
Bldg 6012, Rm. 117
Oak Ridge, TN 37831-6367

Milorad Duduković
Washington University
Department of Chemical Engineering
One Brooking Drive, Campus Box 1198
St. Louis, MO 63130-4899

Charles E. A. Finney
Oak Ridge National Laboratory
Power Systems Section
Engineering Technology Division
P. O. Box 2009
Oak Ridge, TN 37831-8088

James A. Fort
Pacific Northwest National Laboratory
P. O. Box 999, MS K7-15
Richland, WA 99352

Rodney O. Fox
Iowa State University
Chemical Engineering
2119 Sweeney Hall
Ames, IA 50011-2230

Susan J. Gelderbloom
Dow Corning Corporation
P. O. Box 995
Midland, MI 48686-0995

Dimitri Gidaspow
Illinois Institute of Technology
Chemical & Environmental Engineering
10 West 33rd Street
Chicago, IL 60616-3793

Chris Guenther
Fluent, Inc.
National Energy Technology Laboratory
3647 Collins Ferry Road, Suite A
Morgantown, WV 26505

Ahmad Haidari
Fluent, Inc.
10 Cavendish Court
Centerra Resource Park
Lebanon, NH 03766-1442

Jeffery P. Henning
AEA Technology
Engineering Software Inc.
CFX Consulting Services
Omega Corporate Center
1260 Omega Drive
Pittsburgh, PA 15205

Bruce D. Hook
The Dow Chemical Company
B-1402 Building, Texas Operations
2301 Brazosport Blvd.
Freeport, TX 77541

John D. Hottovy
Chevron Phillips Chemical
Kingwood Technical Center
1862 Kingwood Dr., 3107 Bldg. 3
Kingwood, TX 77339

Christine M. Hrenya
University of Colorado at Boulder
Chemical Engineering
Engineering Center ECCH 118
Campus Box 424
Boulder, CO 80309

Rob Johnson
ExxonMobil Research & Engineering
3225 Gallows Road, Room 7A1925
Fairfax, VA 22037

Ian P. Jones
AEA Technology
8.19 Harwell
Didcot, Oxfordshire, UK OX11 0RA

S. B. Reddy Karri
Particulate Solid Research, Inc.
4201 W. 36th St., Suite 200
Chicago, IL 60632

Bryan A. Kashiwa
Los Alamos National Laboratory
Theoretical Div., Fluid Dynamics Group
MS B216
Los Alamos, NM 87545

Ted M. Knowlton
Particulate Solids Research Institute
4201 W. 36th St., Suite 200
Chicago, IL 60632

Kostas Kontomaris
E. I. DuPont de Nemours
Central Research & Development
Experimental Station
P. O. Box 80304
Wilmington, DE 19880-0304

Robert W. Lyczkowski
Argonne National Laboratory
Energy Systems Division
Bldg 362 Room C348D
9700 South Cass Avenue
Argonne, IL 60439-4815

Heshmat Massah
Fluent, Inc.
Centerra Resource Park
10 Cavendish Court
Lebanon, NH 03766-1442

John B. McLaughlin
Clarkson University
Department of Chemical Engineering
Potsdam, NY 23699-5705

Paul H. Merz
Chevron Research and Technology Co.
100 Chevron Way, P. O. Box 1627
Richmond, CA 94802-0627

Reza Mostofi
UOP LLC
25 East Algonquin Road
Des Plaines, IL 60017-5017

Michael E. Muhle
ExxonMobil Chemical Company
Baytown Polymers Center
5200 Bayway Dr.
Baytown, TX 77520-2102

Thomas J. O'Brien
NETL, U.S. Department of Energy
P.O. Box 880, MS NO4
Morgantown, WV 26507-0880

Dickson Ozokwelu
U. S. Department of Energy
Energy Efficiency & Renewable Energy
Office of Industrial Technologies
EE-20, Office of Industrial Process Systems
1000 Independence Ave. NW
Washington, DC 20585-0121

Sreekanth Pannala
Oak Ridge National Laboratory
Computer Science & Mathematics Div.
Mathematical Sciences Section
P. O. Box 2008, Bldg. 6012
Oak Ridge, TN 37831-6367

Rutton D. Patel
ExxonMobil Research & Engineering
Reactor & Fluid Dynamics Section
3225 Gallows Road, Room 7A2136
Fairfax, VA 22037

David W. Pfund
Pacific Northwest National Laboratory
P. O. Box 999, MS K7-15
Richland, WA 99352

Peter W. Runstadler
Fluent, Inc.
10 Cavendish Court
Centerra Resource Park
Lebanon, NH 03766-1442

Paul Scheihing
U. S. Department of Energy
Energy Efficiency & Renewable Energy
Office of Industrial Technologies
EE-20, Office of Industrial Process Systems
1000 Independence Ave. NW
Washington, DC 20585-0121

William W. Schultz
University of Michigan
Mechanical Engineering & Applied
Mechanics
2027 W. E. Lay Automotive Laboratory
1231 Beal Ave.
Ann Arbor, MI 48109-2121

Larry Shadle
NETL, U.S. Department of Energy
P. O. Box 880
Morgantown, WV 26507-0880

Kim A. Shollenberger
Mechanical Engineering Department
California Polytechnic State University
San Luis Obispo, CA 93407

Jennifer L. Sinclair Curtis
University of Florida
Chemical Engineering Building Room 229
P. O. Box 116005
Gainesville, FL 32611-6005

Dale Snider
Arena-flow, LLC
10899 Montgomery Blvd. NE
Albuquerque, NM 87111

Sankaran Sundaresan
Princeton University
Chemical Engineering
A-315, Engineering Quadrangle
Princeton, NJ 08544

Madhava Syamlal
Fluent, Inc.
National Energy Technology Laboratory
3610 Collins Ferry Road
Mail Stop MO2
Morgantown, WV 26507-0880

Tyler B. Thompson
The Dow Chemical Company
Corp. R&D, External Technology
1776 Building
Midland, MI 48674-1776

James M. Tippett
DuPont
Central R&D/Materials Sci & Eng
Experimental Station
P. O. Box 80356
Wilmington, DE 19880-0356

Brian Valentine
U. S. Department of Energy
Energy Efficiency & Renewable Energy
Office of Industrial Technologies
EE-20, Office of Industrial Process Systems
1000 Independence Ave. NW
Washington, DC 20585-0121

W. Brian VanderHeyden
Los Alamos National Laboratory
Theoretical Division
Fluid Dynamics Group, T3
Mail Stop B216
Los Alamos, NM 87545

Sergio Vasquez
Fluent, Inc.
10 Cavendish Court
Centerra Resource Park
Lebanon, NH 03766-1442

Ken Williams
Arena-flow, LLC
10899 Montgomery Blvd. NE
Albuquerque, NM 87111

Yun Xiong
Millennium Chemicals
Research Center – Baltimore
6752 Bay Meadow Drive
Glen Burnie, MD 21060

Wen-Ching Yang
Siemens Westinghouse Power Corporation
Science and Technology Center
1310 Beulah Road
Pittsburgh, PA 15235-5098

Duan Z. Zhang
Los Alamos National Laboratory
T-3, MS B216
Los Alamos, NM 87545

Hardcopies to:

1	MS 0828	A. C. Ratzel, 1500
1	MS 0824	W. L. Hermina, 1510
1	MS 0834	R. D. M. Tachau, 1512
1	MS 0826	D. J. Rader, 1513 (actg.)
1	MS 0834	J. S. Lash, 1514
1	MS 0825	B. Hassan, 1515
1	MS 0836	E. S. Hertel, 1516
1	MS 0836	R. O. Griffith, 1517
1	MS 0885	J. E. Johannes, 1810
1	MS 0734	J. B. Kelley, 6245
1	MS 0521	M. R. Prairie, 2520
2	MS 9018	Central Technical Files, 8944
2	MS 0899	Technical Library, 4536

Electronic only:

MS 0834	J. B. Oelfke, 1512
MS 0834	T. J. O'Hern, 1512
MS 0834	P. R. Tortora, 1512
MS 0834	S. M. Trujillo, 1512
MS 0826	J. R. Torczynski, 1513
MS 0828	A. A. Giunta, 1533